2017

Quantitative Ultrasonic Coda Wave (Diffuse Field) NDE of Carbon-Fiber Reinforced Polymer Plates

Richard Livings
Iowa State University

Quantitative ultrasonic coda wave (diffuse field) NDE of carbon-fiber reinforced polymer plates

by

Richard A. Livings

A dissertation submitted to the graduate faculty

in partial fulfillment of the requirements for the degree of

DOCTOR OF PHILOSOPHY

Major: Engineering Mechanics

Program of Study Committee:
Vinay Dayal, Major Professor
Dan J. Barnard
Nicola Bowler
Ambar K. Mitra
Ronald A. Roberts

Iowa State University

Ames, Iowa

2017

DEDICATION

To my wife, Christelle.

Without your patience, support and unending love, none of this would have been possible. Thank you for sticking by me through the long days and late nights and through all of the difficult and easy times. This work has been a long time coming, and I owe it all to you.

TABLE OF CONTENTS

LIST OF FIGURES

LIST OF TABLES

TABLE OF SYMBOLS

M	Mean
Σ	Standard deviation
Ω	Electrical impedance
ΔF	Width of frequency window
ΔT	Width of time window
α	Attenuation coefficient
β	Fitting coefficient
γ	Scale factor to minimize the mean squared error
ν	Poisson's ratio
δ	Delta function
ζ	Wiener filter stabilization constant
ε	Dilation factor
ε_f	Floating point relative accuracy
ε_{LS}	Least squares standard error
ε_t	Uncertainty in time measurements
ε_{temp}	Uncertainty in the temperature measurement
ε_{therm}	Uncertainty caused by the thermocouple
ε_{sensor}	Uncertainty caused by the sensor
τ	Time delay
ρ	Density
η	Waveform distortion function
μ	Micro
λ	Wavelength
ξ	Material dependent scaling factor
σ	Dissipation constant
θ	Angle
A	Ampere
C	Celsius
C_0	Coefficient, function of E_0 and D
CC	Cross-correlation coefficient
$CFRP$	Carbon Fiber Reinforced Polymer
$CSMW$	Cross-Spectral Moving-Window
CWI	Coda Wave Interferometry
c_i	Wave velocity of the ith mode
D	Diffusivity constant
D_S	Difference spectrum
DCL	Differential curve length
DI	Damage Index
d	Hole diameter
dB	Decibel

E	Ultrasonic Energy
E_0	Initial energy deposited by transmitter
E_{res}	Energy of the residual
$E_{res\text{-}spec}$	Modeled spectral energy of the residual
$E_{res\text{-}temp}$	Modeled temporal energy of the residual
E_S	Spectral energy
E_{spec}	Spectral energy of the residual
E_T	Temporal energy
E_{temp}	Temporal energy of the residual
E_W	Acoustic wave energy density
F	First received signal pulse used in pulse-overlap attenuation
f	Frequency
f_C	Window center frequency
f_S	Sampling frequency
G	Second received signal pulse used in pulse-overlap attenuation
GPa	GigaPascal
h	Plate thickness
J	Joule
j	Imaginary unit
k	Wavenumber
L	Number of points in frequency-domain window
$LoCoh$	Loss of coherence
$LoCor$	Loss of correlation
l	Index for points in frequency-domain window
M	Number of points in time-domain window
m	Index for points in time-domain window
N	Number of points in time-domain signal
n	Index for points in time-domain signal
n_C	Index of time-domain window center
P_S	Power spectrum
P_T	Total spectral power
p	Index for points in frequency-domain signal
p_C	Index of frequency-domain window center
$p2p_{amp}$	Peak to peak amplitude
Q	Quality factor
R	Reflection coefficient
R^2	Coefficient of determination
R_{ij}	Cross-correlation function between signal i and signal j
$RMSE$	Relative Mean Squared Error
r	Distance
SNR	Signal-to-Noise Ratio
T	Temperature
T_r	Transmission coefficient
T_L	Length of time domain signal
T_S	Sampling period of time domain signal
t	Time

t_C	Window center time
t_{first}	Time of first arrival
t_p	Arrival time of peak amplitude
V	Volts
v	Wave velocity
v_L	Wave velocity of the longitudinal mode
v_S	Wave velocity of the shear mode
W	Wiener filter
w	Window function
$w_{LS\text{-}i}$	Least squared weight applied to ith data point
X	Frequency-domain signal
x	Time-domain signal
$x_{LS\text{-}i}$	Least squares ith data point
y	Peak amplitude
$O( )$	"Order of" operator
< >	Ensemble average operator
"	Inches

ACKNOWLEDGEMENTS

I would like to thank my advisor, Dr. Vinay Dayal, for his guidance and patience. Throughout my program, Dr. Dayal always gave me the freedom to pursue my own ideas and provided valuable guidance and support. I am grateful for his eagerness and "let's do it" attitude and for all the exciting discussions on an endless list of scientific, political, philosophical, and personal topics. The door to Dr. Dayal's office was always open and he was always there to listen to my questions, ideas, and problems, especially when I was questioning myself, my PhD, and all of academia. Thank you for supporting me through my PhD.

I thank Dr. Bond for joining my committee as a co-advisor for the last few years of my program. Dr. Bond helped me get my thesis on track, encouraged me to develop more quantitative research skills, and greatly assisted with scientific writing.

My very special gratitude goes to Dan Barnard for his constant enthusiasm, optimism, and great advice. Every experiment started by consulting Dan, and he was always available to help troubleshoot issues and brainstorm interpretation of the results, especially when nothing seemed to work. Dan always treated me as a colleague instead of a student, and that is extremely encouraging. Thanks for all of the great discussions.

I am very grateful for having an exceptional doctoral committee and thank Dr. Nicola Bowler, Dr. Ambar Mitra, Dr. Thomas Rudolphi, and Dr. Ron Roberts for their continual support, encouragement, and tough questions.

My appreciation is due to all of my friends and colleagues that accompanied me for a graduate degree. To Bharat Agrawal, Fangliang Gao, Ruchir Goshwami, Kasra Momeni, Dave

Sikorski, Xiao Wang, Andrew White, and Ben Zimmerman. Thank you for your friendship, support, great conversations, and editing services, they mean the world to me. I extend my thanks to all the students and faculty not explicitly mentioned who have touched my life, for their friendship and encouragement.

This research was funded by the NSF Industry/University Cooperative Research Program of the Center for Nondestructive Evaluation at Iowa State University, and I am grateful for the support.

ABSTRACT

The increasing presence and applications of composite materials in aerospace structures precipitates the need for improved Nondestructive Evaluation (NDE) techniques to move from simple damage detection to damage diagnosis and structural prognosis. Structural Health Monitoring (SHM) with advanced ultrasonic (UT) inspection methods can potentially address these issues. Ultrasonic coda wave NDE is one of the advanced methods currently under investigation. Coda wave NDE has been applied to concrete and metallic specimens to assess damage with some success, but currently the method is not fully mature or ready to be applied for SHM. Additionally, the damage diagnosis capabilities and limitations of coda wave NDE applied to fibrous composite materials have not been widely addressed in literature. The central objective of this work, therefore, is to develop a quantitative foundation for the use of coda wave NDE for the inspection and evaluation of fibrous composite materials.

Coda waves are defined as the superposition of late arriving wave modes that have been scattered or reflected multiple times. This results in long, complex signals where individual wave modes cannot be discriminated. One method of interpreting the changes in such signals caused by the introduction or growth of damage is to isolate and quantify the difference between baseline and damage signals. Several differential signal features are used in this work to quantify changes in the coda waves which can then be correlated to damage size and growth. Experimental results show that coda wave differential features are effective in detecting drilled through-holes as small as 0.4 mm in a 50x100x6 mm plate and discriminating between increasing hole diameter and increasing number of holes. The differential features are also shown to have an underlying basis

function that is dependent on the hole volume and can be scaled by a material dependent coefficient to estimate the feature amplitude and size holes.

The fundamental capabilities of the coda wave measurements, such as error, repeatability, and reproducibility, are also examined. Damage detection was found to be repeatable, reproducible, and relatively insensitive to noise. The measurements are found to be sensitive to thermal changes and absorbing boundaries. Several propagation models are also presented and discussed along with a brief analysis of coda wave signals and spectra.

CHAPTER 1. INTRODUCTION

1.1 Usage and Nondestructive Inspection of Composites in Aircraft

As composites see increased usage in aircraft components, especially critical load bearing structures, the high quality of composite components is essential for reliability and safety. The increase in composite usage from 2% in 1978 to more than 50% by weight in recent years is illustrated in Figure 1-1. Structural components must be free from defects, both production defects and in-service damage/degradation, that would significantly reduce the stiffness, strength, and design life. Regulatory agencies such as the Federal Aviation Administration (FAA) set limits on the minimum remaining strength of a component with damage **[**FAA 2009**]**. Figure 1-2 illustrates the conceptual design loads for increasing damage size. The minimum load is the estimated in-service load which must be sustained, even with damage above the critical size. The limiting and ultimate loads are the sustainable loads of an equivalent structure with damage below the critical threshold and the detectable threshold respectively. The structure must be able to withstand the limiting load even with preexisting damage that grows to the critical damage threshold in between inspections. The estimated time for damage to grow from undetectable to critical therefore dictates an inspection schedule to ensure that any in-service damage is detected while it is in the subcritical stage [Fahr 2014].

A damage tolerant design is required by the FAA for most civilian aircraft. The damage sizes that must be detected and the critical flaw sizes for each component are determined by a combination of analytical and experimental analyses [FAA 2009, Fahr 2014]. Figure 1-3

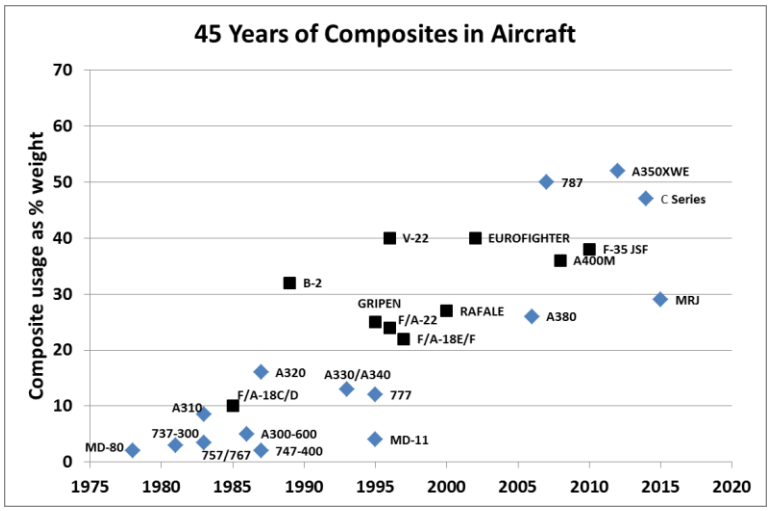

Figure 1-1. Increasing composite usage in commercial (blue diamonds) and military (black squares) aircraft by percent weight. [Compiled from various sources]

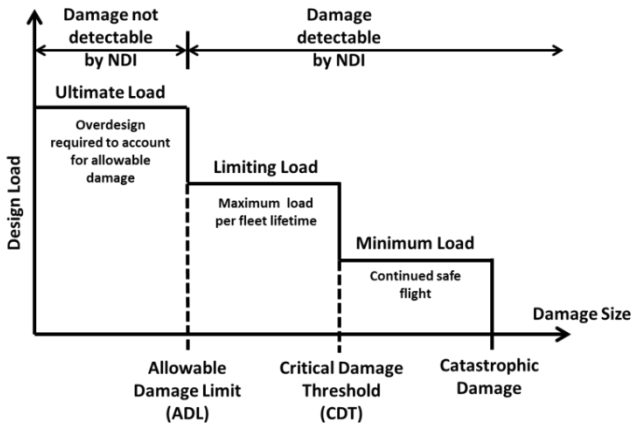

Figure 1-2. Conceptual design loads for increasing damage size. Continued safe flight is required such that an aircraft can operate safely before the damage is detected.

illustrates the reduction in strength of a component due to processing anomalies, damage, and operating conditions. All NDE methods have a "minimum detectable flaw size" capability and a "largest defect missed" limitation, with their statistical variability. FAA regulations require these to be taken into account when designing the inspection guidelines and schedules. On the other hand, composite structures have their inherent manufacturing damage thresholds. As a result of

these two considerations, composite structures are over-designed to compensate for these limitations [Mouritz 2012, Siddiqui 2015]. Improved performance can be obtained by doing the following: (a) Improve damage tolerance (design consideration), (b) improve damage resistance (material consideration), and (c) improve damage detection and characterization (NDT&E consideration). Increasing the sensitivity of nondestructive inspection techniques will allow for the decrease in the Allowable Damage Limit and hence reduce component overbuilding.

Nondestructive Inspection (NDI) of in-service aircraft requires grounding and disassembly while inspection of components during manufacturing can add to the production time and cost by as much as 50% [Mouritz 2012]. Structural Health Monitoring (SHM) systems are therefore of great interest to the aviation industry because in-situ monitoring would greatly reduce the required down time for inspections [Mouritz 2012, Karbhari 2013, Fahr 2015, Siddiqui 2015]. Improved sensitivity and characterization capabilities of NDI techniques will allow for longer periods between scheduled inspections or the use of optimal laminates because the subcritical damage could be detected in a timely manner.

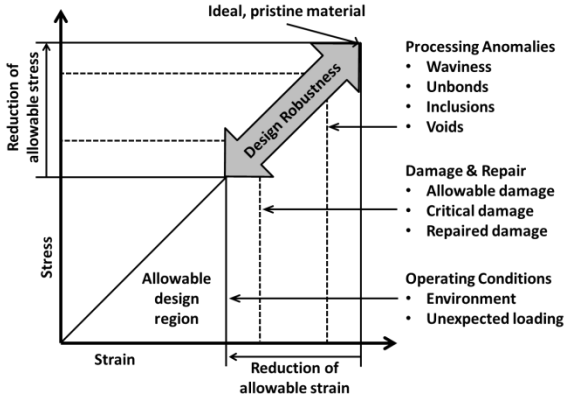

Figure 1-3. Conceptual diagram of designing with anomalies, damage, and other allowables in mind.

When considering ultrasonic NDT&E/SHM, composites must be regarded as very different from metals. Composites tend to be dispersive and highly attenuative to ultrasound (due to both scattering and visco-elastic energy absorption), have low electrical and thermal conductivity, and have significant anisotropy. Composite damage is also multi-modal with different size scales, such as micro-cracks, delaminations, fiber failure, and matrix crushing to name a few. As a result, the damage detection also has to work for different modalities and size scales. Micro-cracks are sub-millimeter in size while delaminations range in size from millimeters to centimeters in diameter spread over the inter-laminar region. There is a continuous need for further development of quantitative NDE techniques for composite inspection that address the technical challenges of microdamage (damage such as microcracking, fiber breakage, and fiber-matrix debonding) sensitivity, lay-up insensitivity, and quick, efficient inspection. [Schwartz 1997, Baker et al. 2004, ASTM 2009, Barbero 2011, ASTM 2012, Hsu 2013]

Nondestructive techniques are based on the detection of damage or defects by observing the change in one or more parameters of the technique being used. In the case of Ultrasonics, the differential parameter is often the arrival time or the amplitude of the received signal. There are a multitude of NDE techniques that have been developed over the past 50 years or so. Each has its specific field of applicability along with specific strengths and limitations, though there is overlap in sensitivity and accuracy of detection. NDE techniques can be divided into three large categories based on how the technique interacts with the test article. Selected techniques are shown in Figure 1-4 organized by frequency of excitation and interaction type.

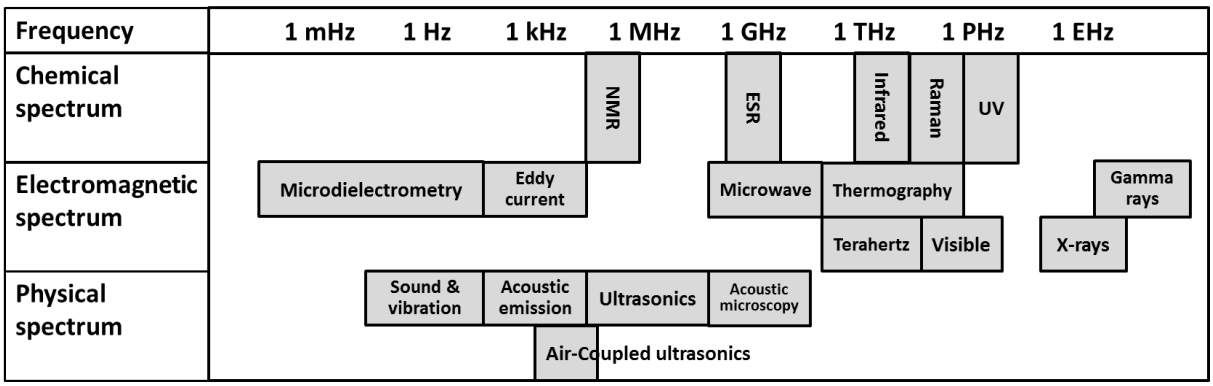

Figure 1-4. Frequency spectrum for selected NDE techniques. ESR = electron spin resonance, NMR = nuclear magnetic resonance. [Recreated and expanded from Schwartz 1997 & Jones 1998]

The literature on the detection and characterization of damage in composites is staggeringly extensive; mostly due to the complex nature of composite materials and damage. The early literature has been reviewed by Schwartz (1997) and Jones (1998), while modern overviews of composite NDE as applied to aerospace structures are given by Mouritz (2012), Karbhari (2013), Fahr (2014), and Siddiqui (2015). There are multiple NDE techniques used with composites, and some of the most popular techniques fall into the categories of (a) visual inspection, (b) tap testing, (c) ultrasonics, (d) acoustic emission, (f) X-ray CT, (g) thermography, and (h) eddy current. Irrespective of the technique employed, the central objective is the accurate detection and localization of the smallest possible defect sufficiently in advance of a failure causing event. Note that for most techniques, the sensor must be directly over (or nearly) the damage.

Ultrasonic guided wave techniques (Rayleigh and Lamb waves) have been the subject of extensive research because the mechanical vibrations interact directly with damage and can travel farther than bulk waves [Michaels 2008]. Rose (2000) provides an overview of guided wave NDE [Rose 2000] while Cawley & Simonetti (2005) and Raghavan & Cesnik (2007) give overviews of guided wave SHM and Su et al. (2006) review guided waves for damage detection in composite

materials. Two major limitations of guided wave methods are that the methods are restricted to components that support their propagation and that for most, if not all, methods require identifying and interpreting individual modes and echoes [Micheals 2008]. Another common limitation is that the damage must be along the propagation path between the transducers unless an array of transducers is used.

Recently, coda waves have been proposed as a way to overcome the limitations of guided waves, which can be easily generated and don't require the identification of specific modes/echoes [Michaels & Michaels 2005, Lu 2007]. The primary advantages of coda waves for SHM are the potentially increased sensitivity to small scale defects and the volumetric interrogation, which means that the damage need not be directly between the transducers to be detected. The primary drawbacks of this technique are the increased sensitivity to environmental effects (e.g. temperature) and the lack of theoretical/computational models to explain the effect of damage on the coda wave.

A coda wave (also referred to as a diffuse field) is a complex superposition of wave modes, both scattered from internal micro-structures and reflected from boundaries over a sufficiently long time period. A good, simple description is a late arriving wave in which specific wave modes are not separable or identifiable. More technical definitions include a wave field created by: 1) statistical summation of random walk ray-paths [Snieder 2006], 2) pseudo-random diffusion of acoustic energy through a highly scattering medium [Anugonda et al. 2001], or 3) equal amplitude excitation of all independent wave modes for all propagation directions and frequencies with uniformly distributed random phases [Egle 1981]. A wave field as strictly defined by Egle (1981) is rarely realizable in practice [Weaver & Lobkis 2000].

Even though these long duration, multiply scattered waveforms have been known to the NDE community for nearly four decades [Vary 1982], their sensitivity and reliability are questionable because the complex waveforms resulting from coda wave NDE are difficult to analyze, interpret, or simulate with physical models. Traditional ultrasonic NDT&E relied on a deterministic wave and its classical properties such as wave velocity, attenuation, and reflection coefficient. These properties are physically understandable and mathematically defined. In the case of coda waves, these properties become undefinable or inapplicable as a coda wave is not a wave but an ensemble sum of wave modes arriving at the receiver from multiple directions and with various time delays.

Although traditional NDT&E has focused on detection, localization, and characterization of the smallest possible defect, there has been a growing recognition in recent years that the largest defect missed and the probability of detection (POD) play a significant role in the assessment of structural health [Bond 2015]. Structural damage may be missed during an inspection due to any one of a multitude of factors (e.g. frequency of interrogating signals, low signal-to-noise ratios, large raster scan steps, and of course human factors).

The reliability of an NDT&E/SHM method is quantifiable by the POD, which takes into account both the physical limitations of detecting small damage and the measurement limitations due to variability that can mask damage [Adams 2007]. The objective is to estimate the typical number of defects missed for a given damage type and size, and thus the largest damage missed by a particular technique. Often POD studies include a large number of representative samples with various flaw types and sizes as well as a large number of human operators [Fahr 2014]. Since most SHM systems are typically automated, the system performance is potentially better described by the receiver operating characteristic (ROC) which plots the true positive rate (also referred to

as the POD) versus the false positive rate based on varying the amplitude threshold between damaged/undamaged for a specific damage index. This is potentially a better measure because it not only measures the likelihood of missing damage of a certain type/size but also the likelihood of false detection due to benign effects (e.g. environment, loading, or acoustic noise). The performance (ROC) of a coda wave SHM system for the detection of drilled through-holes in an aluminum plate in the presence of environmental changes is discussed by Lu and Michaels [Lu 2007, Michaels 2008].

Coda wave NDE is a paradigm change from traditional ultrasonic NDE where a coherent ballistic (direct propagation) wave followed a mathematically traceable path and everything could be described by a deterministic physical model as compared to an indeterministic, incoherent, wave field without a definable travel path. Traditional definitions of NDE parameters such as velocity, attenuation, and wavelength, which are used widely in ultrasonic NDE, become undefinable in this new paradigm due to the indeterministic nature of the wave field. Perhaps the name "coda ***wave***" is unfortunate since it leads people to try to analyze and understand the coda wave signals as actual propagating waves as opposed to the time-varying superposition field sampled at a specific point that they actually are. This thesis addresses questions such as: 1) what the coda wave is comprised of, 2) differentiating coda waves from what has traditionally been referred to as noise, 3) the subtle, nearly unobservable changes in the waveform caused by damage, and 4) what part of the waveform carries the damage information.

1.2 Motivation and Problem Statement

Guided wave interrogation has been extensively studied for both NDT&E and SHM interrogations of composite structures, but suffers from several major limitations. Coda wave SHM, on the other hand, is in the conceptual stage of development and shows promise, but it has to undergo extensive scrutiny before it can be considered seriously. This thesis focuses on several aspects of coda wave interrogation of CFRP plates to evaluate its capabilities and limitations. There are several attractive reasons to consider coda waves for composite SHM: 1) compared to ultrasonic guided waves, coda waves can almost always be generated regardless of geometrical or material complexity, 2) coda wave generation and reception is simple and structure independent, and 3) coda waves can potentially interrogate a larger complex volume with greater sensitivity than other methods, as noted by Lu (2007). That does not mean that an entire 787 wing assembly can be interrogated by a single transmitter-receiver pair. There is a limit to the propagation of coda waves just as there is for any physical phenomenon. Based on the above, coda wave NDT&E has a lot of potential for the interrogation of composite structures and is worthy of further investigation.

Although coda wave methods have shown some sensitivity to damage in concrete and metals [Lu 2007, Planes & Larose 2013], there are several technical obstacles to the adoption of the technique in general and for composite materials specifically. There are two aspects to the technical obstacles hindering the adoption of coda waves for NDT&E and SHM; the first aspect is the sensitivity to benign changes while the second is the analysis difficulties. It is well established that coda waves are sensitive to benign changes (unintended changes in the measurement system that are not damage but may affect the damage indices), such as environmental effects, loading, or transducer misplacement, that may mask damage [Lu & Michaels 2005, Snieder 2006, Weaver & Lobkis 2000, Zhang et al. 2013b]. It is also difficult to analyze the complex waveforms and

correlate changes to damage in a reliable and quantifiable manner. This is due in part to the qualitative manner in which damage has been typically introduced in previous coda wave applications (Alkali-Silica Reaction damage and stress/thermal induced micro-cracking in concrete) while the other part is the lack of good differential signal features to quantify the changes in the waveforms caused by damage.

It is because of the advantages and limitations of coda waves that this thesis focuses on developing a quantitative foundation for the use of coda wave NDE/SHM for the inspection and evaluation of fibrous composite materials. This work includes: 1) a demonstration of fundamental ultrasonic capabilities of coda waves such as: linearity, reciprocity, and reproducibility, 2) measurement of the spread and attenuation of coda wave acoustic energy in plates, 3) correlation of damage[1] in laminates to differential signal features in a quantifiable and reliable manner, 4) determination of the sensitivity of coda wave differential features to damage in fibrous composite plates, and 5) the first steps towards sizing and characterizing defects in fibrous composite plates. For the purpose of this thesis, drilled holes are used in the place of true damage since they are engineered discontinuities whose location, size, and quantity can be controlled.

1.3 Thesis Outline

The remainder of this thesis is organized as follows. Chapter 2 presents a review of the existing literature on diffuse fields and coda waves as they pertain to nondestructive evaluation and details the state of the art in order to provide a foundation upon which the work in this thesis

[1] The use of the word "damage" here refers to drilled holes. Even though it is understood that a drilled hole is not damage, the term "damage" has been used colloquially by many authors, most notably Dr. Jennifer Michaels, to refer to introduced discontinuities (whether engineered or otherwise) in samples.

builds. The review discusses the geophysical origins, the prior applications to NDT&E, as well as the parallel terminology that exists and is often interchanged. Overviews of wave propagation and scattering in composites and Structural Health Monitoring are also presented to provide a wider background for this work. The scope and objectives of the work presented in this thesis are placed in the context of previous research at the end of the chapter.

Chapter 3 presents a summary of the theory involved with coda wave propagation, decay, and measurements. First, several models found in literature are reviewed and discussed. The various measures of attenuation and temporal decay are then presented with a discussion as to the applicability of these measures to coda wave analysis. Lastly, various differencing parameters used to quantify changes in coda waves are examined along with the applicability of these paramaters to different quantities of interest (thermal vs damage).

Chapter 4 describes the experimental configurations, materials, and transducers used to investigate the subjects of this thesis. First, the materials used, sample dimensions and types of engineered damage are described. Then the experimental system is described and characterized. This includes basic transducer characterization and a discussion and measurement of the signal to noise ratio as well as a demonstration of coda wave reciprocity and an analysis of coda wave linearity. The data collection process is also discussed. Next a brief analysis of the coda wave waveforms and spectra is presented which includes a discussion of the scattering regimes encountered in Chapter 6. Finally, an overview of the error analysis approach used in this thesis is presented and discussed. This chapter is intended to be an overview of the experiments discussed in this thesis since each chapter is a different set of experiments.

Chapter 5 presents the experimental results for the propagation, attenuation, and boundary effects of coda waves in plates of several materials. The spreading function of coda waves in plates

is explored by examining changes in several wave parameters with increasing transducer separation and fiber angles. Several methods of measuring coda wave attenuation are then presented and the implications of each are discussed. The linearity of the spreading and attenuation parameters as well as their sensitivity to the pulser-receiver damping setting are then examined. Finally, the variation of the spreading and attenuation parameters due to the plate boundaries is presented and discussed.

Chapter 6 presents the experimental results for the quantitative detection and sizing of drilled through holes in plates of several materials. The definition of the five differential features used and the experimental error are discussed. Validation of the experimental system and signal processing against previously published work is presented. A function describing the behavior of the residual energy features is then derived. A comparison of the feature behavior for the several materials and introduced damage types is discussed and trend lines are fit to the data. The predicted functions are then fit to the experimental data and an estimate of defect sizing accuracy is presented. Towards the end of Chapter 6, the linearity of the differential features and effect of pulser-receiver damping are examined in addition to the reciprocity of defect detection.

Chapter 7 presents the experimental results for the measurement of thermally induced relative velocity variations in plates of several materials and for several transducers. The theory of waveform dilation (relative velocity change) caused by thermal loads and methods to measure the dilation are presented and discussed. A brief analysis of the differences in coda waveforms due to different transducer types and fiber orientations is presented. Next the measured relative velocity variations are examined, the results from different transducers and fiber orientation are compared, and the ramifications of using different transducers are discussed. The chapter ends with the

presentation and discussion of the significance of phase cancelation across the transducer face is examined

Chapter 8 concludes this thesis and provides recommendations for future research.

CHAPTER 2. BACKGROUND

This chapter serves as a review of diffuse fields and coda waves to provide the necessary background for the research presented in this thesis. First the several definitions of diffuse fields and coda waves are presented and discussed along with the distinguishing characteristics of coda wave NDT&E that sets it apart from several other NDT&E methodologies. Second, a brief overview of Acousto-ultrasonics, which is very closely related to coda wave NDE, is given. Next, an overview is given of the development and usage of coda waves as applied to the geophysics community. Then the literature involving that development and application of coda waves for the purpose of NDE is presented and discussed. Following this, the literature involving the application of coda wave NDE to fibrous composite materials is discussed. Next, a brief overview of wave propagation and scattering in fibrous composite materials is given in order to provide a foundation for interpreting the multiply scattered coda wave. Then a brief overview of SHM is given, with particular focus on guided wave SHM of fibrous composite materials is presented in order to provide a comparison of current capabilities with potential coda wave capabilities. Finally, the contributions of this thesis are placed within the context of the current state of the art regarding coda wave NDT&E.

2.1 Structural Health Monitoring

Monitoring critical structural components over their lifetime in order to improve early detection of damage and monitor damage growth is of great interest in many fields such as civil infrastructure and aerospace [Achenbach 2000, Karbhari 2013]. Structural health monitoring (SHM) involves the in-situ monitoring of structures to assess their integrity in near real time. An ideal SHM system should be able to detect, characterize, and locate damage in a structure (damage diagnosis) as well

as monitor its evolution with time and estimate the severity of the structure's reduction in performance (structure prognosis) [Adams 2007].

SHM is of great interest to the aviation industry because of the tight restrictions on structural damage and failure. Application of an SHM system in future aircraft will contribute to reduced maintenance costs, reduced aircraft down time, and improved safety. With the increasing use of composite materials in main structural members and the complex nature of composite damage formation and growth, the interest in the development of SHM systems is also increasing. The most widely applied SHM methodology for composite aerospace structures is guided wave ultrasonics, in which a stress wave travels along a component and changes in the received wave can be used to detect damage. The early literature on ultrasonic SHM has been reviewed by [Ihn & Chang 2003, Rose 2004, Giurgiutiu & Cuc 2005] while the application of SHM methods to aerospace structures is well reviewed by [Veidt & Liew 2013].

Ultrasonic interrogation methods are of interest for SHM due to their proven ability to detect and characterize flaws, as well as their ability to propagate long distances while still remaining sensitive to flaws [Michaels 2008]. Ultrasonic methods can be characterized as either active or passive. Passive methods such as acoustic emission record elastic waves generated by external sources such as propagating damage, leaks, or impacts. Active methods use transducer pairs to send and receive elastic waves. Active methods can be categorized as direct, where the structural assessment is based solely on the current measurement, or differential where the assessment is based on comparing the current measurement to a previous measurement. These methods can be characterized as local or global. A local method only examines a small area, or hot spot (known site of damage initiation, that is of particular interest while a global method examines a large area [Adams 2007, Lu 2007, Michaels 2008].

The limitation of interrogating a structure with guided waves is that they can only be used in structural components that support their propagation. Complex geometries make it difficult to generate guided waves and difficult to interpret the results since a further restriction on guided wave SHM is the need to identify specific wave modes and their arrival time. This is made all the more difficult by the multiple reflections that are likely to occur in hot spot regions.

An alternative ultrasonic method is the use of coda waves that are easily excited in a structure regardless of its geometry or complexity. Coda waves are generated by multiple reflections off of boundaries and multiple scattering due to microstructure. These waves reverberate throughout the structure, flooding it with energy, and effectively interrogating the entire structure. The use of these waves for structural health monitoring has been discussed by [Lu 2007, Michaels 2008, Sabra et al. 2008].

2.2 Wave Propagation and Scattering in Composites

Wave propagation and scattering in fibrous composite materials is significantly more complicated than metallic materials. Fibrous composites are non-isotropic, visco-elastic materials with periodic layers and highly scattering microstructure. The length scales for an example composite laminate are shown in Figure 2-1.

The propagation of elastic waves in generally anisotropic, homogeneous media yields three distinct bulk wave modes with directionally dependent velocities as described by the Christoffel equations [Auld 1973, Achenbach 1976, Rose 1999]. The directionally dependent velocities of the three orthogonal wave modes are shown in Figure 2-2 for a generic quasi-isotropic carbon-fiber/epoxy laminate, assuming an effectively homogeneous material model. Wave propagation in layered media yields further complications and is well discussed by Redwood (1960), Ewing

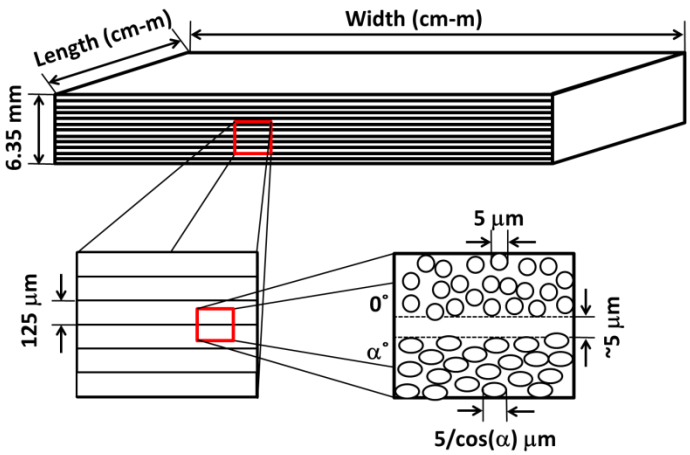

Figure 2-1. Various length scales of a typical Carbon Fiber Reinforced Polymer.

(1957), and Brekhovskikh (1980). Specific treatments of wave propagation in fibrous composites are given by Rokhlin et al. (2011) and Verma (2013) among others where periodic layering and homogenization are discussed. The effect of periodic layering, as occurs in most fibrous composite materials, on wave propagation can be described by Floquet waves, which may or may not exist in the laminate based on incident angle and frequency. The Floquet waves also describe a "homogenization" region where all wave modes exist for low frequencies and near normal incidence. The above analytical models for wave propagation were derived for a linearly elastic material, and although composite are visco-elastic in nature, the models apply equally well due to the elastic/visco-elastic correspondence principle [Achenbach 1976, Khazanovich 2008].

Apart from the challenges of wave propagation, composites also exhibit significant apparent attenuation caused by both internal scattering and visco-elastic absorption. Due to the various length scales found in a typical composite laminate (Figure 2-1) and the directional dependence of the wave velocities (Figure 2-2), several scattering regimes (Table 2-1) may be exist, especially when damage is present. Experimental demonstrations of scattering in composite materials for layer scattering, fiber scattering, and backscatter are given by Rokhlin et al. (2011),

Lee (1994), and Stenström (2008) respectively, while examples of experimental attenuation in composites are given by Verbis et al. (2001) and Kinra & Dayal (1988). Numerical models of scattering and attenuation of multiple wave modes in carbon-fiber/epoxy laminates are given by Biwa et al. [Biwa 2001, Biwa et al. 2003, Biwa et al. 2007, Sumiya et al. 2013], which are based on multiple scattering theories presented in multiple publications over the last forty years (such as [Bose & Mal 1974, Varadan et al. 1986, Yang & Mal 1994, Liu & Kriz 1998, Martin 2006, Conoir & Norris 2010]). The models developed by Biwa et al. show considerable promise for the modeling of coda wave generation and propagation in fibrous composites.

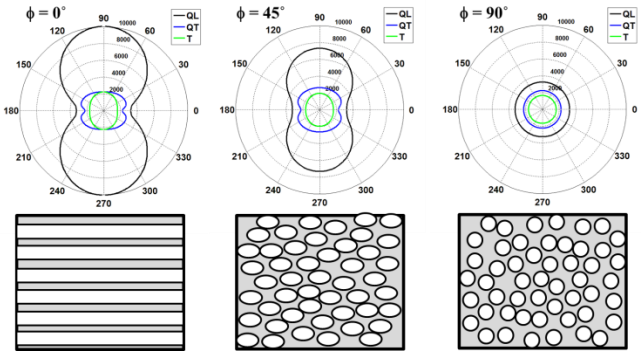

Figure 2-2. Velocity profiles for the three orthogonal wave modes in unidirectional CFRP. [recreated from Rokhlin, Chimenti, and Nagy 2011]

Table 2-1. Scattering regimes of ultrasonic waves. [modified from Eisminger and Bond 2011]

Regime	a/λ	Ultrasonic Attenuation
Rayleigh	<< 1	$\alpha = A_1 D^3 f^4$
Stochastic	≈ 1	$\alpha = A_2 D f^2$
Specular	>> 1	$\alpha = A_1 D$

λ = ultrasonic wavelength
a = average cross-section diameter of the scatterer
α = ultrasonic attenuation
A_n = elastic moduli dependent coefficient
f = ultrasonic frequency

2.3 Coda Wave Definition and Usage

Several terms exist that refer to a long duration wave field that has been scattered multiple times by internal structures and external boundaries, namely: Coda wave, Diffuse field, and Acousto-ultrasonic wave. Coda waves were first explored by the geophysics community starting from the 1960's [Aki 1969, Herraiz & Espinosa 1987] and began to see NDE applications in the 2000's [Planes & Larose 2013]. Diffuse fields were first used by the NDE community (the idea originated with room acoustics) in the 1980's [Weaver & Lobkis 2006] and have seen continued use, and after Lobkis & Weaver discovered that the Green's function could be reconstructed from the diffuse field [Lobkis & Weaver 2001], diffuse fields were adopted by the geophysics community [Weaver & Lobkis 2006]. Acousto-ultrasonic waves were first used by the NDE community to investigate the microstructure of composite materials in the 1980's [Vary & Bowles 1979, Vary 1991] and have seen continued, if limited use. Currently, both coda waves and diffuse fields are used by both the NDE and geophysics communities, and the terms are used somewhat interchangeably.

Although both of the terms "coda waves" and "diffuse fields" nominally refer to the same phenomenon and are used somewhat interchangeably, significant differences exist in the several definitions provided in literature. The early definition of coda waves was provided by Aki as: Late arriving elastic waves with no discernable wave modes which are likely caused by multiple scattering events [Aki 1969, Aki & Chouet 1975, Herraiz & Espinosa 1987]. In this definition, the reference to late arriving waves is used to describe the arrival of significant acoustic energy after the arrival of the ballistic[2] p- and s-waves as indicated in Figure 2-3. Snieder provided a slightly different definition for coda waves based on the assumption of multiple scattering. He defines coda

[2] The use of the term "ballistic" in this case refers to a direct, line-of-sight propagation path between the source and the receiver.

waves as: late arriving elastic waves comprised of multiple wave modes that have each taken different source to receiver paths due to multiple, strong scattering [Snieder 2002, Snieder 2006]. This definition allows for the presence of coda waves without a clear ballistic arrival and lends itself to analysis by a statistical random walk model. Examples of coda waves collected for NDE purposes are shown for Plexiglas and concrete in Figure 2-4 and Figure 2-5 respectively.

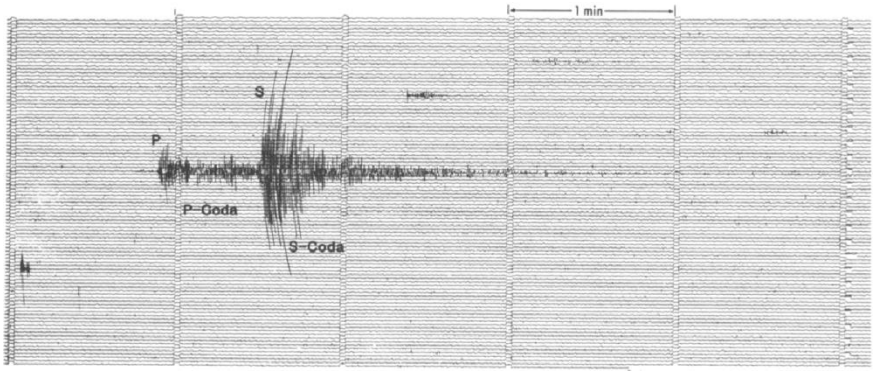

Figure 2-3. Example seismogram showing the arriving P and S waves and the resulting coda from each. [Herraiz & Espinosa 1987] with permission of Springer[3]"

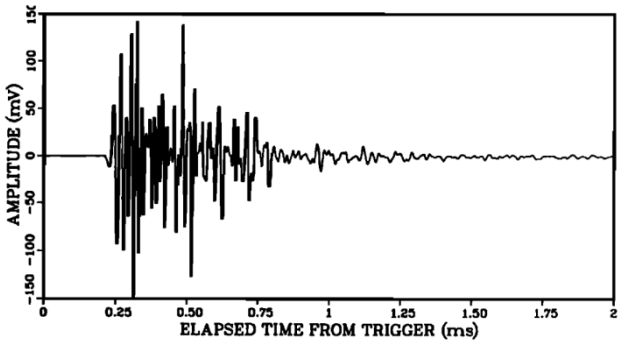

Figure 2-4. Typical coda waveform collected from 61x61x1.25 cm Plexiglas plate using 1 MHz epoxy backed piezo-discs in through transmission (edge-to-edge). Reprinted with permission from [Roberts P. M., Phillips W. S., and Fehler M. C., 1992, "Development of the active doublet method for measuring small velocity and attenuation changes in solids," *J. Acoust. Soc. Am.*, vol. 91, no. 6, pp. 3291-3302.]. Copyright 1992, Acoustic Society of America.

[3] Original title of Figure 2-3 is: "Figure 1 Sample seismogram, showing P- and S- codas, recorded at station GUD (Madrid, Spain), with an M_L = 3.7 at an epicentral distance of 337 km."

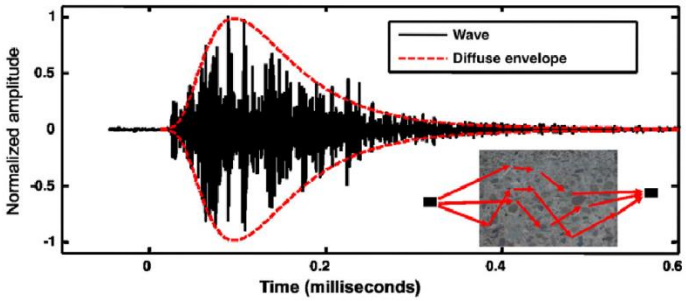

Figure 2-5. Typical normalized coda waveform collected from 20 cm of concrete using 500 kHz longitudinal transducers in through transmission. The best fit diffusion envelope (red dashed line) was determined by fitting the diffusion equation to the waveform. Reprinted from [Planes & Larose 2013]

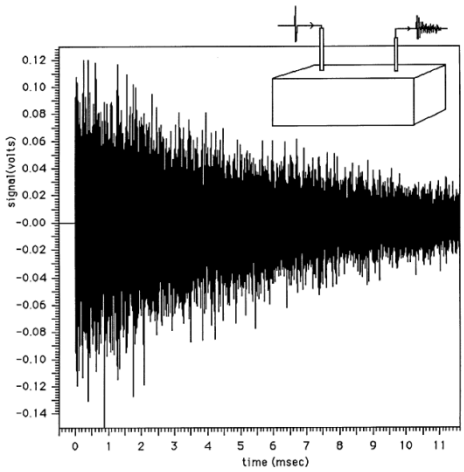

Figure 2-6. Typical diffuse waveform collected from 1.5x1.5x7.5 cm aluminum 6061 billet using pinducers in one-sided pitch-catch configuration. The first several hundred micro-seconds of the waveform have been discarded. Reprinted from [Weaver & Lobkis 2000]

The earliest definition for diffuse fields in solids given by Egle as: a field in which the modes of all propagation directions and frequencies are excited with random amplitudes and random, but evenly distributed phases [Egle 1981]. This definition was immediately modified by Weaver to be: a field in which all possible propagation modes are excited with equal energy and uncorrelated phases [Weaver 1982]. This definition is still one of the most widely cited, but primarily in the geophysics community. An example of a diffuse field waveform collected by

Weaver is shown in Figure 2-6. The main issue with the previous definitions of a diffuse field is that they are not realistically achievable in the majority of cases due to energy loss mechanisms. Nearly twenty years later, Anugonda et al. examined the diffuse field in terms of the propagation of acoustic energy through a highly scattering medium as a diffusion process [Anugonda et al. 2001] which has since become the standard definition of diffuse field in the NDE community.

Several years after the introduction of the diffusion model, Michaels & Michaels refer to the signals used in their work as "diffuse" yet they define the term using elements of both previous coda wave definitions and diffuse field definitions [Michaels & Michaels 2005]. An example of the waveforms collected by Michaels & Michaels is shown in Figure 2-7. Subsequent papers refer to their signals as coda waves, yet show the diffusion envelope such as Planes & Larose (2013) as shown in Figure 2-5. It is clear that there is some ambiguity concerning what term to use when referring to long duration waveforms without discernable wave modes that seem to be well described by the diffusion equation. As can be seen in figures below (Figure 2-4 - Figure 2-8), although the waveforms vary with material and geometry, all show the same basic behavior and should be unified under a single name. Note that the waveform collected by Weaver (Figure 2-6) begins collection right after the peak of the diffuse envelope.

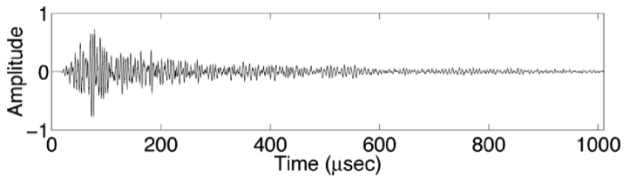

Figure 2-7. Typical normalized diffuse waveform collected from a 5x15.2x0.64 cm aluminum 6061 plate using 2.2 MHz epoxy backed piezo discs in one-sided pitch-catch. [Michaels & Michaels 2005]

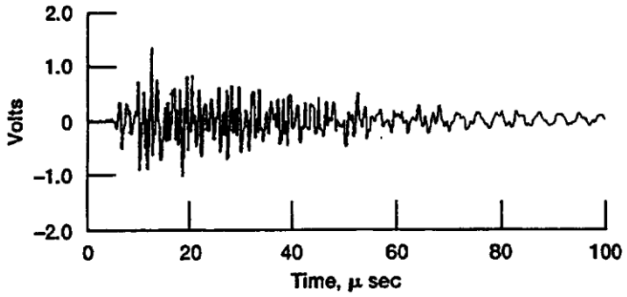

Figure 2-8. Typical diffuse waveform collected from a unidirectional SiC fiber/ RBSN CMC tensile specimen with 2.25 longitudinal transducers in one-sided pitch-catch. [Kautz 1993]

The definition of coda wave used in this thesis is as follows: A long duration waveform (typically hundreds of microseconds) that contains no discernable wave modes, is caused by multiply scattered and reflected wave modes that superimpose at the receiver, and is well fit by the diffuse field envelope. This definition is general enough to include the previous work in both diffuse fields and coda waves, yet is enough to distinguish coda waves from other NDE methods and waveforms.

Current analysis methods of coda wave NDE are no way dependent on knowing what wave modes are present in the structure, the path they took, or the geometry. This approach by previous researchers is due to the complexity of the signals caused by different modes arriving from all different directions with various phases, which interfere with each other and superimpose to create the coda wave. Several of the different possible wave types and ray paths are shown in Figure 2-9. The bulk waves generated by the input transducer will scatter multiple times, either off of the boundaries or the internal structure. Plate waves can be generated by the interaction of the longitudinal waves from the transducer and the shear waves generated by the transducer edges, but this is more prevalent for thin plates (less than a few millimeters). The plate/guided waves can be reflected multiple times for various paths between source and receiver. Coda wave analysis

methods are dependent, however, on repeatable system transfer functions such that the only difference present in measured signal compared to the baseline signal is the effects of damage. The multiple components of the system transfer function are shown in Figure 2-10.

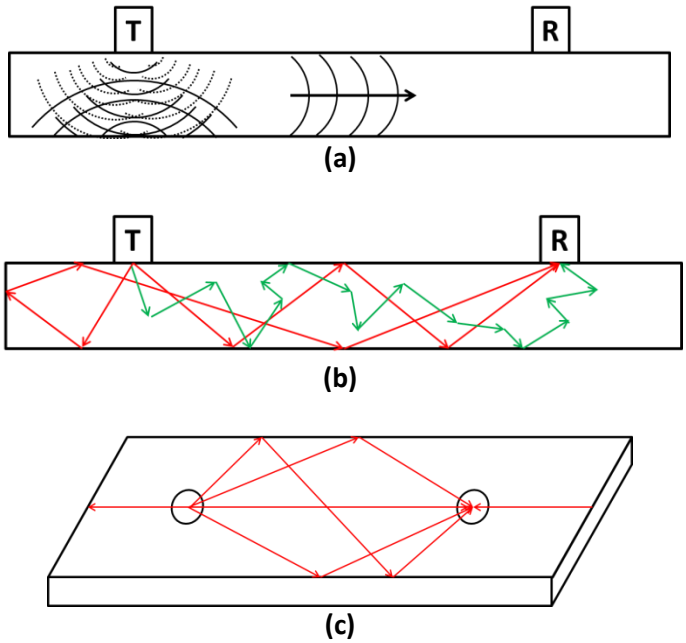

Figure 2-9. Conceptual diagram of the several wave propagation aspects that superimpose to form the coda wave, where a) shows the longitudinal waves generated by the transducer, the multiple modes generated by the transducer edges, and the possible plate waves generated, b) the multiple scattering due to boundaries (red) and internal structures (green), and c) various possible guided wave propagation paths.

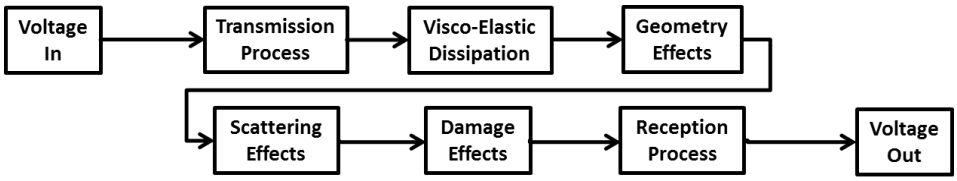

Figure 2-10. Block diagram for the linear system model describing the generation of coda waves.

2.4 Comparison with Selected Traditional Ultrasonic NDE Techniques

Coda wave analysis is currently completely independent of material, geometry, and mode identification or ray tracing. Since coda wave analysis utilizes waveform differencing parameters, the differences due to damage can be detected regardless of the user's knowledge of the structural properties or which wave modes superimpose to make coda waves. That is not to say that the same damage in different structures will yield similar amplitudes for the differencing features. The waveforms themselves can be significantly different for different applications as demonstrated above. Further analysis into the various components that comprise the coda wave may lead to a model to describe the behavior and predict the diagnosis/prognosis capabilities, but that is a subject for future investigations and is not considered in depth within this thesis. Analysis of the various wave modes is expected to be difficult since each application of coda waves (e.g. plate vs. complex geometry) is significantly different.

When coda waves are applied to plate-like structures and materials with a large degree of internal structure causing scattering, questions naturally arise as to what comprises the coda waves and how similar the coda wave analysis is to current methods: because plates are used in this research, plate waves may be the dominant component of the coda wave signals; Since coda waves are typically due to scattering, how is the signal different from backscatter or acousto-ultrasonic signals; and finally, since the signals seem noisy, a contrast to ultrasonic noise must be made. A summary of the comparison between coda wave NDE and previous methods is presented in Table 2-2.

2.4.1 Ultrasonic Lamb and Rayleigh waves

Guided waves (primarily Lamb and Rayleigh) are intimately dependent on the boundaries of the media in which they propagate. Lamb waves require a plate-like structure were the thickness

is comparable to the wavelength and when this thickness is exceeded the waves propagate as Rayleigh waves. Good overviews of the theory and application of guided waves are given by Viktorov (1967) and Rose (1999). In contrast to this, coda waves can be generated in non-plate like structures and coupling a secondary object to the surface in the propagation path does not fully disrupt the coda wave, therefore, coda waves are not solely guided waves. Since guided wave are multi-modal, the majority of guided wave systems need to be tuned to the specific material and thickness of the structure to be interrogated and are excited with a toneburst to select specific modes. This is done for both traditional angle-beam transducers and PZT wafers [Rose 1999, Viktorov 1967, Lu 2007, Michaels 2008, Yu & Leckey 2012]. Generation of coda waves requires no special tuning, configuration, or input. Plate waves are characterized by retrograde elliptic particle motion at the surface while coda waves have no defined particle motion at the surface or otherwise. The final difference between guided waves and coda waves is arrival time of the acoustic energy. Guided wave methods typically look at acoustic energy on a time scale of tens to hundreds of microseconds while coda wave analysis looks at acoustic energy on a time scale of hundreds to thousands of microseconds for the materials and geometries considered in this thesis.

While it is true that a coda wave signal could potentially be comprised solely of multiple guide wave modes, which is unlikely given how well the diffusion equation describes the coda waveform, a coda wave analysis is not dependent on the type and number of guided wave modes/reflections nor is it dependent on the inspector's knowledge of such things. Lu attempted to analyze the coda waveform in small aluminum plates from the standpoint that they were a superposition of guided wave modes [Lu 2007]. His comparison of the performance (ROC) of this method with the differential signal features demonstrated its inferior detection capabilities, which indicates that superposition of guided wave modes is not the best approach.

Table 2-2. Comparison of coda wave NDE with other ultrasonic NDE methods.

Method	Characteristics of Method	Characteristics of Coda Wave	Reference
Guided Waves	-Require a plate-like structure	-No geometry requirements	Viktorov 1967, Rose 1999
	-Difficult to generate in complex structures	-No difficulties with complex structures	Lu 2007, Micheals 2008
	-System is often tuned to the material and thickness	-No tuning	Viktorov 1967, Rose 1999, Lu 2007, Michaels 2008,Yu & Leckey 2012
	-Typically excited with toneburst	-Typically excited with spike or chirp	Yu & Leckey 2012
	-Retrograde elliptic particle motion	-No defined particle motion	Viktorov 1967, Rose 1999
Backscatter	-Generally pulse-echo	-Normal incidence pitch-catch	Goebbels 1994, Ghoshal & Turner 2001, Margetan 2012
	-Single scattering	-Multiple scattering	Margetan 2012, 2016
	-Backward scattering	-Back and forward scattering	Goebbels 1994, Ghoshal & Turner 2001, Margetan 2012
	-Caused by microstructure	-Caused by microstructure and boundaries	Ghoshal & Turner 2001, Margetan 2012
	-A-scan signal relating to specific location/depth	-Signal relates to a volume	
Acousto-ultrasonics	-Diffuse-like wave	-Diffuse-like wave	Fahr 2014
	-Acoustic Emission receiver	-Any type of receiver	Vary 1990
	-Temporary dry coupling	-Permanent/semi-permanent coupling	Vary 1990, ASTM 1997
	-Parameters from single waveform – AE based	-Differential features from multiple waveforms	Vary 1990, ASTM 1997
	-Intended to evaluate microstructure	-Intended to detect damage	Vary 1988, Vary 1990
Noise	-Random, not repeatable	-Very repeatable	
	-Transducer noise	-Signal still exists after deconvolving the system transfer function	
	-Not reciprocal	-Reciprocal	
	-Digitization noise is very small amplitude (typically a few bits)	-Coda wave signal is large amplitude (nearly full bit range)	

2.4.2 Ultrasonic Backscatter

In a scattering environment, it is beneficial to define and segregate several different types of scattering, namely: single, multiple, forward, backward, coherent, and diffuse. A diagram of the different scattering types is shown in Figure 2-11. Single/multiple refers to whether one or more scatterers were encountered during propagation from transmitter to receiver. Backward scattering is used to refer to describe scattered waves that have a propagation direction opposite to the incident wave, and thus are effectively propagation "backward" towards the transmitter. The term forward refers to the general direction away from the transmitter such that when a wave is scattered multiple times, the net travel is towards a second transducer. Coherent scattering is used to describe scattered waves whose propagation direction and phase are aligned with those of the incident wave. Diffuse scattering describes the opposite of coherent scattering. Even though the term "diffuse" is used by many authors, it can cause confusion as it can refer to several different phenomena, such as: the definition provided above, scattering where the wave length is much larger than the scatterer, or the diffusion of acoustic energy through a medium.

Backscattering is typically defined for a pulse-echo measurement when the input pulse is scattered during propagation and a portion of the energy returns to the transceiver [Goebbels 1994, Ghoshal & Turner 2001, Margetan 2012]. The time of flight for backscattered signals tend to be relatively short as the backscatter is typically generated by single scattering events from the microstructure and thus involve shorter sonic travel paths[4]. Coda waves differ significantly from the backscatter definition even though both are caused by scattering from microstructure (backscatter entirely and coda wave partially). Coda waves are a collection of multiple, diffuse, forward scattered waves that sample a larger volume than the conical pulse-echo beam path.

[4] Private communications. Frank Margetan, Iowa State University, April 2016.

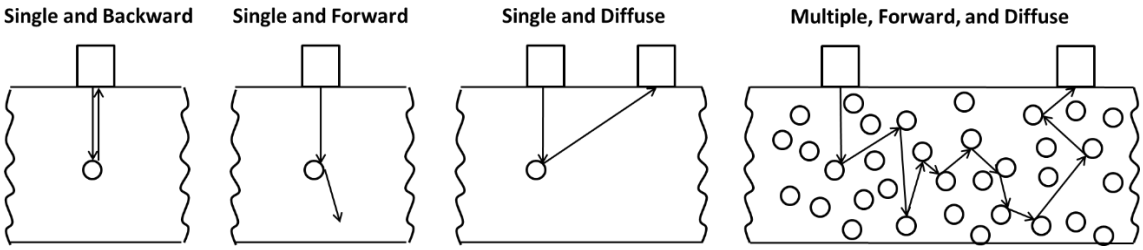

Figure 2-11. Diagram of different scattering terminologies.

2.4.3 Acousto-ultrasonics

It is arguable that the origin of coda wave NDE can be found in Acousto-ultrasonics (AU) as both methods utilize diffuse-like waves to inspect samples. It is clear, however, that coda wave analysis developed separately from AU [Aki 1969, Vary 1988, Roberts et al. 1992, Snieder 2006]. Differences between the methods exist, although several may be written off as a matter of semantics. In the truest sense of the method, AU requires an Acoustic Emission (AE) receiver while coda waves do not [Vary 1990, Planes & Larose 2013]. AU transducers are typically dry-coupled to a part in a temporary manner while coda wave transducers are permanently or semi-permanently attached while all data is collected. The most significant difference between the methods lies in the processing of the waveforms and the intent of the method. AU is primarily concerned with the propagation efficiency of a single waveform and microstructure evaluation (though it is often used for damage detection) while the coda wave method is a comparative method that is primarily concerned with damage detection through measuring differences in the waveforms.

2.4.4 Ultrasonic Signal Noise

A simple and widely used definition of noise for ultrasonic signals is any undesired signal component that obscures the signal of interest [Oppenheim & Schafer 1975]. The undesired signal components may come from a variety of sources (such as electronic receiver noise, digitization noise, or scattering noise) and may be either random or systematic. Typically, noise frequencies are either higher or lower than the frequencies of the signal of interest and can be eliminated with a band-pass filter. Random noise can be minimized during collection with signal averaging, but this has no effect on systematic, coherent noise. Non-random, coherent noise is typically due to scattering or transducer noise. In the case of transducer noise, the transducer transfer function can be deconvolved to eliminate the noise. The scattering noise is exactly what comprises the coda wave so, by the simple definition of noise provided, it is not noise at all. Coda waves are fairly easy to differentiate from noise: 1) the coda waves are repeatable and therefore not random noise, 2) when the transducer transfer functions are deconvolved the coda wave still exists and therefore is not transducer noise, and finally 3) the coda waves are reciprocal while non-scatter noise is not.

2.5 Coda Waves and Diffuse Fields in Acusto-Ultrasonics

The acousto-ultrasonic approach to NDE was first proposed by Vary and Bowels to examine the combined effect of all subcritical flaws and microstructural anomalies of fiber composites [Vary & Bowles 1979]. This method quickly became very popular and resulted in a multitude of publications attempting to measure everything from elastic constants [Minachi & Hsu 1993], bond strength [Fahr 2014], and materials degradation [Vary 1988], to fatigue life prediction [Srivastava & Prakash 1987]. The fundamental hypothesis behind this method is that better stress wave energy transfer corresponds to increased quality, strength, and fracture resistance [Vary

1988]. To this end, the energy transfer efficiency of acousto-ultrasonic signals is measured with stress wave factors (SWF), which are defined based on acoustic emission parameters such as number of counts or energy (MARSE). A typical experimental configuration is shown in Figure 2-12 [ASTM 1997]. Note that the sensors are temporarily coupled to the specimen and as such, there are issues of consistency, repeatability, and reproducibility. Analysis and recommendations for minimizing these issues have been presented by several authors [Mazzeranghi & Vanghi 1999, Gyekenyesi et al. 2002, Dugmore et al. 2002]. Due to the indeterminate nature of the AU waveforms, questions quickly arose as to how the signals were formed. Several publications explore the theoretical basis for AU from different standpoints including ray tracing to mode determination and wave mechanics [Kautz 1988, Kiernan & Duke 1991, Duke 1993, Rose et al. 1993]. The work on Acousto-ultrasonics is well reviewed by several authors [Vary 1988, Vary 1991, Kautz 2002, Fahr 2014].

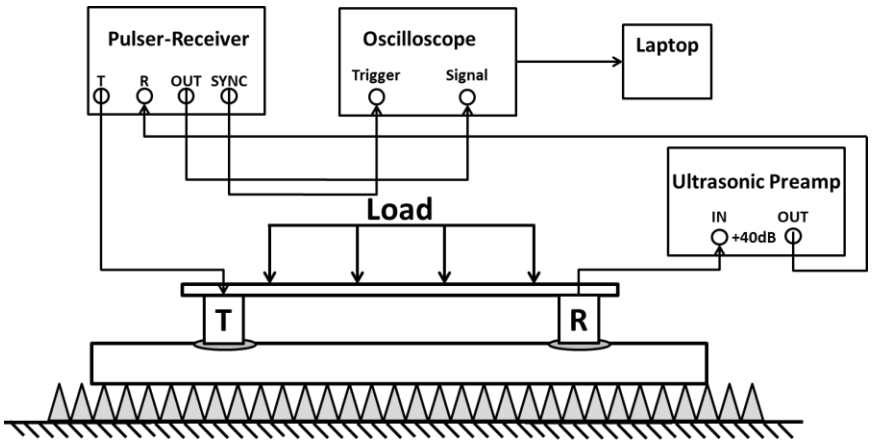

Figure 2-12. Typical configuration for the acousto-ultrasonic inspection of a plate.

2.6 Coda Waves and Diffuse Fields in Geophysics

Coda waves and their analysis originated in the Geophysics community where the term "coda" wave was coined by Aki [Aki 1969, Aki & Chouet 1975]. Aki borrowed the term from music, where a coda is the last portion of a piece of music, and used it to refer to the late arriving energy in seismograms. The goal of the early work involving coda waves was to examine the heterogeneities in the Earth's crust by extracting parameters about the source and the propagation medium (e.g. attenuation and seismic moment). This early work has been reviewed by Herraiz & Espinosa (1987).

Work on coda waves progressed from extracting parameters from a single wave to comparative measurements in order to determine the time lapse properties of the crust. The first comparative measurement was used to determine the temporal variation of S wave velocities in the crust [Poupinet et al. 1984]. They developed the first algorithm to extract the relative velocity change between two coda waveforms. Since the original paper use earthquake doublets, the algorithm is often referred to as the Doublet Technique. A second name for the algorithm is the Cross-Spectral Moving-Window (CSMW) Technique since the algorithm utilizes the cross-spectrum of multiple time windows. The algorithm was subsequently improved and extended to include attenuation measurements [Roberts et al. 1992].

Nearly a decade later, an independent derivation of coda waves as multiply scattered waves yielded a temporal version of the CSMW Technique referred to as Coda Wave Interferometry (CWI) [Snieder et al. 2002]. Although CWI and CSMW are equivalent expressions in the time and frequency domains respectively, CWI has a stronger physics base and became the method of choice. CWI makes no assumptions as to the linearity of the relative velocity change with respect to time. However, if the relative velocity change is linear with time (as is the case for homogeneous

and thermal loads), then the CWI algorithm can be reduced to simple dilation of the second waveform until maximum correlation is achieved [Sens-Schöfelder & Wegler 2006]. Although this drastically simplifies the algorithm, the Stretching Technique becomes a grid search method that requires interpolation and thus is computationally expensive. A comparison of the CWI/CSMW and Stretching methods was presented by Hadziioannou et al. (2009) with the conclusion that the stretching method was more stable and less sensitive to noise.

Currently, the extraction of the coda wave relative velocity change has fallen out of favor in the Geophysics community [Weaver & Lobkis 2006]. The preference of many geophysics researchers now lies with the Green's function extraction method developed by Lobkis & Weaver (2001) for NDE. This method allows for the passive (external source) reconstruction of the ballistic wave propagating between two receivers. Thus received coda waves can be transformed into traditional wave modes and traditional wave analyses (e.g. time of flight or amplitude reduction) apply.

2.6.1 Contributions to Theory

The first analytical treatment of coda waves was presented by Aki (1969). In this work, Aki proposed that the coda waves consisted of singly scattered surface skimming waves. In a later publication, Aki compared his original single scatter model to a diffusion model and noted that neither extreme accurately described the observed coda [Aki & Chouet 1975]. The early work on seismic codas is reviewed by Herraiz & Espinosa (1987). Herraiz & Espinosa divide the evolution of the coda wave modeling efforts into four main groups:

1. Transition from surface wave driven models to S wave driven models. Initiated in 1969.
2. Abandoning the diffusion model. Initiated in 1977.

3. Transition from single scattering dominated to multiple scattering dominated models. Initiated in 1977.
4. Multiple scattering models with more realistic assumptions. Initiated in 1982.

It is concluded in this review that none of the models presented adequately describe the physical mechanisms behind the formation of the coda wave.

Several decades later, Snider et al. introduced a new method for analyzing coda waves and extracting temporal variations by comparing two coda waves [Snieder et al. 2002]. They approach the coda wave from a multiple scattering perspective and examine the statistical perturbations of the positions of scatterers. Estimates of the perturbations are derived from the cross-correlation of the coda waves. For a homogeneous load, the average perturbation is linear with time and is equivalent to a relative velocity change in the material. A review of the theory and several experimental applications is given by Snieder (2006).

2.6.2 Greens Function Extraction

Although originally derived for NDE, the method of recreating Green's function from the cross correlation of received coda waves has seen much greater acceptance and application within the Geophysics community. The body of work concerning the extraction of Green's function from the cross-correlation of coda waves is extensive and an early review is provided by Weaver & Lobkis (2006). Only a brief overview is presented here as Green's function extraction is not the focus of this thesis. The first derivations and experimental demonstrations of Green's function recreation are given by Weaver & Lobkis (2001[5], 2001, 2002). These early derivations were based on normal mode expansion for finite, lossless cavities, but other derivations were soon presented

[5] See Lobkis & Weaver 2001

that did not require the assumption of a finite, lossless cavity. Four distinct derivations have been presented, demonstrating that the Green's function is present in the correlation of coda waves: 1) derivation based on normal mode expansion [Lobkis & Weaver 2001], 2) derivation based on stationary phase [Snieder 2004], 3) derivation based on energy principles [Snieder et al. 2007], and 4) derivation based on ward identities [Weaver 2008].

After the initial introduction of Green's function extraction, proof of the applicability of this method to open, heterogeneous, scattering media was provided by many authors within a few years [Derode et al. (2003a, 2003b), Weaver & Lobkis 2004, Wapenaar et al. 2005, Snieder 2007, Weaver et al. 2009]. The early work has been reviewed by Weaver & Lobkis (2006) and Larose et al. (2006). Several authors noted that the resolution of the reconstructed Green's function could be improved if the correlation of the Green's functions is taken across an array of receivers [Stehly et al. 2008, Froment et al. 2011]. The resulting conclusions from this multitude of work are: 1) the ballistic waveform traveling between two points can be recreated from the correlation of the received coda waves generated from a tertiary source, 2) the recreation can be improved by ensemble averaging the results from multiple sources, 3) the results can be improved by spatially distributing the sources, and 3) the method theoretically works for any material and geometry for which coda waves exist.

2.7 Applications of Coda Wave and Diffuse Fields to NDE

A significant amount of work has been done in applying the coda wave ideas from geophysics to NDT&E and in developing the diffuse field approach, both of which have been primarily applied to concrete and metals [Planes & Larose 2013, Lu 2007]. The result from this

body of work is that the sensitivity of coda waves to subtle changes in material condition and small scale, diffuse defects is widely accepted [Planes & Larose 2013].

Subtle changes caused by loading, small scale damage, or environmental changes are detectable with coda waves from the extraction of differencing parameters [Lu 2007]. In a similar manner to the extraction of Stress Wave factors in the acousto-ultrasonic technique [Vary 1982, Vary 1991, ASTM 1997], useful information is obtained from a coda wave analysis by extracting differencing parameters between waveforms collected before and after a subtle change occurs. A differencing parameter is any characteristic of the waveforms (such as amplitude, energy, or velocity) that can be used to measure changes/differences between two or more waveforms. An ideal differencing parameter is zero for identical signals and benign changes (e.g. temperature variation) but is non-zero and monotonically increasing for damage and damage growth. Relative velocity is currently the most commonly used parameter [Planes & Larose 2013] and is usually determined from the Stretching Technique [Sens-Schonfelder & Wegler 2006, Larose & Hall 2009, Hadziioannou et al. 2009, Liu et al. 2015], though the Cross-Spectral Moving Window [Poupinet et al. 1984, Roberts et al. 1992] and Coda Wave Interferometry [Snieder et al. 2002, Snieder 2006] methods have also been used. It should be noted that the coda wave relative velocity parameter is only defined for a pure waveform dilation, such as those caused by a homogeneous or thermal load [Snieder 2006, Weaver & Lobkis 2000]. The aforementioned methods actually measure the time dependent relative time lag (phase lag), which is equivalent to relative velocity only when the relative time lag increases linearly with time [Snieder 2006]. It should also be noted that the stretching technique assumes the linear relation is present [Sens-Schonfelder & Wegler 2006], but damage is unlikely to present as a linearly increasing relative time lag and has never

been shown to do so. Therefore, using the relative velocity parameter to detect damage directly is an inappropriate application.

Michaels' group first suggested the use of several differencing parameters, termed differential features, to help quantify the differences in coda waves caused by introducing damage [Michaels & Michaels 2005, Yu 2007]. These differential features examine the changes in the energy and structure of the waveforms as opposed to an overall dilation and thus are better suited to damage detection and characterization. Other common parameters used for damage detection include diffusion fitting [Anugonda et al. 2001, Deroo et al. 2010] and Green's function symmetry [Lobkis & Weaver 2001, Weaver & Lobkis 2006, Sabra et al. 2008]. Experimental evidence and theoretical considerations suggest the differential features used by Michaels' group provide a better measure of the differences in diffuse fields caused by damage/defects [Lu 2007] while relative velocity is a better measure of waveform dilation or average scatterer displacement [Weaver & Lobkis 2000, Snieder 2006], diffusion fitting may be best for material evaluation but still has defect characterization potential [Becker et al. 2003, Deroo et al. 2010, In et al. 2012, In et al. 2013], and Green's function symmetry could assist in defect localization [Weaver & Lobkis 2006, Sabra et al. 2008].

2.7.1 Contributions to Theory

As previously mentioned, the majority of work performed to date in the field of coda wave NDE has utilized the relative velocity differencing parameter. The theory describing the relative velocity differencing parameter was developed for the geophysics community and is discussed in the previous section. The contributions from the NDE community to the theory of coda waves lie

in modeling the coda wave field as a diffuse field and in modeling the multiple scattering and reflections that comprise coda waves as an acoustic energy diffusion process.

The first analytical treatment of coda waves as a diffuse wave field, including the portioning of acoustic energy among the wave modes, was presented by Egle [Egle 1981]. His analysis was based on the long period reverberations often encountered in room acoustics, and the main contribution from the work was the inclusion of shear wave modes that exist in solids but not in air. Weaver subsequently modified the analytical proof to include the energy portioning of the acoustic source [Weaver 1982]. Later, Weaver extended the diffuse field idea to plates using the normal modes of the plate and plate waves [Weaver 1984]. He concludes that his proof is not sufficient to describe the coda waves and that there are many cases where the work is unlikely to apply.

Initial support for the idea that the evolution of ultrasonic energy density can be described by a diffusion equation that has been modified to include temporal decay came from Guo et al. (1985), Weaver (1990), and Turner & Weaver (1995). These preliminary works were derived for polycrystalline metals and included several assumptions such as material homogeneity and scattering falling within the Rayleigh limit (ratio of scatterer size to wavelength is less than 0.5). The multiple scattering diffusion theory was then extended by Turner & Anugonda (2001) to include heterogeneous media. The 2D heterogeneous diffusion model was subsequently confirmed experimentally for a concrete sample [Anugonda, et al. 2001]. The heterogeneous diffusion model was later extended to finite and infinite 3D bodies with experimental confirmation [Deroo et al. 2010]. They determined that the finite and infinite models fit the experimental data equally well, though significant measurement errors were encountered.

Two parameters are extracted from fitting the diffusion equation to the received coda wave: the diffusivity, which corresponds to the length of the mean free path of a propagating wave, and the dissipation, which corresponds to the absorption of the acoustic energy. Both of these parameters can potentially be used to detect and characterize defects and material degradation, and thus are of interest for NDE. The current diffusion models have been developed for metals and concrete, which are isotropic, and are not applicable to fibrous composites, which are non-isotropic. There is a potential to extend the diffusion models to fibrous composite materials, which could add useful information to a coda wave analysis. Indeed. the waveforms and log power spectra of coda waves collected from CFRP samples presented in subsequent chapters exhibit the same waveform envelopes and diffusion-type curves as shown by several of the afore mentioned papers [Turner & Anugonda 2001, Anugonda et al. 2001, Deroo et al. 2010].

2.7.2 Applications

The experimental work performed to date has been largely qualitative in manner where microstructural damage is introduced in an unquantifiable manner, such as ASR or stress corrosion cracking in concrete [Planes & Larose 2013, Shokouhi & Lorenz 2014]. Most studies merely detect a change in coda wave differencing parameters without correlating the changes to a specific change in the material or damage state. This is to be expected given the distributed nature of the damage of interest and the difficulty in quantifying the damage growth. The majority of quantitative work in detecting damage deals with measuring the relative velocity due to either thermal or homogeneous loading [Weaver & Lobkis 2000, Zhang et al. 2012, Larose & Hall 2009, Niederleithinger & Wunderlich 2013], though a few papers discuss quantifiable amounts of defects/damage [Seher et al. 2013, Michaels & Micheals 2005]. Some of the earlier work for coda

wave NDE has been reviewed by Planes & Larose with a focus on concrete applications [Planes & Larose 2013].

As noted earlier, several approaches to detecting damage have been applied to concrete; most notably the diffusion fit parameters and the relative velocity change. Diffusion fitting provides three parameters by which damage can be detected/characterized and the material can be evaluated. The diffusion parameters have been used to characterize several cement specimens with various sizes and distributions [Becker et al. 2003], where qualitative trends and some ability to distinguish microstructure were observed. It was noted that better models are needed to analyze scatterer size and distribution. Self-healing concrete was monitored and evaluated in a similar qualitative manner [In et al. 2013]. The qualitative detection of micro damage (damage with a length scale on the order of or smaller than the largest aggregate) in concrete has also been explored with diffusion fitting [Deroo et al. 2010], where it was demonstrated that the diffusivity parameter is sensitive to damage density while the dissipation parameter remained constant. The quantitative applications of diffusion fitting to damage characterization in concrete to date have largely involved measuring the depth of surface breaking macro-cracks. Several publications have demonstrated that the time lag of the peak diffusive energy is well correlated to crack depth [Ramamoorthy et al. 2004, In et al. 2012, Quiviger et al. 2012, Seher et al. 2013]. Payan et al. (2013) were able to improve the characterization by applying dynamic loading to the specimen in the form of a low frequency shaker. The limitation with the macro-crack depth measurements is that the crack is surface penetrating and the transducers have to be on the opposite side of the crack. Several things become clear from these studies: 1) the diffusivity and dissipation parameters can partially but not fully characterize a cementious material, 2) micro damage is detectable with the diffusivity parameter with some potential for characterization, 3) surface breaking macro-

cracks can be sized, and 4) the sensitivity to damage has not been established and it is unlikely that small amounts of damage (a few micro-cracks) can be detected in samples that are cubic meters in volume.

Relative velocity change is the most popular coda wave differencing parameter and can be used to directly measure thermal and structural loads, the acoustoelastic parameter, as well as micro-crack density [Planes & Larose 2013]. One of the first application of relative velocity measurements for NDE purposes correlated structural and thermal loading on Berea sandstone to the change in coda wave relative velocity [Gret et al. 2006]. Parallel and subsequent publications applied relative velocity extraction methods to concrete in order to measure thermal induced velocity variation [Larose et al. 2006, Niederleithinger & Wunderlich 2013, Zhang et al. 2013b]. These studies confirmed the linear phase shift with temperature for concrete materials that was previously demonstrated by Roberts et al. (1992) for acrylic plates and Weaver & Lobkis (2001) for aluminum billets. Several publications also examine the relative velocity variations due to structural loading [Larose & Hall 2009, Stahler & Sens-Schönfelder 2011, Zhang et (2011, 2012)], which confirmed the linear relation of the phase lag with time predicted by Snieder (2006). Zhang et al. (2013a) attempted to examine relative velocity variation due to the heterogeneous stress field generated by 4-point-bending on a concrete specimen, but the research yielded inconclusive results. The linear relation between applied homogeneous stress (or strain) and the coda wave relative velocity indicates the appropriateness of measuring the acoustoelastic parameter with coda waves. The acoustoelastic parameter, first derived by Hughes & Kelly (1953) based on Murnaghan's theory [Murnaghan 1951], is the ratio of the relative velocity change to the change in applied strain. Payan et al. were able to use coda waves to measure the third order elastic constants from Murnaghan's theory in addition to the acoustoelastic parameter in a concrete

specimen. Additionally, several authors have demonstrated the potential capability of the acoustoelastic parameter to detect micro damage and fatigue in concrete [Schurr 2010, Schur et al. 2011a, Schurr et al. 2011b, Zhang et al. 2011]. Coda wave relative velocity has also been qualitatively used by several authors to directly estimate damage (typically stress induced micro-cracking) [Masera et al. 2011, Neiderleithinger et al. 2010, Shokouhi & Neiderleithinger 2012, Shokouhi 2013, Shokoui & Lorenz 2014, Frojd & Ulriksen 2016]. Each of these studies demonstrated an increasing magnitude for the relative velocity change with increasing amounts of damage. While it is true that an increase in the number of micro-cracks should theoretically increase the mean travel time, this will only become apparent for large numbers of micro-cracks.

Improvements in detecting micro-cracks in cementious materials have been observed by several authors when a lower frequency pump wave is included [Toumi et al. 2011, Zhang et al. 2013, Zhang 2013c, Hilloulin et al. 2014a, Hilloulin et al. 2014b, Moradi-Marani et al. 2014]. The lower frequency pump wave opens and closes the micro-cracks, which allows for greater interaction with the coda wave components. The nonlinear mixing between the pump and coda waves also allows for the improved measurements of the nonlinear parameters

Coda wave NDE is a volumetric method and as such no information regarding the location of the damage is extractable using the previously mentioned methods. In order to address this shortcoming, several authors have attempted to locate damage and applied stresses using theoretical spaciotemporal decorrelation kernals to predict the coda wave for an undamaged sample for a given transmitter-receive pair and solving the inverse problem [Planes et al. 2013, Niederleithinger et al. 2014]. Damage and point loads have been located to within several centimeters for large concrete samples.

The two primary methods of analyzing differences in coda waves caused by damage or other subtle changes are based on time dependent phase lag or total waveform energy. While these differencing parameters are useful they only compare global coda wave parameters. An alternative method, first proposed by Michaels & Michaels (2005) for the analysis of coda waves, is to examine the parameters of the residual signal left over after a point-by-point subtraction of two coda waves (e.g. the signal energy contained in the residual). Michaels' have utilized/developed at total of five such features (henceforth referred to as differential features) to characterize changes present in the coda wave due to the introduction of damage and variations in environmental conditions [Michaels & Michaels 2005, Michaels et al. 2005, Lu 2007, Michaels 2008]. These investigations demonstrated that the differential features are sensitive to damage and environmental effects in aluminum plates. They also demonstrated that the environmental effects can be separated from damage and that thermal changes can be compensated for.

2.7.3 Technique Limitations and Barriers to Quantitative Work

Although the sensitivity of coda waves to small changes in material condition and small defects is accepted, it remains a challenge to interpret the changes in coda waves and correlate the changes to specific defects in a quantitative and reliable manner. Hindrances to quantitative work can be grouped into two main areas: 1) Increased sensitivity to benign changes and 2) The indeterminate nature of the coda wave field and the unquantifiable nature of the damage that has been of interest.

The increased sensitivity to subtle changes means that the differencing parameters are also sensitive to changes in the system between data collection, namely transducer misalignment and environmental factors such as temperature changes [Planes & Larose 2013, Snieder 2006, Weaver

& Lobkis 2006]. It is noted by multiple authors that one of the barriers to quantitative work is the masking of damage by thermal loads and other environmental effects [Michaels 2005, Larose et al. 2006, Lu 2007, Planes & Larose 2013, Zhang et al. 2013b]. To combat this, several authors have proposed mitigation methods including: keeping a constant ambient temperature, collecting baselines at various temperatures and selecting the baseline closest in temperature, and utilizing a secondary undamaged sample and subtracting the thermal shift in differencing parameters [Mazzeranghi & Vangi 1999, Lu & Michaels 2005, Lu 2007, Zhang et al. 2013]. Only the work by Michaels' group has attempted to discriminate damage from environmental changes. As mentioned earlier the coda wave relative velocity is sensitive to waveform dilations caused by thermal loads and thus provide a good discriminator between damage and thermal effects [Michaels & Michaels 2005]. Permanently or semi-permanently attaching the transducers, as is the case with a SHM system, can also reduce the measurement error and improve the results. Note that the use of coda waves for SHM has been suggested and evaluated by Michaels' group with favorable results [Lu 2007, Michaels 2008].

2.7.4 Summary

As can be seen from the review of literature on coda wave NDE, the majority of work was not concerned with developing a quantitative technique and introduced damage in an unquantifiable manner. This is to be expected given the distributed nature of the damage of interest in concrete. The majority of applications have also been focused on relative velocity measurements, either by themselves or to determine the acousto-elastic parameter, and lack good differential features to quantify changes in the waveforms themselves that are caused be damage.

There was also a lack of good models to explain the physics of damage detection with coda waves, which left researchers at a loss to explain anything more than homogeneous loads.

A significant number of publications exist in the field of coda wave NDE, yet the basic capabilities have not been addressed. Questions of measurement error, repeatability, accuracy, reproducibility, and sensitivity have not been tackled. The limitations on the size of the inspection volume, minimum detectable flaw size (and largest defect missed), and limiting SNR have not been considered. The shear components of the coda wave field have been almost completely ignored in experiments. Additionally, the formation, propagation, and any theory of coda waves for non-isotropic materials is severely lacking.

2.8 Applications of Coda Waves and Diffuse Fields to NDE of Composites

Very few instances of coda wave NDE applied to fibrous composite materials exist in available literature. The first application, reported by Taylor et al. (2013), sought to compare a version of coda wave NDE with guided wave NDE to detect fatigue cracking near the root of a CX-100 wind turbine blade. This work calculates the receiver operating characteristics (ROC) for several transmitter-receiver pairs to compare the damage detection capabilities of the two methods, but several issues are present. The first and foremost is even though the paper seeks to utilize coda waves, the authors do not validate their estimate of the impulse response function. The second issue is that the researchers waited until a fatigue crack penetrated the surface of the blade to differentiate between the damaged and undamaged states.

The second application, reported by Tippman et al., measured the break in symmetry of the reconstructed Green's function to detect engineered damage [Tippman & Lanza di Scalea 2014, Tippman et al. 2015]. This work is largely qualitative though the second paper provides a

more quantitative analysis of the breaks in symmetry. Additionally, even though the recreation of Green's function has been demonstrated by a multitude of papers [Lobkis & Weaver 2001, Derode et al. 2003, Sabra et al. 2005, Wapenaar et al. 2005, Sabra et al 2008], Tippman et al. (2014, 2015) do not validate their processing method extraction of Green's function is not clear. In addition to the improved analysis presented by the second paper, where they sought to localize damage, but the process was not well explained and did not show promising results.

All in all, the applications of coda waves for the inspection of fibrous composite materials are scarce, mostly qualitative in nature, and not well validated. If coda wave NDE is to be a viable option for the inspection of fibrous composite materials, then significant quantitative work is required.

2.9 Research Context

From the literature review on the use of coda waves (AKA diffuse fields) for the purposes of NDT&E, it is clear that coda wave NDT&E is in the nascent stage of development, lacks good quantitative applications for damage detection, and has seen limited applications to fibrous composite materials. Therefore, it is necessary provide a quantitative foundation for the continued utilization of coda waves for NDT&E, especially the NDT&E of fibrous composites. Since coda waves can be easily generated and there are a multitude of signal processing approaches, the major challenges exist in proving the sensitivity, accuracy, reliability, and repeatability of the signals and the damage indices as well as developing models (both analytical and numerical) that accurately describe and predict the behavior of the damage indices.

Several steps are required in order to provide the quantitative foundation required for successful coda wave NDT&E as briefly described in Figure 2-13. The first step analyses some of

the most basic properties and processing of the coda waves. This step involves five main tasks: a) Determine the effect of environmental changes (e.g. temperature change) on the coda wave and any damage indices, b) Develop and verify the processing algorithms, c) Determine the spreading function for coda wave acoustic energy, d) Develop definitions of attenuation and measure the attenuation of coda wave energy, and finally e) Determine the effect of boundaries on the development and propagation of coda waves. These tasks are absolutely necessary in order to develop a quantitative method. The propagation, attenuation, and boundary effect measurements help determine the maximum sensor spacing and the applicability to large structures. The measurement of environmental effects allows for the separation of benign effects from the effects of damage and thus will allow for improved detection and characterization.

The second step involves detecting simulated damage and analyzing the basic damage detection capabilities such as repeatability, sensitivity, and reproducibility. This step includes three main tasks: a) Detect defects such as drilled holes, b) Determine the detection capabilities, and c) Determine the behavior of the damage indices (DI) by developing a model that relates the value of the damage indices to a damage parameter such as volume. Using drilled holes for this stage of development is ideal since they are easy to fabricate and quantify as both the size (volume) and location are known. Once the basic detection capabilities are known and a model is developed for the DI, then damage size can be estimated based on the DI amplitude. This prediction capability is absolutely necessary for successful quantitative applications in the field.

The third step includes three main tasks: a) Detect realistic defects such as micro-cracking, damage caused by fastener holes, and barely visible impact damage, b) Monitor damage growth by means of fatigue and/or compression after impact, and c) Field testing. The realistic defects

listed are of particular interest to aerospace community, especially the barely visible impact damage, which is very common and difficult to detect.

The first two steps are addressed in this thesis while the third task is outside the scope of this work and is left to future research. The integration of all these experiments and analyses provides the quantitative foundation needed to transform coda wave NDT&E from an immature, qualitative idea into a mature, quantitative technique that is applicable for NDT&E/SHM of fibrous composites.

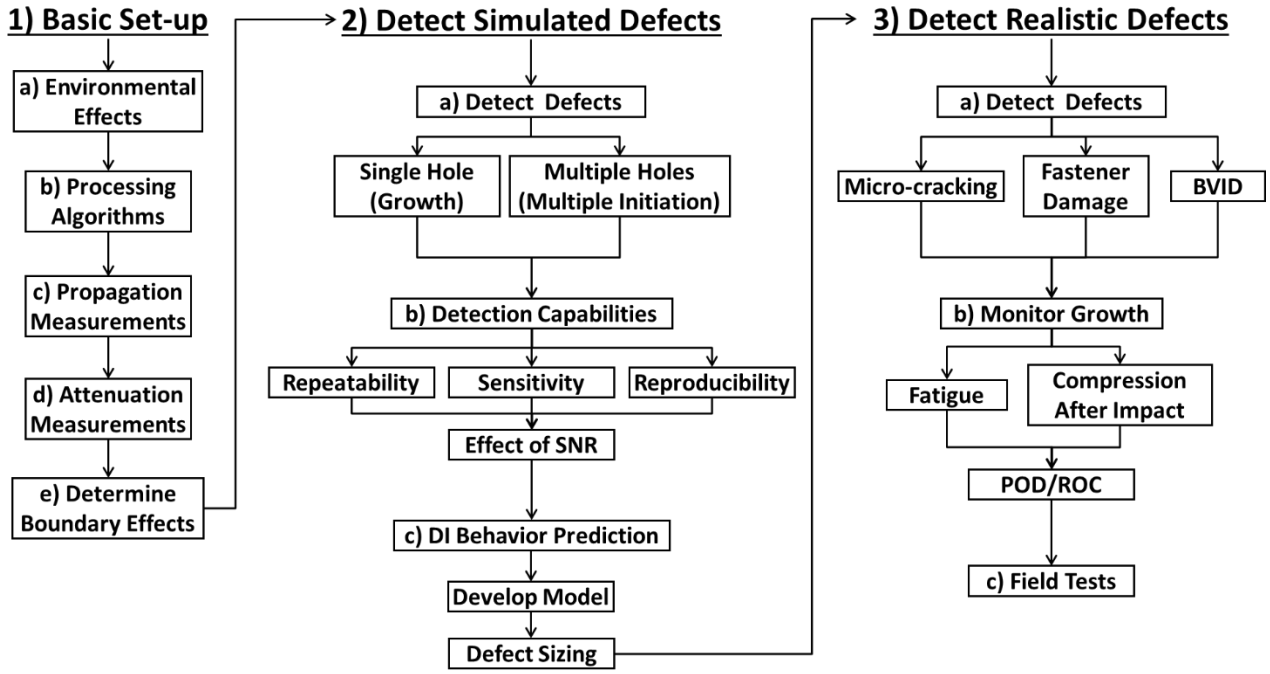

Figure 2-13. Block diagram describing several of the necessary steps when transforming coda wave NDT&E from an immature and qualitative method to a mature, accepted quantitative NDT&E/SHM technique. (SNR = Signal to Noise Ratio, DI = Damage Index, BVID = Barely Visible Impact Damage, POD/ROC = Probability of Detection/Receiver Operating Characteristic)

CHAPTER 3. THEORY

This chapter provides a presentation and discussion of several aspects of physical theories relating to the existence, production, and propagation of Coda waves (diffuse fields). Section 3.1 presents the work performed to date on coda wave propagation and discusses the impact of the work as well as the theories put forward. Work and theories relating to the temporal and spatial decay of coda waves is examined in Section 3.2. Finally, in Section 3.3, the theory behind several signal differencing parameters is presented and discussed.

3.1 Coda Wave Propagation

3.1.1 Propagation Models

Propagation models capable of explaining coda waves have been under investigation since the advent of coda waves in Seismology [Heraiz & Espinosa 1987]. For NDE applications, researchers have examined: guided wave propagation, bulk wave propagation, normal mode expansion models, and diffusion models. There is a clear transition from deterministic to indeterministic propagation models between pre and post 2000. In this section, the guided wave (deterministic) and diffusion (inderterminate) propagation models are examined.

It stands to reason that the first arrival is the ballistic arrival of a wave mode. Several researchers have been able to generate plate waves using single-sided, normal-incidence, pulse-echo configurations [Moon et al. 1988, Kautz (1992, 1993), Zhenqing 2000]. Guo and Cawley (1993) also explore the possible relation between Lamb waves and coda waves, but without much analysis. Moon et al. (1988) were able to generate Lamb waves in a 3 mm thick CFRP laminate using a windowed toneburst, but the intent of their work was to generate Lamb waves, not analyze

coda waves. Because of this, they were able to demonstrate that Lamb waves can be generated in place of coda waves with a coda wave configuration. Kautz (1992, 1993) examined 2.2 mm thick samples of Ceramic Matrix Composites (CMC's) and Metal Matrix Composites (MMC's) using coda waves and found that the first arrivals corresponded to Lamb waves. Later Zhenqing (2000) used a toneburst to generate Lamb waves in 2 mm thick aluminum and 2.05 mm thick composite plates.

The above examples of Lamb wave generation all use thin plates ($h \leq 3$ mm) were Lamb waves are more easily excided. Excitation of Lamb waves in plates of intermediate thickness ($0.3 \leq h \geq 1.0$ cm) using broadband pulses is much less likely, and excitation in thick plates ($h \geq 1.0$ cm) is very unlikely. Hsu and Margetan (1992), working in acousto-ultrasonics, examined the case of a thick (h = 2.5 cm) CFRP plate and found that the early portion of the coda wave consisted primarily of multiply reflected bulk waves while the first arriving portion was found to be a Rayleigh wave. It is clear from these various investigations that multiple waves modes exist in the coda wave and that in certain cases (either very thin or thick plates) some of the wave modes can be identified from the coda signal. In contrast to deconvolving wave modes approach to analyzing coda wave propagation, several authors have proposed multi-mode propagation approaches. Lobkis & Weaver (2001) proposed a normal mode wave field model, and although the model itself cannot be directly tested, it lead to the development of Green's function extraction from coda waves. Snieder et al. (2002) expanded the normal mode wave field idea to include a random walk component for all wave modes as they scatter and reflect off of boundaries. Neither models by Lobkis & Weaver (2001) or by Snieder (2002) are able to predict the shape of the coda wave given material parameters. This limitation was addressed by Anugonda et al. (2001), who developed the

diffusion model to describe coda waves. This model treats the propagation of coda waves as an energy based diffusion process.

Preliminary investigation into possibility of coda waves consisting of Lamb waves was performed using an aluminum plate (~150x50x6 mm) described by Figure 4-1c and a 12.7 mm, 1 MHz longitudinal receiver. The coda wave spectrum was segmented using Tukey windows with 12% taper on either side, transformed back into the time domain, and the arrival time determined. The velocities for ballistic arrival for the various frequency thicknesses were then determined and compared to the dispersion curves as shown in Figure 3-1a. Several of the velocities correspond well with the dispersion curves, which indicates the possibility of low frequency anti-symmetric Lamb wave modes contributing to the formation of the coda.

Further investigation was performed using a pinducer receiver to eliminate any possible phase cancellation. Coda waves were received at five locations ranging from 5 to 10 cm by 1.25 cm increments on both the top and bottom surfaces and were processed in the same manner as the previous signal. A comparison of the velocities for ballistic arrival for the various frequency thicknesses ae compared to the dispersion curves in Figure 3-1b. Lamb waves exhibit five properties that must be met before a wavelet can be considered a Lamb wave: 1) velocities must match the dispersion curves, 2) the same velocity must be observed on both the top and bottom of the plate, 3) the same displacement magnitude must be observed on both the top and bottom of the plate, 4) the wavelets received on the top and bottom must be either in phase or 90˚ out of phase, and 5) the same mode must be observed at each location on a given surface, but with increasing time delay with increasing travel distance. Figure 3-1b1 clearly shows that conditions 1 & 2 are not met. The inability to meet all five Lamb wave conditions indicates that the low frequency components of the collected coda waves are not Lamb wave modes. It should be noted, however,

that decoupling superimposed wave modes is possible if and only if the superimposed wave modes can be completely isolated (i.e. no overlap of the envelope) in either the time of frequency domains. The results discussed here are the attempted decoupling of the coda wave into constituent parts, and although multiple windows were attempted, it was not possible to completely decouple the modes.

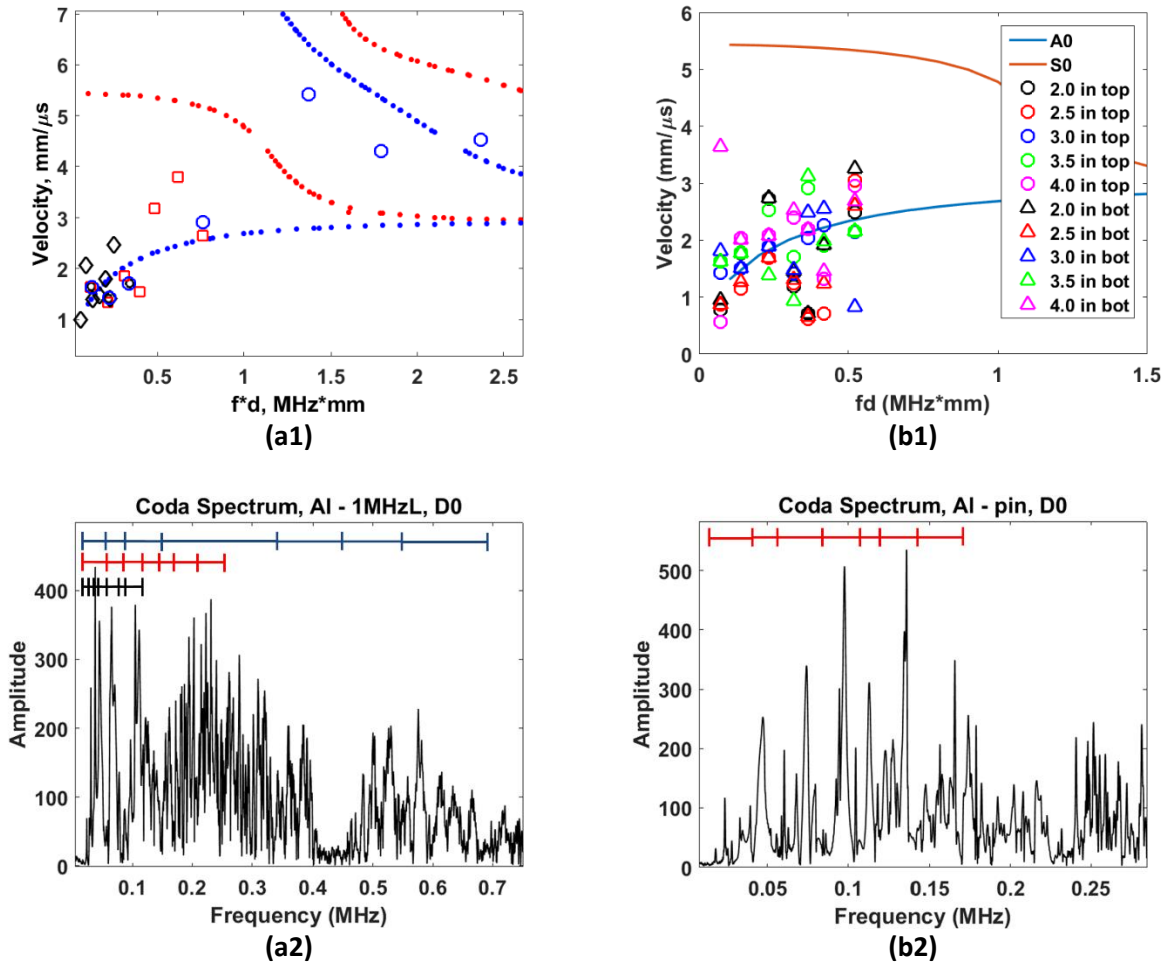

Figure 3-1. Decoupling coda wave components and comparing velocities to Lamb wave dispersion curves for a) 12.7 mm, 1 MHz longitudinal receiver and b) 2 mm pinducer. The dispersion curves for aluminum are shown in (1) while the spectra and windows are shown in (2). The signals were transmitted using a 12.7 mm, 1 MHz longitudinal transducer with a spike excitation.

Given the difficulty inherent in the deterministic propagation approach, the indeterministic propagation models have gained popularity since the early 2000's. Although the normal mode expansion and random walk models have their uses, the diffusion model can predict the envelope of the coda wave received at a given location. The diffusion of ultrasonic energy (E) is given by Anugonda et al. (2001) as:

$$D\frac{\partial^2}{\partial r^2}\langle E(r,t)\rangle - \frac{\partial}{\partial t}\langle E(r,t)\rangle - \sigma\langle E(r,t)\rangle = E_0\delta(r)\delta(t) \tag{3.1}$$

where D is the ultrasonic diffusivity, σ is the dissipation (decay rate), E_0 is the initial energy deposited by the transmitter, r is the distance between transmitter and receiver, t is time, and δ is a delta function. The solution to (3.1) is given as:

$$\langle E(r,t)\rangle = E_0\frac{1}{2\sqrt{\pi Dt}}e^{-r^2/4Dt}e^{-\sigma t} \tag{3.2}$$

Taking the natural logarithm of (3.2) and multiplying by t gives:

$$\left(\ln\langle E(r,t)\rangle + 0.5\ln(t)\right)t = -\sigma t^2 + C_0 t - \frac{r^2}{4D} \tag{3.3}$$

which can now be used for least squares linear regression. C_0 is a coefficient including E_0 and D.

To examine the applicability of the diffusion equation, coda wave signals were collected from aluminum, polycarbonate, and quasi-isotropic plates described by Figure 4-1c using a 12.7 mm 1 MHz longitudinal receiver. A second coda wave was collected from the aluminum sample using a pinducer receiver. In a similar manner to the calculation of the decay rate, the time domain signals are first equipartitioned using Tukey windows with 12% taper on either side. Next the power spectrum of each window is calculated and equipartitioned into frequency bins. The natural

logarithm of the total spectral power for a particular frequency bin is plotted against window center time and (3.3) is fit to the data using least squares. The results of this procedure are shown in Figure 3-2. All coda wave signals are moderately to well described by the diffusion envelope with the signal from the aluminum-pinducer combination exhibiting the best fit. Even the coda wave signal collected from polycarbonate is in good agreement with the diffusion envelope.

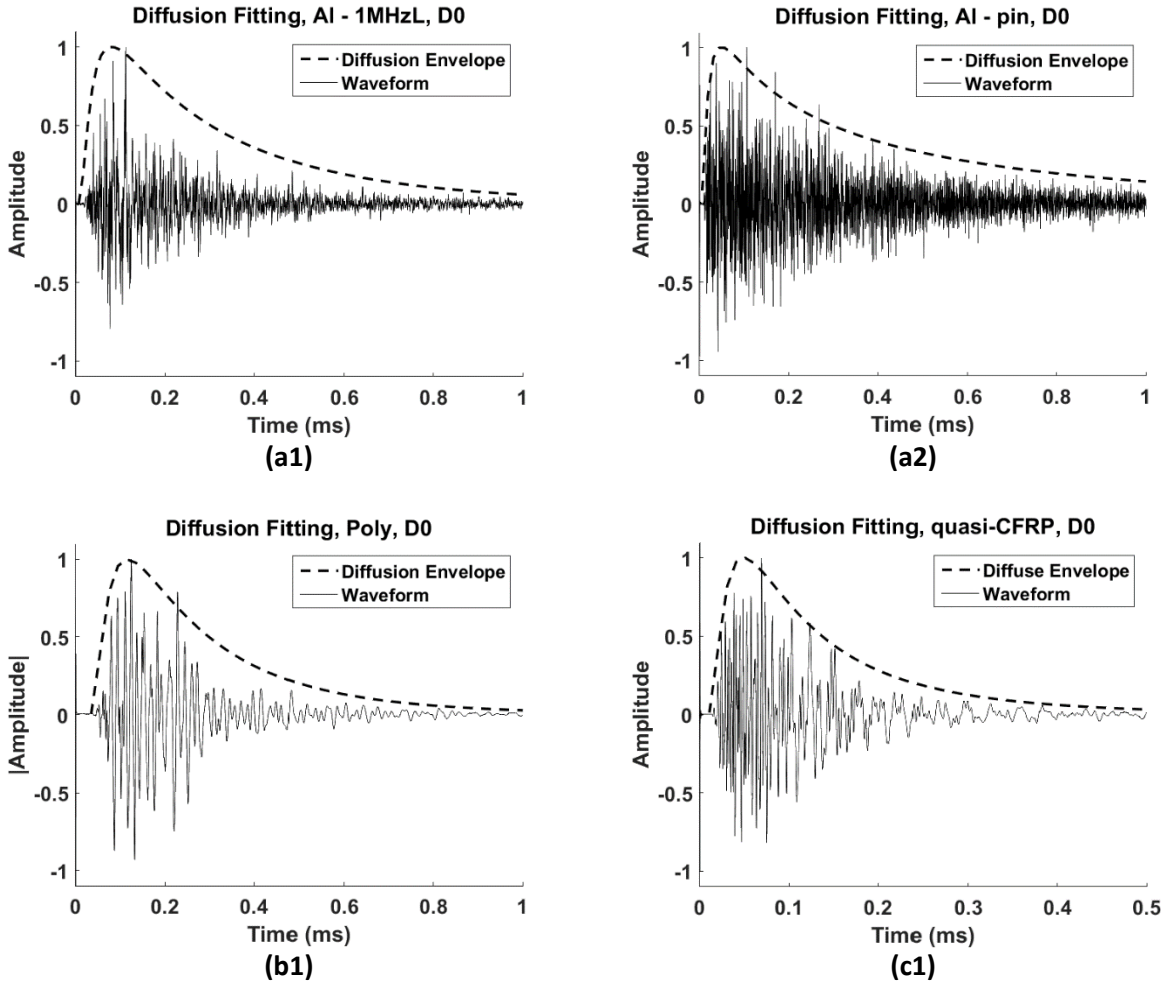

Figure 3-2. Fitting the diffusion equation to coda waveforms collected from a) aluminum and b) polycarbonate plates using 1) a 12.7 mm 1 MHz longitudinal receiver and 2) a 2 mm pinducer. CFRP is included for reference (c), but the diffusion equation is for isotropic materials only.

This unequivocally demonstrates that the diffusion model is a much better model for the propagation of coda waves than trying to decouple individual wave modes. Note that the coda wave signal from the quasi-isotropic CFRP sample is well described by the diffusion equation even though it was derived for isotropic materials.

The diffusion equation does not perfectly describe the coda wave signals. There are clear differences between the coda wave signals received with the 12.7 mm longitudinal transducer and the 2 mm pinducer. These signals were collected from the same sample at the same transducer separation without decoupling the transmitter, and yet the coda waves are significantly different, and these differences cannot be attributed to coupling differences. This is an example of the effects of phase cancellation.

3.2 Coda Wave Decay

3.2.1 Attenuation

A general definition for attenuation is given as the reduction in amplitude of a traveling wave, which can be termed "apparent" attenuation [Auld 1973]. Figure 3-3 illustrates this definition. A better definition can be given as the combined loss of ultrasonic energy due to conversion into other energy forms and the scattering of ultrasound out of the transmitter-receiver path after accounting for geometrical spreading, dispersion, and imperfect reflections and transmissions [Papadakis 1979, Weaver 1987]. Scattering and absorption of ultrasonic energy are inherently distinct physical mechanisms that remove energy from a propagating wave, and hence can potentially be decoupled by examining the time dependent decay of the scatter field.

Traditional measures of attenuation typically fit an exponential decay to the propagating waveform at various transmitter-receiver separations or to the multiple echoes from the back wall

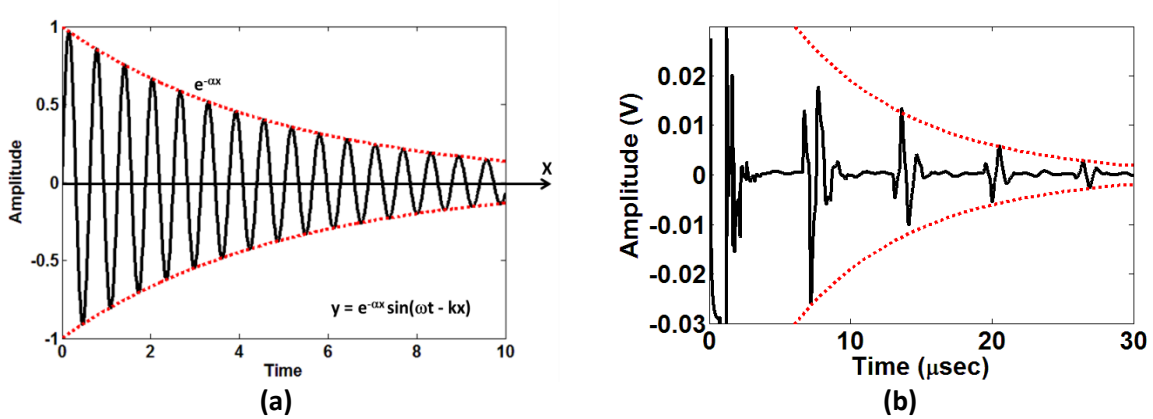

Figure 3-3. Illustrations of apparent attenuation of waves traveling in lossy media. a) General exponential decay of the wave amplitude. b) Apparent attenuation of multiple back wall echoes collected from a polycarbonate plate.

(Figure 3-3) either with or without correcting for beam spread, dispersion, and reflection coefficients. Correction for geometrical spreading etc. cannot be calculated for coda wave attenuation as a coda wave is a superposition of numerous wave modes that have been multiply scattered and/or reflected and the path of each wave mode is unknown. Coda wave attenuation is therefore limited to determining the apparent attenuation, and several methods of measurement are used in this chapter. The simplest measure of attenuation is the exponential fit of the maximum received amplitude vs. transducer separation. This can be expressed with the following model where y is the separation dependent peak amplitude, x is the separation, β is a constant coefficient, and α is the constant valued attenuation coefficient.

$$y(x) = \beta e^{-\alpha x} \tag{3.4}$$

A more complete picture of attenuation is given when the frequency dependent coefficient, $\alpha(f)$, is calculated. This is typically done by taking sequential signal pulses (e.g. back wall echoes) and dividing in the frequency domain in order to deconvolve the information of the material path

from the system transfer function [Papadakis 1979, Schmerr & Song 2007]. The wavenumber (k) for a wave propagating in a lossy medium must be complex (eq. 3.5), where the real portion describes the propagation and the imaginary part describes the attenuation [Achenbach 1973]. The attenuation is then calculated by dividing the signal transfer functions as per eq. 3.6 and 3.7, where G and F are the signal pulses, F^* is the complex conjugate of F, TR are the necessary transmission/reflection coefficients, r is the travel distance, W is the Weiner filter, and ζ is a stabilization constant.

$$k = k_1 + ik_2 \tag{3.5}$$

$$\alpha(f) = k_2(f) = \ln\left(\left|\frac{G(f)}{F(f)}\right| / T_r R\right) / r = \ln\left(|W(f)|TR\right) / r \tag{3.6}$$

$$W(f) \cong \frac{G(f)F^*(f)}{|F(f)|^2 + \zeta^2 \max\left\{|F(f)|^2\right\}} \tag{3.7}$$

Note that the purpose of dividing the signal transfer functions is to isolate the material transfer function and is only applicable when G contains the material transfer function in addition to the path transfer function contained in F. A complete description of this process for thick and thin plates is provided by Kinra & Dayal (1988). This method is included here for completeness but is not applicable to coda wave attenuation measurements. Unlike with the pulse-overlap method, the spectral magnitudes (or transfer functions) of coda wave signals collected at different transducer separations cannot be divided since the path information is different for each measurement and cannot be divided out (i.e. G does not contain the same path transfer function contained in F). In order to circumvent this difficulty and get a meaningful, frequency dependent attenuation coefficient, the signal spectra are calculated, partitioned into equal length windows, then inverse

Fourier transformed and the peak amplitude (y) determined. This is repeated for signals collected with different transducer separations. The peak amplitudes for each frequency window (with center frequency f_C) are then plotted vs. transducer separation and an exponential decay is fit (as a function of transducer separation). Determining the exponential fits for each of the frequency windows yields the frequency dependent apparent attenuation as given by Eq. 3.8 & 3.9.

$$y(r, f_c) = \beta(f_c) e^{-\alpha(f_c) r} \tag{3.8}$$

$$\alpha(f_c) = \frac{-\ln(y(r, f_c) / \beta(f_c))}{r} \tag{3.9}$$

3.2.2 Decay Rate

The method for calculating the decay rate of coda wave signals was developed by Weaver (1987). The intention of this method is to disambiguate true and apparent attenuation by determining the absorption of ultrasound due to internal friction. While the scattering of ultrasonic energy away from the beam path will be affected by cracks, pores, and interfaces, the internal friction will be more sensitive to microstructural condition. It has been shown that the coda wave decay rate is sensitive to impact damage and fiber/matrix bond strength in SiC/SiC composites [Lott & Kunerth 1990] as well as fabrication parameters and treatments of SiC fiber/RBSN composites [Kautz 1993].

The frequency dependent coda wave decay rate is determined by equipartitioning the time domain signal into equal length, non-overlapping time windows, calculating the power spectrum (P_S) for each time window, equipartitioning the power spectrum into non-overlapping frequency bins, then fitting a decaying exponential to the natural log of the total power vs. time window plot

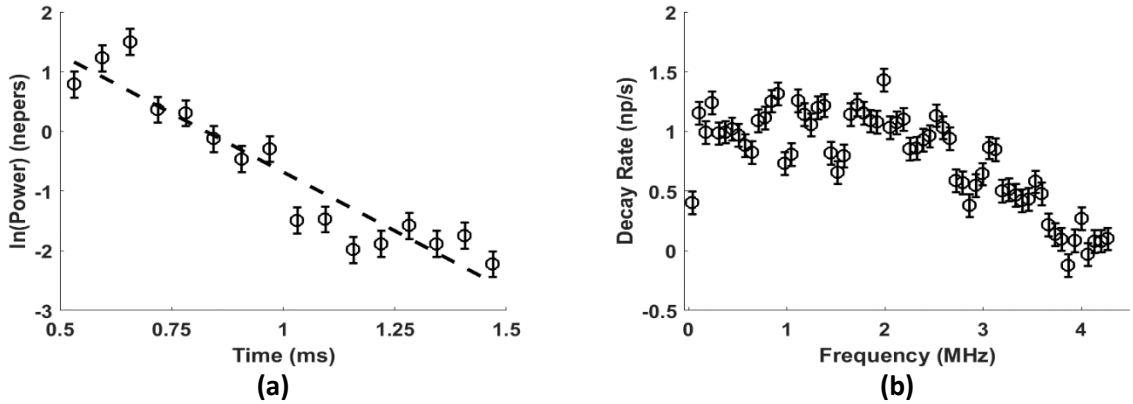

Figure 3-4. Steps in calculating the coda wave decay rate. (a) fitting the exponential decay and (b) the final frequency dependent decay rate. Signal was transmitted and received with 12.5 mm 2.25 MHz longitudinal transducers excited by a spike pulse in aluminum 6061 plate.

for each frequency bin (Figure 3-4). The decay rate is then half of the fitted slope with units of nepers per second. The accuracy of this method is several orders of magnitude higher than other methods of measuring pure attenuation [Weaver 1987].

Consider two continuous time-domain signals, a baseline signal, $x_0(t)$, and a signal collected after a disturbance, $x_1(t)$, hereafter referred to as the measured signal, both of fixed length T_L. The signals are sampled with a sampling period T_S such that $x_i[n]$ corresponds to the sample at time $t = nT_S$, with a total number of N points and n is the index. The discrete frequency representation (with index k) of the signal is then given by Eq. 3.10 and the spectral power by Eq. 3.11, where M is the number of points in the time-domain window with index m, L is the number of points in the frequency-domain window with index l, and w is the window function. The frequency dependent decay rate, α, is then given as Eq. 3.13.

$$X[n_c, p] = \sum_{m=0}^{M-1} x[m] w_1[m - n_c] e^{-j2\pi pm/M} \tag{3.10}$$

$$P_S[n_c, p_c] = \sum_{\ell=0}^{L-1} X^2[n_c, \ell] w_2[\ell - p_c] \Delta f \tag{3.11}$$

$$P_S(t, f) = \beta(f) e^{-2\alpha(f)t} \tag{3.12}$$

$$\alpha(f) = \frac{-\ln(P_S(t, f)/\beta(f))}{2t} \tag{3.13}$$

3.3 Differencing Parameters

Differencing parameters are parameters that quantify the difference or similarity between two waveforms. Commonly used differencing parameters include Cross-correlation Coefficient (CC) and Mean Squared Error (MSE).

3.3.1 Coda Wave Relative Velocity Extractions

Coda Wave Interferometry (CWI) was developed to detect small time-domain perturbations in the propagation medium that are normally undetectable using coherent waves by using a multiple scattering medium (scattering or reflections) as an interferometer [Snieder 2002]. The scattered waves repeatedly sample a region and accumulate small perturbations so that they become observable; this increases sensitivity when compared to coherent wave analysis [Zhang 2013]. The later the coda wave arrives the more pronounced the small perturbations become. Figure 3-5 shows the difference in the sensitivity to a small velocity perturbation between the early and late arrival portions of the received wave. Typical CWI is concerned with determining the relative time lag $\Delta t/t$ and the similarity between a baseline and post-perturbation waveforms. In

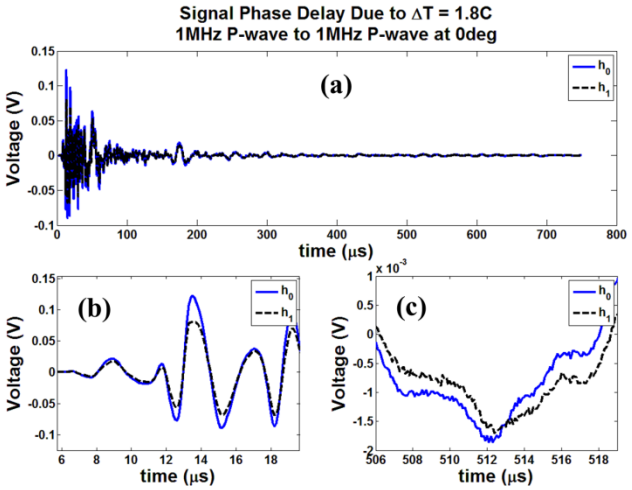

Figure 3-5. Ultrasonic waveforms collected from one-sided pit-catch UT on a 0.8 cm unidirectional CFRP plate subject to a 1.8 C temperature change. The two signals, h_0 and h_1, are collected before and after the temperature variation are the same in all three plots with a) the entire recorded signal, and windowed signals at b) early propagation time, and c) late propagation time. The signals are transmitted and received with 1.25 cm, 1 MHz longitudinal transducers.

the case of constant, homogeneous velocity perturbations, the relative time lag is the negative of the relative velocity, $\Delta v/v = -\Delta t/t$.

Three signal processing methods are widely used in literature to estimate the relative velocity variation produced by comparing collected signals before and after thermal loading: Cross-Spectral Moving-Window (CSMW, also known as doublet) [Roberts et al. 1992], Windowed Correlation (CWI, also known as Coda Wave Interferometry) [Snieder 2002], and Stretching [Sens-Schönfelder & Larose 2008]. A study by Hadziioanou et al. (2009) demonstrated that for pure, linear dilations, Stretching provides more stable and accurate results, especially in the presence of noise. The Stretching method was selected for this study based on the results of Hadziianou et al. (2009) and the consideration that thermal loads produce almost pure dilation [Weaver & Lobkis 2000].

Estimation of the coda wave relative velocity variation is dependent on the propagation velocity and path of the different wave modes present. Monitoring the propagation for each individual mode is quite difficult to do since each scattering event will produce mode conversion. The superposition of these modes can be treated statistically, however, and the relative velocity variations can be calculated based on the propagation of acoustic energy and the mode conversion rates as (3.14) for constant velocity perturbations in an isotropic medium with longitudinal velocity v_l and shear velocity v_S. For a Poisson medium, the relation reduces to (3.15) [Snieder 2006]. This indicates that the coda wave relative velocity can be determined by a change in moduli.

$$\frac{\Delta v}{v} = \frac{v_s^3}{2v_l^3 + v_s^3}\frac{\Delta v_l}{v_l} + \frac{2v_l^3}{2v_l^3 + v_s^3}\frac{\Delta v_s}{v_s} \tag{3.14}$$

$$\frac{\Delta v}{v} = 0.09\frac{\Delta v_l}{v_l} + 0.91\frac{\Delta v_s}{v_s} \tag{3.15}$$

Although the estimation of coda wave relative velocity is fairly straight forward in homogeneous and isotropic materials, for composite materials such as CFRP provide much more of a challenge. Wave modes in CFRP have different velocities in different directions and the thermally induced velocity change of each mode will also be different in all directions. This combined with the dispersive and attenuative nature of the material make analytical estimation of the relative velocity variation very difficult. It is likely, however, that the relative velocity change in the transverse direction will be larger than in the fiber direction due to dominance of matrix properties for transverse propagation and the increased sensitivity of the matrix moduli to thermal changes.

3.3.1.1 Stretching Technique

The Stretching method compares two time-domain signals, a baseline signal, $x_0(t)$, and a signal collected after a disturbance, $x_1(t)$, hereafter referred to as the measured signal. The measured signal is then dilated in time by dilation factor ε, giving $x_1(t(1-\varepsilon))$ [Sens-Schönfelder & Wegler 2006]. The similarity between the baseline and the dilated, measured signals is determined by the normalized cross-correlation coefficient evaluated at zero lag (3.16). A grid search is then used to find the dilation factor that maximizes the similarity between the baseline and dilated, measured signals: $CC(\varepsilon_k) = \text{Max}(CC(\varepsilon_i))$. If the velocity perturbation is linear, as it is for a homogeneous thermal load, then the relative velocity is proportional to the dilation factor ε_k: $\Delta v/v = -\varepsilon_k$. The drawbacks of this technique are that it is computationally intensive since it involves a grid search and that its accuracy depends on the resolution of the dilation factor.

$$CC(\varepsilon_i) = \frac{\int x_0(t(1+\varepsilon_i))x_1(t)dt}{\sqrt{\int x_0^2(t(1+\varepsilon_i))dt \int x_1^2(t)dt}} \tag{3.16}$$

Both continuous time-domain signals are sampled with a sampling period of T_S such that $x_i[n]$ corresponds to the sample at time $t = nT_S$. The total number of samples is given as N. If the signals have been sampled using Nyquist criteria, then the continuous signal can be completely reconstructed using ideal bandlimited reconstruction (3.17).

$$x(t) = \sum_{n=-\infty}^{\infty} x[n] sinc\left(\frac{t - nT_s}{T_s}\right) \tag{3.17}$$

A discreet signal can be perfectly reconstructed by evaluating (3.17) for specific time values giving ideal bandlimited interpolation (3.18). Since actual ultrasonic signals can be assumed to have zero amplitude for $n < 0$ and $n > N$, a summation over the number of points in the signal is sufficient.

$$\hat{x}[t(m)] = \sum_{n=0}^{N} x[n] sinc\left(\frac{t(m) - nT_s}{T_s}\right) \tag{3.18}$$

Interpolation of the dilated signal is necessary in order to compare it to the baseline signal since the samples do not otherwise line up and any further processing would be meaningless. For a dilated, discreet signal in the time domain, the sampling period becomes $T_S(1+\varepsilon)$, therefore the interpolated signal is given by (3.19), where $t(m) = t(n)$ for

$$\hat{x}[t(m)] = \sum_{n=0}^{N} x[t(n)] sinc\left(\frac{t - nT_s(1+\varepsilon)}{T_s(1+\varepsilon)}\right) \tag{3.19}$$

Recently, work has been presented attempting to improve the efficiency of the Stretching Technique by implementing a Taylor Series expansion [Liu et al. 2015]. The dilated continuous wave can be expressed as:

$$\mathbf{x}_1(t) = \mathbf{x}_0(t(1-\varepsilon)) + \eta(t) \tag{3.20}$$

where ε is the dilation factor and $\eta(t)$ is distortion in the waveform. If the stretch parameter is much less than 1, which it is guaranteed to be for any coda wave analysis, and the distortion is minimal, then the dilated wave can be expressed using the Taylor Series expansion.

$$\mathbf{x}_1(t) = \mathbf{x}_0(t) + \hat{\mathbf{x}}_0(t) t\varepsilon + O(t\varepsilon) \tag{3.21}$$

The dilation factor can then be solved for a sampled signal (with sampling frequency f_S) as follows:

$$\varepsilon = \frac{1}{N} \sum_{n=0}^{N} \frac{x_1[t(n)] - x_0[t(n)]}{x'_0[t(n)] t(n)} \approx \frac{2}{N f_S} \sum_{n=1}^{N-1} \frac{x_1[t(n)] - x_0[t(n)]}{t(n)\left(x_1[t(n+1)] - x_0[t(n+1)]\right)} \tag{3.22}$$

While this proposed improvement is significantly more computationally efficient in our opinion it has significant errors, especially for later window start times and larger dilation factors. Therefore, this new method is not used in this research.

3.3.2 Coda Wave Differential Features

One strategy for the detection and characterization of damage in structures when individual wave modes cannot be identified is to quantify how ultrasonic signals change between measurements via differential features [Michaels 2008]. A differential signal feature is a differencing parameter between two signals. The change in signal amplitude due to the reflection/scattering from a flaw is an example of such a feature. An ideal differential feature is zero for identical signals and benign changes (e.g. temperature variation) but increases with increasing damage severity. The most useful features should be normalized to be independent of the original signal amplitude. In the following sections, a signal that is taken from a pristine sample (one without damage, defect, or introduced discontinuity) is referred to as a "baseline" signal while a signal taken from a damaged sample (one with damage, defect, or introduced discontinuity) is referred to as "measured" signal.

Five distinct time-domain and frequency-domain features [Michaels & Michaels 2005, Lu 2007] are implemented for the quantitative comparison of baseline and measured signals for the detection of artificially damaged samples. They are: (1) residual temporal energy, (2) residual spectral energy, (3) loss of temporal coherence, (4) loss of correlation, and (5) differential curve length. These features are computed from time-domain signals. Consider two continuous time-domain signals, a baseline signal, $x_0(t)$, and a signal collected after a disturbance, $x_1(t)$, hereafter

referred to as the measured signal, both of fixed length T. The signals are sampled with a sampling period T_S such that $h_i[n]$ corresponds to the sample at time $t = nT_S$ with a total number of N samples.

3.3.2.1 Temporal Energy of the Residual

Temporal residual energy (E_{temp}) is a modified version of simple baseline subtraction that measures how closely the shapes of the measured and baseline signals match. This feature was first proposed by Michaels & Michaels (2005). The measured signal is first scaled to unity energy (3.23), then the baseline signal is scaled by γ to minimize the mean squared error between the two signals (3.24). The residual temporal energy is then the energy of the difference signal obtained by subtracting the scaled baseline signal from normalized measured signal over a specified time window from n_1 to n_2 (3.25).

$$\widetilde{x_1}[n] = \frac{x_1[n]}{\sqrt{\sum_{n=0}^{N-1} x_1^2[n]}} \tag{3.23}$$

$$\gamma = \frac{\sum_{n=0}^{N-1} \widetilde{x_1}[n] x_0[n]}{\sum_{n=0}^{N-1} x_0^2[n]} \tag{3.24}$$

$$\mathrm{E_{temp}} = \sum_{\mathrm{n=0}}^{\mathrm{N-1}} \left(\widetilde{xh_1}[n] - \gamma * x_0[n]\right)^2 \tag{3.25}$$

3.3.2.2 Spectral Energy of the Residual

Spectral residual energy (E_{spec}) quantifies the changing structure of the ultrasonic signal caused by damage/defects by measuring the scattered energy. This differential feature was first proposed by Michaels & Michaels (2005). The spectrograms of both signals are computed from the short-time Fourier transform (STFT) (3.26), where $w[n]$ is a Tukey window function of length $M < N$ and k is the frequency index ($0 \leq k < M$). Similar to the residual temporal energy, the

baseline signal is subtracted from the measured signal after normalizing the spectrograms to unity energy. The subtraction is performed for each time-frequency window (3.27). Integrating the square of the difference spectrum (D) over the frequency window yields the residual spectral energy (3.28).

$$X_i[n,p] = \sum_{m=0}^{M-1} x_i[m]w[m-n]e^{-j2\pi pm/M} \tag{3.26}$$

$$D[n,p] = \frac{|X_1[n,p]|}{\sqrt{\sum_{\hat{n}=n_1}^{n_2}\sum_{\hat{p}=p_1}^{p_2} X_1[\hat{n},\hat{p}]X_1^*[\hat{n},\hat{p}]}} - \frac{|X_0[n,p]|}{\sqrt{\sum_{\hat{n}=n_1}^{n_2}\sum_{\hat{p}=p_1}^{p_2} X_0[\hat{n},\hat{p}]X_1^*[\hat{n},\hat{p}]}} \tag{3.27}$$

$$E_{spec} = \sum_{n=n_1}^{n_2}\sum_{p=p_1}^{p_2} D^2[n,p] \tag{3.28}$$

3.3.2.3 Loss of Coherence

Loss of coherence (*LoCoh*), temporal, not spectral coherence, is a cross-correlation (*R*) (3.29) based measure of the time-dependent shape change between the baseline and measured signals. A differential feature based on this was proposed by Michaels & Michaels (2005). Normalizing the cross-correlation (3.30) makes this differential feature an amplitude-independent measure of damage. The peak coherence for each time window is the maximum correlation coefficient and the time delay is the delay corresponding to the maximum correlation. The loss of coherence is then computed by subtracting the mean peak coherence (one for each time window) from the maximum peak coherence (3.31).

$$R_{01}[\tau,t] = x_0[t] \cdot x_1^T[t-\tau] \tag{3.29}$$

$$\hat{R}_{01}[\tau,t] = \frac{R_{01}[\tau,t]}{\sqrt{R_{00}[0,t]R_{11}[0,t]}} \tag{3.30}$$

$$LoCoh = \max\left[\max_{\tau}\left(\hat{R}_{01}[\tau,t]\right)\right] - \text{mean}\left[\max_{\tau}\left(\hat{R}_{01}[\tau,t]\right)\right] \tag{3.31}$$

3.3.2.4 Loss of Correlation

The correlation of two signals is a measure of the overall match in waveform shape between the two signals and is a basic feature for ultrasonic damage detection [Zhang et al. 2004]. Therefore, the loss of correlation, as proposed by Michaels & Michaels (2005), measures the amount of temporal change between the baseline and measured signals. (3.32) gives the correlation between two signals expressed in terms of signal mean, *M*, standard deviation, *Σ*, and sampling period, Δ*t*. The loss of correlation (*LoCor*) is then computed as (3.33).

$$R_{01} = \frac{\Delta t}{\Sigma_0 \Sigma_1}\{(x_0[n] - \mathrm{M}_0) \cdot (x_1[n] - \mathrm{M}_1)^T\} \tag{3.32}$$

$$LoCor = 1 - R_{01} \tag{3.33}$$

3.3.2.5 Differential Curve Length

A signal's curve length is related to the complexity of the signal, so the differential curve length measures the change in complexity of the difference signal (measured – baseline). This feature was first proposed by Lu (2007). The differential curve length (*DCL*) is given by:

$$DCL = \sum_{n=0}^{N-1} |(\tilde{x}_1[n] - \tilde{x}_0[n]) - (\tilde{x}_1[n-1] - \tilde{x}_0[n-1])| \tag{3.34}$$

where $\tilde{x}$ again is the signal normalized to unity energy as per (3.23).

3.3.3 Equating Signal Energy with Wave Energy

Determining the relationship between different physical quantities in systems where the exact physics is very complex or not fully understood, is possible by comparing the fundamental dimensions of each quantity. In the case of ultrasonic systems where the transducer is an electro-

mechanical converter, input signal is a voltage, which passes to a piezoelectric material and is converted to a mechanical wave. The electrical fundamental unit for resistance and ampere, is not shared with mechanical quantities and can provide a barrier to determining a relationship between the two quantities. Nevertheless, the signal energy and wave mechanical energy can be related with the use of electrical impedance. Thus it is possible to relate electrical and mechanical quantities. A function predicting the behavior of differential signal features can be derived by analyzing the units of each feature. Such an analysis is fairly straight forward for the residual energies.

The temporal energy contained in the continuous signal *x(t)* is:

$$E_T = \int_{-\infty}^{\infty} |x(t)|^2 dt. \tag{3.35}$$

Here, the term energy is used in the generalized sense of signal processing with units of V^2s [Norton & Karczub 2003, Oppenheim & Schafer 1975]. The equivalency of temporal and spectral energy for discrete signals is given as:

$$E_t = \sum_{n=0}^{N} (|x[n]|^2 \Delta t) = \frac{1}{N} \sum_{n=0}^{N} (|X[n]|^2 \Delta f) = E_S \tag{3.36}$$

following Parseval's theorem, where *x[n]* is the discrete time-domain signal and *X[n]* is the discrete frequency-domain signal. Thus, residual temporal and spectral energy have the same units. The equivalency requirement between temporal and spectral energy from Parseval's theorem does not hold for residual energies since they are calculated differently. Signal energy is related to the acoustic wave energy through Ohm's law by dividing the signal energy by the electrical impedance as shown in (3.37) [Oppenheim & Schafer 1975].

$$\frac{V^2 s}{\Omega} = \left(\frac{kg*m^2}{A*s^3}\right)^2 s * \left(\frac{A^2*s^3}{kg*m^2}\right) = \left(\frac{kg*m^2}{s^2}\right) = J \tag{3.37}$$

The acoustic wave energy density is given as:

$$E_w = \frac{1}{2m}\rho \sum_{i=1}^{m} c_i^2 \tag{3.38}$$

where ρ is the material density, c_i is the velocity of the ith wave mode, m is the number of wave modes, and the units are J/m^3 [Achenbach 1976]. A volume is needed to convert the units of acoustic wave energy density into Joules.

Based on the units of residual energy, the function describing the behavior of the residual energy differential features takes the following form:

$$E_{res} = \xi * \rho * c_i^2 * D^2 * h * \Omega \tag{3.39}$$

where ξ is a scaling factor, c_i is the wave velocity of one of the modes, d is the hole diameter, h is the hole depth, and Ω is the system electrical impedance.

Determining the function for the other three features based on unit analysis is more difficult. Loss of coherence and differential curve length are unitless quantities while loss of correlation has units of time. This suggests that a function based on material properties cannot be derived without a way to cancel out the units of ampere from the electrical impedance. It is very likely that these features have no physical significance.

CHAPTER 4. EXPERIMENTS

This chapter provides an overview of the materials and equipment used in the experiments presented in this thesis. Section 4.1 describes the materials and samples examined in subsequent experiments. The experimental system, equipment, and data collection are detailed in Section 3.2. Measurement errors are discussed in Section 4.3. Finally, several characteristics of the experimental system are analyzed in Section 4.4. This includes the transducer transfer function, system signal-to-noise ratio, and wave form properties.

4.1 Samples

Measurements were made on five materials throughout this thesis: 6061 aluminum, polycarbonate, acrylic, uni-directional and quasi-isotropic carbon-fiber reinforced polymer as detailed in Table 4-1. Torayca 3900-series highly toughened carbon fiber-reinforced epoxy prepreg (Toray P235W-19) was chosen for the carbon-fiber material since it is the material that is used for the Boeing 787. Material was donated to Iowa State University by Boeing Corporation. The size scales for a typical CFRP laminate are shown in Figure 2-1.

Coda waves can form in nearly any material and geometry. Consider three extreme scattering cases: polycarbonate, aluminum, and CFRP. In a pristine sample of polycarbonate, the formation of the coda wave is due solely to the boundary scattering and waves propagate with little visco-elastic absorption. When a defect is introduced, both boundary and defect scattering cause the coda wave. In a damaged aluminum sample, grain, boundary, and defect scattering are superimposed to form the waves, which propagate without visco-elastic absorption. Coda waves in CFRP are significantly more complex: along with ply, fiber, boundary, and defect scattering,

Table 4-1. Material properties.

		Density (g/cm^3)	Young's Modulus (GPa)	Shear Modulus (GPa)	Poisson's Ratio	Longitudinal Velocity (m/s)	Shear Velocity (m/s)
Aluminium 6061		2.7[1]	68.9[1]	26[1]	0.33[1]	6300	3150
Polycarbonate		1.2[2]	2.35[2]	0.85[2]	0.38[2]	2400	1070
Acrylic		1.19[1]	3.10[1]	1.15[1]	0.35[1]	2040	980
CFRP (unidirectional)	In-plane	1.6[3]	154,12.8	5.96,3.27		10030[3],2900[3]	1930[3],1430[3]
Toray P2353W-19	Transverse		12.8	5.96,3.27		2900[3], 2900[3]	1930[3],1430[3]
CFRP (quasi-isotropic)	In-plane	1.6[3]	62.1	24.4, 9.0	0.27, 0.15	6940[3], 6400[3]	3900[3], 2370[3]
Toray P2353W-19	Transverse		12.8	9.0, 9.0	0.15, 0.15	2900[3], 2900[3]	2370[3], 2370[3]

[1] asm.matweb.com
[2] PD5103_AR1 0915 www.aetnaplastics.com
[3] measured or calculated

Table 4-2. Summary of specimens and introduced damage.

Specimen Number	Specimen Description	Material	Damage/Loading Description	Damage Location	
				Hole Number	Coordinates (mm)
1	304.8 x 304.8 x 8.5 mm	CFRP-uni CFRP-quasi Acrylic	Thermal loading Heated to 30˚, cooled slowly	--	--
2	152.4 x 50.8 x 6.35 mm	Aluminium 6061 CFRP-quasi Polycarbonate	Single through-hole 0.397 – 7.94 mm Drilled full through Stepped by 0.397mm	--	(25.4, 12.7)
3	152.4 x 50.8 x 6.35 mm	CFRP-quasi Polycarbonate	Single through-hole 1.59 – 6.35 mm Drilled halfway, then through Stepped by 0.397mm	--	(0, 0)
4	152.4 x 50.8 x 6.35 mm	CFRP-quasi Polycarbonate	Multiple through-holes 0.397 mm diameter Drilled full through 1-5 holes by 1	1 2 3 4 5	(10, 0) (-10, 0) (0, 10) (0, -10) (-4, 7.5)

visco-elastic absorption is prominent. Moreover, the orthogonal waves have distinct velocities that vary depending on propagation direction with respect to fiber direction.

A summary of the specimens discussed in this thesis is presented in Table 4-2. A plate size of 304.8 x 304.8 mm was chosen for specimen #1 as it is the largest plate that can be fabricated with available resources. The size and thickness of the aluminum sample described by specimen #2 was chosen to closely match the sample used in previous publications for comparison purposes [Michaels & Michaels 2005, Lu & Michaels 2005, Lu 2007, Michaels 2008]. The sizes and thicknesses of the CFRP and polycarbonate samples described by specimen #2, 3, and 4 were selected to match the aforementioned aluminum sample and thus account for sample geometry when comparing damage detection in different materials.

4.1.1 Samples Used for Wave Propagation

Measurements were made on several samples: 30x30x0.8 cm plates of Plexiglas (isotropic), unidirectional CFRP (transversely isotropic, and quasi-isotropic CFRP; 15.24x5.08x0.64 cm plates of aluminum 6061, polycarbonate, and quasi-isotropic CFRP. The acrylic samples, although simple in terms of material and geometry, are of interest because there is little to no internal scattering and minimal attenuation due to absorption. Therefore, the development of coda waves will be due to reflections from the boundaries. By contrast, the CFRP plate is complex in terms of material with simple geometry: Development of coda waves will be due to multiple, strong scattering from the fiber-matrix interface and the multiple plies in addition to the boundary reflections. The CFRP plate also exhibits high attenuation due to absorption, dispersive effects, and bulk wave velocities that vary with direction. The sample geometries, transducer locations and measurement locations are shown in Figure 4-1.

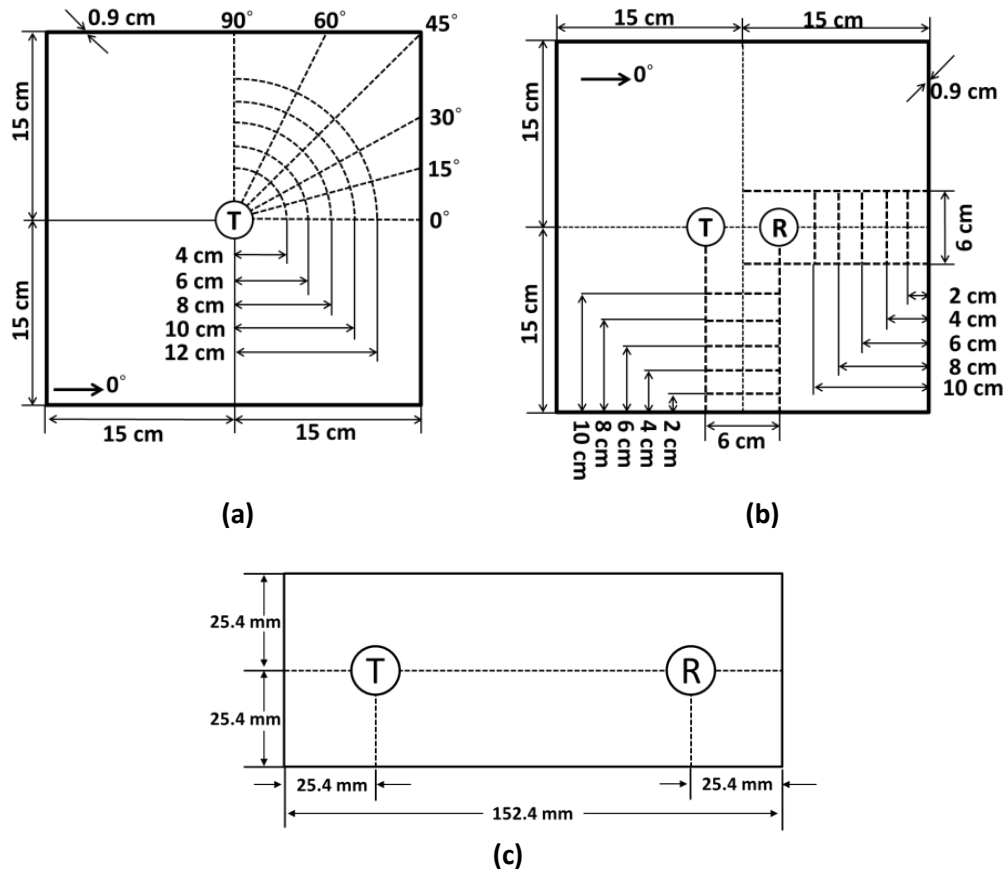

Figure 4-1. Illustrations of the unidirectional CFRP plate showing the sample dimensions and the transducer placement locations with a) a schematic of the sample and data collection points for the coda wave propagation in CFRP, b) a schematic of the sample and data collection points for the boundary effects in CFRP, and c) small plate configuration for finite vs. semi-infinite boundary measurements.

4.1.2 Samples Used for Drilled Hole Detection

Measurements were made on three materials: 6061 aluminum, polycarbonate, and carbon-fiber reinforced polymer as illustrated in Figure 4-2 and detailed in Table 4-2. Although these specimens are simple in geometry, each offers distinct wave scattering and propagation characteristics. Aluminum is isotropic with grain scattering, polycarbonate is isotropic with no internal scattering, and CFRP is quasi-isotropic with ply and fiber scattering as well as visco-elastic absorption.

Damage was introduced either by drilling a single through-thickness hole of increasing size (specimen #1 & #2) or by drilling multiple through-thickness holes of uniform size (specimen #3). For specimen #1, the damage was introduced as a single 0.397 mm (1/64") diameter through-thickness hole. The hole diameter was then gradually increased to 7.94 mm (5/8") by increments of 0.397 mm (1/64"). The damage for specimen #2 was introduced by drilling halfway through the plate then completely through, as illustrated in Figure 4-3. Hole diameter ranged from 1.59 mm (4/64") to 4.37 mm (11/64") by steps of 0.397 mm (1/64")..In specimen #3, the damage consists of five 0.397 mm (1/64") diameter through-thickness holes. Ultrasonic signals were recorded after each subsequent hole or enlargement of the hole. The ambient temperature of the lab was taken for each signal collection. The temperature remained steady at 21.1 $^{\circ}C \pm 0.1$. Table 4-2 summarizes the three specimens and introduced damage.

4.1.3 Samples Used for Determining Thermal Effects

Measurements were made on two samples; a 30x30x0.9 cm Plexiglas plate (isotropic) and a 30x31.8x0.9 cm unidirectional CFRP plate (transversely isotropic) with the material properties summarized in (Table 4-1). The Plexiglas plate, although simple in terms of material and geometry, is of interest because there is little to no internal scattering and minimal attenuation due to absorption. Therefore, the development of coda waves will be due to reflections from the boundaries. By contrast, the CFRP plate is complex in terms of material with simple geometry: Development of coda waves will be due to multiple, strong Rayleigh scattering from the fiber-matrix interface in addition to the boundary reflections. The CFRP plate also

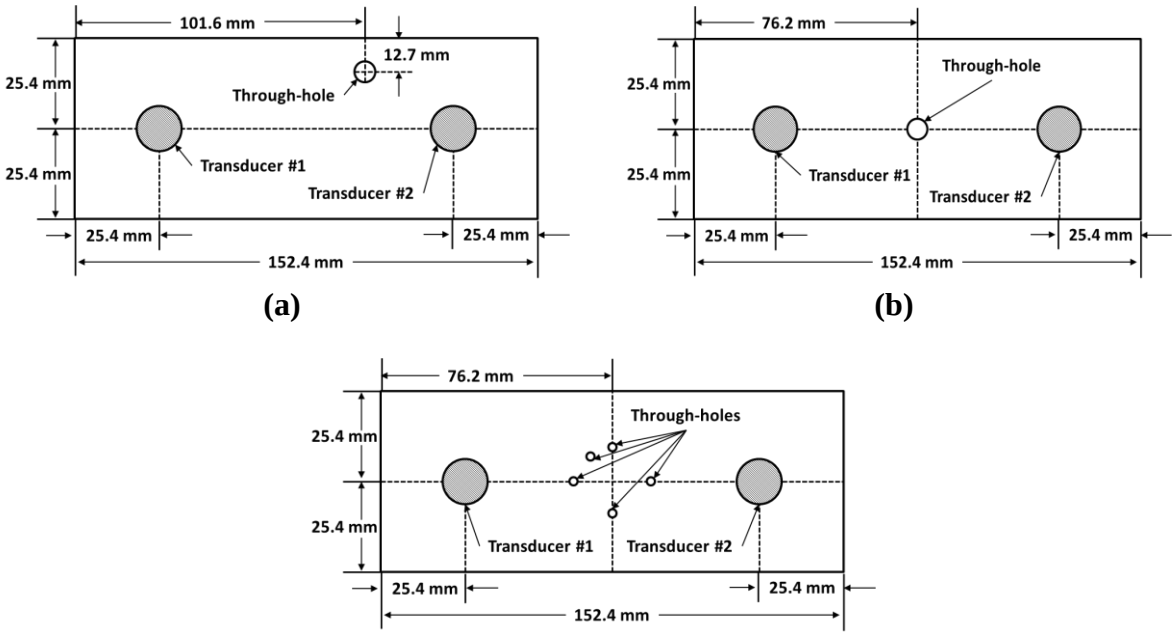

Figure 4-2. Illustration of the samples (thickness of 6.35mm) with damage and transducer placement. (a) Specimen #1, rectangular plate with single through-hole of increasing diameter. (b) Specimen #2, rectangular plate with single through-hole of increasing diameter and depth. (c) specimen #3, rectangular plate with multiple through-holes of constant diameter clustered around the plate center.

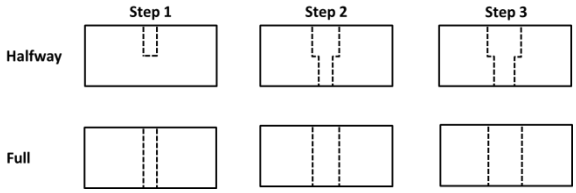

Figure 4-3. Illustration of introducing damage in specimen #2.

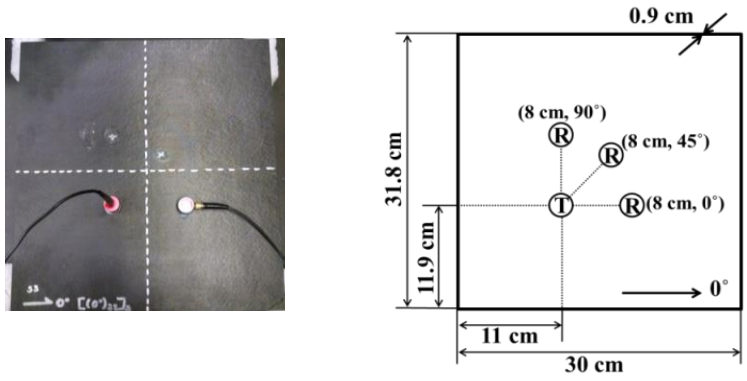

Figure 4-4. Illustrations of the unidirectional CFRP plate showing the sample dimensions and the transducer placement locations.

exhibits high attenuation due to absorption, dispersive effects, and bulk wave velocities that vary with direction.

The specimens were subjected to thermal variations by heating them to 30 ± 2.1 ˚C and allowing them to cool freely in an insulated enclosure (to slow down the specimen cooling rate) while monitoring the temperature with an Omega HH12 type-K thermocouple. Allowing the plate to cool down slowly in an enclosure helps to eliminate heterogeneous temperature zones and hence heterogeneous velocity variations by ensuring a consistent temperature throughout the plate. Coda wave signals were collected during the cool down of the specimens starting at 24 ± 2.1 ˚C and continuing until room temperature was reached, which was 20.0 ± 2.1 ˚C. During processing, 21.0˚C is considered to be room temperature so that both positive and negative waveform dilatation can be examined. Two separate thermal couples were used to verify the variations in temperature, they varied by less than 0.1 ˚C.

4.2 Experimental Configuration

A conventional Panametrics 5052 PR ultrasonic pulser-receiver was used for a 300V spike excitation as well as reception and signal amplification. Primary amplification of the signals came from a Panametrics 40 dB constant gain ultrasonic preamp. A LeCroy HDO 4022 12-bit digital oscilloscope (Teledyne LeCroy Corp., Chestnut Ridge, NY, USA) digitized the signals with a 50 MHz sampling frequency. Each recorded signal was averaged 200 times to increase the signal to noise ratio. Figure 4-5 shows a schematic of the ultrasonic system configuration. The pulser-receiver damping settings were varied and a 6 dB attenuation was applied to the excitation signal from a RITEC RA-30 high power attenuator (RITEC Inc., Warwick, RI, USA) in order to test the linearity of the system and the coda wave parameters.

Several piezoelectric transducers are used throughout this thesis and are described in Table 4-3. The Panametrics transducers were selected for their sensitivity for the higher frequency spectral energy in the coda waves (Figure 5-3). While the majority of energy in the coda wave lies below the bandwidth of these transducers precision measurements can still be made since the measurements are comparative by nature and the configuration is not changed between subsequent measurements.[6] The pinducer will encompass more than 90% of the spectral energy, but suffers a large reduction in power (power is r^2 dependent) and are notoriously noisy.[7] The transducers are either coupled temporarily using honey or semi-permanently using Crystalbond 555 (a water soluble wax with a flow point of 66˚C). The transmitting transducer is semi-permanently attached in all experiments while the receiver is semi-permanently attached during damage detection. Semi-permanently coupling the transducer minimizes changes in coupling, but the changes in coupling with time or degradation of the coulpling with Crystalbond 555 has not been addressed. The effect

[6] Private communications, Frank Margetan, Dan Barnard, Jennifer Michaels, July 2015-May 2016.
[7] Private communications, Frank Margetan, Ron Roberts September 2015.

of decoupling and recoupling the transducers on the coda wave repeatability is discussed in Chapter 5.

All the waveforms in this work are collected over 0-2000 μs and are digitized with 50 MHz sampling frequency. This window length is sufficient to capture all of the waveform energy since increasing the collection time increases the signal energy by less than 1E-3%. It should be noted that this collection time is long enough for a longitudinal wave in aluminum to travel more than 12 m (13 m for CFRP and 4 m for polycarbonate). Since prior literature often used lower bit-depths (8bit) and sampling frequencies (2—15 MHz), both the bit-depth and the sampling frequency were reduced during post-processing to determine if there were any significant differences in the results. Though this modification does affect the accuracy of the amplitude (peak amplitude/2^bit depth) and time measurements (0.5/sampling frequency), it does not affect the coda wave parameters discussed in subsequent chapters.

Figure 4-6 through Figure 4-8 shows typical baseline and damage signals from each of the three specimens. Although the signals are significantly different for the different materials, a visual comparison of the baseline and damage signals yields only subtle differences. No obvious temporal or spectral signal differences are present between the baseline and the 0.4 mm damage signals by which damage is detectable or characterizable. Significant differences are observable, however, between the baseline signal and the 6.4 mm signals.

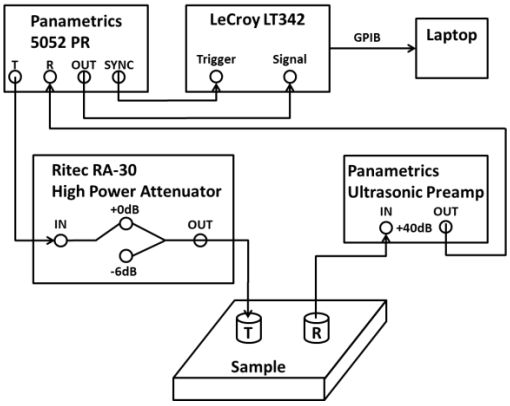

Figure 4-5. Experimental Configuration for one-sided pitch-catch ultrasonic transmission.

Table 4-3. Ultrasonic receiver characteristics as provided by manufacturer.

Manufacturer	Part #	Wave Type	Diameter (mm)	Center Freq (MHz)	-6dB Bandwidth (MHz)
Panametrics	**V103**	**L**	12.7	1.0[2]	0.5-1.5[1]
Panametrics	**V153**	**S**	12.7	1.0[2]	0.5-1.5[2]
Panametrics	**V106**	**L**	12.7	2.25[2]	0.5-2.75[1]
Digital Wave Corp.	**B1025**	**L**	6.25	1.0[2]	0.05-2.0[2]
Valpey-Fischer	**--**	**L**	2.0	5.0[2]	0.001-10.0[2]

L = longitudinal
S = shear

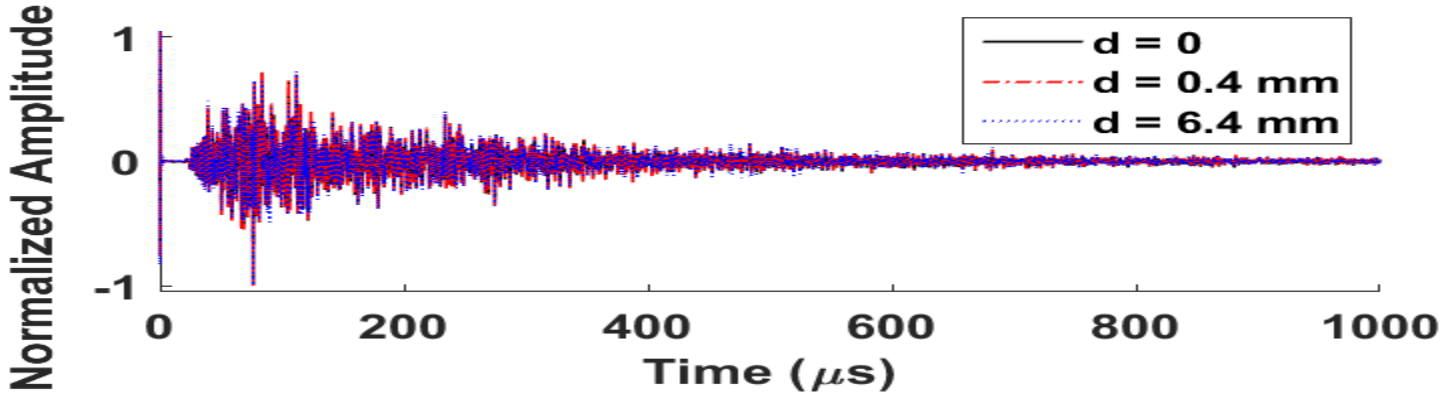

(1)

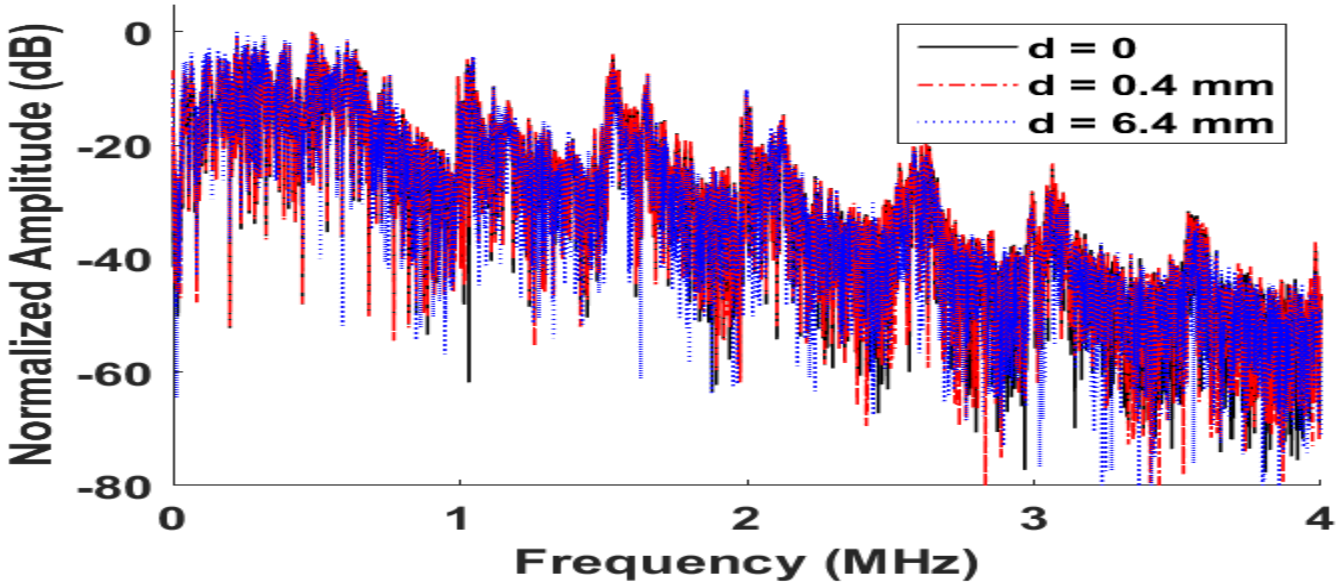

(2)

Figure 4-6. Representative waveforms (1) and spectra (2) collected from aluminum with various size drilled through-holes. The signals are transmitted and received with a pair of 12.7 mm 2.25 MHz longitudinal transducers excited with a spike pulse.

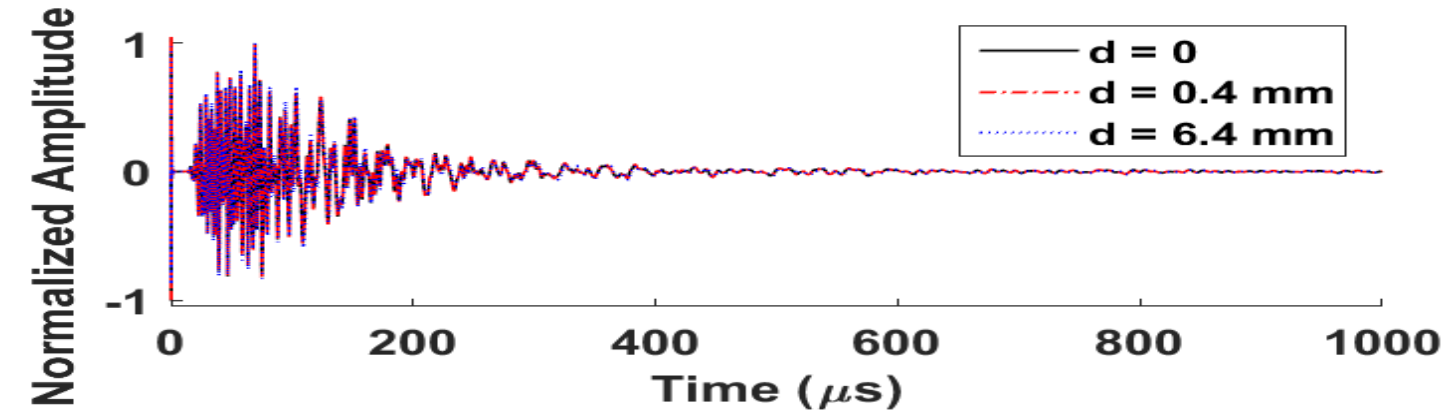

(1)

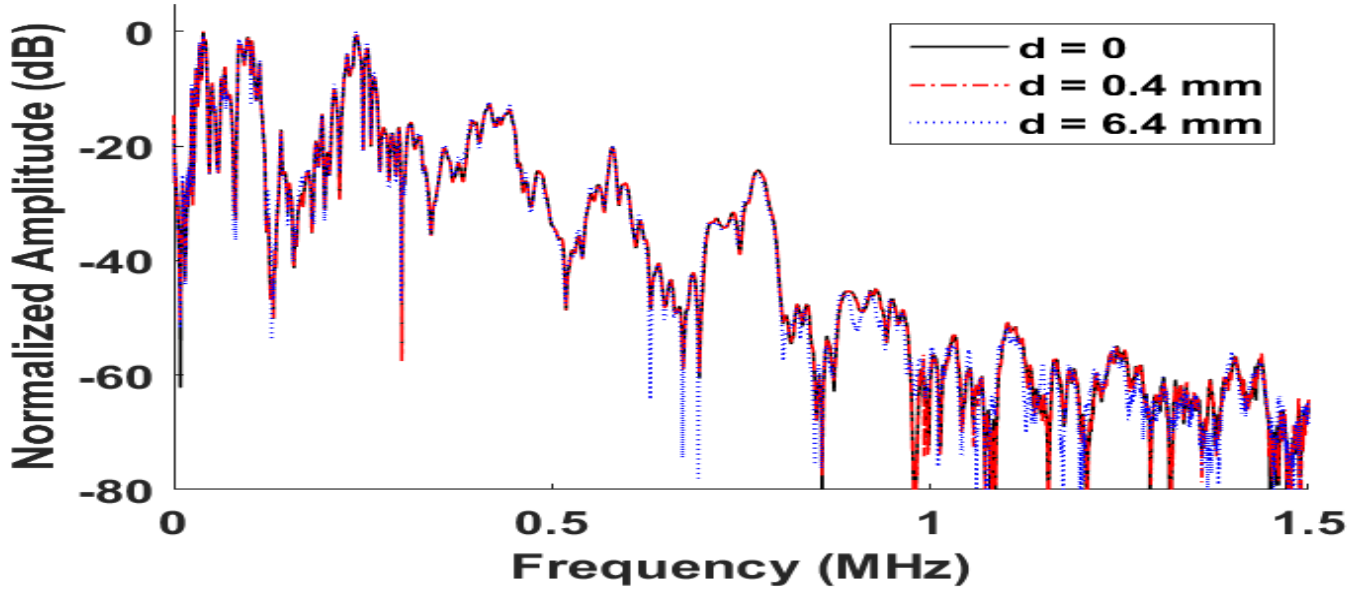

(2)

Figure 4-7. Representative waveforms (1) and spectra (2) collected from quasi-isotropic CFRP with various size drilled through-holes. The signals are transmitted and received with a pair of 12.7 mm 1.0 MHz longitudinal transducers excited with a spike pulse.

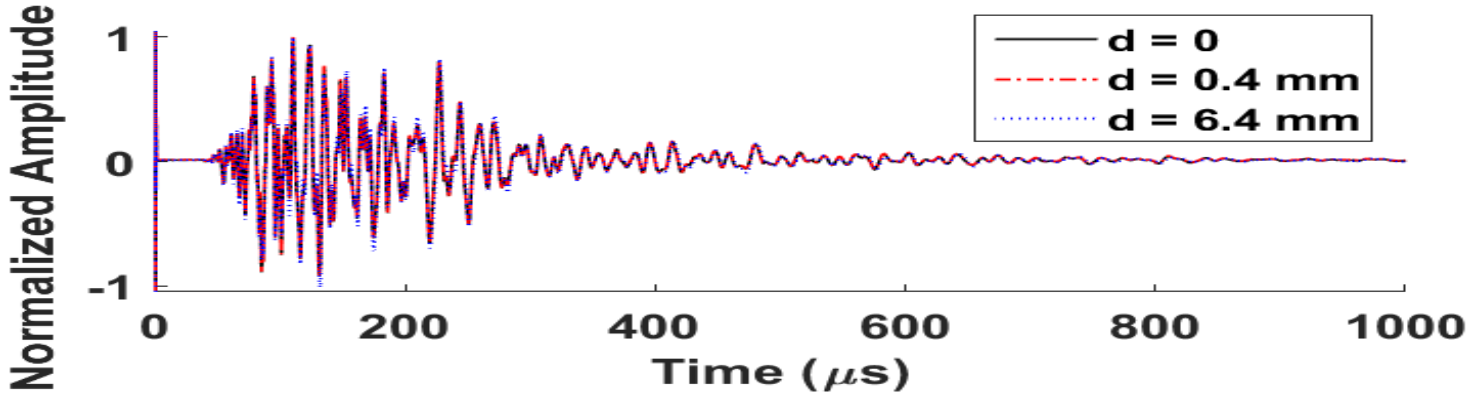

(1)

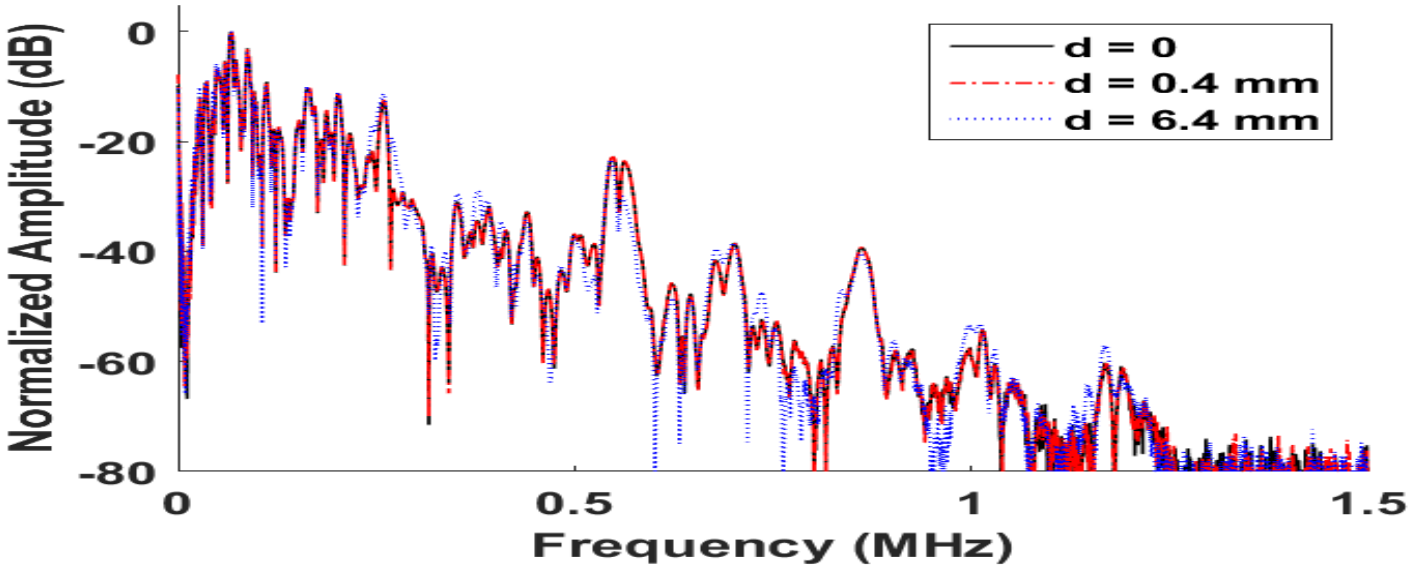

(2)

Figure 4-8. Representative waveforms (1) and spectra (2) collected from polycarbonate with various size drilled through-holes. The signals are transmitted and received with a pair of 12.7 mm 1.0 MHz longitudinal transducers excited with a spike pulse.

4.3 Error Analysis

A standard error analysis is not possible to perform with coda wave measurements. The coda wave consists of many superimposed wave modes, each with a different propagation/scattering path, which is very difficult to trace. It has been shown that the dominant errors in coda wave analysis stem from transducer placement errors, coupling inconsistencies, system noise, and environmental changes [Mazzeranghi & Vangi 1999, Gyekenyesi et al. 2002, Snieder 2006, Lu 2007, Zhang et al. 2013b]. Errors from transducer placement and coupling are eliminated by semi-permanently attaching the transducers for a given experiment. Errors from environmental changes are minimized by collecting data over a short period of time while room temperature and humidity remain steady.

4.3.1 Measurement Uncertainty

One method of error analysis is to examine the standard deviation of repeated measurements [Topping 1979, JCGM 2010], but this is a measure of precision, not accuracy. Measurement uncertainty is comprised of accuracy error and precision error. The accuracy error is the difference between the measure value and the true value caused by systematic errors such as calibration offsets and repeatable measurement biases while the precision error is the variation in repeated measurements caused by random processes. Figure 4-9 illustrates the measurement uncertainty for a distribution of repeated measurements where the accuracy error appears as an offset and the precision error appears as the standard deviation.

Difference measurements are computed by subtracting a baseline from a measured quantity when both the baseline and measurement are measured with the same experimental configuration. This type of measurement yields a relative quantity (e.g. change in temperature)

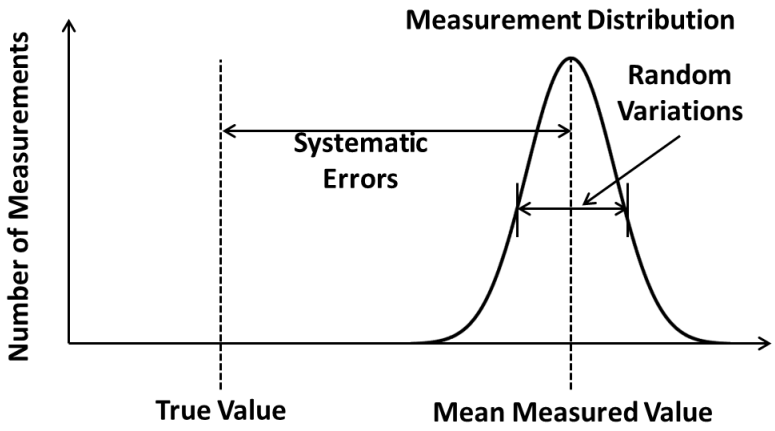

Figure 4-9. Measurement uncertainty for repeated measurements.

and is often more accurate than single measurements because the systematic errors are eliminated by the subtraction. The only error left is the random measurement error caused by system noise, EMF fluctuations, or other non-systematic error sources. These errors are observable in the standard deviation of repeated comparative measurements.

4.3.2 Experimental and Signal Processing Errors

A/D conversion was performed with a 12-bit system with a maximum recorded peak-to-peak amplitude of 1.6 V. Thus the uncertainty in the amplitude measurement is $4.69_E{}^{-2}$ mV. Likewise, the uncertainty in the time measurement can be determined from $\varepsilon_t = 1/2*F_s$, where F_s is the sampling frequency. For this study, the sampling frequency was 50 MHz, giving a time uncertainty of 10 ns.

The errors involved with calculating the attenuation come from errors in the measurement of amplitude, time, and transducer location, errors in the FFT algorithm, and errors in the Least Squares (LS) process. Since the amplitude, time, and location errors are the same for each data

point, they do not affect the results of the weighted LS process. The FFT algorithm has an associated root mean squared error of $O(\varepsilon_f (\log N)^{0.5})$, where ε_f is the floating point relative accuracy and N is the number of data points. This gives a maximum value of $4.477_E{}^{-15}$ for this work, and is thus negligible. Weighted LS gives standard errors in the calculated slope of the linear fit [Hughes & Hase 2010], namely:

$$\varepsilon_{LS-i} = \sqrt{\frac{\sum_i w_{LS-i}}{\sum_i w_{LS-i} \sum_i w_{LS-i} x_{LS-i}^2 - \left(\sum_i w_{LS-i} x_{LS-i}\right)^2}} \tag{4.9}$$

Where x_{LS} is the independent variable and w_{LS} is the weight applied to each data point. The weight is set to the inverse square of the uncertainty of each data point.

The errors in the coda wave decay rate calculations are similar to those for the attenuation calculations with the addition of an uncertainty in the calculation of the power spectrum. The uncertainty of the power spectrum is given by [Weaver 1987]:

$$a_i = P_{T-i} \left(\Delta T \Delta F\right)^{-1/2} \Rightarrow w_{LS-i} = P_{T-i}{}^{-2} \left(\Delta T \Delta F\right) \tag{4.10}$$

Where P_T is the value of the total power, ΔT is the width of the time window, and ΔF is the width of the frequency window. The inverse square of the power spectrum uncertainty is used as the weights for the LS regression. The decay rate errors reported are approximately eight times larger than those reported by Weaver due to the fact that the length of our time domain signal is approximately one eighth Weaver's.

Errors reported for the waveform parameters, attenuations, and damage indices are taken as three standard deviations of the repeated measurements, which will encompass 99% of the measurements. The errors are propagated according to standard practices [Hughes & Hase 2010, Topping 1972].

The temperature measurement error is a combination of the sensor error and the thermocouple error, where ε_{sensor} = 0.3% of measurement + 1˚C and ε_{therm} = max(0.4% of measurement, 1.1˚C) [www.omega.com]. Since the error of the thermal couple wire is a calibration constant, it is only necessary when determining absolute temperature. When considering relative temperature measurements, the wire calibration does not affect the measurement and the measurement error is due solely to the sensor error. This was confirmed experimentally by using two separate thermocouple wires simultaneously with the same sensor. When measuring temperature differences (as we are in this study) the cold junction compensation (CJC) error, which normally dominates the sensor error, becomes insignificant as long as the sensor itself is held at near constant temperature. The error in consecutive temperature measurements is therefore given as ε_{temp} = 0.3% of measurement.

4.4 System Characterization

4.4.1 Transducers

Signals were collected in pulse-echo mode on a sample of fused silica in order to determine the transducer transfer functions for the 12.7 mm 1 MHz and 2.25 MHz longitudinal transducers. The 6.4 mm AE receiver and 2 mm pinducer were not evaluated due to their inability to be used with a high voltage pulse-echo configuration, low transmission power, and their limited use in this work. The transducer functions were isolated by correcting for beam spread, attenuation, and transfer losses via deconvolution in the frequency domain using the propagation models and Weiner filter described by Schmerr & Song (2007). Figure 4-10a shows the measured, frequency dependent transducer functions for a PR damping setting of 0. The -6 dB bandwidth determined from the figure is listed in Table 4-3. Several pulse-echo signals were subsequently collected at

different PR damping settings (0, 3, 6, 9) to examine its effect on the transducer functions, and the results are shown in Figure 4-10b. An increase in damping (decreasing the electrical impedance) decreases the spectral amplitude up to several orders of magnitude and increased the peak frequency by several tens of kHz. It should be noted that the decrease in spectral amplitude of the transducer functions illustrates the reduction of signal energy, but not reduced sensitivity of the transducers as the first derivative of the transducer functions (when normalized to unity) vary by less than 5%. Also note that the transducer function will change when coupled to different materials[8] [Adams 2007]. This effect has not been well characterized in literature and is not analyzed here, but this effect does not significantly modify the transducer transfer function.

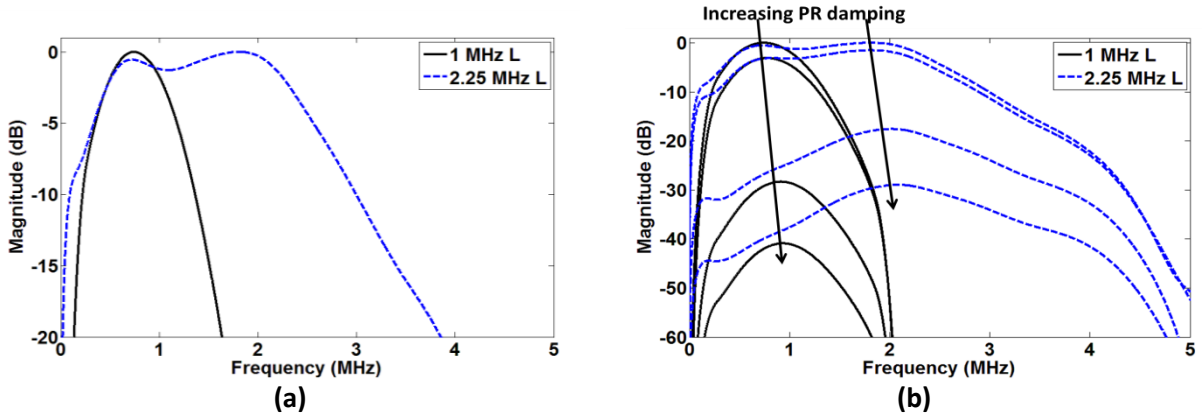

Figure 4-10. Transducer characteristics. (a) comparison of 1 MHz and 2.25 MHz longitudinal transducers and (b) effect of increasing the pulser-receiver damping setting. All results are normalized to the peak amplitude at a PR damping setting of 0.

[8] Private communications, Frank Margetan, Dan Barnard, Jennifer Michaels, July 2015-May 2016

4.4.2 Signal-to-Noise Ratio

The ratio of the signal amplitude to noise (signal-to-noise ratio, *SNR*) is an important factor that determines if a signal component can be distinguished from the background noise. A good definition for noise is any undesired signal components that obscure the signal components of interest. From this noise definition, it is fair to say that *SNR* is a good measure of the detectability of a flaw for traditional ballistic wave inspection [NDT Resource Center 2014]. In the cases where this statement holds, the goal is to distinguish a specific signal feature from all extraneous signal features. Thus the extraneous features are referred to as "noise." Often, the signal features corresponding to scattering and reflections are undesirable and referred to as noise [Chiou et al. 1995, Howard et al. 1995]. Examples of unwanted signal features that are usually referred to as noise are illustrated in Figure 4-11 and Figure 4-12. Multiple reflections from a typical pulse-echo of a pristine plate are shown in Figure 4-11. The first, second, and third back wall reflections are easily distinguishable as desirable signal. On the other hand, the low amplitude signal in between these reflections is undesirable since it is not directly related to the back wall reflection, and hence is commonly referred to as noise (e.g. back-scatter noise). The amplitude of the forth back wall reflection is so low that it is nearly indistinguishable from the noise.

There are nearly as many quantitative ways to define signal to noise ratio as there are applications that are interested in it [Howard et al. 1995]. A rule of thumb for ultrasonic inspection based on the ratio of the flaw signal amplitude to the background amplitude is that 3 dB > SNR >40 dB is required [NDT Resource Center 2014]. The subtle changes in coda waves due to small scale damage is are not separable from the coda wave, and hence the preceding *SNR* rule of thumb is not necessarily applicable. A proper definition of *SNR* depends on the definition of noise and how the data is processed. Coda wave NDE utilizes the multiply scattered signal that was

traditionally referred to as noise, therefore, the only noise left in the signal is due to the equipment, cabling, and transducers.

The theoretical SNR limit for any analog to digital converter (ADC) is the ratio of a single bin to half the total number of bins (the number of bins = $2^{\text{number of bits}}$). Thus, the maximum theoretical SNR for an 8 and 12 bit ADC is 42 and 66 dB respectively. This theoretical limit can be easily surpassed by adding dither, drastically oversampling (e.g. more than 100 times the Nyquist frequency), and low pass filtering [Smith 2003].

The *SNR* of coda wave signals can be determined either by (#1) estimating the system noise (DAC quantization noise, cabling noise, thermal noise, and electronic noise) by examining extremely late portions of the waveform (t > 2 ms) or (#2) by decoupling the transducers from the sample and collecting the signal. It should be noted that the *SNR* will change with different materials and coupling conditions[9] [Adams 2007]. *SNR* estimation method #1 is illustrated in Figure 4-13. Table 4-4 Lists the measured SNR for coda waves in unidirectional CFRP as described by "specimen #1" (Table 4-2). The peak *SNR* was determined with a 0-1 ms time window while the 1 ms *SNR* was determined with a 0.95-1.05 ms time window.

Because of the differing definitions of what is noise and what is signal, the *SNR* of coda wave signals is often much higher than that of traditional ballistic UT signals. Since coda wave consist of reflected and scattered waves (traditionally termed noise), the only unwanted portions of the waveform is the random system noise, which can be reduced significantly by averaging, and the electronic noise, which is often only a few bins. In many cases *SNR* of 50-60 dB for the peak signal amplitude are not unreasonable. Recent work has demonstrated that useful information can still be extracted from coda waves with even when the *SNR* for the peak amplitude is 1

[9] Private communications. Frank Margetan, Dan Barnard, September 2015-May 2016.

[Hadziioannou et al. 2009]. The work presented in this thesis uses data from coda waves signals with a 0-1 ms time window.

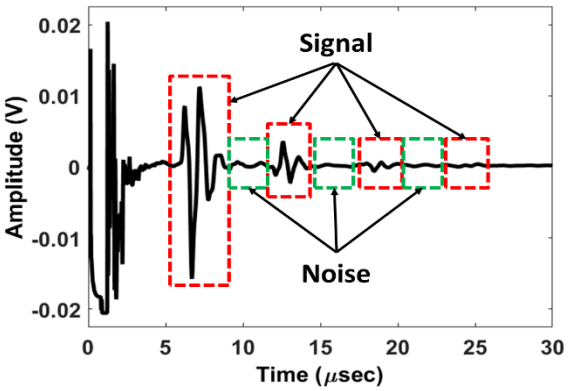

Figure 4-11. Differentiation of what is considered signal and what is considered noise in a typical pulse-echo waveform. The signal was collected in quasi-isotropic CFRP with a 1MHz longitudinal transducer excited with a spike pulse.

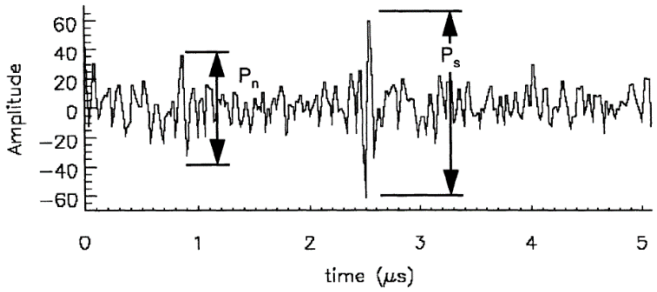

Figure 4-12. A typical signal collected from a Titanium sample showing the grain noise (Pn) and the flaw signal (Ps). [Howard et al. 1995].

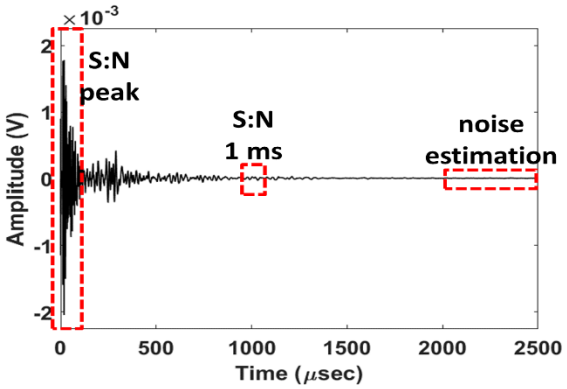

Figure 4-13. Diagram of noise and signal to noise ratio estimation locations for SNR method 1. Signal shown was collected from a unidirectional CFRP plate as described by "Specimen #1" (Table 4-2). The signal was transmitted with a 1 MHz longitudinal transducer and was received with a 1 MHz shear transducer at a separation of 6 cm (Table 4-3).

Table 4-4. Signal to noise measurement results The waveforms were collected from a uni-directional CFRP sample (Specimen #1). Signal was transmitted and received with 1 MHz longitudinal transducers.

Method	Signal Location	Fiber Angle	1 MHz L (dB)	1 MHz S0 (dB)	1 MHz S90 (dB)	Pinducer (dB)
1	Peak	0	55	50	55	58
		90	50	47	49	48
	1 ms	0	5	5	12	12
		90	10	9	12	10
2	Peak	0	60	60	50	55
		90	60	35	47	48
	1 ms	0	13	14	8	9
		90	19	5	6	10

L = longitudinal mode
S0 = shear mode polarized along fiber 0˚ direction
S90 = shear mode polarized along fiber 90˚ direction

4.4.3 Waveform Reciprocity

The reciprocity of ultrasonic measurement systems was first introduced into the NDE community by Kino (1978) and Auld (1979) and has since been widely accepted [Thompson & Gray 1989, Schmerr & Song 2007]. To test the reciprocity of the measurement system used for this thesis specifically and of coda waves in general, signals were collected from an aluminum sample as described by "Specimen #2" (Table 4-2) where the signals were transmitted and received by 12.5 mm 2.25 MHz transducers as described in the experimental configuration above.

Visual comparison of two signals sent from left to right (forward wave) and one signal sent from right to left (backward wave) is shown in**Figure 4-14**. **Figure 4-14**a shows that signals as recorded while **Figure 4-14**b shows a small portion of the expanded signal corresponding to the black outline. No appreciable difference is visually discernable between the three waveforms. To quantify the degree of similarity between the forward and backward waves, the cross-correlation coefficient was computed at zero lag for the entire waveform (50 million pts). The average cross-

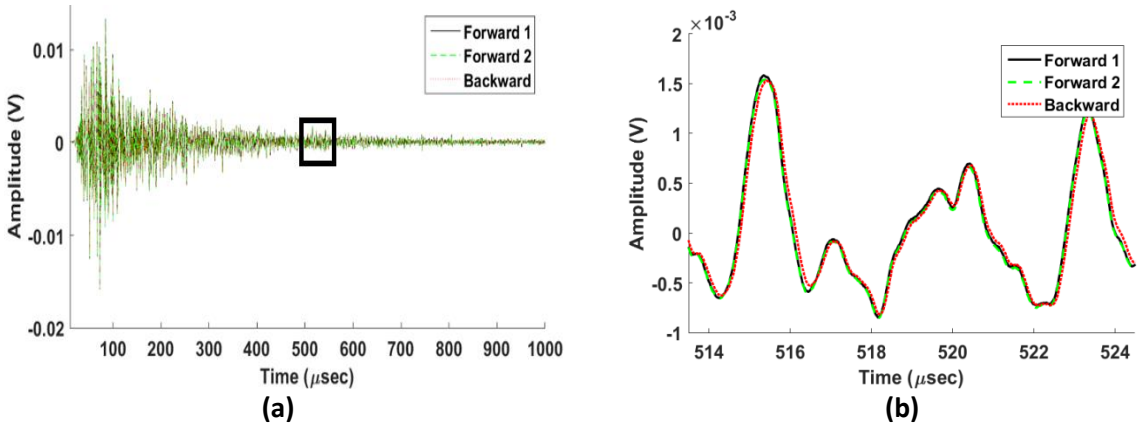

Figure 4-14. Example of the reciprocity of coda waves by switching the transmitting and receiving transducers. A) the full waveforms and b) enlarged section. The waveforms were collected from an aluminum sample as described by "Specimen #2" (Table 4-2). Signal was transmitted and received with 2.25 MHz longitudinal transducers.

correlation coefficient for ten repeated forward signals is 0.9999 while the average coefficient between a forward and ten backward signals is 0.9988. This indicates a high degree of similarity between the forward and backward waves.

A better method to characterize the similarity or dissimilarity between waveforms is to use the differential signal features defined in Chapter 3. Ten forward and ten backward signals were compared (windowed 0-1.0 ms using a Tukey window), and the results are listed in Table 4-5. To give a reference for the values listed, several other comparisons are also made. The first row of the table confirms that the various differential features yield a value of zero for identical waveforms as expected. The second line shows the comparison of the two forward signals (10 signals each) with the same transducer emitting and the same transducer receiving in each case. Several of the differential features are listed, and the difference between the two forward signals are all on the order of 1/10,000 to 7/10,000. This is also a measure of repeatability. The next row shows the results when the second signal is reversed, which means that the transmitter and receiver are interchanged. The differential features are an order of magnitude larger than the previous line, but

Table 4-5. Characterization of the similarity in reciprocal waveforms using differential features (Ch. 5). The waveforms were collected from an aluminum sample as described by "Specimen #2" (Table 4-2). Signal was transmitted and received with 2.25 MHz longitudinal transducers.

	Etemp (V^2s)	**Espec (V^2s)**	**LoCoh**	**LoCor**
Forward 1 vs. Forward 1	0.00	0.00	0.00	0.00
Forward 1 vs. Forward 2	3.30E-4	1.91E-4	7.36E-4	1.09E-4
Forward 1 vs. Backward	7.56 E-3	4.00 E-3	1.20 E-3	3.68 E-3
Forward 1 vs. Forward w/ 0.794 mm through-hole	4.00 E-2	8.47 E-2	3.52 E-2	1.99 E-2

Etemp = residual temporal energy
Espec = residual spectral energy
LoCoh = loss of coherence
LoCor = loss of correlation

are still on the order of 1/1000 to 8/1000. Finally, the last row contains the results when the forward signal taken from a pristine sample is compared to the forward signal from the same sample but with a single through-hole of 0.794 mm diameter. It is needless to say the differential features will be larger, but what is noteworthy here is that the features are an order of magnitude larger but in the same range (i.e. 2/100 to 9/100). The comparison of several different waveforms shows:

- Repeatability of the measurement: 20 signals were recorded with differential feature amplitudes within 1/1000.
- Reciprocity of the measurement: 10 forward and10 backward signals were recorded with differential feature amplitudes within 1/100.
- The presence of a single 0.794 mm (1/32") diameter through-hole causes a change in the differential feature amplitudes which is an order of magnitude larger than the reciprocity variance and two orders of magnitude larger than the repeatability variance.

This is the first experimental confirmation of the repeatability and reciprocity of coda waves. Reciprocity holds for the experimental system used in the thesis specifically and coda waves in general.

4.4.4 Waveform Linearity

One of the central objectives of this research is to convert coda wave methods from binary damage indicators to a mature, measurement based technique. Towards this end, the effect of the input power and pulser-receiver damping setting on the measurement have been studied. A field technician may not be aware of all the subtleties of the coda wave measurement. If the recorded signal and the final result are independent of the equipment used, then the instrument setting variability is removed, thus making the task of the user easier.

The system is operating linearly if no new or differing structures appear in the waveform or spectrum with changing input power level. A comparison of waveform amplitudes at 100% and 50% input power for the three materials is shown in Figure 4-15. The waveforms are normalized to the maximum amplitude of the 100% power signal for each material. A 50% reduction in the power of the input signal corresponds to an amplitude reduction of ~40% for each sample and a 60-65% reduction of energy, but no new/differing structures are apparent. Since no new or differing structures are present, the waveforms are considered to behave linearly. The correlation coefficient was calculated at zero time lag to confirm the similarity of the waveforms, which yielded correlation values of 0.9965, 0.9995, and 0.9980 for aluminum, CFRP, and polycarbonate respectively. The difference between the full and half power waveforms is very subtle, and could be attributable to noise.

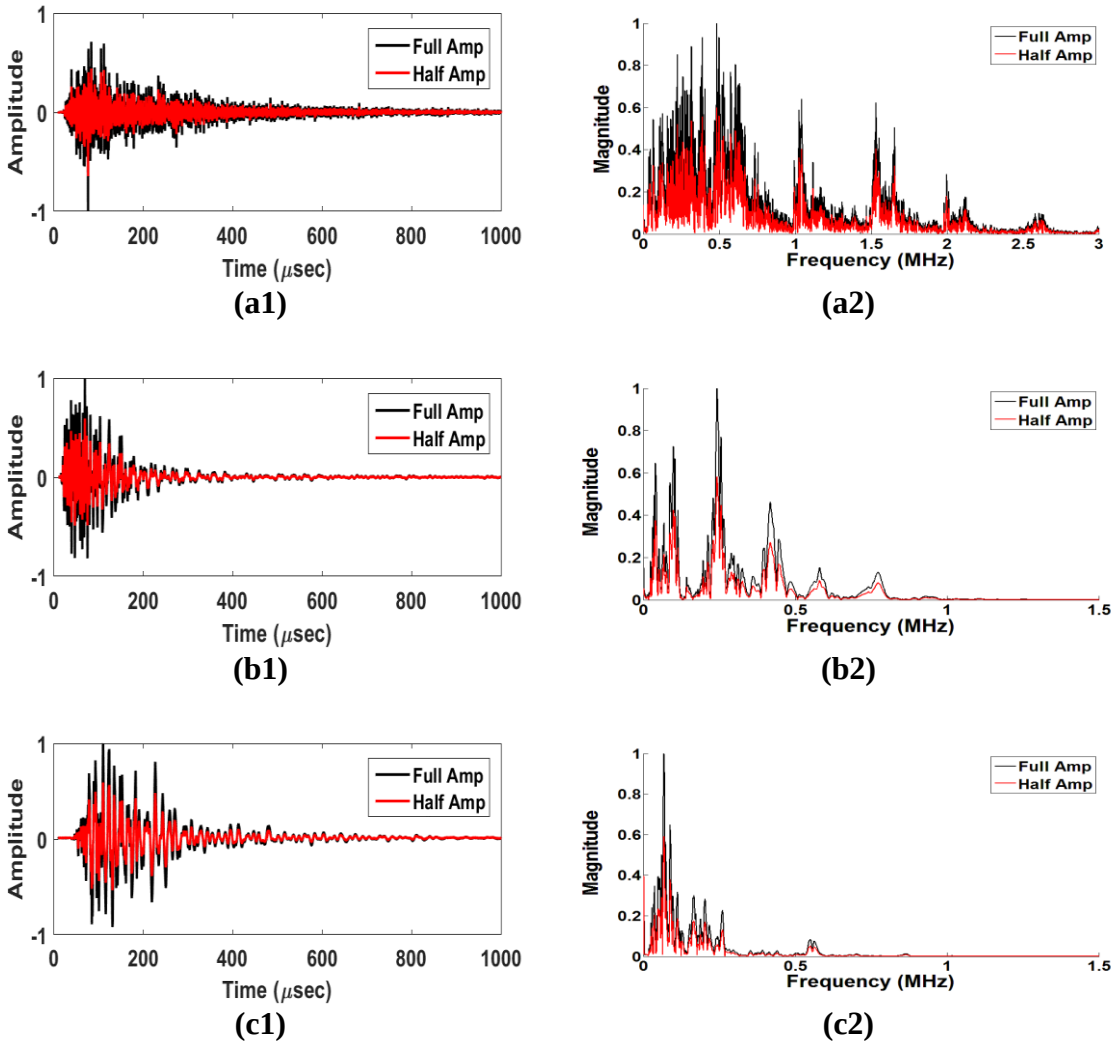

Figure 4-15. Comparison of (1) waveforms and (2) spectra from full strength signals and signals with -6dB input collected from (a) aluminum, (b) CFRP, and (c) polycarbonate samples. The received waveforms are normalized to the maximum amplitude of the 100% power waveform for each pair.The signals are transmitted and received with a pair of 12.5mm longitudinal transducers (2.25 MHz for aluminum and 1 MHz for CFRP and polycarbonate) excited with a spike pulse.

Adjusting the electrical impedance ratio between the pulser-receiver (PR) and the transducer is standard practice to maximize the received signal amplitude and reduce noise as much as possible. The impedance setting on the PR has the effect of damping the ring-down of the transducer. Lower damping (higher impedance) increases the length of the ring-down, which increases energy and decreases bandwidth. The cabling and transducer ideally have an electrical impedance of ~50 Ω.

Figure 4-16 shows the envelope of the waveforms collected at pulser-receiver impedance settings of 94, 80, and 40 Ω (corresponding to damping settings of 0, 3, and 6 respectively on the PR) for the three materials. Increasing the PR impedance from 80% to ~190% of the cable-transducer impedance has the effect of drastically increasing the temporal energy of the received coda wave, especially at mid to late times: this is most notable for the polycarbonate sample (Figure 4-16c). The arrival time of the envelope peak amplitude also increases with increasing PR impedance: most notable in the CFRP sample (Figure 4-16b). The total waveform energy for all materials is plotted in Figure 4-16d. It should be noted that changing the damping setting on the PR does change the transfer function of the PR [Schmerr & Song 2007], which is the primary cause of small changes in waveform structures.

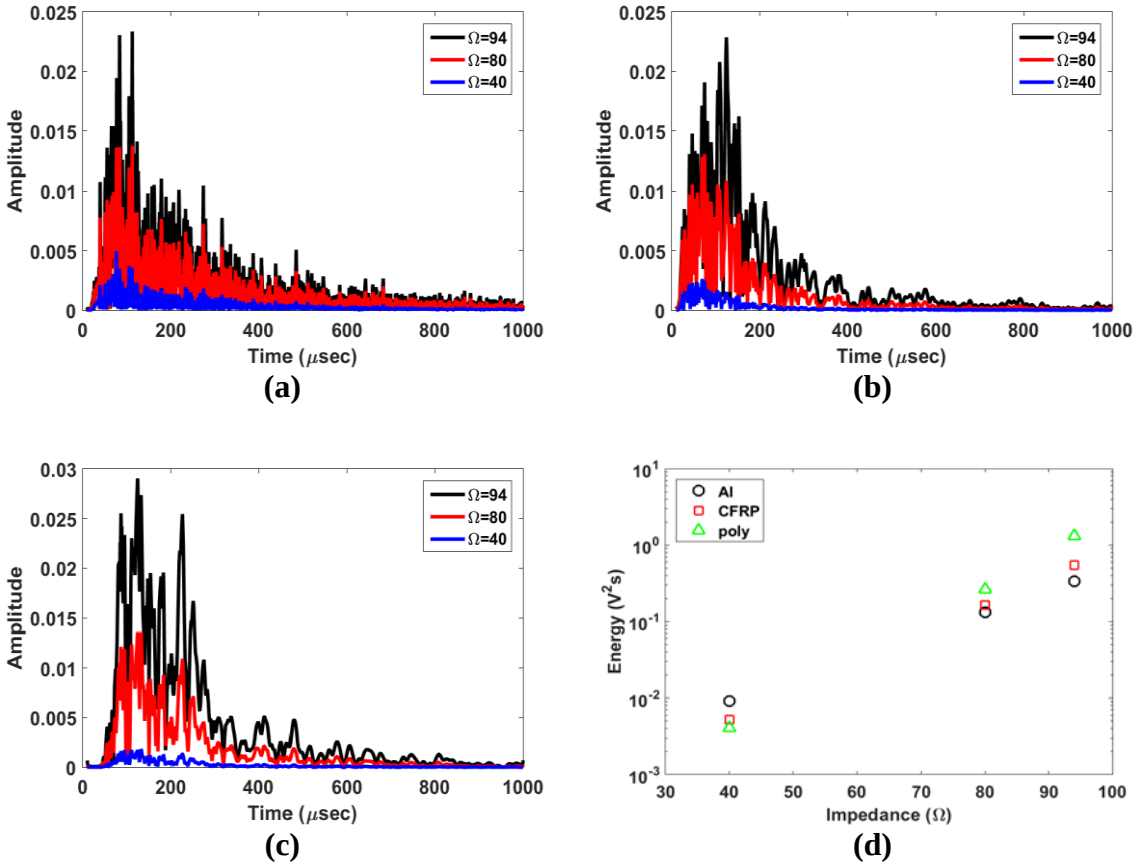

Figure 4-16. Comparison of waveforms collected from (a) aluminum, (b) CFRP, and (c) polycarbonate samples at three different PR damping settings. Plotted is the magnitude of the Hilbert transform. Total waveform energy is plotted in (d) for all materials. The signals are transmitted and received with a pair of 12.5mm longitudinal transducers (2.25 MHz for aluminum and 1 MHz for CFRP and polycarbonate) excited with a spike pulse.

CHAPTER 5. PROPAGATION OF CODA WAVES

This chapter discusses the propagation and attenuation of coda waves in carbo-fiber/epoxy plates. The influence of plate boundaries on coda waves is also discussed. Section 4.1 discusses the repeatability of coda wave measurements. The waveforms and spectra are discussed in Section 5.2. Section 5.3 presents, analyzes, and discusses the results for the propagation and spreading function of coda waves. Several distinct measures of attenuation are then presented and discussed in Section 5.4. Finally, the work and conclusions presented in this chapter are summarized in Section 5.5.

5.1 Repeatability

Coda waveforms themselves were shown earlier Section 4.4 to be both repeatable and reciprocal. Here the variances of several parameters that describe the coda waveform are examined. These parameters are shown in Figure 5-1 and include: peak amplitude, arrival time of the peak amplitude, spectral energy, and coda wave decay rate.

Multiple coda waveforms were collected from the 30x30 cm unidirectional CFRP and quasi-isotropic CFRP plate samples with an orientation of 0 and 90 degrees and from the 30x30 cm Plexiglas plate sample with an orientation of 0 degrees to determine the repeatability of collection and processing. The transducer pair had a separation of 8 cm with the transmitter coupled using crystal bond and the receiver coupled using honey. A transducer separation of 8 cm was selected to maximize the signal energy while still providing high frequency content. Signals (200 averages) were collected ten times without detaching the receiver for all three configurations, and then ten signals were collected after detaching and reattaching the receiver in-between each

collection. Each of the collected signals were then averaged, processed and the mean and standard deviation of several parameters (Figure 5-1) are presented in Table 5-1 & Table 5-2.

The repeatability of measurements is characterizable by the sharpness of the measurement distribution. Thus the quality factor, *Q*, and the standard deviation, σ, can be used to quantify the repeatability of measurements. The percent variance is also a useful measure of repeatability since it quantifies the width of the measurement distribution compared to the mean value. Mean values of the measurement distributions are typically an order of magnitude (or more) greater than the standard deviation. This yields a percent variance that is generally lower than 5% for most of the parameters calculated. This is true even when detaching and reattaching the transducers, however, there is a marked increase in the percent variance and a decrease in the *Q* values due to the decoupling and recoupling process.

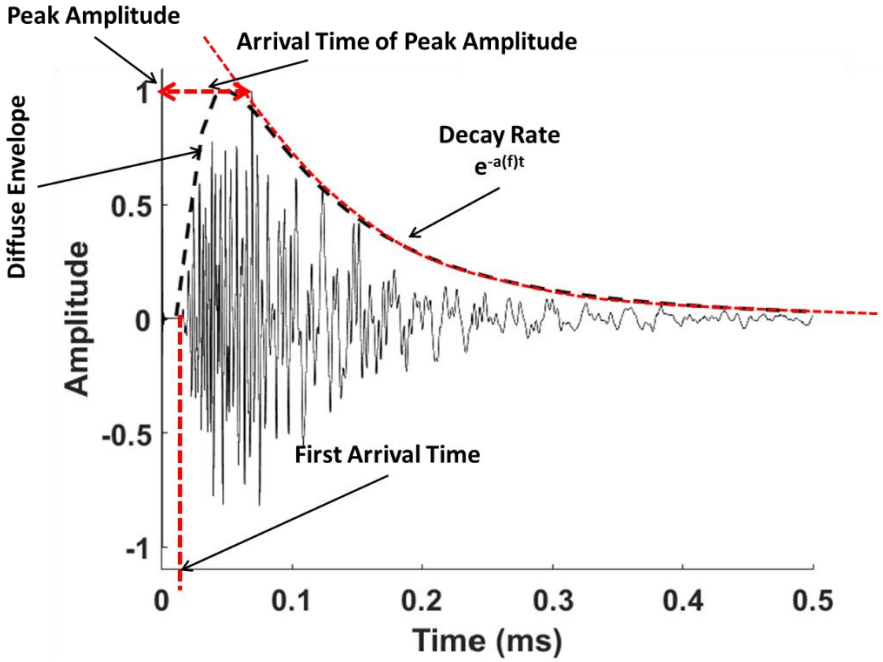

Figure 5-1. Illustration of parameters that describe the coda wave.

Table 5-1. Repeatability of coda wave measurements with attached transducers.

			Peak Amplitude (mV)				Arrival time of peak amplitude (μs)				Spectral Energy (mV^2s)				Coda Wave Decay Rate (np/ms)			
			M ± 0.4	Σ	Q	Σ / M (%)	M ± 0.01	Σ	Q	Σ / M (%)	M ± 0.0016	Σ	Q	Σ / M (%)	M ± 18.4%	Σ	Q	Σ / M (%)
CFRP $[(0)_{32}]_S$	0°	L	27.1	5.78E-2	7.3	0.21	18.60	0.37	1.1	1.99	51.17	0.19	2.2	0.37	10.50	0.32	1.3	3.05
		S0	18.9	0.14	3.1	0.72	13.05	0.0	--	0.00	25.00	0.34	1.2	1.36	10.32	0.18	2.4	1.74
		S90	4.2	6.72E-2	6.3	1.60	19.00	1.6E-2	26.5	0.08	1.26	0.015	28.3	1.19	8.92	0.16	2.7	1.79
		P	8.0	0.12	3.6	1.46	12.46	0.0	--	0.00	16.73	0.52	0.8	3.11	14.35	0.12	3.5	0.84
	90°	L	10.6	0.12	3.5	1.15	18.70	0.37	1.1	1.98	54.83	1.64	0.3	2.99	10.33	0.43	1.0	4.16
		S0	18.3	1.10	0.4	6.01	17.61	2.40	0.2	13.63	21.18	3.87	0.1	18.27	10.21	0.52	0.8	5.09
		S90	4.8	0.42	1.0	8.71	18.81	7.2E-2	5.9	0.38	1.30	0.19	2.2	14.62	9.20	0.72	0.6	7.83
		P	7.4	0.36	1.2	4.91	12.48	2.6E-2	16.3	0.21	16.34	0.61	0.7	3.73	13.40	0.48	0.9	3.58
CFRP $[(0/45/-45/90)_8]_S$	0°	L	17.3	0.13	3.3	0.74	22.76	8.4E-3	50.6	0.04	27.35	0.26	1.6	0.95	8.85	2.6E-2	16.3	0.29
		S0	3.2	2.49E-2	17.1	0.78	22.74	0.0	--	0.00	4.99	0.27	1.6	5.41	10.61	8.5E-2	5.0	0.80
		S90	0.76	6.5E-3	65.3	0.86	67.51	1.7E-2	25.1	0.03	0.71	6.8E-3	62.5	0.96	9.08	0.77	0.6	8.48
		P	2.8	1.37E-2	31.0	0.49	48.64	9.4E-3	45.2	0.02	6.59	6.9E-2	61.5	0.1	8.38	5.7E-3	74.5	0.07
	90°	L	20.4	0.13	3.30	0.63	23.96	8.4E-3	50.6	0.04	21.18	0.23	1.8	1.09	8.58	4.0E-3	106.2	0.05
		S0	0.84	7.2E-3	59.0	0.86	26.04	1.1	0.4	4.22	0.97	1.0E-2	42.5	1.03	7.91	4.9E-2	8.7	0.62
		S90	3.3	4.93E-2	8.6	1.49	24.29	1.0E-2	42.5	0.04	6.46	0.41	1.0	6.35	10.89	4.5E-2	9.4	0.41
		P	2.5	2.47E-2	17.2	0.99	49.40	8.4E-3	50.6	0.02	7.83	0.17	2.5	2.17	9.23	2.6E-2	16.3	0.28
Plexiglas	0°	L	11.1	0.21	2.10	1.86	45.34	2.0E-2	21.2	0.04	59.82	2.53	0.2	4.23	9.27	0.07	6.1	0.76
		S0	3.1	3.49E-2	12.2	1.13	58.36	2.1E-2	20.2	0.04	5.38	0.39	1.1	7.25	10.84	0.15	2.8	1.38
		S90	3.0	3.47E-2	12.2	1.16	58.02	1.9E-2	22.4	0.03	5.37	0.37	1.1	6.89	10.86	0.17	2.5	1.57
		P	2.7	2.75E-2	15.4	1.02	45.56	0.14	3.0	0.31	2.84	6.8E-2	6.2	2.39	9.02	5.4E-2	7.9	0.60

L = 1 MHz longitudinal
S0 = 1 MHz shear with polarization along the fibers
S90 = 1 MHz shear with polarization transverse to fibers
P = pinducer

M= mean
Σ = standard deviation
Q = quality factor

Table 5-2. Repeatability of coda wave measurements with detached and reattached transducers.

			Peak Amplitude (mV)				Arrival time of peak amplitude (μs)				Spectral Energy (mV^2s)				Coda Wave Decay Rate (np/ms)			
			M ± 0.4	Σ	Q	Σ / M (%)	M ± 0.01	Σ	Q	Σ / M (%)	M ± 0.0016	Σ	Q	Σ / M (%)	M ± 18.4%	Σ	Q	Σ / M (%)
CFRP $[(0)_{32}]_S$	0°	L	27.9	0.44	1.0	1.58	36.65	0.00	--	0.00	37.76	0.52	0.8	1.38	10.22	0.26	1.6	2.54
		S0	1.2	2.0E-2	21.2	1.67	54.35	1.58E-2	26.9	0.03	0.56	0.02	21.2	3.57	8.31	0.02	21.2	0.24
		S90	2.0	4.48E-3	94.8	0.22	49.00	1.6E-2	26.5	0.03	0.95	0.00	--	0.00	10.31	0.26	1.6	2.52
		P	2.1	1.12E-2	37.9	0.53	44.51	9.7E-2	4.4	0.22	4.55	0.07	6.1	1.54	8.86	0.03	14.2	0.34
	90°	L	12.0	0.63	0.7	5.25	38.66	3.11	0.1	8.04	44.06	2.49	0.2	5.65	10.44	0.21	2.0	2.01
		S0	1.2	0.13	3.3	10.83	54.04	0.19	2.2	0.35	0.46	0.11	3.9	23.91	8.70	0.27	1.6	3.10
		S90	2.7	0.31	1.4	11.48	48.75	0.18	2.4	0.37	1.94	0.25	1.7	12.89	10.37	0.29	1.5	2.80
		P	2.3	9.9E-2	4.3	4.30	44.56	4.8E-2	8.8	0.11	5.33	0.26	1.6	4.88	9.25	0.12	3.5	1.30
CFRP $[(0/45/-45/90)_8]_S$	0°	L	16.0	0.61	0.7	3.81	22.96	9.7E-2	4.4	0.42	24.61	0.13	3.3	0.53	8.50	0.22	1.9	2.59
		S0	3.6	0.15	2.8	4.17	19.02	1.31	0.3	6.89	5.40	0.27	1.6	5.00	10.84	0.23	1.8	2.12
		S90	0.68	8.02E-2	5.3	11.79	75.08	5.21	0.1	6.94	0.55	0.16	2.7	29.09	10.54	0.77	0.6	7.31
		P	2.8	7.89E-2	5.4	2.82	48.64	1.91E-2	22.2	0.04	7.18	0.32	1.3	4.46	8.77	0.20	2.1	2.28
	90°	L	20.3	0.62	0.7	3.05	23.86	9.3E-2	4.6	0.39	20.08	0.78	0.5	3.88	8.35	0.26	1.6	3.11
		S0	0.82	6.88E-2	6.2	8.39	28.45	6.80	0.1	23.90	0.85	8.99E-2	4.7	10.58	9.24	0.52	0.8	5.63
		S90	3.4	0.14	3.0	4.12	22.90	1.63	0.3	7.12	5.84	0.47	0.9	8.05	11.87	0.78	0.5	6.57
		P	2.5	8.75E-2	4.9	3.50	49.39	6.87E-2	6.2	0.14	7.71	0.32	1.3	4.15	9.32	0.40	1.1	4.29
Plexiglas	0°	L	11.4	0.48	0.9	4.21	47.90	1.87	0.2	3.90	63.61	2.09	0.2	3.29	10.85	1.18	0.4	10.88
		S0	3.4	0.23	1.8	6.76	45.13	4.65	0.1	10.30	5.19	0.80	0.5	15.41	10.67	0.35	1.2	3.28
		S90	3.6	0.22	1.9	6.11	45.19	4.75	0.1	10.51	5.23	0.83	0.5	15.87	10.59	0.41	1.0	3.87
		P	2.7	5.49E-2	7.7	2.03	45.59	0.14	3.0	0.31	2.75	6.8E-2	6.2	2.47	8.92	0.65	0.7	7.29

L = 1 MHz longitudinal
S0 = 1 MHz shear with polarization along the fibers
S90 = 1 MHz shear with polarization transverse to fibers
P = pinducer

M = mean
Σ = standard deviation
Q = quality factor

5.2 Waveform and Spectra Analysis

Typical waveforms and spectra collected throughout this thesis are shown in Figure 5-3. Similar waveforms can be received anywhere on the plate (specimen #1), save for when the receiver is directly across from the transmitter on the opposite face or within several transducer diameters (then the signal resembles a pulse-echo signal). The coda wave amplitude does diminish with increasing separation, which is dictated by the quality[10] of the material (specifically composite material quality) under inspection.

Periodic and decaying arrivals, such as those observed for multiple back-wall echoes, cause spectral peaks in the frequency domain with a specific separation of $\Delta f = c/2h$, where h is the plate thickness [Kinra & Dayal 1988]. As an example, for an aluminum plate, the thickness resonance peaks should be at $\Delta f = 6300/(2*6.35E^{-3}) = 0.496$ MHz. These peaks can be asily seen in Fig. 5-2 a2 and 5.3 a2. For composite materials, the velocity used is that of a longitudinal wave propagating in the thickness direction. The existence and generation of these spectral resonances is shown in Figure 5-2 for aluminum, quasi-isotropic CFRP, and polycarbonate. It has been suggested that the noisiness of coda spectra may be due in part to similar resonances [Kautz 1988].

It has been noted [Krautkramer & Krautkramer 1969] that layered interfaces along an ultrasonic ray path give rise to multiple arrival times in the waveform that show up as peaks in the spectrum. Kautz (1988) notes that spectral peaks are also caused by arrival of signals from different propagation paths. The coda wave spectra, which may otherwise be referred to as noisy, are full of interfering spectral peaks that may be caused by a specific path resonance or the many varied paths taken by acoustic energy due to multiple scattering.

[10] Quality is used here as a catch-all and refers to the amount a defects (e.g. porosity) introduced during fabrication, the level of homogeneity of the laminate, and the precision/strength of the fibers.

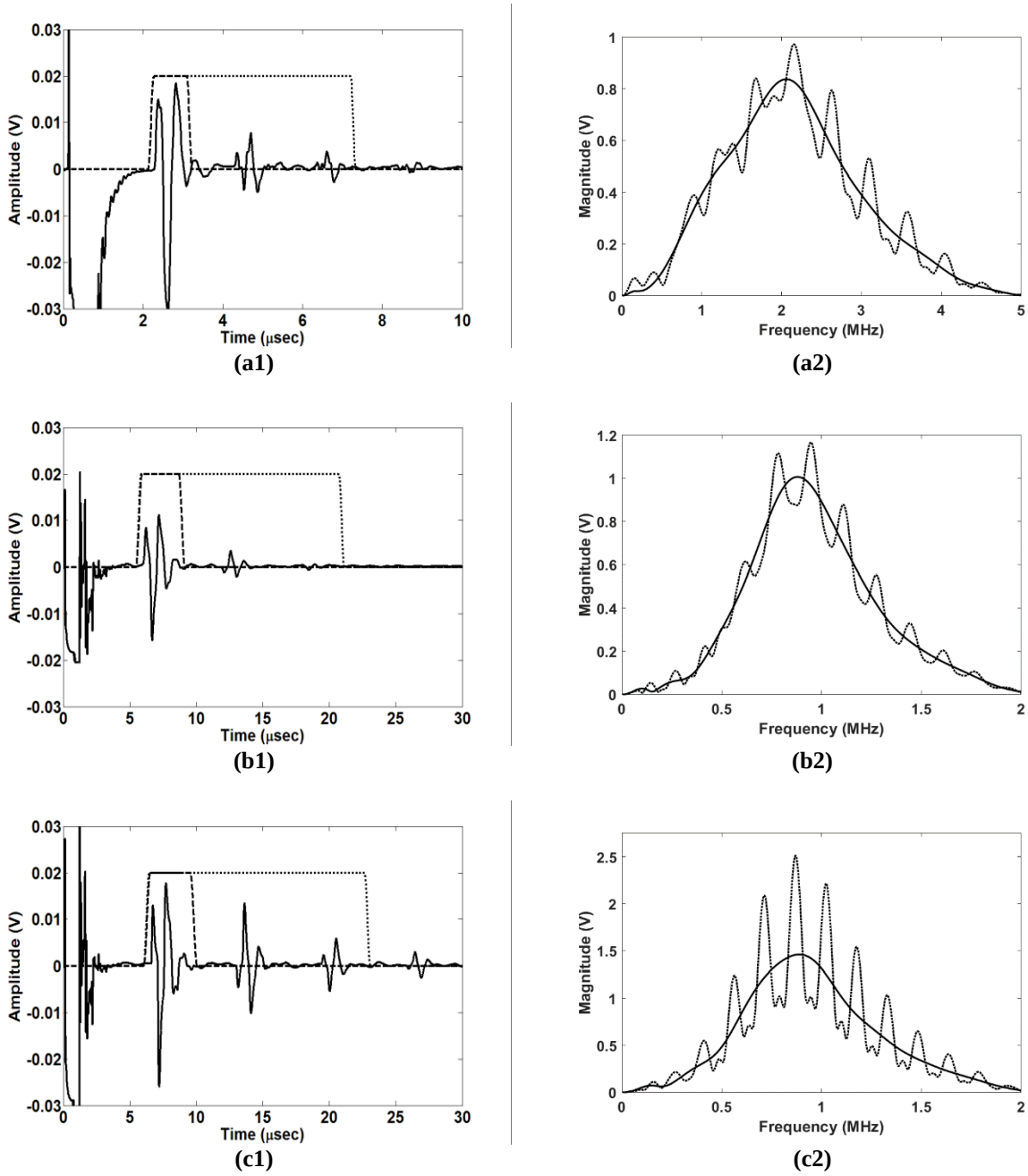

Figure 5-2. Demonstration of thickness resonances in the (2) spectra by changing window length in the (1) waveforms from signals collected from (a) aluminum, (b) CFRP, and (c) polycarbonate. The dashed line encompasses a single back-wall echo while the dotted line encompasses three back-wall echoes.

Large, periodic spectral peaks can be observed in the coda wave spectra in Figure 5-3, though not nearly as well defined as the spectral peaks in Figure 5-2. A comparison of the spectral peaks in the two figures indicates that the peaks in the coda wave spectra do correspond to a thickness resonance. This apparent thickness resonance is caused by the periodic release of the acoustic energy that is confined between the transmitter and the back-wall. For each successive trip downwards from the transmitter, a certain percentage of the acoustic energy is scattered away from the path of the beam. Since the structure does not change in between successive passages of the acoustic energy, it can be assumed that the portion of energy that is scattered away from the incident beam will always take the same path to the receiver, thus arriving $\Delta t = 2h/c$ after the previous arrival and exhibiting an apparent attenuation equivalent to that of successive back-wall reflections.

Figure 5-3 shows that the majority of acoustic energy is clustered around the peak frequency of the coda wave in the tens to hundreds of kHz, but small amounts of energy exist into the low MHz range (Figure 5-3).

A defect in the structure causes interaction between the defect and the propagating wave modes. The relative size of the defect to the wavelength of the propagating wave is an important factor in understanding the scattering interaction between the two. Table 5-3 lists the ratio of defect size to wavelength for the materials and defect sizes considered in this study. Here the wavelength corresponds to the longitudinal velocity (L) or the shear velocity (S). For composite materials, the fastest and slowest of each wave type is used as denoted by the “fast” and “slow” subscripts. The additional scattering due to the introduction of defects is primarily Rayleigh scattering based on the wavelength to hole diameter ratio for the majority of coda wave energy, which is not possible

to differentiate from the complex coda waveform. The small amounts of energy in the MHz range experience intermediate to specular scattering for the majority of defect sizes.

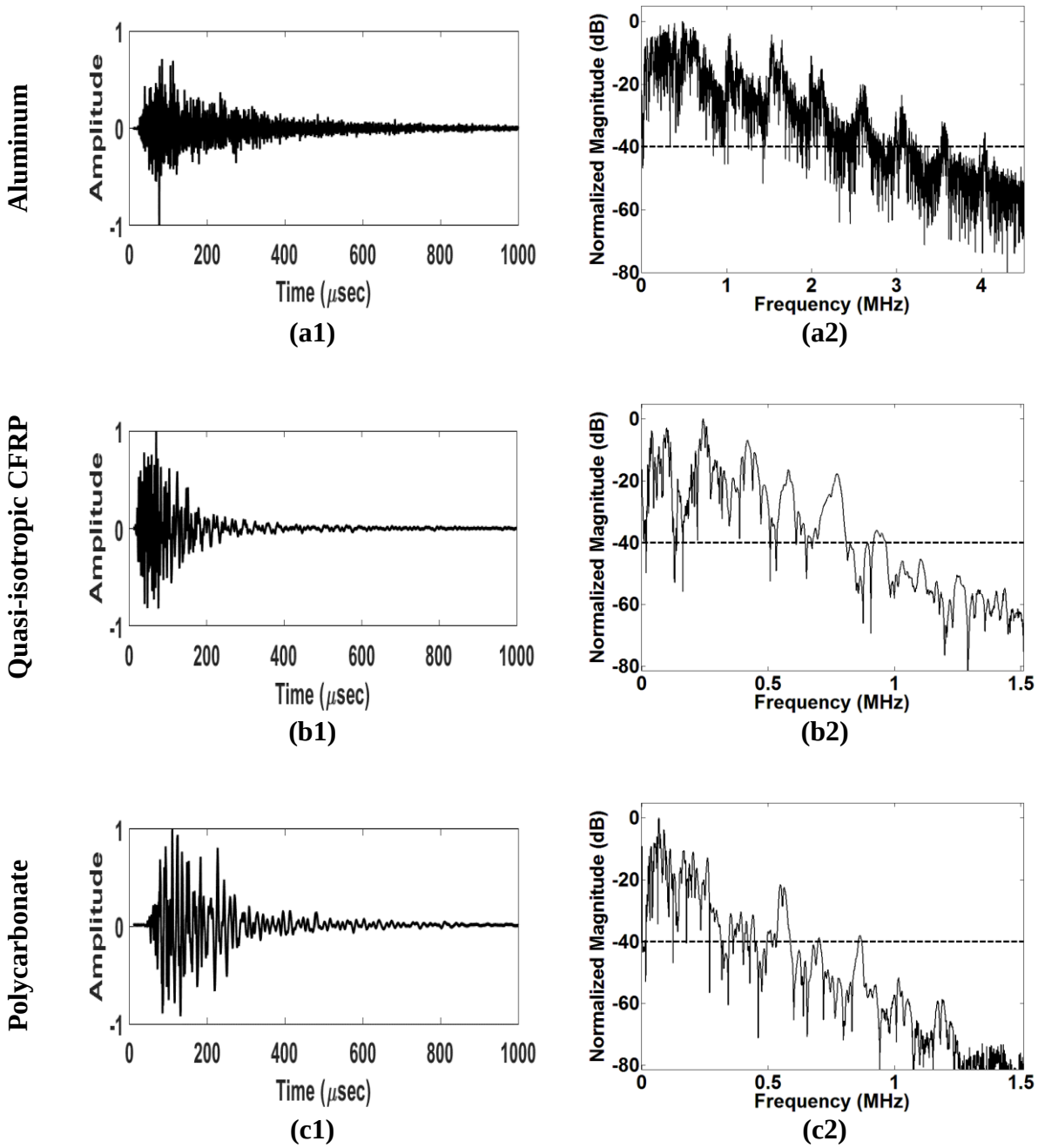

Figure 5-3. Representative (1) waveforms and (2) spectra collected from (a) aluminum, (b) CFRP, and (c) polycarbonate. The signals are transmitted and received with a pair of 12.5mm longitudinal transducers (2.25 MHz for aluminum and 1 MHz for CFRP and polycarbonate) excited with a spike pulse.

Table 5-3. Range of defect size to wavelength ratios for various wavelengths in various materials.

	Frequency	Wave type	d/λ
Aluminium 6061s	f_c	**L**	0.0125- 0.25
		S	0.025 – 0.5
	f_{max}	**L**	0.16 – 3.2
		S	0.32 – 6.4
Polycarbonate	f_p	**L**	0.0088 – 0.18
		S	0.018 – 0.35
	f_{max}	**L**	0.18 – 3.5
		S	0.36 – 7.0
CFRP (quasi-isotropic) Toray P2353W-19	f_p	L_{fast}	0.002 – 0.04
		L_{slow}	0.006 – 0.12
		S_{fast}	0.008 – 0.16
		S_{slow}	0.012 – 0.24
	f_{max}	L_{fast}	0.062 – 1.2
		L_{slow}	0.22 – 4.4
		S_{fast}	0.25 – 4.8
		S_{slow}	0.44 – 8.8

F_p = peak frequency of coda wave
f_{max} = frequency peak at -40 dB maximum spectral amplitude
d = the effective diameter of drilled holes
λ = wavelength in the material at the specified frequency

5.3 Spreading Function

Waveforms were collected from the specimens (30x30 cm) described in Figure 4-1 were analyzed to determine several propagation and attenuation parameters: peak amplitude, arrival time, spectral energy, amplitude and energy attenuation, and power decay rate. The signals were collected from simply supported, pristine samples at room temperature[11] (21.2 ˚C ± 2.1). The 0-1000 μs time windows considered were identical across all specimens and receivers and were selected to include more than 99.9% of the temporal energy and exclude the bleed-through of the excitation used in the pulser-receiver. Increasing the window length to encompass the full 2000 μs

[11] Samples were kept in the lab for a minimum of 12 hours before testing to allow the sample temperature equilibrate with the ambient temperature of the lab, which varied by less than 0.1˚C for the several hours before and during the experiment.

of recorded data did not affect the results. Unless otherwise stated, all spectrograms were calculated for the entire 0-1000 μs time window and a frequency window from 0 to 1.5 MHz: again this frequency range encompasses more than 99.9% of the spectral energy for all signals.

Traditional ultrasonic inspection detects and characterizes damage/defects through the examination of waveform parameters. Typical parameters include: peak amplitude, arrival times of different portions of the waveform, and waveform energy [ASM 1989, Henneke 1990, Hsu 2013]. In order to determine the behavior of coda waves in composite plates, four waveform parameters are extracted and examined for each of the three orthogonal components (longitudinal, shear 0˚, and shear 90˚) of the coda wave field at the plate surface. The parameters examined in this section are: peak waveform amplitude, first arrival of acoustic energy, arrival time of peak amplitude, and waveform spectral energy. Measuring these parameters at various locations on the plate helps to map out the wave field and determine the coda wave spreading function. This will help predict the behavior and the values of the wave parameters in future applications. The spreading function is also useful in determining the optimal transducer placement in addition to the spread and decay of information.

A truly diffuse wave field, which is one of the models for coda waves, ideally has equal energy at every spatial location within a volume. The samples under examination in this chapter are not small, lossless volumes; therefore, the energy should vary with spatial location. In particular, the waveform amplitude and energy should decay with transducer separation. Based on this consideration, several trends can be expected regarding the behavior of the wave parameters in the various samples. For isotropic, homogeneous materials (in this case the Plexiglas and the quasi-isotropic CFRP), which are identical in all directions, the peak amplitude and the waveform

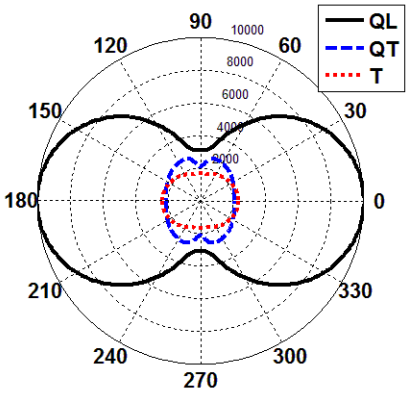

Figure 5-4. Illustration of bulk wave mode phase velocities for a unidirectional composite plate where the modes are propagating in the plane of the plate and (r, θ) in the plot correspond to velocity and fiber angle respectively [Rokhlin et al. 2011].

energies are expected to be uniform with θ and decrease exponentially with r. The arrival times should likewise be uniform with θ but decrease linearly with r. These should result in a circularly expanding, exponentially decaying spreading function. For unidirectional composite plates (transversely isotropic), wave modes propagating in the plane of the plate exhibit dumbbell/elliptical spreading functions with the semi-major axes aligned to the fiber direction since the fibers support a much higher wave velocity than the transverse direction (Figure 5-4). Arrival times are then expected to vary linearly with r and elliptically (or with a dumbbell shape) with θ. Wave modes propagating along the fibers travel faster and experience less attenuation than the wave modes propagating in the transverse direction. The waveform energy is therefore also expected to vary elliptically with θ but exponentially with r. These should result in an elliptically (or with a dumbbell shape) expanding, exponentially decaying spreading function.

Typical rectified waveforms collected from unidirectional CFRP, quasi-isotropic CFRP, and Plexiglas plates are shown in Figure 5-5 for transducers pairs aligned with the 0˚ and 90˚ fiber angles. Peak amplitudes are indicated by black circles for ease of identification. The waveforms exhibit the expected behavior. The waveforms from the isotropic (or quasi-isotropic) plates are

very uniform in θ, with cross-correlation coefficients greater than 0.90. The cross-correlation coefficient decreases with transducer separation and slight differences in the waveform cross-correlations and locations of the peak amplitude arrivals can be observed. These are caused by imperfect symmetry in the coda wave superposition field caused by imperfections in the homogeneity of the plates. As expected, less waveform uniformity in θ is observed for the quasi-isotropic CFRP plate compared to the Plexiglas plate since composite materials are less homogeneous than Plexiglas. The waveforms from the transversely-isotropic plate show no uniformity in θ and the energy arrives nearly three times faster for the 0˚ orientation compared to the 90˚ orientation, both of which are expected.

Figure5-6 shows typical spectra collected from unidirectional CFRP, quasi-isotropic CFRP, and Plexiglas plates for transducers pairs aligned with the 0˚ and 90˚ fiber angles the spectra shown correspond to the waveforms shown in Figure 5-5. Again it is noted that the isotropic (quasi-isotropic) plates show much more uniformity in θ than the transversely-isotropic plate where the isotropic plates exhibit cross-correlation values greater than 0.9. Reductions in the cross-correlation and hence the uniformity are observed for the quasi-isotropic CFRP plate compared to the Plexiglas plate, which is due again to the imperfect homogeneity of the material. The spectral energy for the unidirectional plate occurs within a 0.25-1.0 MHz bandwidth for the 0˚ orientation while energy for the 90˚ orientation occurs below 0.5 MHz. This difference in spectral energy is expected since the fiber dominated propagation supports higher frequencies while the matrix dominated propagation attenuates higher frequencies. Note that the difference in spectral amplitude between the 0˚ and 90˚ fiber angles is accompanied by a difference in the spread of the spectral energy, which indicates that the total energy may be uniform in θ for transversely-isotropic materials. This is explored further below.

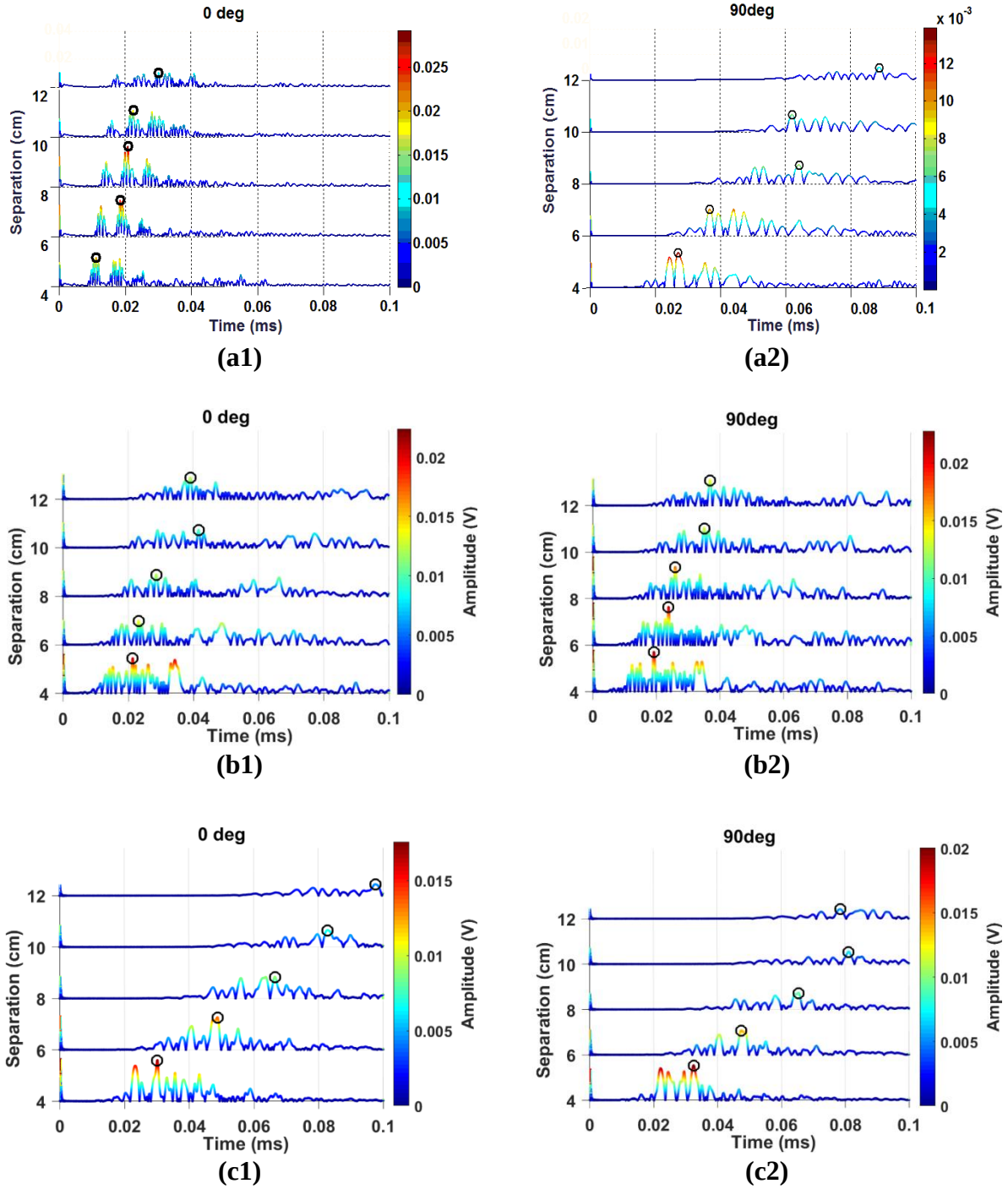

Figure 5-5. Typical rectified ultrasonic waveforms collected at 1) 0˚ and 2) 90˚ fiber orientations from one-sided pitch-catch UT on a 30x30x0.9cm a) unidirectional CFRP plate, b) quasi-isotropic CFRP plate and c) Plexiglas plate. Signal was transmitted and received with a 1.25 cm, 1 MHz P-wave transducer. The peak amplitudes are indicated with black circles.

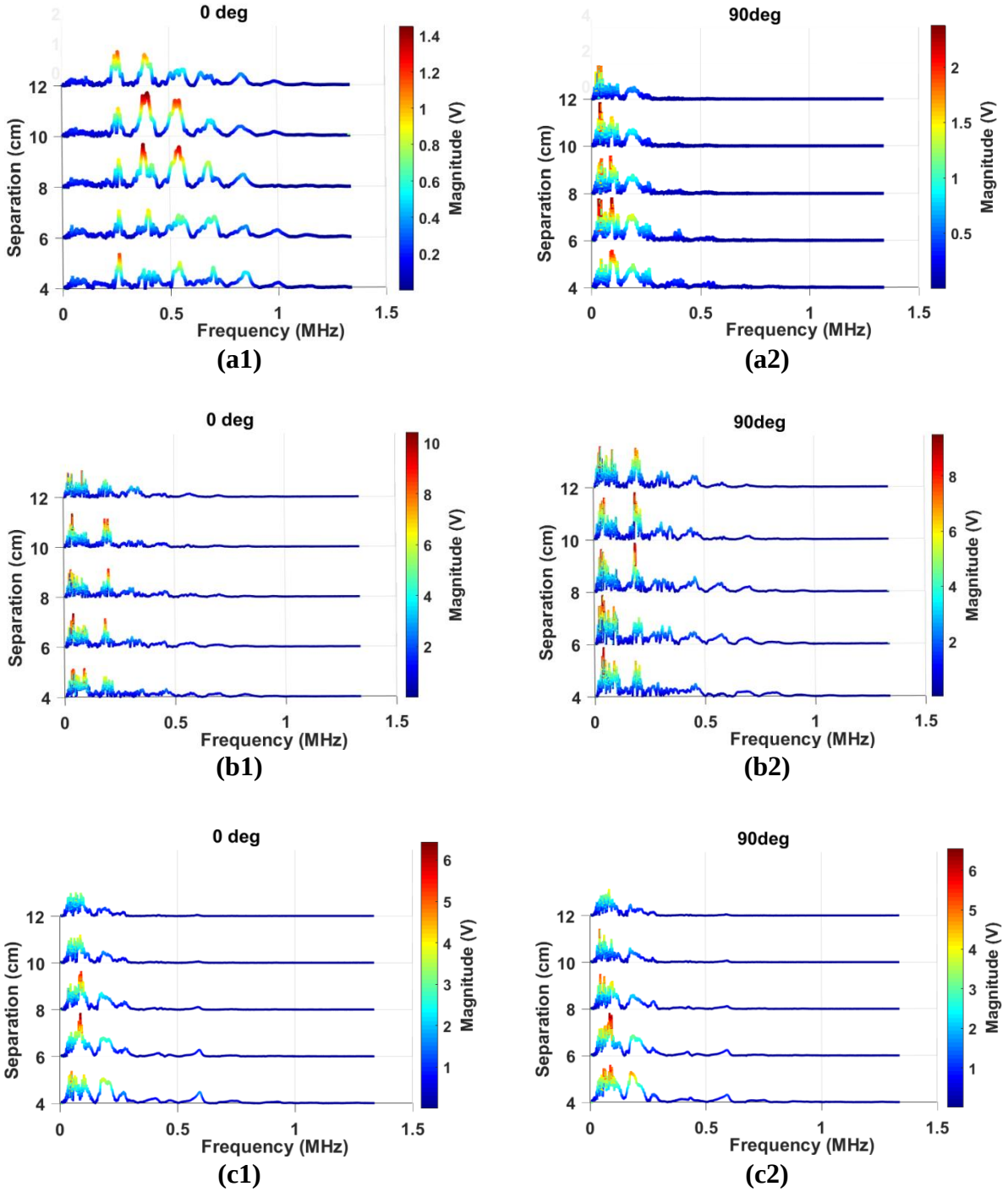

Figure5-6. Typical rectified ultrasonic spectra collected at 1) 0˚ and 2) 90˚ fiber orientations from one-sided pitch-catch UT on a 30x30x0.9 cm a) unidirectional CFRP plate, b) unidirectional CFRP plate and c) Plexiglas plate. Signal was transmitted and received with a 1.25 cm, 1 MHz P-wave transducer.

Arrival times can be very useful in determining the spreading function of a wave mode. Even though the coda wave is a superposition of multiple modes, the first arrival time of the coda wave will correlate to the arrival of a specific wave mode. The first arrival of energy must occur after a characteristic time defined by the fastest possible wave mode traveling the shortest possible trajectory between transmitter and receiver. The arrival times are therefore expected to increase linearly with increasing transducer separation.

The first arrival times presented here are defined as the time of the first crossing of a set amplitude threshold. Typically, in ultrasonic NDE the amplitude threshold is set to an arbitrary amplitude that is large than the noise floor or is set to a specified signal-to-noise ratio. The intent of either threshold is to determine the arrival time of the signal while eliminating false arrivals due to noise. Some of the collected waveforms (specifically the shear components) suffered from significant bleed through from the spike pulse, which made setting a noise based threshold difficult. The threshold was therefore defined as -40 dB from the peak amplitude as opposed to a specific signal-to-noise ratio. Phase cancellation is a concern for large diameter transducers when more than one wave mode is arriving at the same time. For first arrivals there should only be a single mode, and hence there should be no phase cancellation, and a pinducer is employed in addition to the 12.7 mm transducer for confirmation purposes.

Figure 5-7 & Figure 5-8 plot the measured first arrival times for the isotropic, quasi-isotropic, and transversely isotropic plates while the first arrival times for various wave modes traveling 4 cm as shown in Table 5-4 for comparison purposes. It should be noted that absolute first arrival time measurements are approximate due to the uncertainty in selecting the actual first arrival and in determining the travel distance. For the single sided configuration used, the travel

path of the wave modes is not necessarily a direct path from transmitter-center to receiver-center. The travel path could be from the transmitter-edge to the receiver-edge, which for this configuration would reduce the path length by 1.27 cm. Comparative velocity measurements are more accurate since the same point on the waveforms is used and the change in travel distance is known. For this reason, the relative arrival time between 4 and 8 cm is also included in Table 5-4.

First arrival times in the unidirectional CFRP plate are linearly increasing with separation, which indicates the ballistic arrival of a wave mode as expected. Comparing the first arrival times and relative arrival times with the calculated arrival times of various wave modes indicates that the first arriving wave modes are likely longitudinal modes for low fiber angles and shear modes for high fiber angles since the arrivals are within a few microseconds of the mode arrivals. For intermediate fiber angles, the arrival times are between the longitudinal and shear arrivals and are therefore more likely to be scattered or reflected versions of the longitudinal or shear wave modes. There is also the possibility of the first arrival being caused by a symmetric Lamb wave mode at low frequency-thickness since the symmetric mode velocity falls in between the longitudinal and shear mode velocities. This possibility is explored further in the next section. The first arrival time measured from the pinducer signals agree within a six percent with those measured the 12.7 mm signals, which means that phase cancellation is not an issue for first arrivals as postulated. Based on the first arrival times, the coda wave spreading function for unidirectional CFRP laminates is elliptical.

For the sake of comparing and contrasting transversely isotropic and isotropic materials, the first arrival times for coda waves collected from a Plexiglas plate were also measured. Since the sample is homogeneous and isotropic, the ballistic arrivals should be linearly increasing with travel distance and the spreading function should be circular. This is indeed the case for this sample

since the arrival times for 0˚, 45˚, and 90˚ all increase linearly and agree with each other to within a six percent. As with the unidirectional CFRP plate, the first arrival correlates well with the arrival of a ballistic longitudinal mode, but a low frequency-thickness symmetric Lamb wave mode is also possible. Some variability is observed in 12.7 mm transducer data, which is due to imperfect homogeneity and imperfect coupling, but the agreement between the data is improved when using the pinducer.

When examining just the longitudinal component of the coda wave first arrival, the arrival times strongly indicate either a longitudinal arrival or a low frequency-thickness symmetric Lamb wave. Considering the two surface shear components of the coda wave adds more information to the analysis. It is very interesting that both shear components arrive within a few μs of the longitudinal component. This is too fast to be a shear wave, which leaves only three possible sources of the shear components: 1) a longitudinal wave coming in at an angle, 2) a Lamb wave, or 3) the Poisson effect from a longitudinal or Lamb wave. The particle displacement for a Lamb wave is retrograde elliptic, but 2D, which means the transverse displacement parallel to the direction of propagation is due to the elliptical motion and the transverse displacement perpendicular to the direction of propagation would have to be due to Poisson's effect and should be approximately 1/3 the parallel displacement. If the first arrival is a longitudinal wave, there will also be transverse components due to Poisson's effect. The transverse displacements do not follow these pattern, which indicates that the first arrival is a longitudinal mode arriving at an angle.

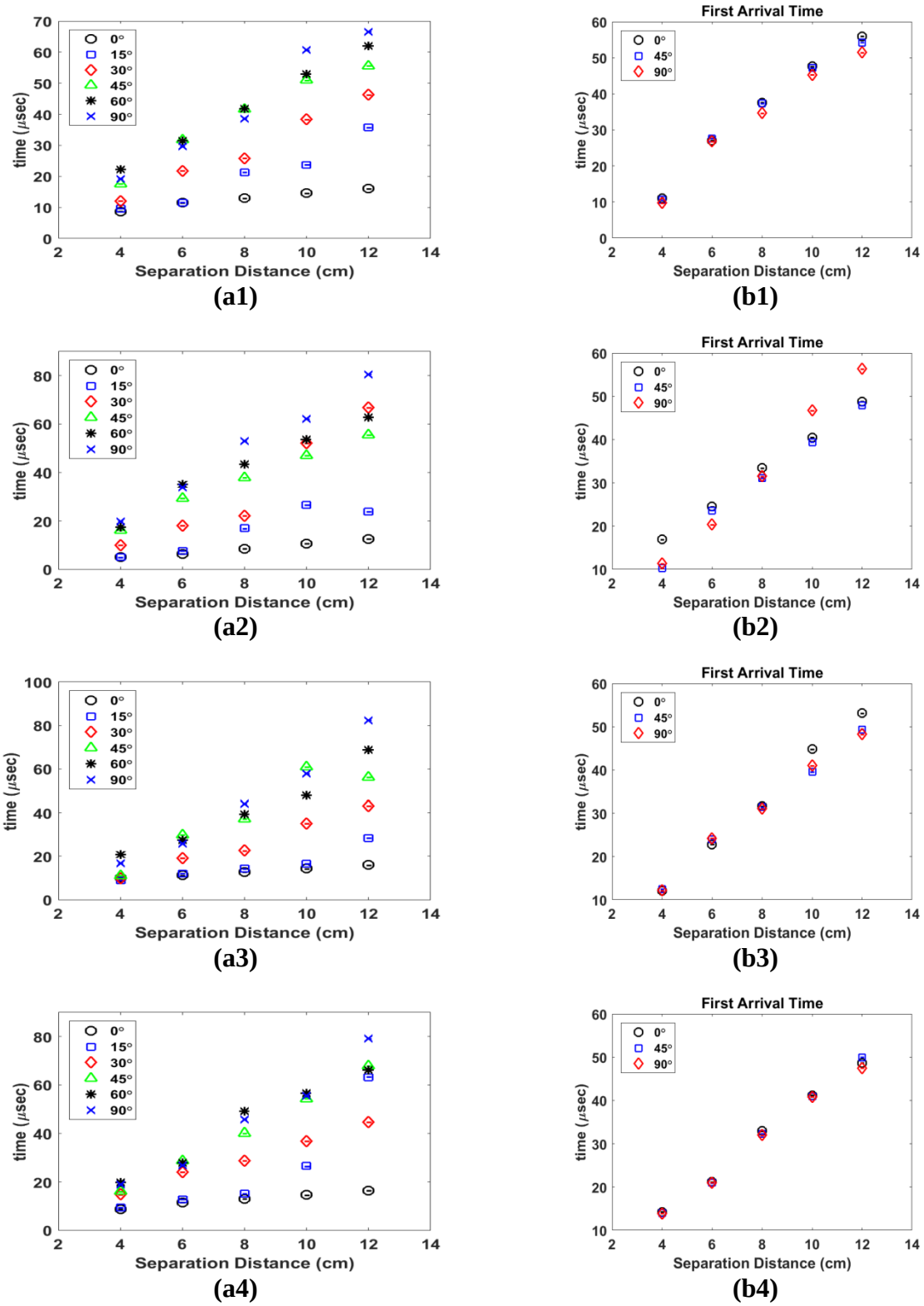

Figure 5-7. First arrival time of the received waveform for amplitude with S:N = 30 for a) a 0.9 cm unidirectional CFRP plate and b) a 0.9 cm Plexiglas plate. Signal was transmitted with a 1.25 cm, 1 MHz longitudinal transducer and received with 1) 1 MHz L, 2) 1MHz S0, 3) 1MHz S90, and 4) pinducer transducers.

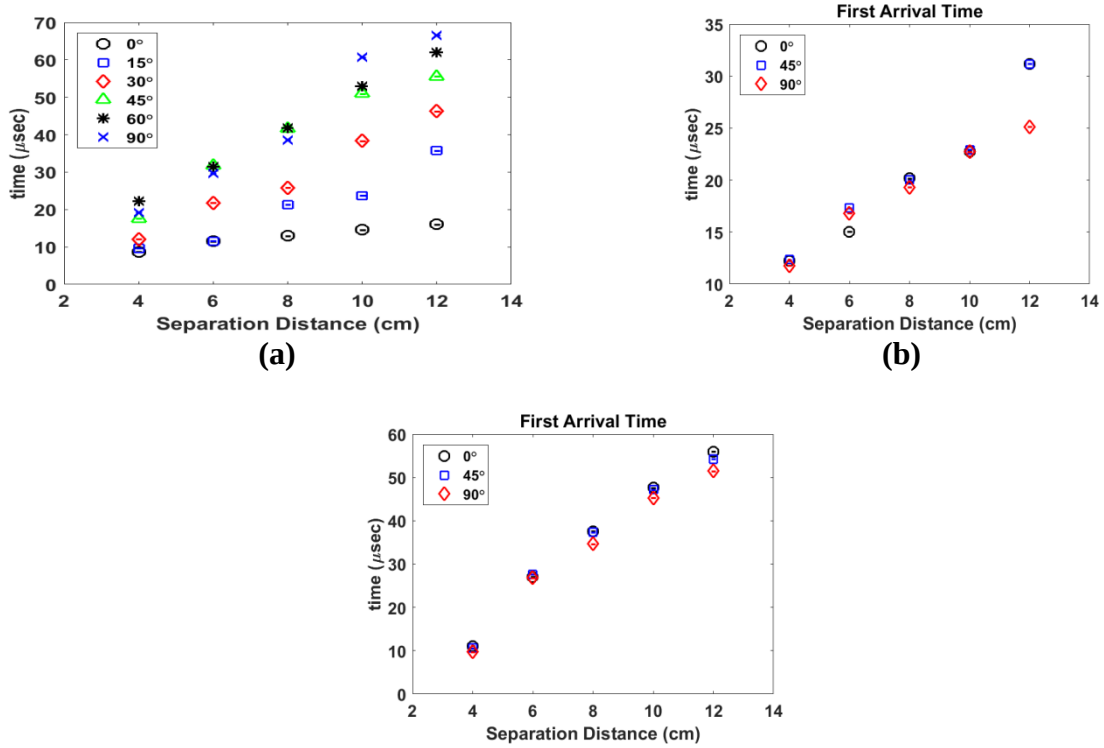

Figure 5-8. First arrival time of the received waveform for amplitude with S:N = 30 for a) a 0.9 cm unidirectional CFRP plate, b) a 0.9 cm quasi-isotropic CFRP plate and c) a 0.9 cm Plexiglas plate. Signal was transmitted and received with a 1.25 cm, 1 MHz longitudinal transducer.

Table 5-4. Calculated ballistic arrival times (μs) for various wave modes for a 4 cm center-to-center travel path and measured coda wave first arrival times with a 4 cm separation.

	Unidirectional CFRP						Plexiglas
	0˚	**15˚**	**30˚**	**45˚**	**60˚**	**90˚**	**0˚**
t_{cl}	3.99	4.12	4.56	5.46	7.34	12.31	14.52
t_{cs1}	18.18	17.47	16.39	15.21	14.29	17.94	31.50
t_{cs2}	17.78	18.18	19.05	20.41	22.10	24.24	31.50
t_{cR}	--	--	--	--	--	--	33.72
t_{cw}	8.70	9.65	12.10	17.55	22.30	19.20	13.68
Δt_{cw}	4.25	11.65	13.70	24.00	19.50	19.40	19.54

l = longitudinal
s = shear
R = Rayleigh wave
cw = coda wave

Figure 5-8 shows the comparison the longitudinal coda wave component for the three material models. Only a single plot of the quasi-isotropic results is shown since the data trends are the same as those for the isotropic material, but with a little more scatter in the data due to the imperfect isotropy and homogeneity of the plate. The dependence of the arrival time on fiber angle is clear for the transversely isotropic material while the quasi-isotropic material exhibits almost no angular dependence and the isotropic material exhibits no angular dependence.

Although the coda wave first arrival should consist of a single wave mode that either arrives directly of is scattered/reflected a single time, the three orthogonal wave components at the surface of the plate make identification of the wave mode difficult. A symmetric Lamb wave mode seems a likely candidate for the first arrival until the shear components are included. Nearly identical arrival times or the three components and amplitudes that disagree with Lamb waves make the longitudinal mode the most likely candidate for the coda wave first arrival.

Another waveform parameter that is useful in determining the spreading function of a wave mode is the spectral energy of the waveform. This parameter describes the propagation and decay of information. Given that all wave modes that superimpose to create the coda wave decay exponentially with travel distance, the total spectral energy of the coda wave is also expected to decay exponentially with increasing transducer separation. The coda wave spectral energies are plotted in Figure 5-9 & Figure 5-10 for the isotropic, quasi-isotropic, and transversely isotropic plates. All energies are normalized to the highest energy and converted to dB. Therefore, an exponential decay will appear linear. With a few notable exceptions, the coda wave energies do decay exponentially (least squares fit) with increasing transducer separation. A plausible reason for the exceptions is that there may be some constructive/destructive interference of some modes at certain distances.

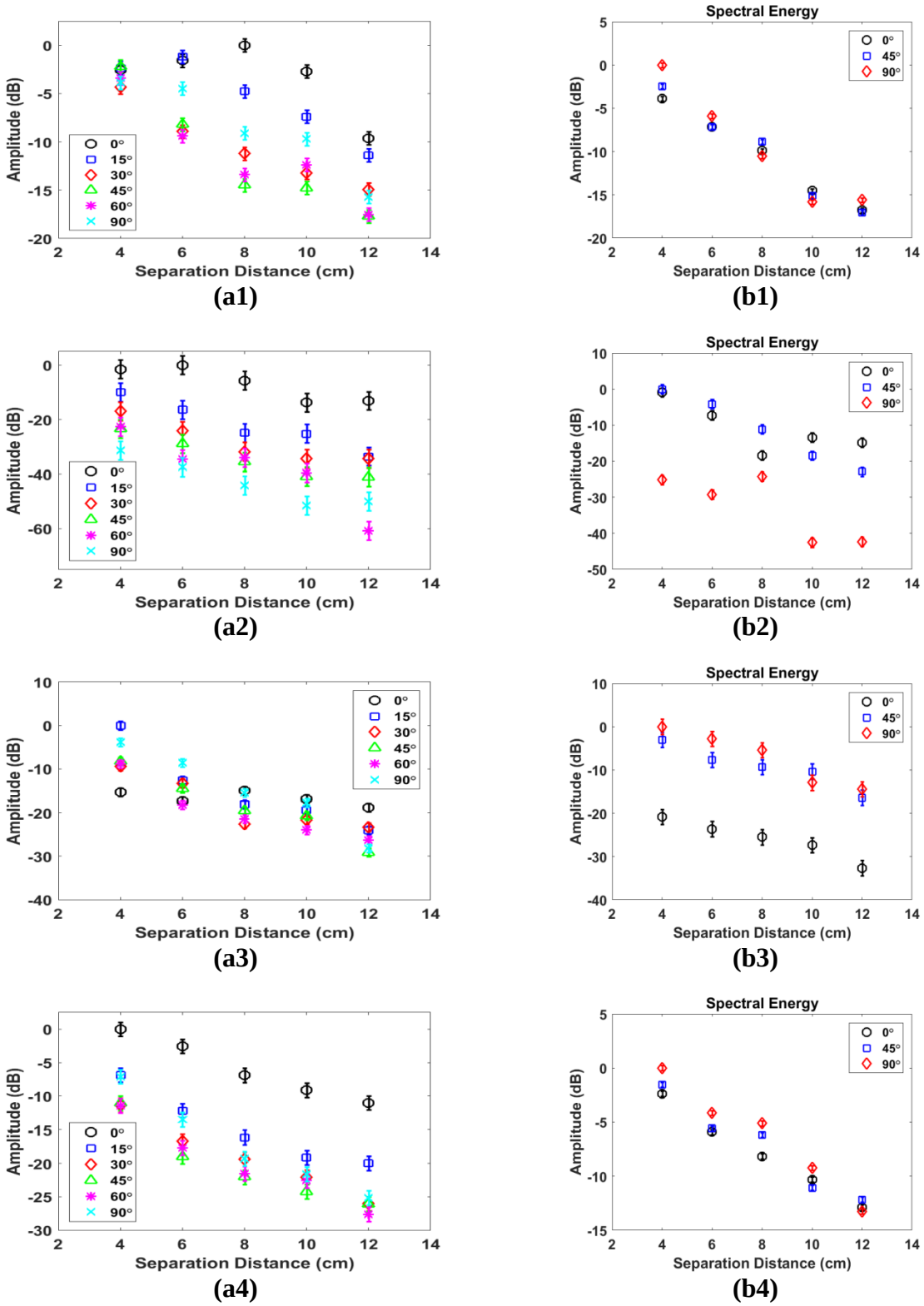

Figure 5-9. Spectral energy of the received waveforms for a) a 0.9 cm unidirectional CFRP plate and b) a 0.9 cm Plexiglas plate. Signal was transmitted with a 1.25 cm, 1 MHz longitudinal transducer and received with 1) 1 MHz L, 2) 1MHz S0, 3) 1MHz S90, and 4) pinducer transducers.

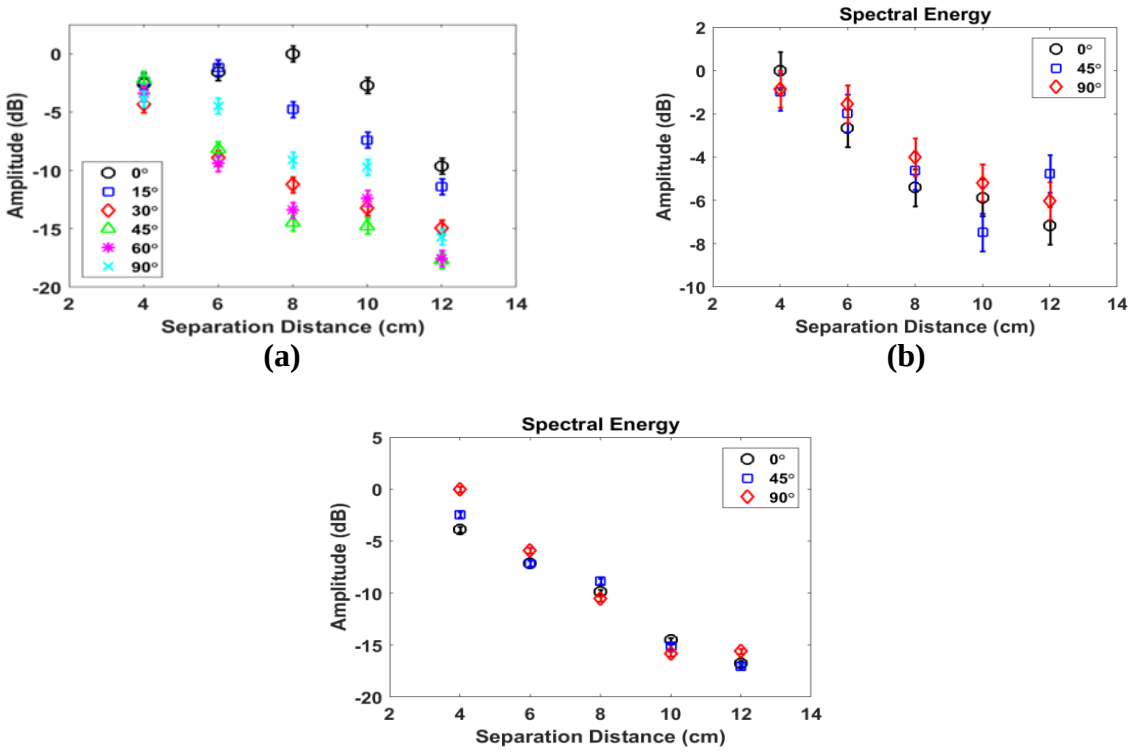

Figure 5-10. Spectral energy of the received waveforms for a) a 0.9 cm unidirectional CFRP plate, b) a 0.9 cm quasi-isotropic CFRP plate and c) a 0.9 cm Plexiglas plate. Signal was transmitted and received with a 1.25 cm, 1 MHz longitudinal transducer.

5.4 Attenuation

Attenuation measurements can be very useful for ultrasonic NDT&E by assisting with the determination of configuration parameters (such as travel distance) for experimental measurements or directly measuring microstructure (such as porosity in CFRP [Jeong & Hsu 1995]). Coda wave signals, however, are not traditional propagating waves and traditional definitions for ultrasonic wave parameters do not necessarily apply to coda waves. Alternate definitions of attenuation must be sought that yield useful information about the behavior of the coda wave field. Several attenuation definitions are explored and analyzed in this section.

5.4.1 Spatial Attenuation

As described above (Section 3.2.1), division of sequential signal pulses in the frequency domain, also known as the pulse-overlap method [Kinra & Dayal 1988], is a straight forward method of determining the frequency dependent attenuation of harmonic waves propagating in space. This method of attenuation measurement is very well suited to pulse-echo configurations because the transfer functions of the two pulses contain identical information save for the material transfer function of the difference in path length between them. The key assumption to this method is that both pulses contain the same spectral content where the spectral amplitude of the second pulse is lower than the amplitude of the first pulse. As shown above and in Figure 5-11b, this is generally not the case with coda wave spectra as the transducer separation distance is increased. Indeed, frequently the spectral amplitude increases with separation distance as can be seen. Thus the pulse-overlap method is not applicable for coda wave attenuation measurement and is included in here only for completeness.

The resulting frequency dependent amplitude attenuation of coda waveforms collected from the unidirectional CFRP plate with the transducer pair aligned to 0˚ fiber orientation is shown in Figure 5-11a while the corresponding spectra are shown in Figure 5-11b. Negative amplitude attenuation values are readily apparent. It is a tendency to erroneously assume that negative attenuation values mean energy is being added to the system and that the signals are growing in strength as they propagate, which would violate conservation laws. A negative attenuation does not indicate the addition of energy, but in actuality it merely means that the amplitude of the second point is greater than the amplitude of the first point. Keep in mind that coda wave signals are not propagating waves but are spatially sampled, time-dependent superposition field. Thus coda wave signals need not follow the same restrictions as propagating harmonic waves. Also note that

amplitude measurements taken from various locations on a plate that is resonating will also yield negative attenuation as illustrated in Figure 5-12. This is a simple illustration that traditional definitions for ultrasonic wave parameters do not necessarily apply to coda waves.

The most basic definition of attenuation is the decay of waveform (or wavelet) peak amplitude with increasing travel distance. This definition is logical for a single traveling wave mode as it measures the loss of information with travel distance due to scattering and absorption, but may not be very applicable to a superposition of multiple wave modes. One of the best methods

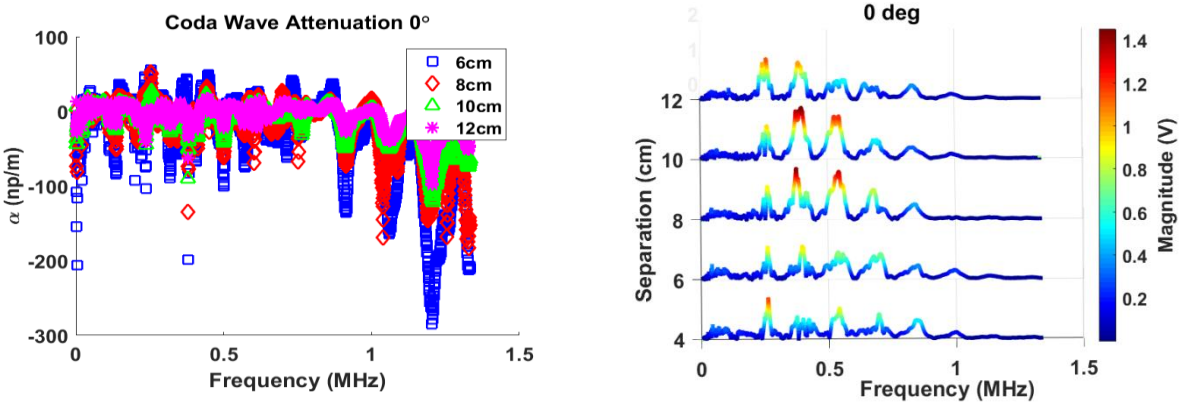

(a) **(b)**

Figure 5-11. Attenuation calculated by frequency domain division with a) typical attenuation curves and b) typical spectra of waveforms collected at different transducer separations. Measurements were made on a 0.9 cm unidirectional CFRP plate with transducer separations as listed. The signal was transmitted and received with a 1.25 cm, 1MHz longitudinal transducer.

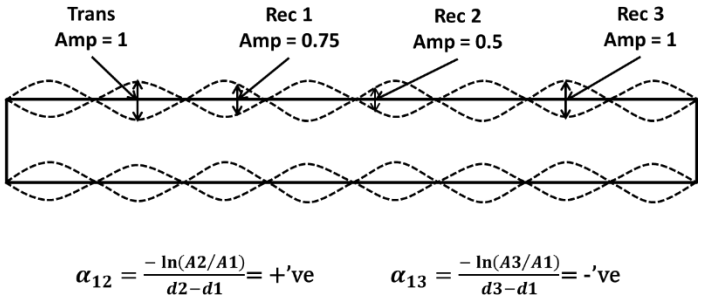

Figure 5-12. Illustration of positive and negative attenuation due to measuring the amplitudes of a plate resonance mode at various locations.

of characterizing the loss of information with travel distance for coda waves would be to use a parameter that characterizes the entirety of the waveform, such as spectral energy. In this case the decay of energy correlates to the decay of information. Both of these attenuation measures were applied to the coda wave components collected from the isotropic, quasi-isotropic, and transversely isotropic plates. The attenuations are determined by fitting a line to the natural logarithm of the peak amplitude (or spectral energy) versus transducer separation plots using least squares. The slope of the line is the attenuation while the standard error of the fit is the measurement error. Typical attenuation results and corresponding coefficients of determination (R^2) are plotted in Figure 5-13. $R^2 > 0.6$ is considered a good fit, and the majority of the data yield R^2 values greater than 0.9, which indicates that the reductions in amplitude and spectral energy are well described by an exponential decay. The lowest R^2 value observed is 0.4.

The measured attenuation of the peak amplitudes and the spectral energies are plotted in Figure 5-14 & Figure 5-15. The spatial attenuation of a waveform (or wavelet) in an isotropic material, regardless of whether it is the attenuation of the peak amplitude or the energy, is expected to be insensitive to orientation angle.

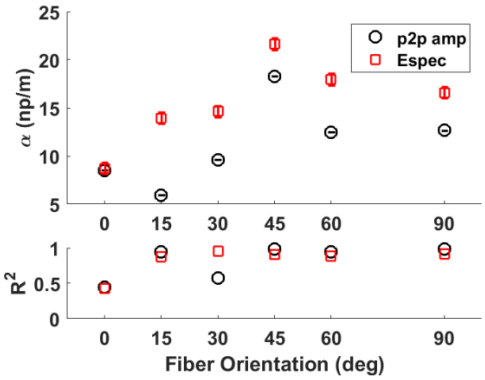

Figure 5-13. Typical results (Figure 5-14a1) from fitting an exponential to the data sets using least squares where α is the value of the exponential decay and R^2 is the coefficient of determination between the fit line and the data set.

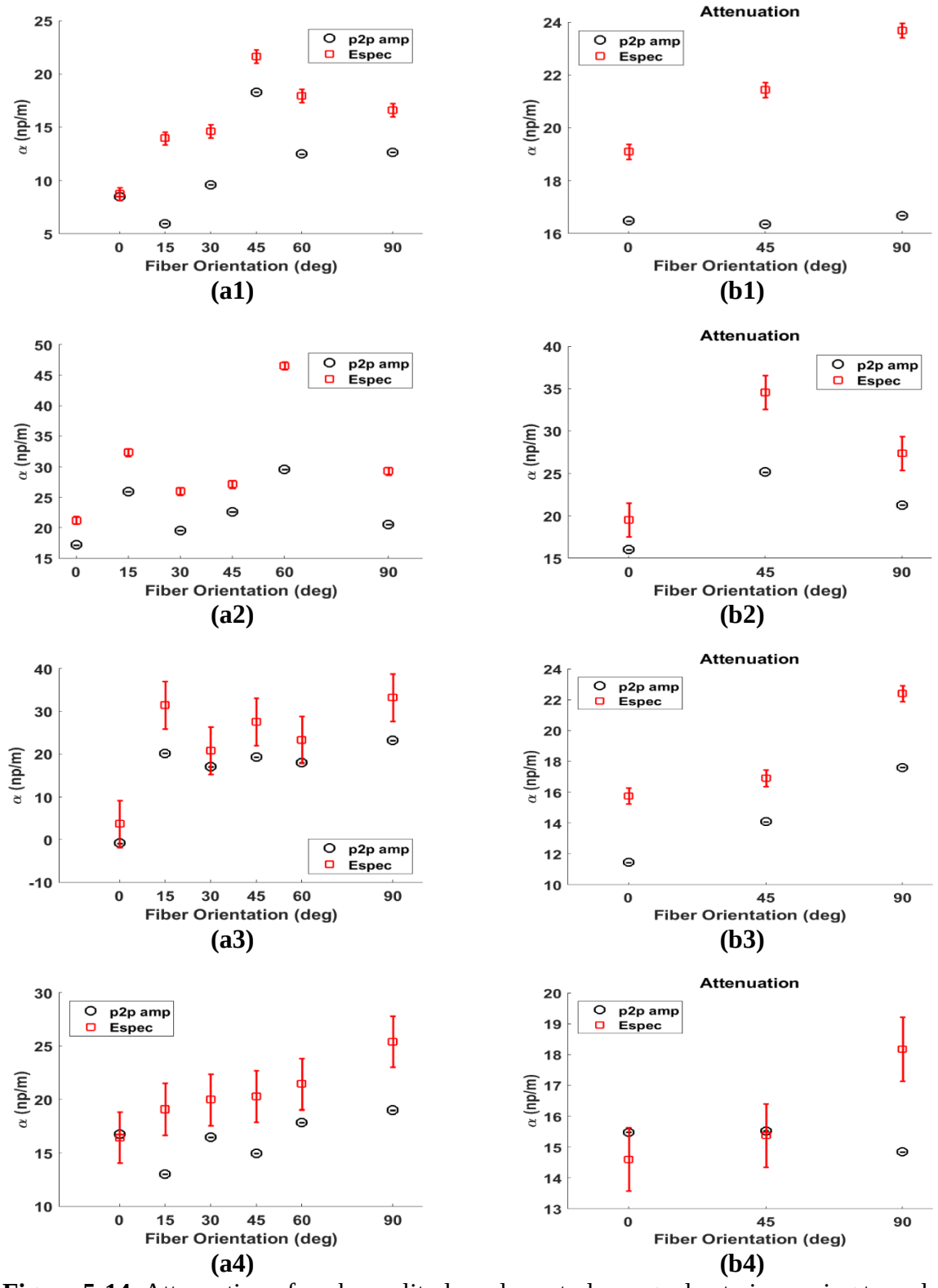

Figure 5-14. Attenuation of peak amplitude and spectral energy due to increasing transducer separation with fiber angle for a 30x30x0.9 cm a) unidirectional CFRP plate and b) Plexiglas plate. Signal was transmitted with a 1.25 cm, 1 MHz longitudinal transducer and received with 1) 1 MHz L, 2) 1MHz S0, 3) 1MHz S90, and 4) pinducer transducers.

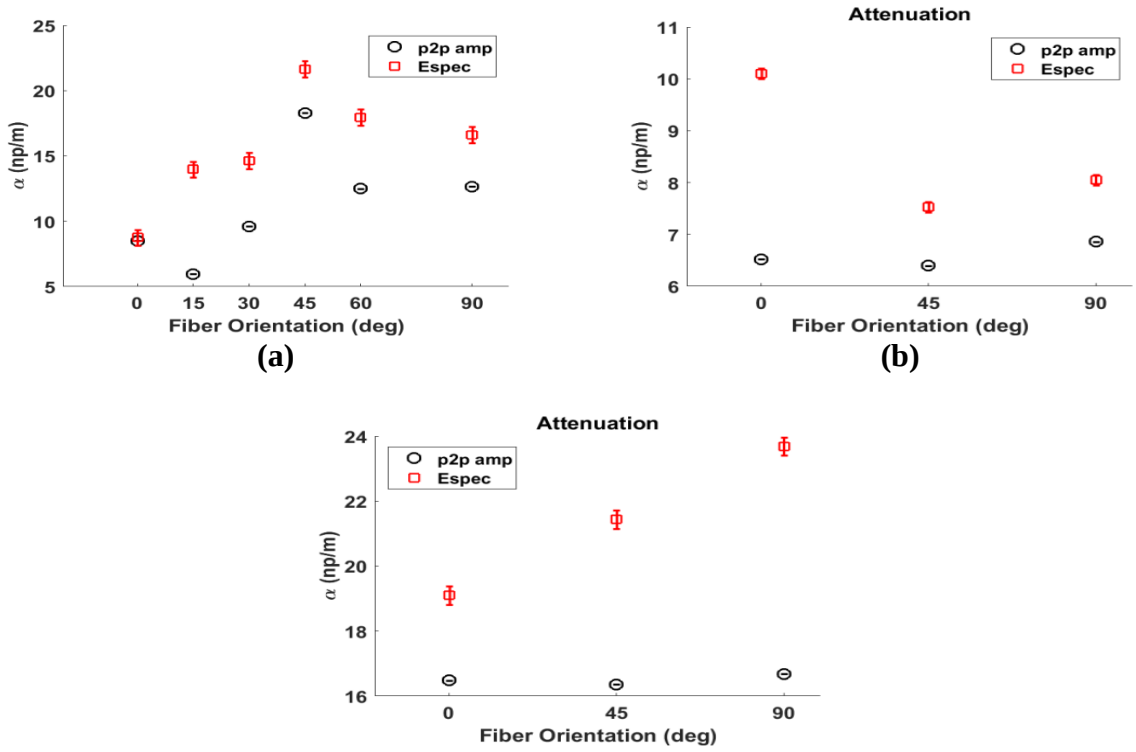

Figure 5-15. Attenuation of peak amplitude and spectral energy due to increasing transducer separation with fiber angle for a) a 0.9 cm unidirectional CFRP plate, b) a 0.9 cm quasi-isotropic CFRP plate and c) a 0.9 cm Plexiglas plate. Signal was transmitted and received with a 1.25 cm, 1 MHz longitudinal transducer.

The spatial attenuations of coda wave peak amplitudes and spectral energies may provide a measure of the decay of the information carried in waveform as the waveform spreads, but gives no indication of the spatial decay of specific frequency components. Typically, the frequency dependent attenuation is determined by the pulse-overlap method, but this method is not applicable as demonstrated previously. To overcome this, the coda wave spectra are equipartitioned using Tukey windows with 12.5% tapers on both sides then inverse transformed back into the time domain. The natural logarithm of the peak amplitudes of the time domain waveforms corresponding to a specific frequency bin are then plotted versus transducer separation and a line is fit to the data using least squares linear regression. The attenuation for that particular center

frequency is then the slope of the line and the error in the attenuation measurement is the standard error of the fit.

Attenuation results and corresponding coefficients of determination (R^2) are plotted in Figure 5-16. $R^2 > 0.6$ is considered a good fit, and the majority of the data yield R^2 values greater than 0.8, which indicates that the reduction in amplitude is well described by an exponential decay. Several R^2 values are quite low (mostly along the 0˚ orientation for the unidirectional CFRP). This is typically caused by a single datum that is significantly out of alignment with the other data during the regression, which is usually caused by significant differences in the spectra with increasing separation. The spectra for the 0˚ orientation for the unidirectional CFRP exhibits the most variation with respect to transducer separation. This is similar to one of the issues that invalidated the pulse-overlap method for coda waves. Poor regression fits usually result in negative attenuations.

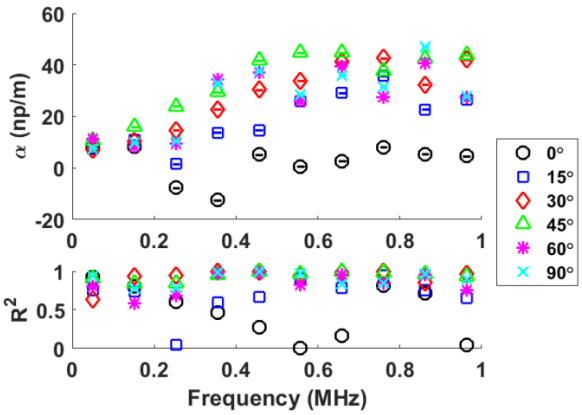

Figure 5-16. Example results from fitting an exponential to the frequency windowed data sets using least squares where α is the value of the exponential decay and R^2 is the coefficient of determination between the fit line and the data set.

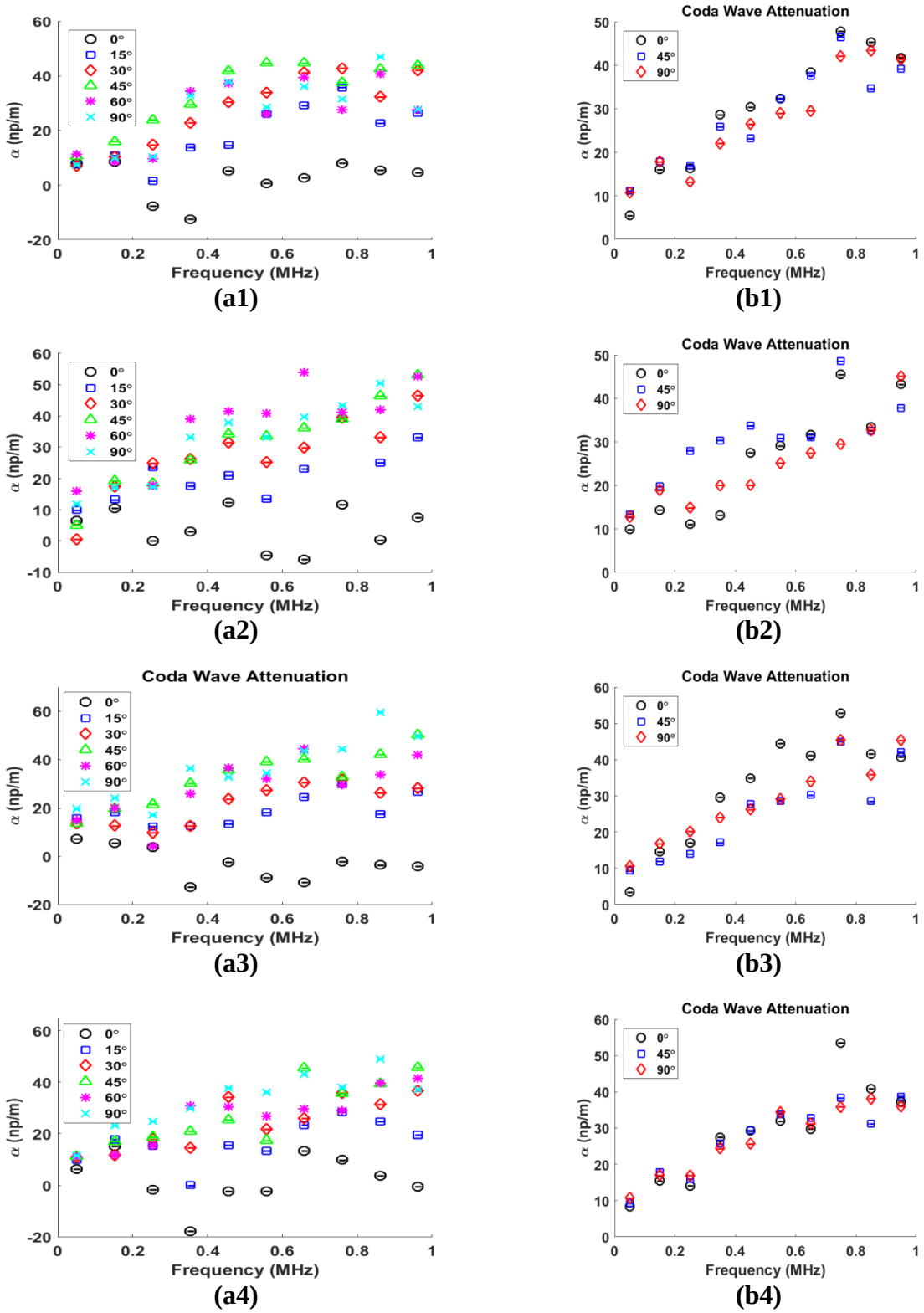

Figure 5-17. Frequency-windowed attenuation of peak amplitude due to increasing transducer separation with fiber angle for a) a 0.9 cm unidirectional CFRP plate and b) a 0.9 cm Plexiglas plate. Signal was transmitted with a 1.25 cm, 1 MHz longitudinal transducer and received with 1) 1 MHz L, 2) 1MHz S0, 3) 1MHz S90, and 4) pinducer transducers.

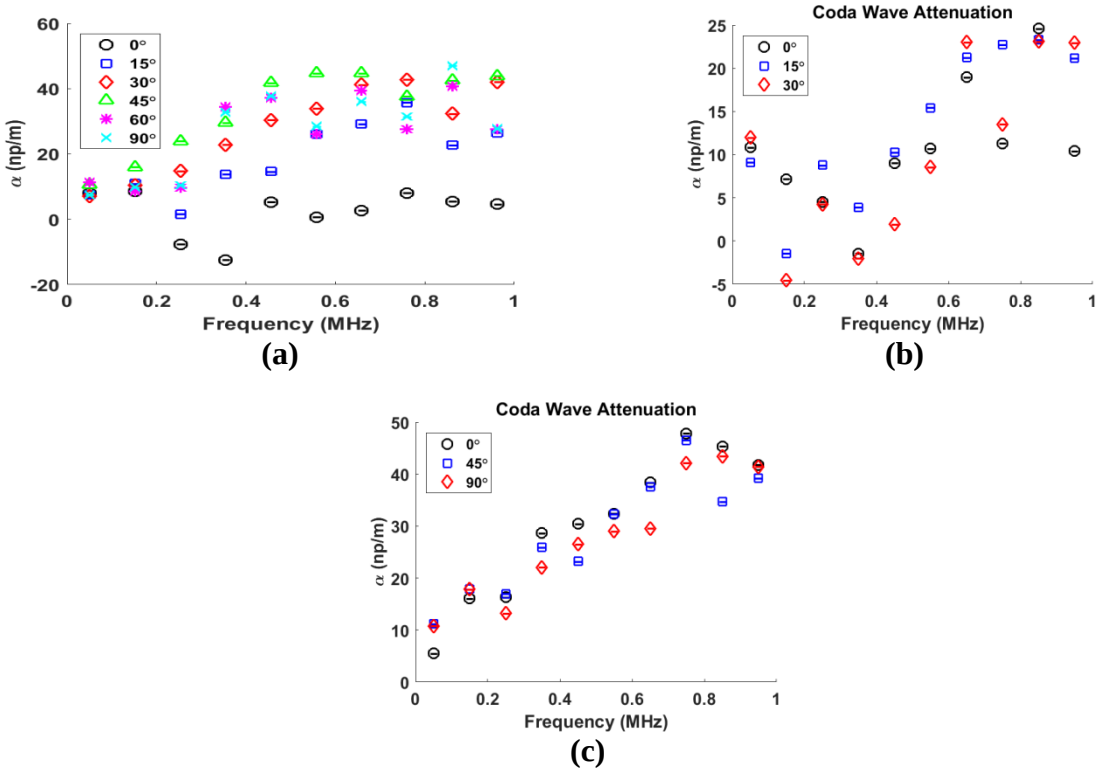

Figure 5-18. Frequency-windowed attenuation of peak amplitude due to increasing transducer separation with fiber angle for a) a 0.9 cm unidirectional CFRP plate, b) a 0.9 cm quasi-isotropic CFRP plate and c) a 0.9 cm Plexiglas plate. Signal was transmitted and received with a 1.25 cm, 1 MHz longitudinal transducer.

Frequency dependent attenuation results are plotted in Figure 5-17 & Figure 5-18 for the three materials and the wave components. The difficulty in measuring the coda wave attenuation for the unidirectional CFRP sample at 0˚ orientation is clear, and most of the data must be discarded. Attenuation of the longitudinal component increases with frequency until 0.5 MHz then plateaus. It also increases with fiber angle until 45˚ then decreases slightly until 90˚. This agrees with the peak amplitude observations. In a similar manner, there is also disagreement between the longitudinal attenuation measured with the 12.7 mm and 2 mm transducers. The differences in peak amplitude was due to the phase cancellation, but the differences in attenuation are due to the increased noisiness of the pinducer spectra. The attenuation of the shear components shows a general upward trend without plateauing.

For an ideal, symmetrically expanding wave field the isotropic and quasi-isotropic attenuation curves should be insensitive to orientation angle. This is not the case, however, with the measured coda wave attenuation as the data exhibits significant variation with orientation. The superposition field is not composed of ideal, symmetrically expanding wave fields and as such there is no reason to suppose that the coda wave field itself is circularly symmetric or that the attenuation should be insensitive to orientation.

5.4.2 Temporal Attenuation

The above methods of measuring coda wave attenuation attempt to quantify how the coda wave field attenuates with distance. These measurements do not decouple scattering loss and absorption loss and thus are measures of apparent attenuation. The coda wave decay rate, on the other hand, is a measure of how the wave field sampled at a single spatial point attenuates with time. For a multiply scattered wave field (one that can be modeled with the diffusion equation) the decay rate should be a measure of non-scattering loss mechanisms [Weaver 1987]. This includes both absorption and energy leakage, but the leakage into air is negligible since the normal incidence reflection coefficient between air and aluminum/CFRP is greater than 99%. Kautz, however, observes that the coda wave decay rate is affected by volumetric scattering caused by porosity [Kautz 1993]. Weaver likewise noticed that the decay rate is sensitive to surface finishes [Weaver 1987]. Spatial averaging of decay rates was not examined for either of these observations, which could potentially account for the variations observed.

For homogeneous, isotropic materials, the decay rate of a coda wave should be constant and independent of spatial location. The process of calculating the decay rate is very similar to the diffusion fitting proposed by Anugonda et al. (2001) where the main difference is that Weaver

excludes early time signal components which eliminates the characteristic diffusion shape and allows for an exponential fit. Diffusion fit parameters were found to vary with spatial location [Deroo et al. 2010], therefore, it is likely that the decay rate also varies, at least to some degree, with spatial location.

Coda wave decay rate measurements made on an aluminum (Al 6061-T6511) sample (Figure 4-1c) were compared with published data [Weaver 1987]. Weaver used a 1.2x1.2x7.5 cm volume of aluminum (Al 6061-T651) and pinducers to transmit and receiver with a similar experimental configuration to the one used here. The respective waveforms and data are shown in Figure 5-19. The data resulting from using the same number of temporal and spectral windows as Weaver yields an average decay rate that is an order of magnitude larger than the average value reported by Weaver (1.75 and 0.17 respectively). It is unlikely that this difference results from the use of 12.7 mm 1 MHz longitudinal transducers instead of pinducers. Indeed, the waveforms are an order of magnitude different in time, yet the power spectral densities for the windows agree to within 10%. The waveform provided by Weaver is also an order of magnitude longer than waveforms published elsewhere for the same material [Michaels & Michaels 2005]. Figure 5-19 also shows the envelope as calculate using the frequency window method. Both Weavers decay rate (0.17) and the one calculated here (1.75) fit the data equally well, showing the validity of the values. The power spectrum data matching also validates our calculations.

The discrepancies between the data presented by Weaver (1997) on one side and this thesis and Michaels & Michaels (2004) on the other can be resolved by one of two explanations. The more likely explanation is that the Coda Wave decay rate is proportional to the ratio of the volume to surface area. Thus coda waves should be considered as “leaky” waves in a similar manner to Lamb waves [Dayal & Kinra 1988, 1991]. The less likely explanation is that the sampling

frequency reported by Weaver is an order of magnitude smaller than the actual sampling frequency used. This can be demonstrated by scaling the waveform presented here to match the length of Weaver's. The decay rates then agree to within 30% error. This can be further improved to 1% error is the waveform is scaled by a factor of 10.5 instead of 15, which is conceivable since no very little information is proved by Weaver on the conditions for his collection window. This topic of differing decay rates for the same material warrants further investigation.

The calculated decay rates for the transversely isotropic, isotropic, and quasi-isotropic plates are shown in Figure 5-20, Figure 5-21, and Figure 5-22 respectively. Each collection point for all materials yields the same basic decay curve, which is similar to the diffusion envelope shown above. The largest decay rate is observed for the unidirectional CFRP plate at an orientation of 0˚, which is expected since the 0˚ signals have significant high frequency energy that quickly dies off with time while the signals are comprised of low frequency energy that dies off slowly. The results close to 0 MHz are questionable since the decay rate drops close to zero. Weaver postulates that this is due to the problematic validity of diffuse fields (coda waves) at low frequencies [Weaver 1987].

Decay rates are expected to be insensitive with orientation for the isotropic and quasi-isotropic materials since the absorption of ultrasound is a material property. The orientation angle, however, affects the decay rate for all samples and all components, at least to some extent. The quasi-isotropic material exhibits the least sensitivity to orientation while the isotropic plate shows sensitivity in only a few cases. The unidirectional plate is more interesting. The decay rate is fairly uniform with orientation for small separations, but as the separation increases, the decay rate quickly drops with increasing orientation angle. If the decay rate was truly just a measure of the absorption of ultrasound, then the decay rate should be insensitive to the transducer separation for

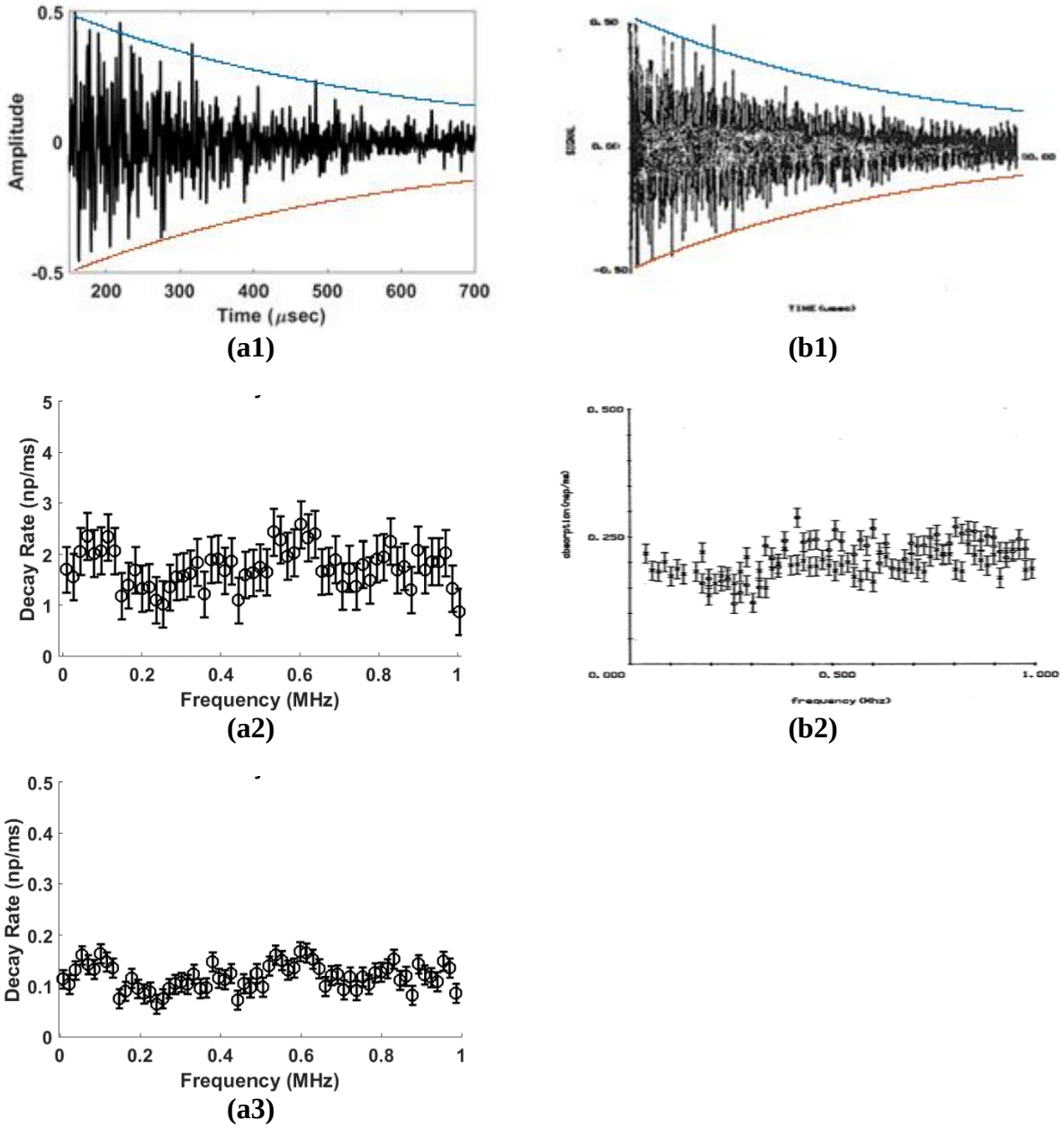

Figure 5-19. Comparison of (a) coda wave decay rate for Al 6061-T6511 with (b) results published by Weaver, [Weaver 1987] with permission of Springer [12]". 1) waveform used, 2) results obtained using the same number of windows as Weaver, and 3) results obtained using the same number of windows and scaling the time to match Weaver's. In (a) and (b) the decay curves shown for Weaver's (0.17) and current (1.75) decay rates.

[12] Original title of Figure 5-19b1 is: "Figure 2: A typical captured waveform-8192 microseconds of data are captured starting at a time shortly after, not at, the time of the main bang, in order to assure the presence of a fully developed diffuse field. The signal is artificially broken into successive time windows of width Δt = 512 microseconds and then Fourier transformed window by window."
Original title of Figure 5-19b2 is: "Figure 5: The absorption rates after vigorously cleaning the machined specimen (o's) and after polishing the machined surface (x's). Compare with Figure 4 and note that the cleaning and polishing seems to remove most, but not all, of the machining induced changes."

isotropic materials and ideally diffuse waves in a finite volume. The results from the isotropic plate contradict this since they exhibit the most dramatic variations in decay rate with increasing transducer separation. This discrepancy can be readily explained by considering the decreasing peak amplitude with separation combined with the consistently high amplitude low frequency content the cause the coda wave to appear to decay more slowly.

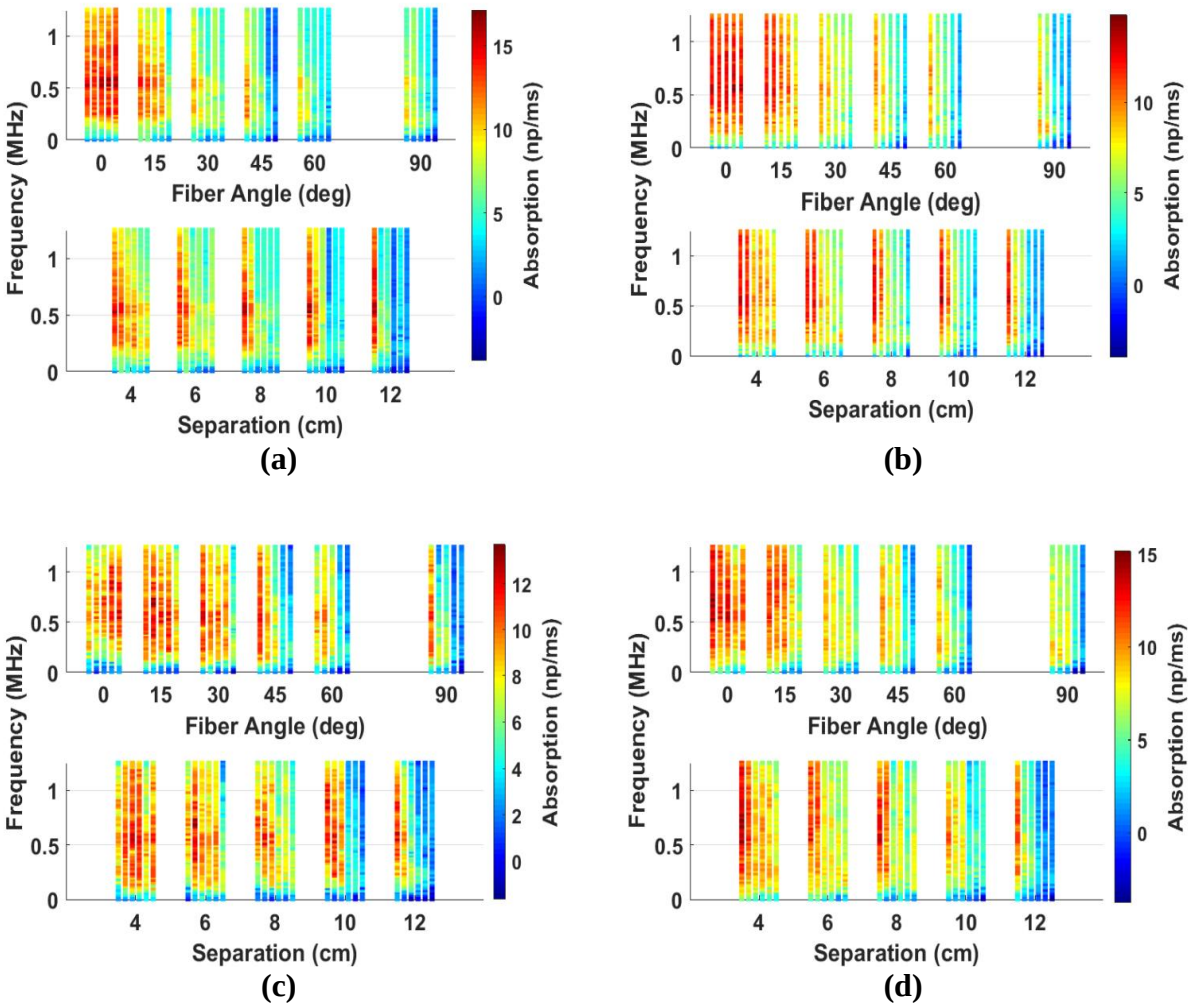

Figure 5-20. Coda wave decay rates at different transducer pair orientations for a 0.9 cm unidirectional CFRP plate. The upper plot compares transducer separation for each angle while the lower plot compares the orientation angle for each separation. Signal was transmitted with a 1.25 cm, 1 MHz longitudinal transducer and received with a) 1 MHz L, b) 1MHz S0, c) 1MHz S90, and d) pinducer transducers.

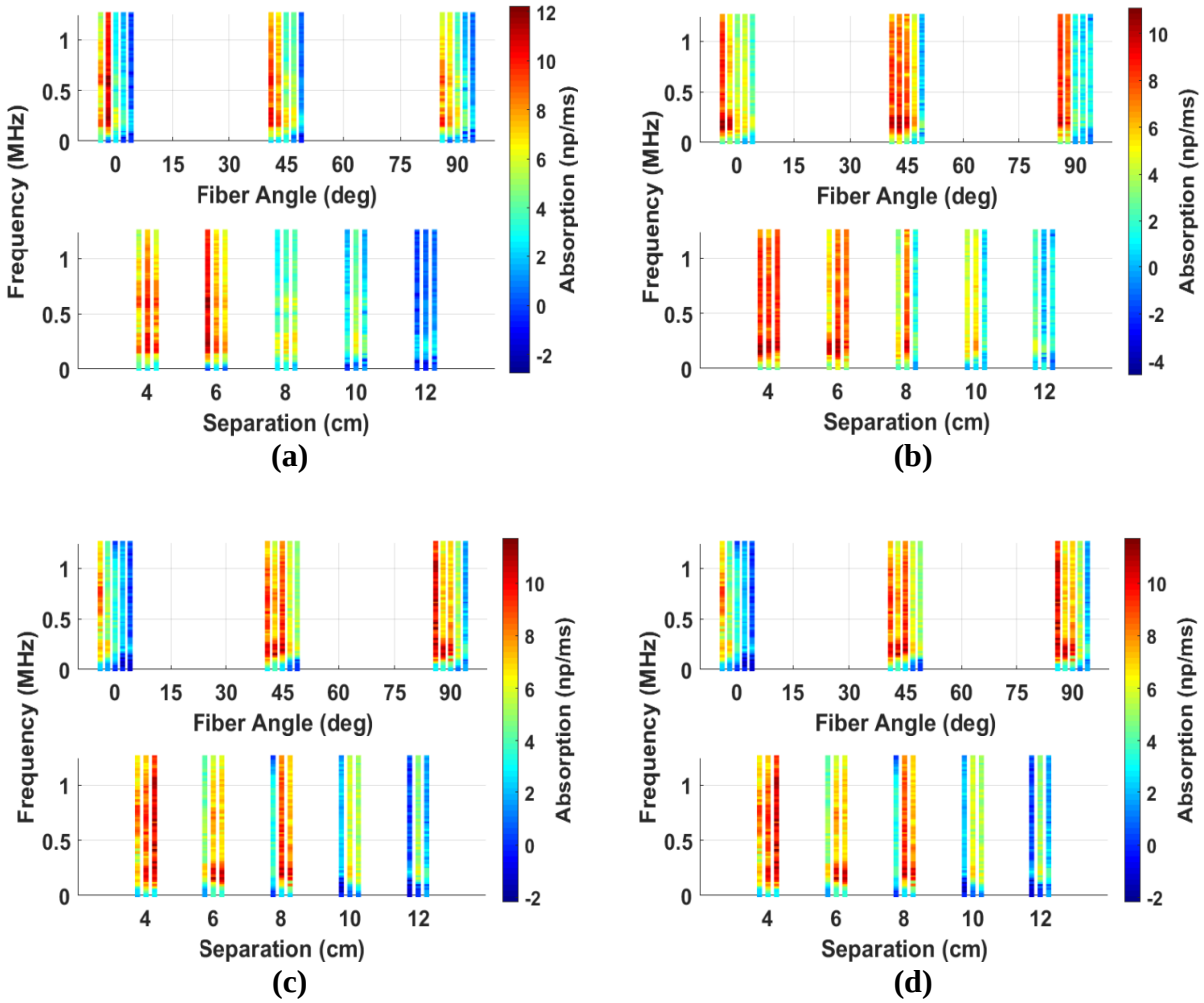

Figure 5-21. Coda wave decay rates at different transducer pair orientations for a 0.9 cm plexiglas plate. The upper plot compares transducer separation for each angle while the lower plot compares the orientation angle for each separation. Signal was transmitted with a 1.25 cm, 1 MHz longitudinal transducer and received with a) 1 MHz L, b) 1MHz S0, c) 1MHz S90, and d) pinducer transducers.

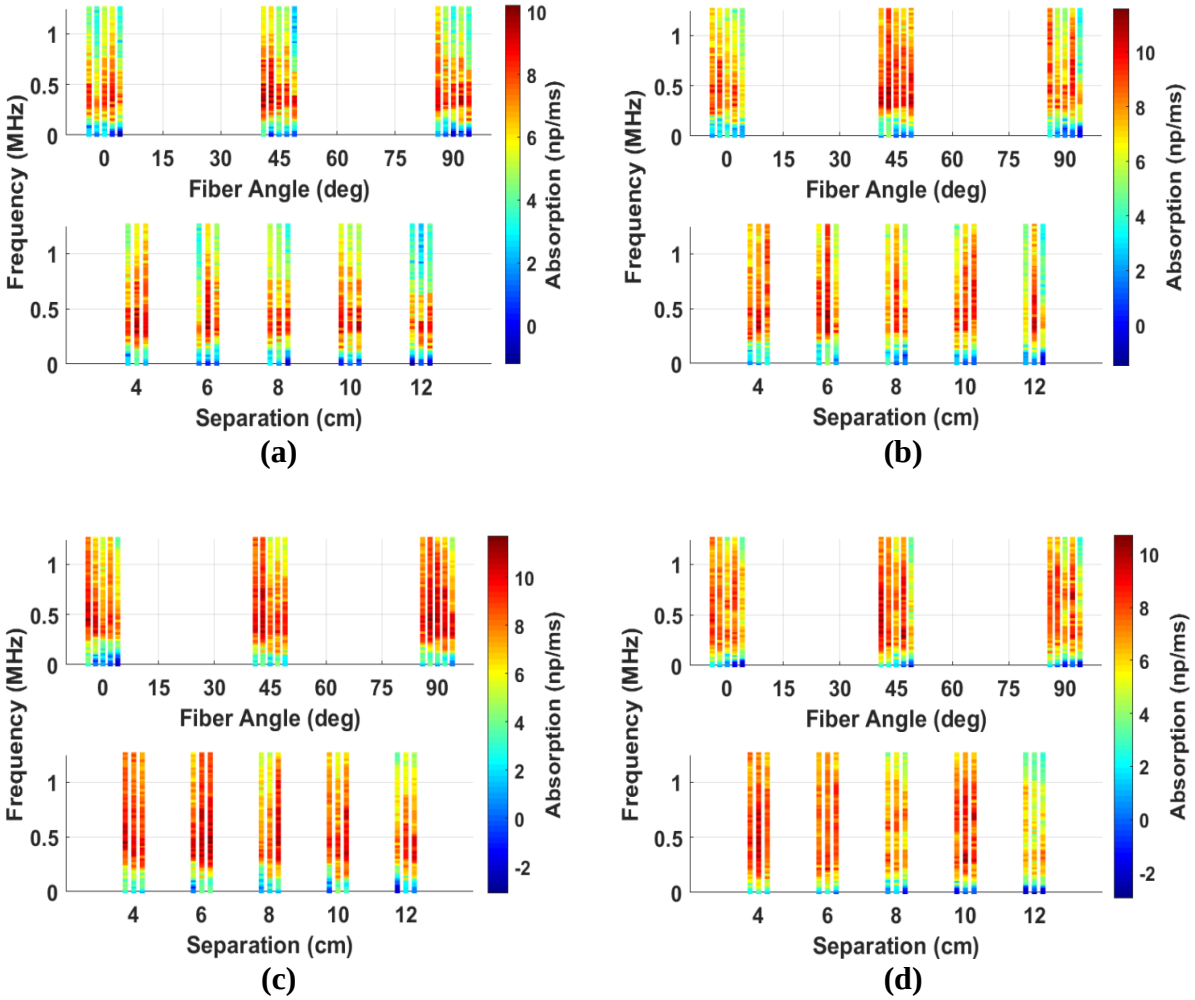

Figure 5-22. Coda wave decay rates at different transducer pair orientations for a 0.9 cm quasi-isotropic CFRP plate. The upper plot compares transducer separation for each angle while the lower plot compares the orientation angle for each separation. Signal was transmitted with a 1.25 cm, 1 MHz longitudinal transducer and received with a) 1 MHz L, b) 1MHz S0, c) 1MHz S90, and d) pinducer transducers.

5.5 Conclusions

Coda measurements were shown to be repeatable, reciprocal, and reproducible. This indicates that coda wave NDE has the potential for sensitive measurements for the detection of damage. The measurements presented in this thesis were performed under controlled laboratory conditions: the transducers were semi-permanently attached during each data collection stage and the data was collected quickly so that the ambient room temperature in the lab varied by less than

0.1 ˚C. Measurements were made with decoupled and recoupled receivers to examine the variability introduced by the changing coupling conditions. The repeatability of the coda wave parameters was an order of magnitude lower when decoupling and recoupling the transducers.

Coda wave propagation and attenuation were also examined. It was found that the time of first arrival of the coda wave occurred between the arrival time of a ballistic longitudinal mode and a ballistic shear mode. This corresponds either to a S_0 Lamb wave mode or a reflected longitudinal wave. Extracting Lamb wave modes was examined and found to inapplicable as the wave modes are not separable in either the time or frequency domains. Based on the first arrival times, the coda waves have an elliptical to barbell shaped spreading function. This indicates a propagating wave mode. In fact, the diffusion equation was fit to the coda waves with good agreement for aluminum, polycarbonate, and quasi-isotropic CFRP plates. The arrival times of the peak amplitude does not exhibit an elliptical/barbell spreading function which contradicts the propagating wave mode assumption. This is expected since the coda wave is a superposition field and not a wave mode.

Several attenuation measures were applied to the coda waves collected. The attenuations did not behave as would be expected for a propagating wave mode (i.e. well described by a decreasing exponential fit). This further indicates that traditional ultrasonic NDE measurements are not applicable in a coda wave analysis. One of the best measures of coda wave attenuation examined was the attenuation of signal energy with time (i.e. coda wave decay rate) as the definition is not dependent on the propagation of a specific wave mode. As expected, the isotropic materials exhibit circular attenuation function while the uni-directional CFRP plate exhibits an angular dependence. It is noted, however, that the size of the plate and reflecting vs. absorbing plate edges can dramatically affect the decay rate.

CHAPTER 6. QUANTITATIVE DETECTION OF DRILLED THROUGH HOLES

This chapter presents a quantitative examination of damage in fibrous composite materials using diffuse field differential features. A general introduction and summary fo the work performed is given in Section 6.1. The repeatability of measurements is presented and discussed in Section 6.2. Next, the validation of the experimental configuration and calculations is examined in Section 6.3. Immediately following, in Section 6.4, all of the results for the detection and quantification of drilled holes are presented, analyzed, and discussed. Afterwards, the effect of several system parameters on the detection of drilled holes is examined in Section 6.5. Finally, Section 6.6 summarizes the work and conclusions presented in this chapter.

6.1 Introduction

Drilled through-holes ranging in size from 0.397 mm (1/64") to 7.94 mm (20/64") were introduced to CFRP, aluminum, and polycarbonate samples. The smallest available mechanical drill sizes were used to simulate damage. It is understood that a micro-crack is even smaller than this, but since this size is nearest to a micro-crack, the damage is simulated with these drill bits. Larger damage sizes are also employed in order to examine the overall behavior of the features over a large range of damage. Basis functions are fit to the experimental data to determine the underlying behavior of the features and what aspect of the increasing damage produces a change in the differential features. A dimensional analysis of the differential features was performed to derive functions capable of accurately describing the behavior of two of the five features in order to allow for quantitative defect sizing based on 95% confidence bounds. Several types of drilled

holes were examined to demonstrate the sensitivity of the differential features to the effective defect volume as predicted by the derived functions. The derived functions were then fit to the experimental data and results are presented. Several regions of differing behavior for the differential features, which correspond to changing scattering regimes, were observed and are examined. This chapter also presents a discussion of diffuse field repeatability and the effects of system parameters such as input power and pulser-receiver damping of the behavior of differential features.

6.2 Repeatability

Repeatability of the signal and damage detection capability is one of the fundamental aspects of ultrasonic testing. An NDE technique must be both repeatable and reproducible in order to be viable for implementation. The sensitivity of coda wave parameters such as energy and decay rate to experimental conditions such as coupling and temperature has been previously discussed [Mazzeranghi & Vangi 1999, Gyekenyesi et al. 2002]. These studies concluded that several coda wave parameters are sensitive to damage but that experimental conditions can mask damage and impair repeatability. Here the repeatability of the coda wave differential features is analyzed for the first time by collecting five signals before damage and five signals after each damage increment, which are termed “baseline” and “measured” signals respectively. All signals were collected with the transducers semi-permanently attached to the specimen so that coupling variability was minimized. A round-robin comparison of the five baselines to the five measured signals yields 25 distinct measurements for each damage increment. The set of baseline measurements is constructed by comparing the five baseline signals with themselves, which ideally

would all be zero. As discussed previously (sect. 4.3), the distribution mean is taken as the measurement and the standard deviation is taken as the measurement error.

Figure 6-1a shows the baseline and several damage increment distributions of repeated measurements of the temporal residual energy differential signal feature collected from a quasi-isotropic CFRP sample (50x150x6mm). Generally, the standard deviation of each distribution is an order of magnitude smaller than the distribution means. The high quality factor (*Q*, peak amplitude over the half amplitude width), or the sharpness, of the baseline distribution indicates that the waveforms themselves are very repeatable while the high *Q* values of the damage

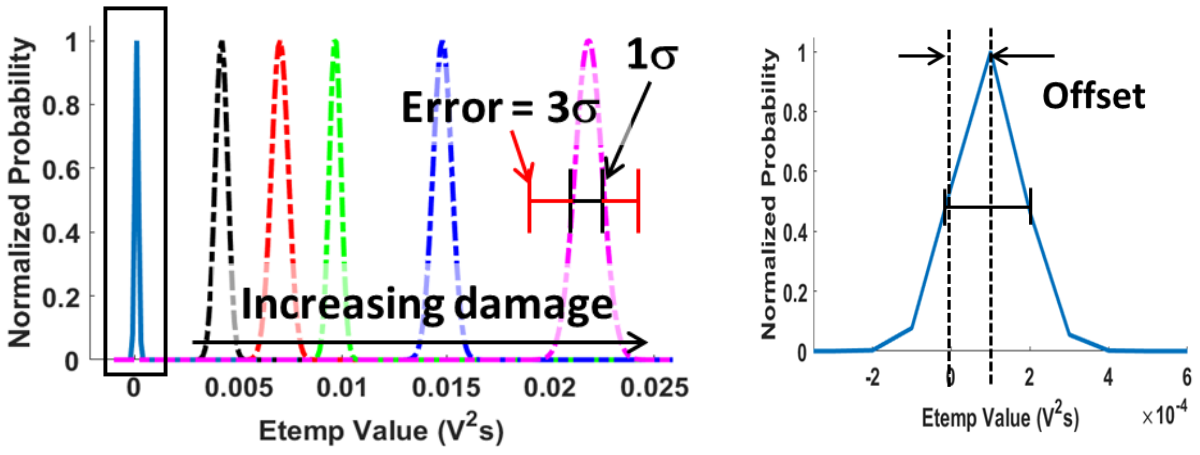

Figure 6-1. Normalized probability density function of repeated measurements for the residual temporal energy differential feature for a) several different hole diameters and b) the repeated baseline signals. The baseline in a) is indicated by the black outline.

distributions indicate that differences in the coda waveform measured by the differential features are also very repeatable. This indicates that the observed changes in the coda waveforms are in fact due to the presence of damage since the distributions do not overlap and the only difference between the subsequent collections is the introduced damage. Also noteworthy is the fact that the distributions remain distinct (non-overlapping), which means that the damage increments can be easily distinguished from each other.

Figure 6-1b shows an enlarged version of the baseline (highlighted with a black outline in Figure 6-1a) showing the standard deviation and offset. Ideally when comparing multiple baseline signals, the mean value of the differential feature distribution is zero with a standard deviation of zero since there is no change in the sample, environment, or measurement configuration. Small changes in the waveforms due to random noise will increase the spread of the baseline measurements (and hence measurement error) and will cause a shift in the distribution mean, which indicates that both of these quantities are measures of noise. Measurement systems often need to be calibrated due to a constant offset in the measurements. In a similar manner, the offset of the baseline distribution can be considered as a calibration constant since the mean value should be zero. It is subsequently shown (Sec. 5.7.4) this offset is a noise dependent quantity that can generally be removed from the measurements.

A comparison of the baseline distribution means and standard deviations is given in Table 6-1 for the five differential features extracted from repeated baseline signals collected for aluminum, polycarbonate, and quasi-isotropic CFRP samples (specimen #1). Note that all baseline measurements have an offset with the largest offsets measured for the differential curve length feature and for the aluminum sample in general. The aluminum offset is not unexpected as the coda waveform collected from aluminum contains more energy than the waveforms from polycarbonate or CFRP. Small variations in the aluminum waveforms will therefore result in larger values for the differential signal features. This is confirmed when detecting the same damage in the three materials.

Table 6-1a. Repeatability of coda wave baseline measurements of 50x150x0.6 mm plates using 12.7 mm longitudinal transducers (2.25 Mhz for Al and 1.0 Mhz for Poly and CFRP).

		Residual Temporal Energy				Residual Spectral Energy				Loss of Coherence			
		M	Σ	Q	Σ / M(%)	M	Σ	Q	Σ / M (%)	M	Σ	Q	Σ / M (%)
Al	100%	7.9e-3	4.8e-3	88	60.76	5.6e-3	3.8e-3	111	67.86	1.5e-2	5.2e-3	82	34.67
	50%	5.5e-3	1.0e-3	424	18.18	6.5e-3	2.0e-3	212	30.77	2.0e-2	3.4e-3	125	17.00
Poly	100%	2.1e-4	1.5e-4	2831	71.43	6.2e-4	5.5e-4	772	88.71	1.3-3	1.1e-3	386	84.62
	50%	1.8e-4	9.3e-5	4566	51.67	4.6e-4	3.6e-4	1180	78.26	7.8e-4	2.9e-4	1464	37.18
CFRP	100%	3.5e-4	2.9e-4	1464	82.86	2.0e-4	1.2e-4	3539	60.00	3.4e-3	2.2e-3	193	64.71
	50%	2.1e-4	1.5e-4	2831	71.43	5.7e-4	5.9e-4	720	103.51	1.3e-2	1.3e-2	33	100.00

M = mean
Σ = standard deviation
Q = quality factor

Table 6-2b. Repeatability of coda wave baseline measurements of 50x150x0.6 mm plates using 12.7 mm longitudinal transducers (2.25 Mhz for Al and 1.0 Mhz for Poly and CFRP).

		Loss of Correlation				Differential Curve Length			
		M	Σ	Q	Σ / M (%)	M	Σ	Q	Σ / M (%)
Al	100%	1.1e-3	2.8e-3	152	254.55	0.93	0.16	3	17.20
	50%	7.1e-4	1.0e-3	425	135.14	1.3	0.12	4	9.23
Poly	100%	3.1e-6	5.2e-5	8167	1677.40	8.3e-2	1.0e-2	43	12.05
	50%	6.0e-7	4.1e-5	1036	6833.30	0.14	1.0e-2	43	7.14
CFRP	100%	1.4e-5	2.2e-4	1930	1571.40	5.5e-2	1.6e-3	265	2.91
	50%	6.1e-6	4.7e-5	9035	770.49	9.6e-2	1.6e-2	27	16.67

M = mean
Σ = standard deviation
Q = quality factor

6.3 Experimental Validation

Three of the differential features obtained for aluminum (residual temporal energy, residual spectral energy, and loss of coherence) in this study were compared with the published experimental data of specimen #1 from Michaels & Michaels (2005). Published experimental data for loss of correlation and differential curve length are not available. The two data sets are plotted together in Figure 6-2.

The data sets are in good agreement for all features for hole diameters between 1.98 and 4.76 mm. A quantitative comparison of the two data sets can be performed using the relative mean squared error (*RMSE*), which is the square of the relative L2-norm. The percent error between the two data sets is 5.56%, 1.82%, and 2.28% for the temporal residual energy, the spectral residual energy, and the loss of coherence respectively. This demonstrates the reproducibility of the coda wave differential features in the presence of damage. In the data presented by Michaels & Michaels (2005), a plateau starts with the 5.56 mm hole while the data presented here continues to rise. Michaels & Michaels (2005) do not discuss the error in their measurements nor is any attempt made to explain the cause of the plateaus in the data.

Several noteworthy differences exist between the two experimental configurations: Michaels & Michaels (2005) use 12.7 mm 2.25 MHz piezo discs, an 8-bit oscilloscope, and digitizes the received signals at 12.5 MHz while this study uses 12.7mm 2.25 MHz longitudinal transducers, a 12-bit oscilloscope, and digitizes the received signals at 50 MHz. Both the data bit depth and sampling frequency can be reduced during post-processing to replicate Michaels' parameters and determine whether these may have influenced the data processing and created the plateaus in Michaels' data. Reducing the bit depth and sampling frequency did not affect our data and thus did not cause the plateaus. Several aluminum samples were also examined in order to try

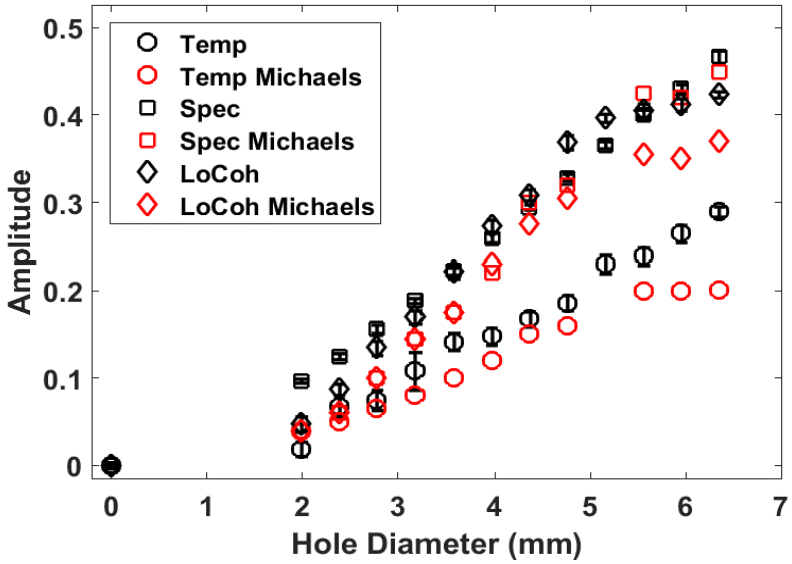

Figure 6-2. Comparison of three differential signal features (Residual Temporal Energy (Temp), Residual Spectral Energy (Spec), and Loss of Coherence (LoCoh)) from this study with those from Michaels and Michaels 2005.

to recreate the plateaus observed in Michaels' data, but the plateaus were unable to be recreated. Therefore, as a pure conjecture the plateaus are due to a parameter of the experimental configuration used by Michaels & Michaels.

6.3.1 Reciprocity of Damage Detection

The reciprocity of coda waveforms was presented and discussed previously (Section 4.4.3) where it was shown that variation in reciprocal waveforms is an order of magnitude larger than the variation in repeated waveforms and an order of magnitude smaller than the variation caused by the introduction of a 0.8 mm drilled through-hole. Such reciprocity is required by conservation principles. Here the reciprocity of damage detection via coda wave differential features is examined to demonstrate that coda waves are more than just noise and do carry damage information. Coda wave signals were collected from an aluminum sample (50x150x6 mm) where

the transmission from transducer #1 to transducer #2 shall be referred to as the "forward" signal and the transmission from transducer #2 to transducer #1 shall be referred to as the "backward" signal. Note that although the sample under examination has the transducers aligned along one line of symmetry the drilled through-hole is not symmetric with regard to the plate or transducers. This is significant since breaks in problem symmetry can break reciprocity.

Five forward and five backward signals were collected for each damage step and the five differential signal features were calculated. Figure 6-3 shows the resulting differential feature amplitudes which are nearly identical for the forward and backward signals over a range of through-hole diameters. Generally, the two data sets fall within 1 measurement error of each other, with the exception of the differential curve length (*DCL*). Percent *RMSE* was calculated for each of the five features to provide a quantitative comparison (Table 6-3). The spectral residual energy (*Espec*) feature was the most similar, *RMSE* = 0.0125%, while the differential curve length (*DCL*) feature was the least similar, *RMSE* = 1.16%. This demonstrates the remarkable reciprocity of coda wave differential features in the presence of damage, further proves that coda waves do carry damage/defect information, and indicates the repeatability and reproducibility of this technique.

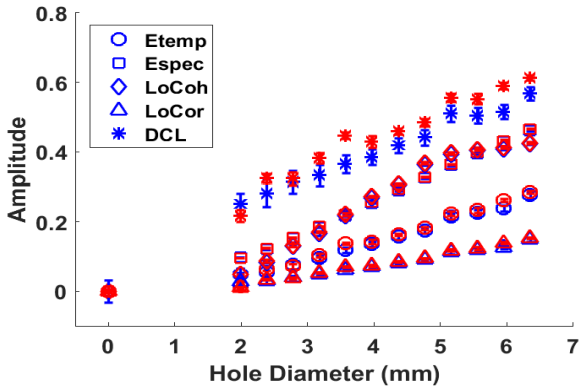

Figure 6-3. Example of the reciprocity of five differential features. Repeated signals were collected in both the forward and backwards directions in the presence of damage.

Table 6-3. Percent Relative Mean Squared Error quantifying the similarity of differential features for forward and backward propagating coda waves in the presence of damage.

Etemp	Espec	LoCoh	LoCor	DCL
0.68	1.25E-2	1.53E-2	0.73	1.16

6.4 Results

Collected waveforms were analyzed using the five methods previously described: residual temporal energy, residual spectral energy, loss of coherence, loss of correlation, and differential curve length. For each specimen, a set common baseline signals was used for all five methods. The baselines correspond to a simply supported, pristine sample at room temperature[13] (21.2 ˚C ± 2.1). The 10-1010 μs time windows considered for feature extraction were identical across all specimens and methods and were selected to replicate the work by Michaels & Michaels (2005). Increasing the window length to encompass the full 2000 μs of recorded data did not affect the results. All spectrograms were calculated for the entire 10-1010 μs time window and a frequency window from 0 to 3.5 MHz: again the window was chosen to replicate the work of Michaels & Michaels (2005). This frequency range does encompass more than 99% of the spectral energy for all signals. Center frequencies were approximately 200, 50, and 40 kHz for aluminum, CFRP, and polycarbonate samples respectively, but significant energy was present up to 3.5, 1, and 0.75 MHz respectively.

[13] See footnote 11, pg. 107.

6.4.1 Differential Features

The range of hole diameters was extended from 1.98-6.35 mm (used by Michaels & Michaels (2005)) to 0.397-7.94 mm to examine the detection limits and resolution of differential signal features. Differential feature extraction is also extended to fibrous composite and polymeric materials to determine the applicability and limits of this technique. The resulting differential features are plotted in Figure 6-4 & Figure 6-5 where the abscissa is the hole diameter and the ordinate is the feature amplitude for each damage stage. Secondary and tertiary abscissa are given in Figure 6-4 indicating the ratio of the hole diameter to the longitudinal and shear wavelength at 1 MHz respectively. For all cases, the features are well correlated to defect size and show promise for future defect characterization. With only a few exceptions, the parameters are generally increasing with defect size, which demonstrates their effectiveness in detecting and discriminating defects. Figure 6-4 shows plots of the five differential features for each of the three specimens. All parameters easily detect the 0.397 mm hole for CFRP and polycarbonate and the 0.794 mm hole for aluminum. The diameter increase of 0.397 mm is easily resolvable in most of the cases with the arguable exception of features with large error bars. The deviation in repeatability for the features in polycarbonate and differential curve length in CFRP and aluminum signifies that the 0.397 mm resolution is not achievable with a single measurement in these cases. The resolution is achievable in these plots with five repeated measurements. Note that the error bars in the figure encompass 99.7 percent of the measurements.

Spectral residual energy is the most sensitive to defects across the three specimens, though loss of coherence is also observed to be quite sensitive. Differential curve length and loss of correlation are the least sensitive to defects, though perform well when normalized, as shown below. Differential curve length also has consistently large repeatability error for all specimens.

The combination of low sensitivity and low repeatability indicates this feature should not be used for this type of defect. Kinks in the otherwise monotonically increasing data are observable in all features for CFRP and polycarbonate. The CFRP data below 2 mm increases linearly, then drops in amplitude and continues to increase quadratically. This change in behavior occurs during the transition from Rayleigh to intermediate scattering regimes. The polycarbonate data exhibits a substantial reduction of amplitude for all features at 6 mm. It is interesting to note that even though Perseval's theorem suggests that the temporal and spectral energy should be equivalent, only the polycarbonate exhibits equivalent energy.

Figure 6-5 shows the comparison of each feature's behavior in the three specimens. The CFRP and polycarbonate features have similar amplitudes that are typically one fourth the amplitudes in aluminum. This is due to the similarities in the received waveforms for CFRP and polycarbonate. The aluminum waveform has spectral content at higher frequencies and a longer "ring-down" period. This allows for an increased sensitivity to minute changes and thus a larger differential feature amplitude. The most likely cause of the waveform shape differences between aluminum and CFRP/polycarbonate is the elastic vs. visco-elastic wave propagation. Also noteworthy is that the 'S' shaped curvature in the aluminum loss of coherence is also present in both the CFRP and polycarbonate samples, though at later times. This suggests the parameter 'loss of coherence' asymptotically approaches 0.5 at very large defects. Such behavior is expected since the temporal coherence of uncorrelated white noise is approximately 0.5.

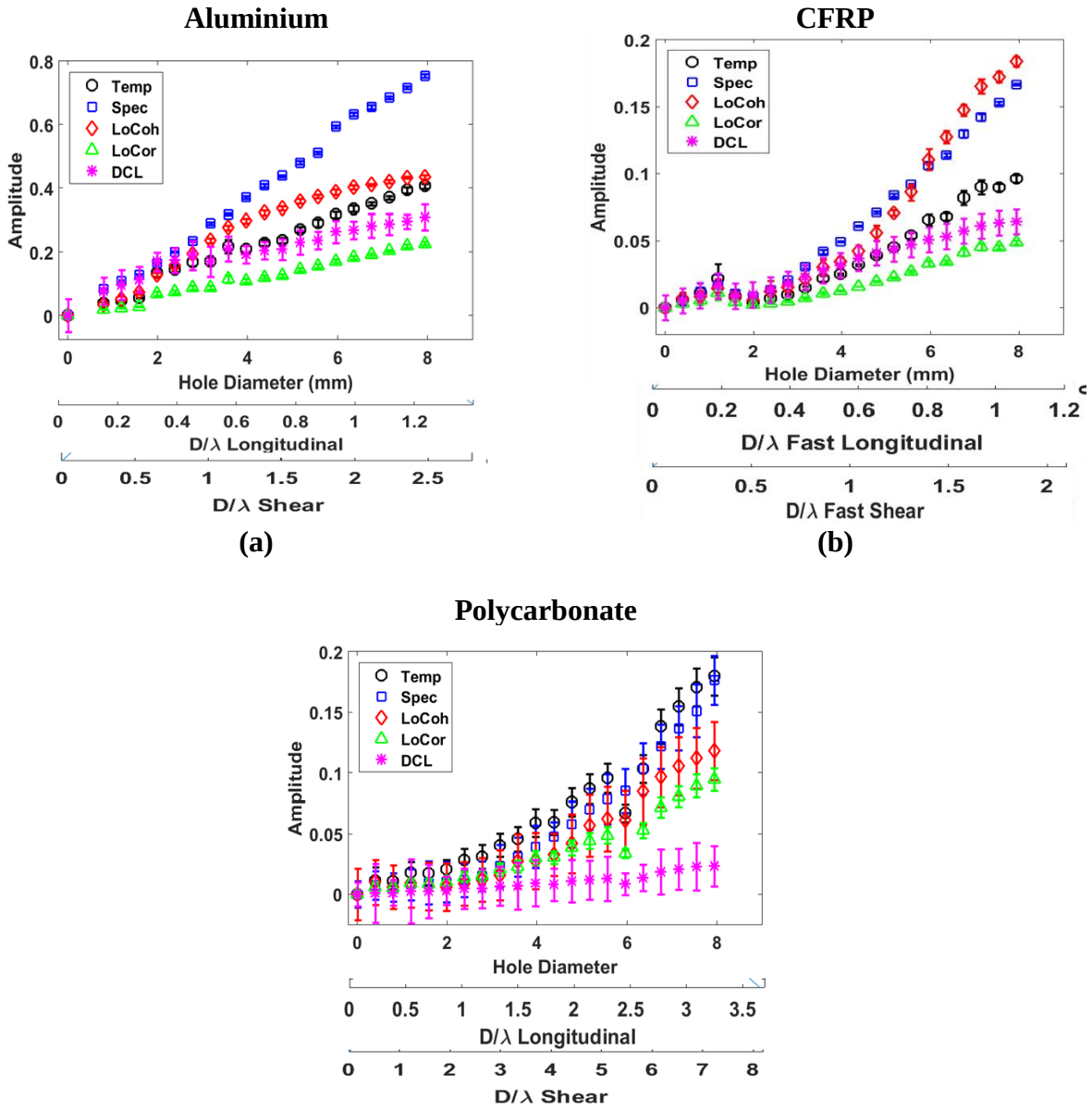

Figure 6-4. Increase in the amplitude of the five differential signal features with increasing hole diameter for (a) aluminum, (b) CFRP, and (c) polycarbonate. The signals are transmitted and received with a pair of 12.5mm longitudinal transducers (2.25 MHz for aluminum and 1 MHz for CFRP and polycarbonate) excited with a spike pulse.

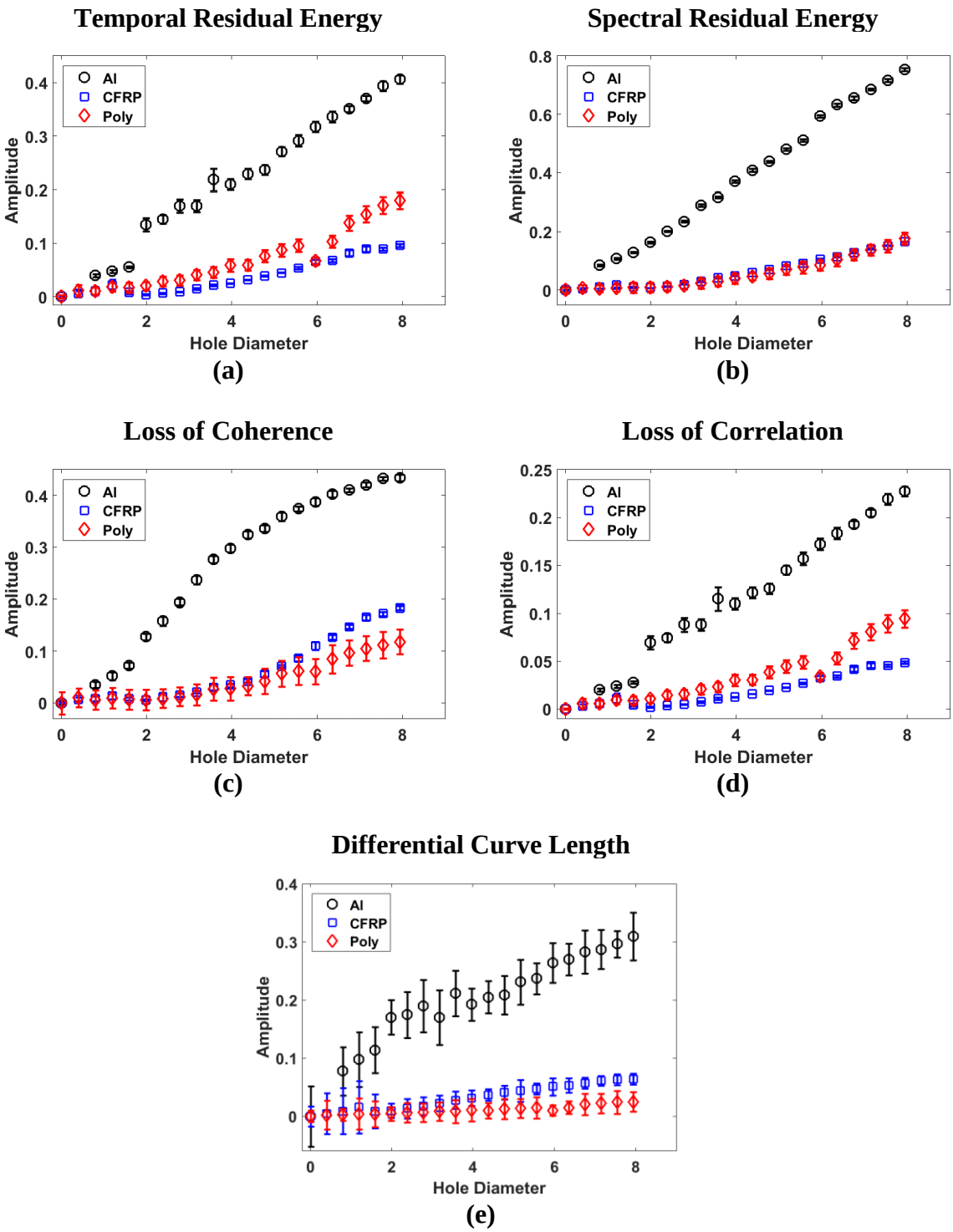

Figure 6-5. Comparison of differential signal features (a) residual temporal energy, (b) residual spectral energy, (c) loss of coherence, (d) loss of correlation, and (e) differential curve length extracted from the three materials considered in this study. The signals are transmitted and received with a pair of 12.5mm longitudinal transducers (2.25 MHz for aluminum and 1 MHz for CFRP and polycarbonate) excited with a spike pulse.

This work demonstrated that a 0.397 mm increase in the diameter of through-thickness holes is resolvable with differential signal features. To further examine the resolvability of small scale changes in damage the work is extended to include two additional damage types: single partial/full through hole (Figure 4-2b & Figure 4-3) and multiple through-holes of constant diameter (Figure 4-2c). The resulting differential features are plotted in Figure 6-6 - Figure 6-7 where the abscissa is the effective hole diameter and the ordinate is the feature amplitude for each damage stage. For all cases, the features are well correlated to defect size. With only a few exceptions, the parameters are monotonic with defect size, which demonstrates their effectiveness in detecting and discriminating defects.

Figure 6-6 shows plots of residual temporal and spectral energy for the half/full hole (specimen #2) CFRP and polycarbonate samples. The other three differential features show similar behavior. All parameters easily detect the 1.59 mm diameter half-hole in both materials and can differentiate between half-holes and full-holes. Both the increase in diameter and hole depth are resolvable and distinguishable from each other in most cases with the best performance occurring for residual spectral energy from the polycarbonate sample. Residual spectral energy generally performs better than the other features and features in polycarbonate generally perform better than those for CFRP as the features in CFRP have difficulty distinguishing between half and full holes when the diameter is greater than 3 mm. Deviations from the observed trends for through-holes and the inability to distinguish hole depth in certain cases is caused in part by the increased scattering from the sharp edges of the half hole.

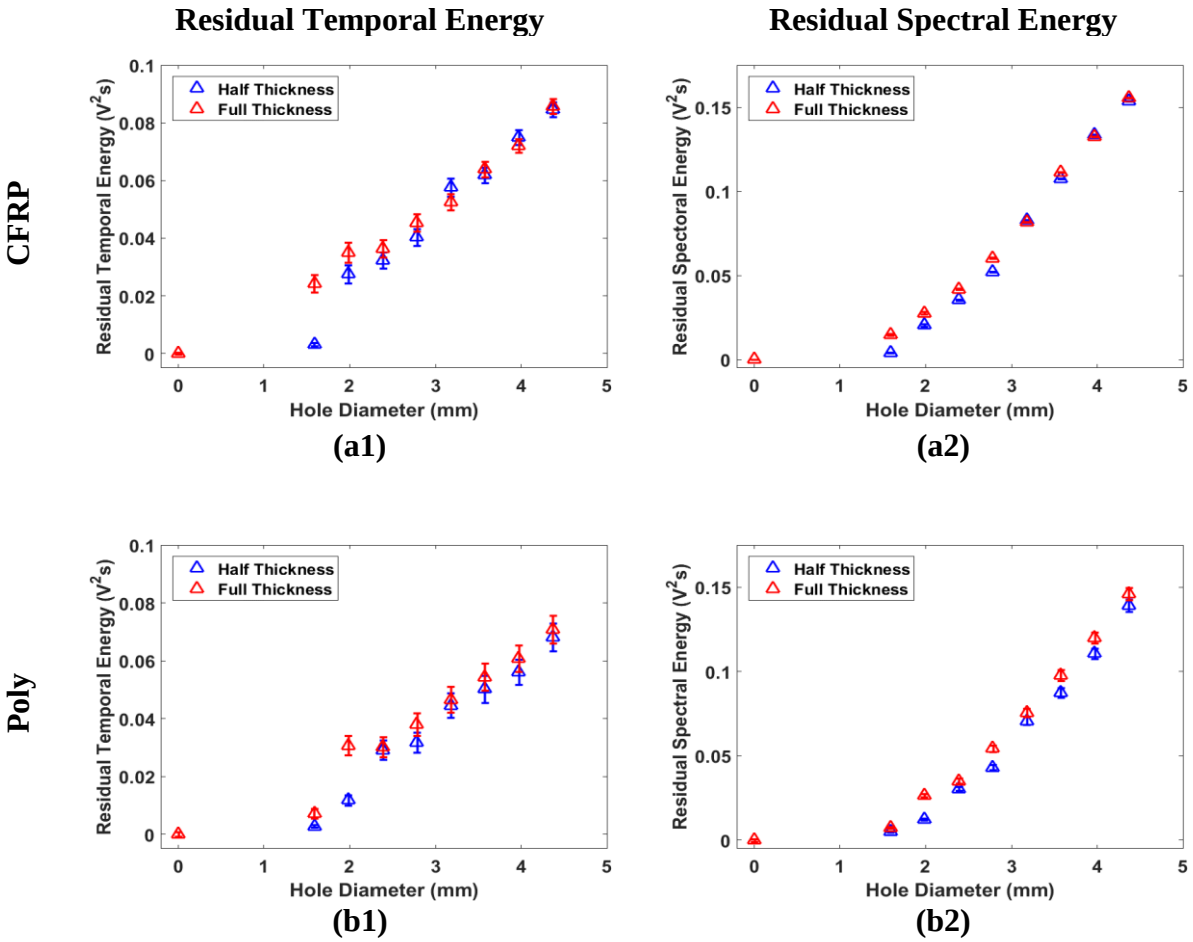

Figure 6-6. Increase in the amplitude of (1) the residual temporal energy and (2) residual spectral energy with increasing damage size for (a) CFRP and (b) polycarbonate specimen #2. The signals are transmitted and received with a pair of 12.5mm 1 MHz longitudinal transducers) excited with a spike pulse.

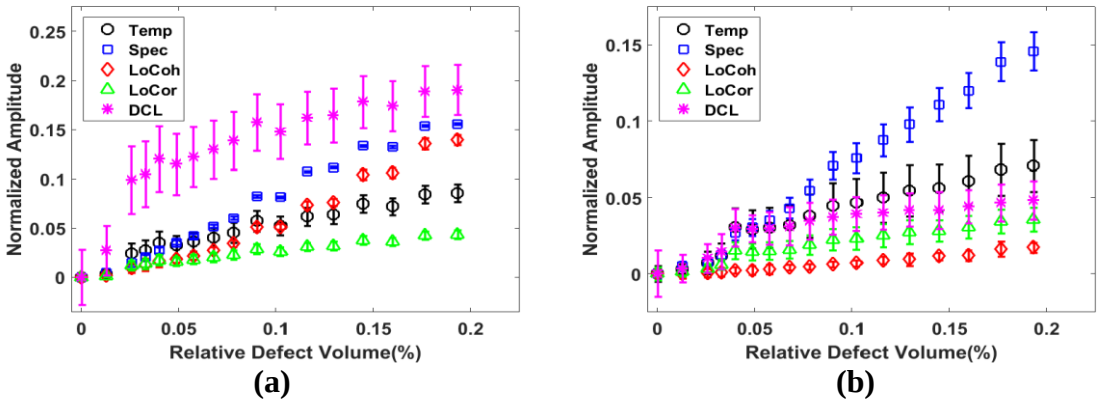

Figure 6-7. Increase in the amplitude of the five differential features with increasing damage volume for (a) CFRP and (b) polycarbonate specimen #2. The signals are transmitted and received with a pair of 12.5mm 1 MHz longitudinal transducers) excited with a spike pulse.

The dependence of the feature amplitude on both hole diameter and depth suggests that changing the abscissa to defect volume would be useful. A comparison of the five differential features for both CFRP and polycarbonate samples is shown in Figure 6-7. Spectral residual energy is the most sensitive to defects for the two specimens. Differential curve length and loss of coherence are the least sensitive to defects, though perform well when normalized. Differential curve length also has consistently large repeatability error for all specimens. The combination of low sensitivity and low repeatability indicates this feature should not be used for this type of defect. The poorer repeatability for the features in polycarbonate and differential curve length in CFRP signifies that the desired resolution is not achievable with a single measurement in these cases. The resolution is achievable in these plots with five repeated measurements. Note that the error bars in the figure encompass 99.7 % of the measurements.

Figure 6-8 shows plots of residual temporal and spectral energy for the multiple through-hole (specimen #3) CFRP and polycarbonate samples. The other three differential features show similar behavior. All parameters easily detect the first through-hole and can resolve subsequent 0.397 mm through-holes with a linear dependence. All features, save residual spectral energy, begin to plateau for the fifth hole, which indicates that the second hole partially masks the fifth hole. Contrary to the results from the other two specimen sets, differential curve length shows the highest sensitivity to defects, followed by temporal residual energy. This set of specimens represents the smallest increase in damage volume and shows off the resolution and detection capabilities of coda wave differential features. The diameter of these drilled holes is approximately three times the width of a micro-crack, which is likely detectable and countable with coda wave differential features.

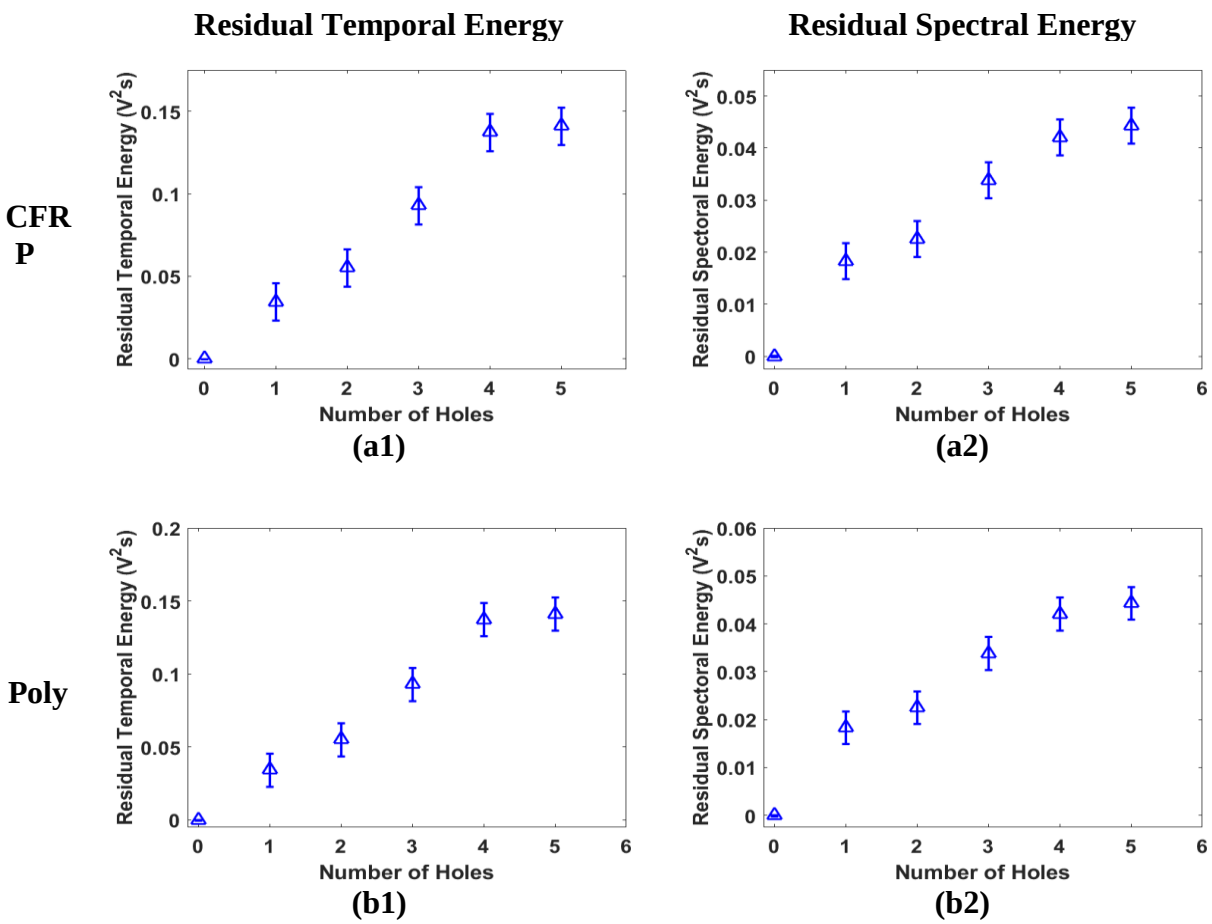

Figure 6-8. Increase in the amplitude of (1) the residual temporal energy and (2) residual spectral energy with increasing damage size for (a) CFRP and (b) polycarbonate specimen #3. The signals are transmitted and received with a pair of 12.5mm 1 MHz longitudinal transducers) excited with a spike pulse.

6.4.2 Normalized Differential Features

The differential signal features were normalized to allow for comparison of the features for each material and between materials. Features were normalized so that the feature amplitude corresponding to the 4.76 mm hole is unity for each specimen. The 4.76 mm diameter hole was chosen because it is the largest hole diameter before the data from Michaels & Michaels (2005) plateaus, and allows for the best comparison.

Figure 6-9 plots the normalized features for each specimen: (a) aluminum data from Michaels and Michaels, (b) aluminum, (c) CFRP, and (d) polycarbonate. Again, secondary and

tertiary abscissa are given indicating the ratio of the hole diameter to the longitudinal and shear wavelength at 1 MHz respectively. Although the features follow the same general trend for each specimen, they tend to diverge around the 5.5 mm hole. This is most apparent for CFRP. The features also express the same structures in each specimen that deviate from the trend: the plateau for large hole diameters in Michaels' aluminum, the kink for small hole diameters in CFRP, and the abrupt drop in amplitude at the 5.5 mm hole in polycarbonate. This is indicative of a physical phenomenon such as a transition in the scattering regime or of intrinsic system behavior such as non-linearity.

The features are well correlated ($CC > 0.95$) for aluminum, polycarbonate, and Michaels' aluminum. This indicates that the features for each of these materials are governed by the same function with different scaling and that they give similar information about the material and defects. The feature divergence for these specimens is largely due to the increasing dissimilarity between the baseline and measured signals, which affects each feature differently, but also corresponds to the transition from Rayleigh to intermediate scattering regimes for the coda wave center frequency. The features in CFRP are more complex with three distinct regions: linear region below 2 mm, quadratic region 2-5.5 mm, and divergent region above 5.5 mm. These regions roughly correspond to the Rayleigh, intermediate, and specular scattering regimes respectively. Initially the features in CFRP are well correlated ($CC > 0.98$), but diverge significantly after the 4.76 mm hole. The feature divergence is largely due to the features tracking different physical phenomena as they follow different basis functions.

Comparison of each differential feature across materials is shown in Figure 6-10. All five features are well correlated between the CFRP and polycarbonate samples, due in part to the divergence of the features in polycarbonate. The features in aluminum differ considerably from

the CFRP and polycarbonate features, save for differential curve length. These results are significant because they indicate the physical processes affecting the coda wave are similar for CFRP and polycarbonate but different for aluminum where the main difference between CFRP/polycarbonate and aluminum is visco-elastic vs. elastic propagation.

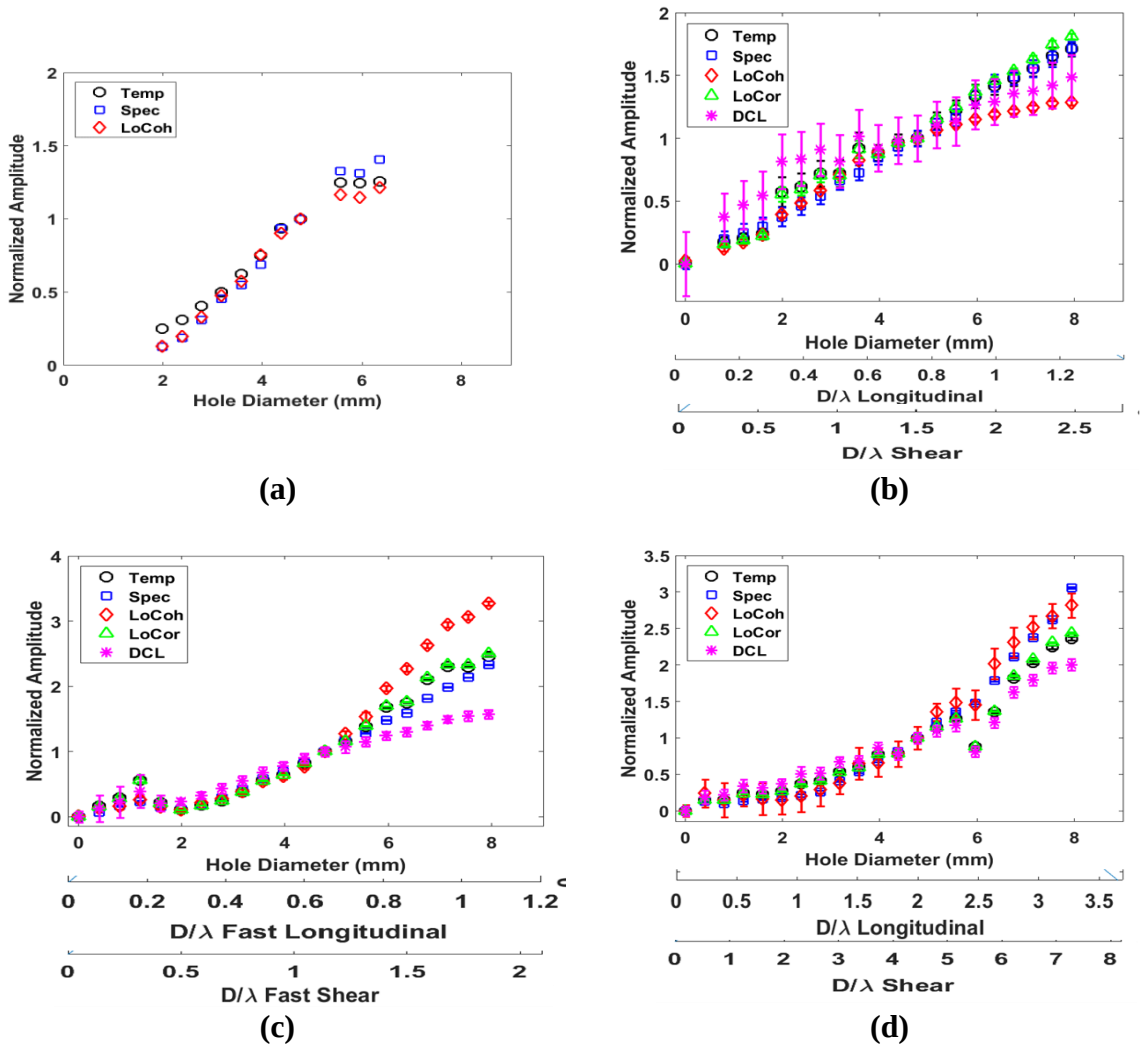

Figure 6-9. Normalized amplitude for the differential signal features with increasing hole diameter for (a) Michaels and Michaels 2005, (b) aluminum, (c) CFRP, and (d) polycarbonate. Amplitudes were normalized so that the amplitude corresponding to the 4.76 mm hole is unity. The signals are transmitted and received with a pair of 12.5mm longitudinal transducers (2.25 MHz for aluminum and 1 MHz for CFRP and polycarbonate) excited with a spike pulse.

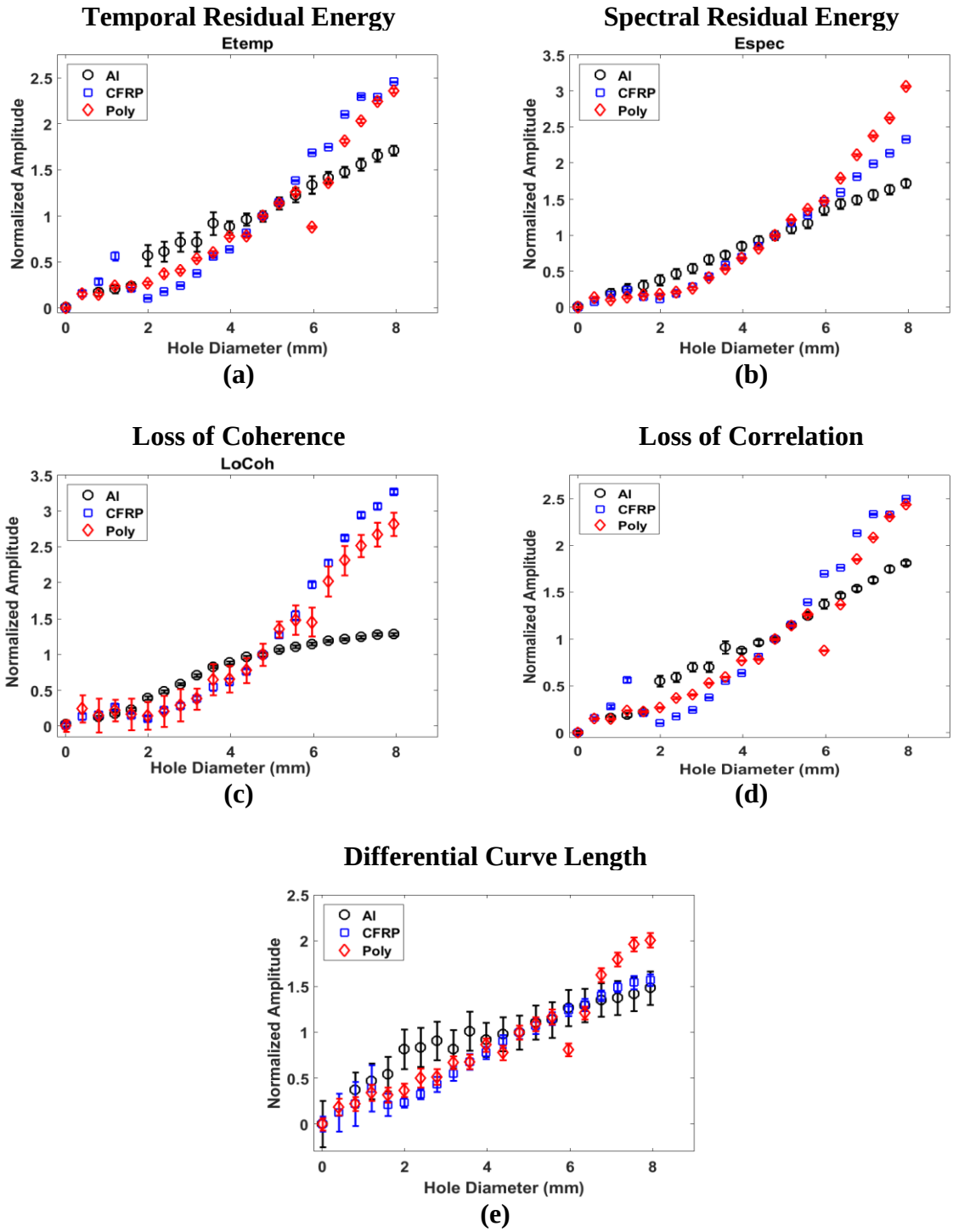

Figure 6-10. Comparison of normalized differential signal features (a) residual temporal energy, (b) residual spectral energy, (c) loss of coherence, (d) loss of correlation, and (e) differential curve length for the three materials considered in this study and the data from Michaels and Michaels 2005. Amplitudes are normalized so that the amplitude corresponding to the 4.76 mm hole is unity. The signals are transmitted and received with a pair of 12.5mm longitudinal transducers (2.25 MHz for aluminum and 1 MHz for CFRP and polycarbonate) excited with a spike pulse.

6.4.3 Trend lines of Differential Features

Four of the five differential features increase monotonically, between the first and second kinks, with increasing hole diameter for all three samples. Thus, future defect sizing can be achieved by fitting a physical model to the current data. Constant coefficients were eliminated by normalizing the features to themselves, which allows for the determination of the basis function. The initial best fit of the differential features is an arbitrary third order polynomial determined by weighted least squares. This indicates that the features are volume (or length^3) dependent while the coefficients are material dependent. An appropriate volumetric dependence is the hole volume since it increases with hole diameter. Normalizing the hole volume in a similar manner to the deferential features yields a d^2 (where d is the hole diameter) function since the plate thickness is constant. Two other basis functions, d^3 and d, are selected based on Rayleigh and Stocastic scattering regimes respectively since most of the features are proportional to scattering loss.

Figure 6-11 shows plots of normalized differential features and normalized basis functions for aluminum, CFRP, and polycarbonate. The adjusted coefficient of determination, $\overline{R}^2$, of the basis functions are listed in Table 6-4 Differential features extracted from the aluminum sample are best described by the linear basis function with $\overline{R}^2 > 0.95$. Loss of coherence begins to plateau around the 5.57 mm diameter hole. For CFRP, the residual energies and loss of correlation are best described by the quadratic basis function with $\overline{R}^2 > 0.97$, while differential curve length fits the linear function and loss of coherence fits the cubic function. All features are well described by the basis functions for hole diameters between 2.38 and 6.35 mm. In a similar manner to the aluminum sample, loss of coherence begins to plateau around the 6.35 mm hole. All features extracted from the polycarbonate sample (including differential curve length) are well described by a quadratic basis function which has $\overline{R}^2 > 0.94$. It should be noted

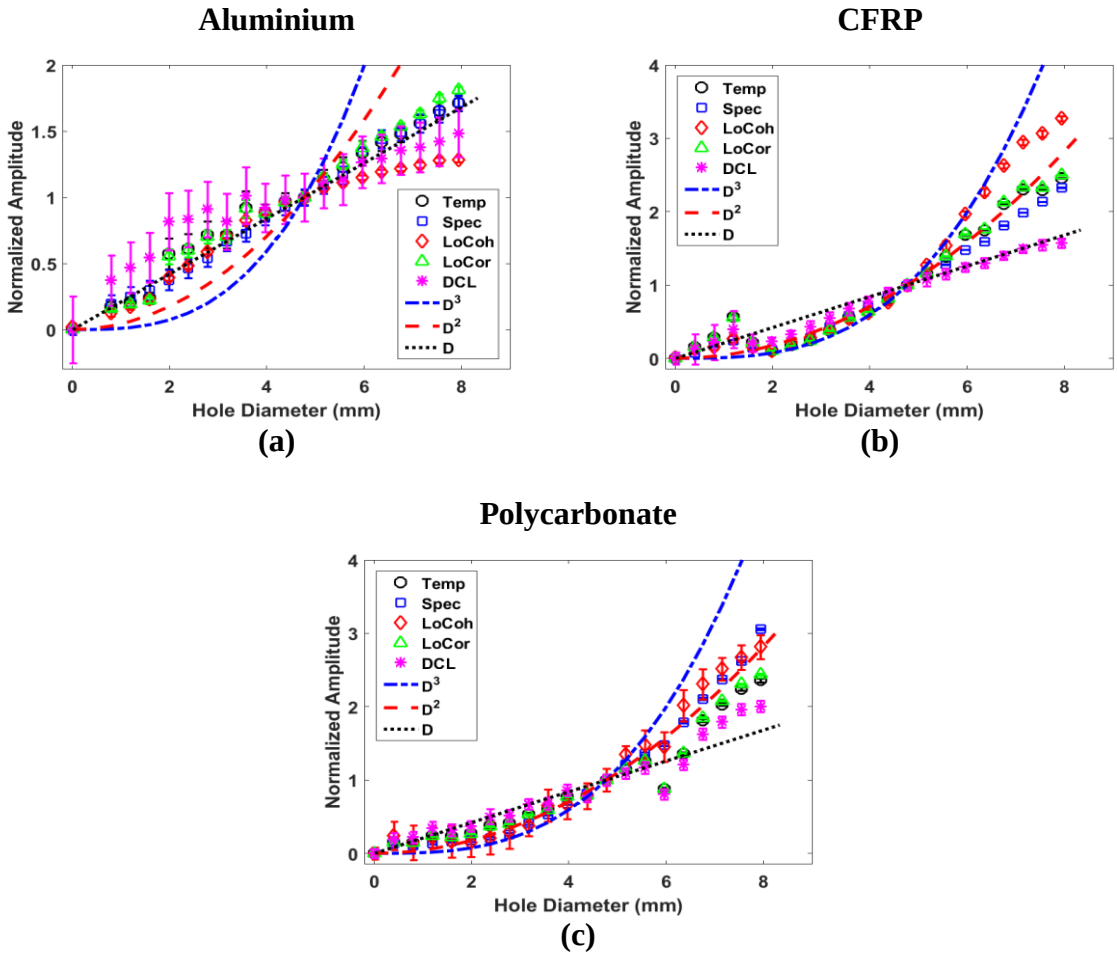

Figure 6-11. Normalized differential signal features for (a) aluminum, (b) CFRP, and (c) polycarbonate with normalized fitting curves (powers of hole diameter). Amplitudes are normalized so that the amplitude corresponding to the 4.76 mm hole is unity The signals are transmitted and received with a pair of 12.5mm longitudinal transducers (2.25 MHz for aluminum and 1 MHz for CFRP and polycarbonate) excited with a spike pulse.

that the value of $\overline{R}^2$ is dependent on the choice of data point used for normalization and can vary up to 10%. The good fits of the basis function indicate the behavior of the non-normalized differential features may be describable with the appropriate material dependent coefficients.

When multiple features correspond to the same basis function, the features are measuring the same physical phenomenon. When a feature changes basis functions between materials, the phenomenon is different. Both aluminum and polycarbonate are isotropic materials but have differential features with linear and quadric basis functions respectively. Therefore, the cause of

the different basis functions must be due to difference in scattering between the materials. The aluminum has stochastic boundary scattering and internal grain scattering while polycarbonate has stochastic boundary scattering. CFRP is more complex than either aluminum of polycarbonate, both in terms of elastic properties/scattering and differential features. CFRP supports three distinct basis functions. This more complicated behavior is due to the many wave velocities that exist in CFRP in addition to the scattering from boundaries, fibers, and plies. Residual temporal energy, residual spectral energy, and loss of correlation are described by the quadratic basis function in both CFRP and polycarbonate, but are described by the linear basis function in aluminum. This indicates that these features are measuring a physical phenomenon that exists in polymers, but not in metals. It is clear that the underlying causes of the differences in the differential feature behavior are convoluted and will be difficult to determine without good models.

The behavior of the five differential features was noted elsewhere as being generally quadratic in nature with respect to hole diameter. It was also noted that several damage regions exist that seem to correspond to changing scattering regimes: the low damage region corresponds to Rayleigh scattering, has higher slope, and appears linear; the intermediate region corresponds to intermediate scattering, has medium slope, and appears quadratic; the large damage volume region corresponds to specular scattering, has low slope, and is characterized by deviating from the previous basis functions.

Figure 6-12 shows the five differential features for each of the three specimens and CFRP and polycarbonate materials. The feature amplitude is normalized such that the feature amplitude corresponding to the 4.4 mm hole (a & b) or the fourth 0.397 mm hole (c) is unity. The abscissa is normalized to relative defect volume to allow for comparison between the three damage types. Distinct damage regions are apparent for specimens #1 & #2. Similar feature behavior is observed

between the half/full hole (specimen #2) CFRP and polycarbonate samples where loss of coherence follows cubic behavior, spectral residual energy follows quadratic behavior, and the other three features follow linear behavior. These basis functions deviate from those observed for specimen #1, though the deviation is less significant for polycarbonate. The deviation is caused in part by the sharp corners of the half holes that increase the amount of scattering. For specimen #3, temporal residual energy, loss of coherence, and loss of correlation tend towards quadratic behavior while spectral temporal energy and differential curve length tend towards linear behavior.

Table 6-4. Adjusted Coefficient of determination ($\bar{R}^2$) between differential features and fit lines.

		D^3	D^2	D
Residual Temporal Energy	Al M	0.00	0.70	**0.89**
	Al	0.00	0.28	**0.97**
	CFRP	0.22	**0.96**	0.75
	Poly	0.00	**0.89**	0.83
Residual Spectral Energy	Al M	0.28	**0.90**	0.81
	Al	0.00	0.39	**0.99**
	CFRP	0.00	**0.95**	0.84
	Poly	0.61	**0.99**	0.70
Loss of Coherence	Al M	0.00	0.70	**0.89**
	Al	0.00	0.00	**0.88**
	CFRP	0.88	**0.91**	0.56
	Poly	0.61	**0.97**	0.68
Loss of Correlation	Al	0.00	0.47	**0.96**
	CFRP	0.28	**0.96**	0.74
	Poly	0.00	**0.91**	0.81
Differential Curve Length	Al	0.00	0.00	**0.74**
	CFRP	0.00	0.23	**0.97**
	Poly	0.00	0.77	**0.87**

Al M = Data on aluminum from Michaels & Michaels 2005

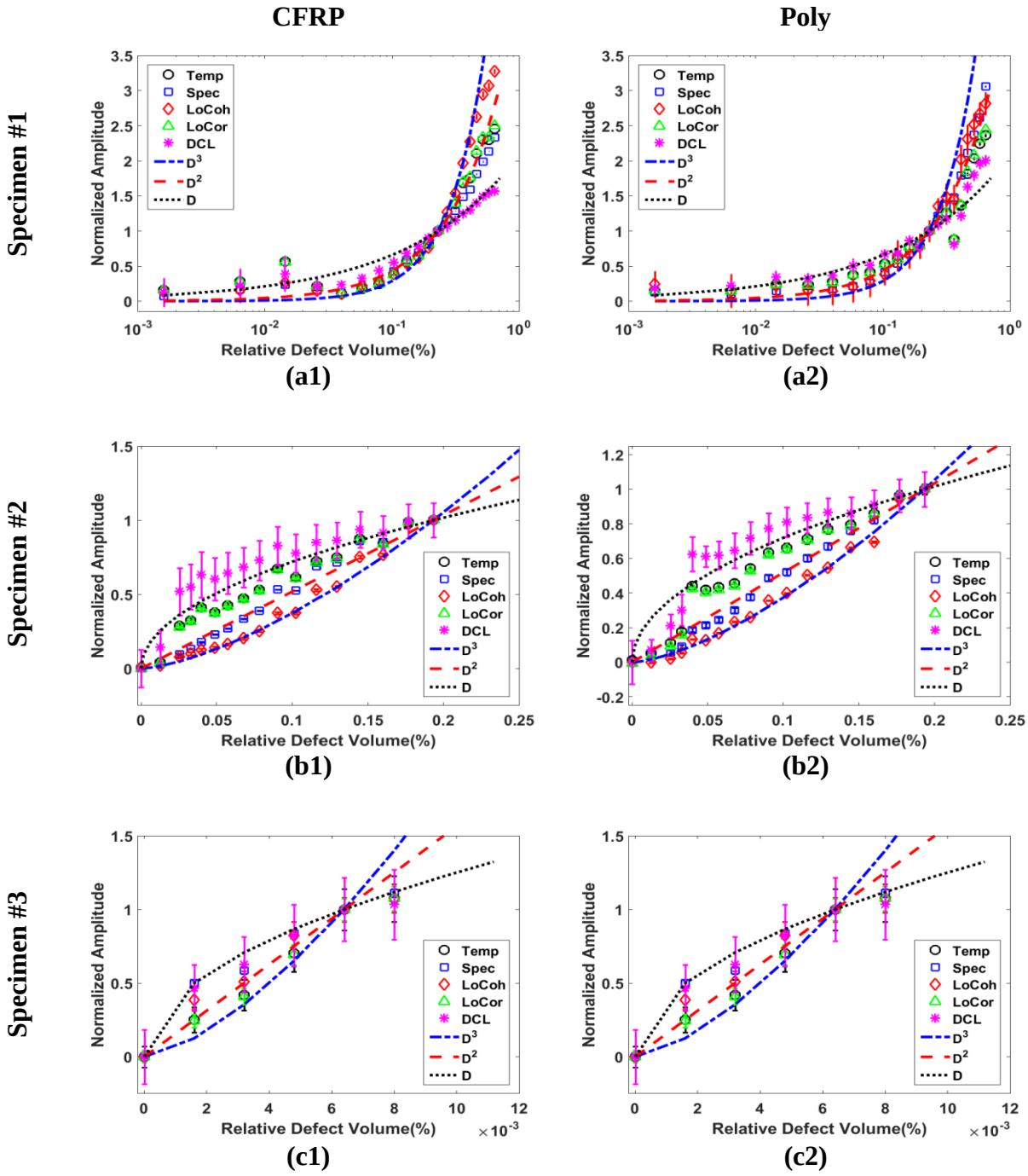

Figure 6-12. Normalized Differential Signal Features with normalized fitting curves (powers of hole diameter) for (a) specimen #1, (b) specimen #2, and (c) specimen #3 with materials (1) CFRP and (2) polycarbonate. Amplitudes were normalized so that the amplitude corresponding to (a & b) the 4.4 mm or (c) the fourth 0.397 mm hole is unity. The abscissa was normalized to the defect volume over the plate volume. The signals were transmitted and received with a pair of 12.5mm 1MHz longitudinal transducers excited with a spike pulse.

Table 6-5. Adjusted coefficient of determination ($\bar{R}^2$) between normalized differential features and fit lines.

	Specimen	Material	hD^3	hD^2	hD
Residual Temporal Energy	1	Al	0.00	0.28	**0.97**
		CFRP	0.22	**0.96**	0.75
		Poly	0.00	**0.89**	0.83
	2	CFRP	0.37	0.82	**0.91**
		Poly	0.51	**0.87**	0.85
	3	CFRP	0.38	0.68	**0.79**
		Poly	**0.86**	0.84	0.48
Residual Spectral Energy	1	Al	0.00	0.39	**0.99**
		CFRP	0.00	**0.95**	0.84
		Poly	0.61	**0.99**	0.70
	2	CFRP	0.84	**0.98**	0.65
		Poly	0.91	**0.98**	0.52
	3	CFRP	0.92	**0.99**	0.65
		Poly	**0.95**	0.89	0.44
Loss of Coherence	1	Al	0.00	0.70	**0.89**
		CFRP	0.00	0.00	**0.88**
		Poly	0.88	**0.91**	0.56
	2	CFRP	**0.98**	0.90	0.20
		Poly	**0.99**	0.88	0.11
	3	CFRP	0.78	**0.94**	0.79
		Poly	**0.87**	0.81	0.42
Loss of Correlation	1	Al	0.00	0.47	**0.96**
		CFRP	0.28	**0.96**	0.74
		Poly	0.00	**0.91**	0.81
	2	CFRP	0.40	0.83	**0.90**
		Poly	0.52	**0.88**	0.84
	3	CFRP	0.38	0.68	**0.79**
		Poly	**0.86**	0.83	0.47
Differential Curve Length	1	Al	0.00	0.00	**0.74**
		CFRP	0.00	0.23	**0.97**
		Poly	0.00	0.77	**0.87**
	2	CFRP	0.00	0.00	**0.87**
		Poly	0.00	0.37	**0.91**
	3	CFRP	0.11	0.53	**0.82**
		Poly	0.86	**0.91**	0.62

6.4.4 Damage Regions

When examining the behavior of the differential features, three damage regions quickly become apparent. The feature amplitude for the first three holes has a significantly higher slope and higher amplitude than the subsequent holes. This indicates that a change in the underlying physics of the problem occurs in the transition between 1.19 and 1.98 mm. This transition in hole diameter also corresponds to the transition in scattering regimes (Figure 6-13), Rayleigh to intermediate, for the high frequency energy contained in the coda wave signals. The third damage region (the first being the small holes and the second being the intermediate holes) is evidenced by the deviation of the data points from the basis function fit lines (dashed lines) starting around 5.95 mm (Figure 6-11). The transition between intermediate and specular scattering for the high frequency energy and the transition between Rayleigh and intermediate scattering for mid frequency energy occurs starting around 5.95 mm.

The feature amplitudes for the first few holes of the CFRP specimen #1 (Figure 6-13a) exhibit a significantly higher slope and higher amplitude than the subsequent holes. This is an indication that the differential features are more sensitive to small scale damage. These first few holes in specimen #1 are within the Rayleigh scattering regime; the holes in the CFRP specimen #3 are also within the Rayleigh scattering regime (Figure 6-13b). If the features are indeed more sensitive to small scale damage and are scattering dependent, then the feature amplitudes should increase linearly with increasing number of holes but not with increasing diameter. A comparison of the first few holes from specimen #1 and the holes from specimen #3 is provided in Figure 6-13c. The feature amplitudes do increase linearly for specimen #3 (multiple holes) and with a larger slope than amplitudes for specimen #1 (single hole) which do not increase linearly. Note that the feature amplitudes for the first hole in both samples, which is nominally identical, agree

to within 1 measurement error. This unequivocally demonstrates that the differential features are more sensitive to small scale damage and are affected by the scattering regime of the damage. This also demonstrates that the number of damage sites can be distinguished from damage volume.

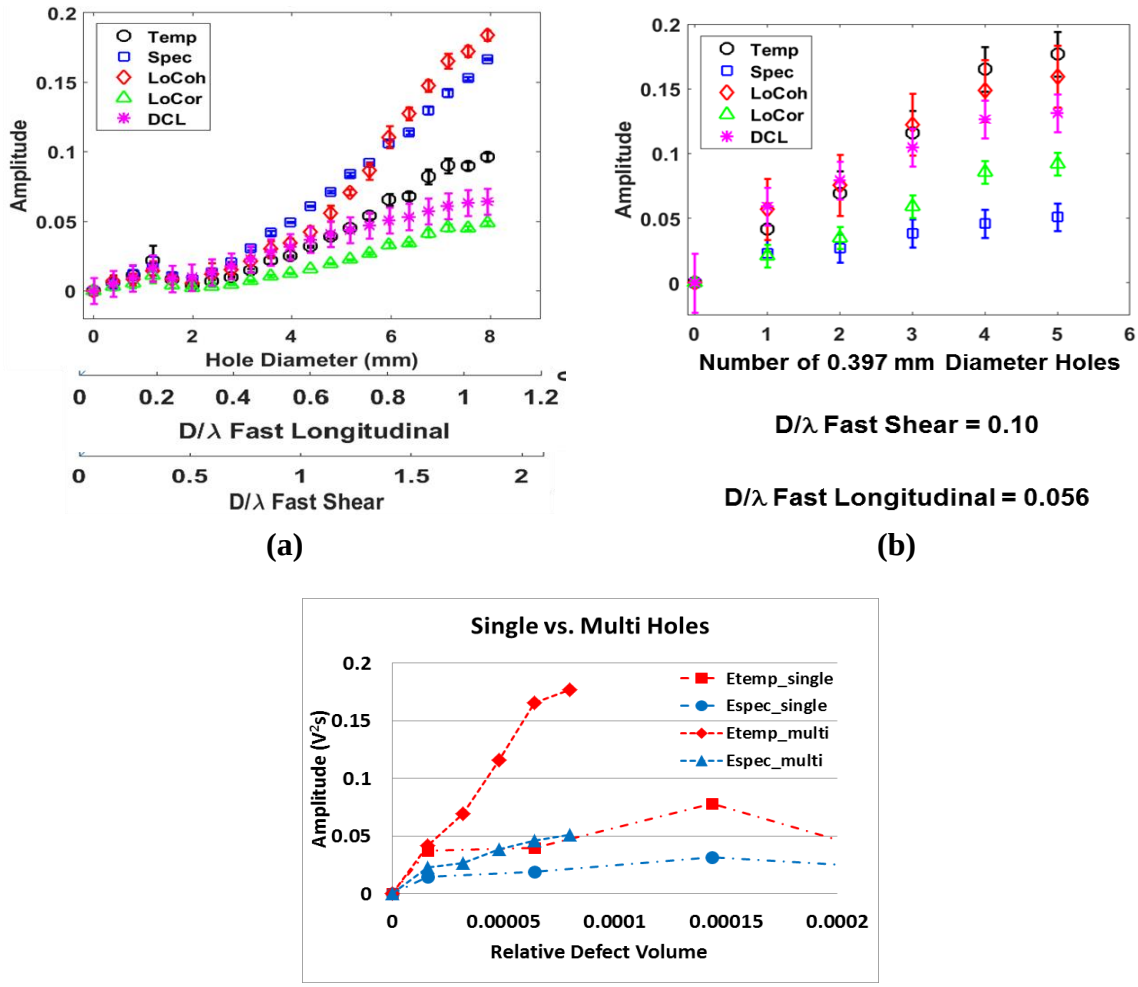

Figure 6-13. Comparison of the detection of drilled through-holes in a) sample 1 and b) sample 2. A comparison of the single and multiple holes is presented in c). Three abscissa are shown in a) and b) which correspond to the hole diameter/number and the ratio of the hole diameter to the wavelength (1 MHz) for fast shear and fast longitudinal waves.

A distinct change can also be observed in the amplitudes and basis functions of the differential features for relative defect volumes less than 0.03% (1.59 mm hole) in aluminum and 0.02% (1.19 mm hole) in CFRP and polycarbonate. This can also be observed in Figure 6-12. The slope of the features in the low damage volume region tends to be significantly larger than the subsequent slope, which gives a higher sensitivity to smaller defects.

Figure 6-14 shows the five differential features for the single through-hole (specimen #1) aluminum, CFRP, polycarbonate samples. In these plots, the feature amplitudes have been normalized such that the amplitude corresponding to the 1.59 mm (aluminum) or 1.19 mm (CFRP and polycarbonate) hole is unity. There is a distinct difference between the feature behavior in the two defect volume regions. Whereas the features generally exhibit quadratic behavior with respect to hole diameter, the features exhibit linear behavior in the low damage volume region. The difference in feature behavior corresponds to the transition from Rayleigh to intermediate scattering for the higher frequency energy of the coda signal (Figure 6-4, Figure 6-9). The increased sensitivity to small damage volumes presented here and confirmed by multiple drilled through-holes (specimen #3) indicates the potential for coda wave NDE to detect and possibly characterize micro-cracks in CFRP materials.

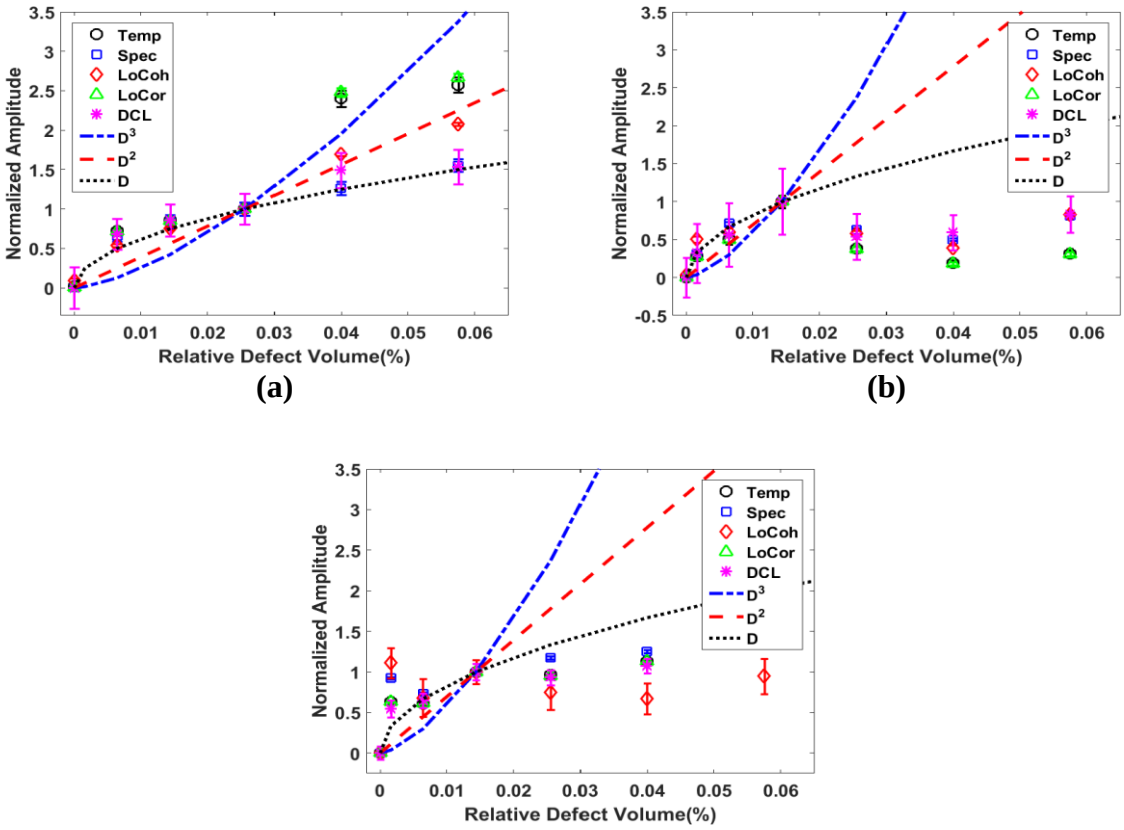

Figure 6-14. Normalized Differential Signal Features with normalized fitting curves (powers of hole diameter) illustrating the damage region for small diameter holes for specimen #1 with materials (a) aluminum, (b) CFRP, and (c) polycarbonate. Amplitudes were normalized so that the amplitude corresponding to (a) the 1.59 mm or (b & c) the 1.19 mm hole is unity. The abscissa was normalized to the defect volume over the plate volume. The signals were transmitted and received with a pair of 12.5mm 1MHz longitudinal transducers excited with a spike pulse.

6.4.5 Residual Energy Fit Equations

Dimensional analysis of the residual energy differential features yields an equation that is dependent on the damage volume (d^2h), the impedance of the system (Ω), and material properties (ρc^2). The quadratic dependence of the residual energy features on the hole diameter was demonstrated previously, while the dependence on hole depth is demonstrated above. Even though the effect of the system electrical impedance on the differential features has been shown experimentally, it is not considered in the fit equations presented here.

Figure 6-15 shows the experimental data, fit equations (black line), and the 95% confidence bounds (gray lines) [Bluman 2004] for the residual energy features for a single drilled through-hole of increasing diameter (specimen #1) for both CFRP and polycarbonate materials. Error bars for the data are approximately the same size as the data points and are not shown. The data is well fit with adjusted coefficient of determination, $\overline{R}^2$, greater than 0.95 (Table 6-6). The best fits were achieved by using the longitudinal velocity for the temporal energy and the shear velocity for the spectral energy as follows:

$$E_{res-temp} = \xi_1 \frac{\pi}{4} \nu \rho c_l^2 D^2 h \tag{6.1}$$

$$E_{res-spec} = \xi_2 \frac{2\pi}{4} \nu^2 \rho c_s^2 D^2 h \tag{6.2}$$

where ν is Poisson's ratio and ξ_1, ξ_2 are material dependent constant coefficients. For Figure 6-15, ξ_1 takes the values 1.6E-5 and 1.6 E -6 for CFRP and polycarbonate respectively while beta takes the values 1 E -4 and 4 E -4 respectively. It is important to note that CFRP is non-isotropic and that many wave velocities exist which depend on the direction of propagation. The maximum longitudinal velocity and corresponding ν were used for the temporal energy while the minimum shear velocity and corresponding ν were used for the spectral energy.

Residual spectral energy in polycarbonate provides the best performance in terms of defect sizing, with ± 0.5 mm accuracy, while providing the worst performance for CFRP, with ± 1 mm accuracy for larger holes. The quality of fit and defect sizing performance can be drastically improved if the data points for the first several drilled holes in CFRP and the outlier at 6 mm for polycarbonate are discounted. Over the diameter range of 2-6 mm, a sizing accuracy of ± 0.1 mm is achievable (Figure 6-15b). The experimental data, fit equations (black line), and the 95% confidence bounds (gray lines) for the residual energy features for multiple drilled through-

holes(specimen #3) for both CFRP and polycarbonate materials is shown in Figure 6-16. Again, equations (6.1) & (6.2) were used to fit the data where ξ_1 takes the values 1.6E-4 and 7.5E-5 for CFRP and polycarbonate respectively while ξ_2 takes the values 1.5E-4 and 2E-4 respectively. The best sizing performance is observed in polycarbonate with an accuracy of ± 0.75 holes while the best achievable in CFRP is ± 1 hole.

As discussed in the previous section, three different regions of differential feature behavior are observable in the data sets. Furthermore, these regions correspond to different scattering regimes, and each scattering regime is governed by different physical relations. It is difficult to derive equations that accurately describe the behavior of a quantity in all three scattering regimes. The equations derived here are optimized for the central data region since that is the largest data set. Even though the residual energy equations are derived specifically for the central data region, which corresponds to intermediate scattering, they can still accurately describe the Rayleigh scattering regime as demonstrated by Figure 6-16.

These results are significant because they indicate that fairly accurate defect sizing can be performed in a material as complex as CFRP with an in-situ volumetric scan. More accurate detection and defect sizing can be achieved with immersion UT, but that is a point-by-point scan that requires significant time. Guided waves are semi-volumetric but can still require significant time, are not as sensitive to small scale damage, and require multiple interrogations. With these considerations, it is clear that coda wave NDE has the potential to perform better than other ultrasonic methods with a single interrogation of a volume.

Table 6-6. Adjusted coefficient of determination ($\bar{R}^2$) between residual energies and fit equations.

Specimen	CFRP		Polycarbonate	
	Etemp	Espec	Etemp	Espec
1	0.96	0.94	0.95	0.98
2	0.95	0.94	0.98	0.97

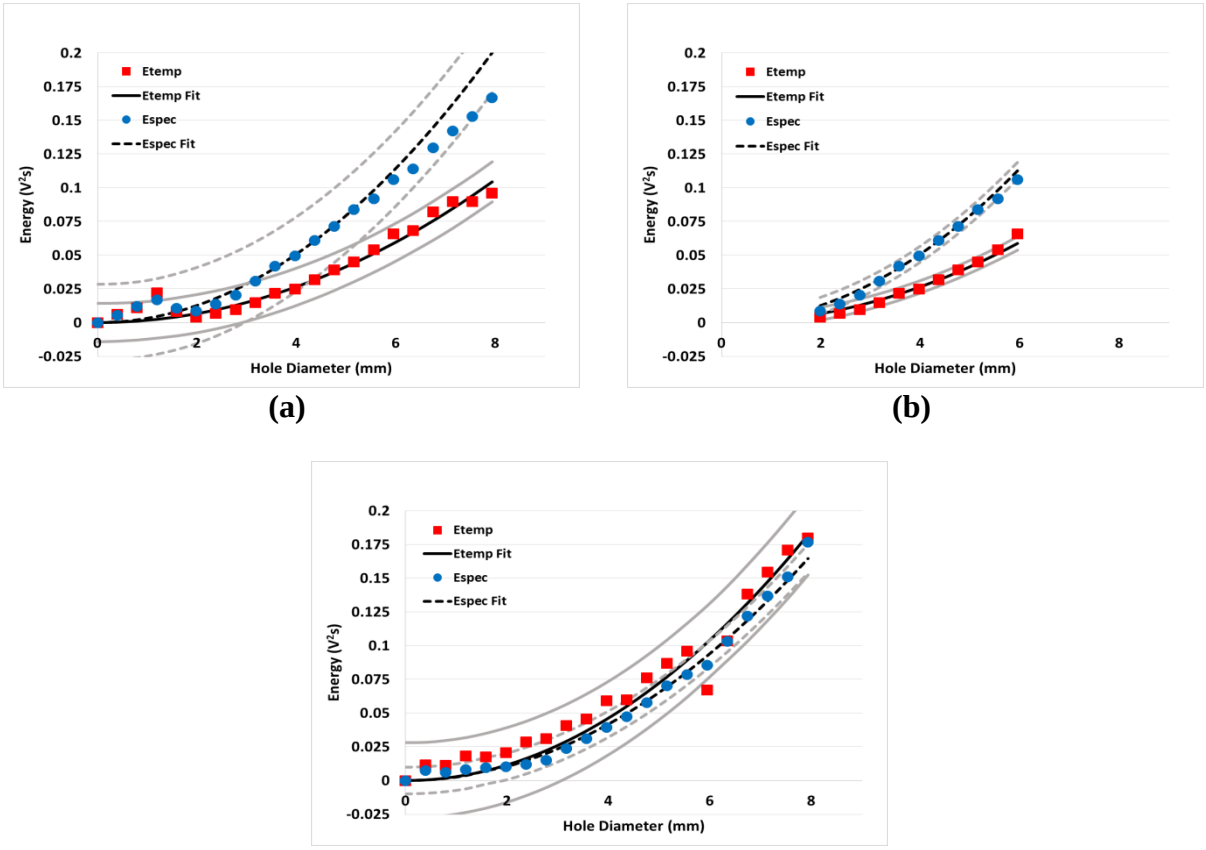

Figure 6-15. Fit equations (black lines) and 95% confidence bounds (gray lines) for non-normalized residual energy data for specimen #1 with (a & b) CFRP and (c) polycarbonate. Improved confidence bounds for 2-6 mm diameter range. The signals are transmitted and received with a pair of 12.5 mm 1MHz longitudinal transducers excited with a spike pulse.

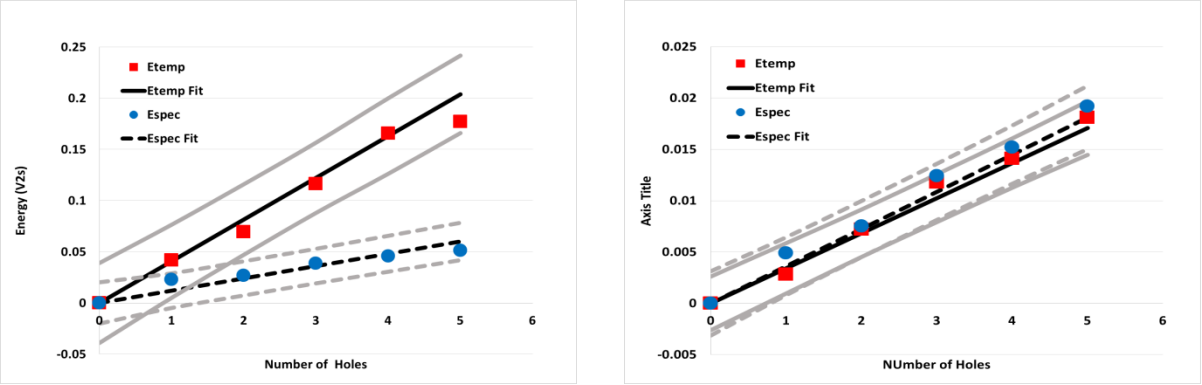

(a) **(b)**

Figure 6-16. Fit equations for non-normalized residual energy data for specimen #3 with (a) CFRP and (b) polycarbonate. The signals are transmitted and received with a pair of 12.5 mm 1MHz longitudinal transducers excited with a spike pulse.

6.4.6 Defect Sizing

In order to test the sizing accuracy of the derived residual energy feature equations (eq. 6.1 & 6.2) in a simulated "field inspection," coda wave signals were collected from a secondary (nominally identical) quasi-isotropic CFRP sample identical experimental configurations and hole locations as described by (Specimen #2) and Figure 4-2a respectively. The measured residual energy feature amplitudes for several drilled through-holes are listed in Table 6-7 along with the estimated hole diameters and the nominal drill bit sizes. The difference between the nominal hole diameters and the estimated diameters is within 0.5 mm for all cases, and is generally quite a bit closer with one case correctly estimating the diameter to within a few thousandths of a millimeter. This sizing accuracy is quite remarkable considering that coda waves are a volumetric interrogation method and that these holes represent a relative volume (hole volume over plate volume) of a few thousandths of a percent.

Error in estimating the size of the drilled holes is attributable, at least in part, to the spindle run-out (bit wobble), which will cause enlarged holes. The spindle run-out was determined to be

Table 6-7. Estimation of hole diameter for drilled through-holes in quasi-isotropic CFRP based on equations (5.18) and (5.19)

Measured Values		Estimated Size		Actual Drill Bit Size	Error (%)	
Etemp (V^2s)	Espec (V^2s)	Etemp (mm) ±0.75	Espec (mm) ±0.5	(mm) $\pm 2.5E^{-3}$	Etemp	Espec
0.0087	0.0125	2.30	1.98	1.984	15.9	0.2
0.0116	0.0272	2.60	2.93	2.756	5.7	6.3
0.0202	0.0426	3.50	3.66	3.160	10.8	15.8
0.0289	0.0712	4.20	4.20	4.335	3.1	3.1

within 0.075 mm for all cases. This yields relative errors of less than a few percent. Other unquantifiable factors that may affect the sizing accuracy are fiber tear-out, delaminations, and back surface splintering. Care was taken while drilling to minimize these, and none of these were observed during visual inspection of the hole.

This simple example demonstrates the reproducibility of the differential features, the capability to quantify damage, and the capability to size defects based on differential feature amplitude. As noted previously, equations 6.1 and 6.2 do not accurately describe the feature amplitudes for all of the data points (small and large scale damage). Small scale damage size can still be estimated if the equations' coefficients are modified as shown in Figure 6-16.

6.5 Effect of System Parameters

6.5.1 Feature linearity

Coda waveforms were collected using several power levels with identical transducer placement and coupling to check the linearity of the received waveforms and extracted differential

features. Coda wave propagation is inherently non-linear since a coda wave consists of a superposition multiple wave modes and propagation paths, but the ultrasonic system is expected to be linear since the measurements are made within the linear region of each component. The differential features are not expected to change with power level since they are normalized to unity energy.

The system is operating linearly if no new or differing structures appear in the waveform or spectrum with changing power level. A comparison of waveform amplitudes at 100% and 50% input power for the three materials is shown in Figure 6-17. The waveforms are normalized to the maximum amplitude of the 100% power signal for each material. A 50% reduction in the power of the input signal corresponds to an amplitude reduction of ~40% for each sample and a 60-65% reduction of energy, but no new/differing structures are apparent. The correlation coefficient was calculated at zero time lag to confirm the similarity of the waveforms, which yielded correlation values of 0.9965, 0.9995, and 0.9980 for aluminum, CFRP, and polycarbonate respectively. The only difference between the full and half power waveforms is very subtle changes attributed to noise. The nature of these subtle differences was examined further by calculating the five differential features with the 100% power signal as baseline and the 50% power signal as the measured signal. The features' mean values and standard deviations are on par with those listed in Table 6-1, again demonstrating that the only difference between the full and half power signals is the lower signal-to-noise ratio of the half power signal. The correlation coefficients and differential features prove that no new or differing features are present with changing power levels. Therefore, the system is linear.

Figure 6-18 shows plots of residual temporal energy, residual spectral energy, loss of correlation with increasing hole diameter for each of the three samples. The differential features

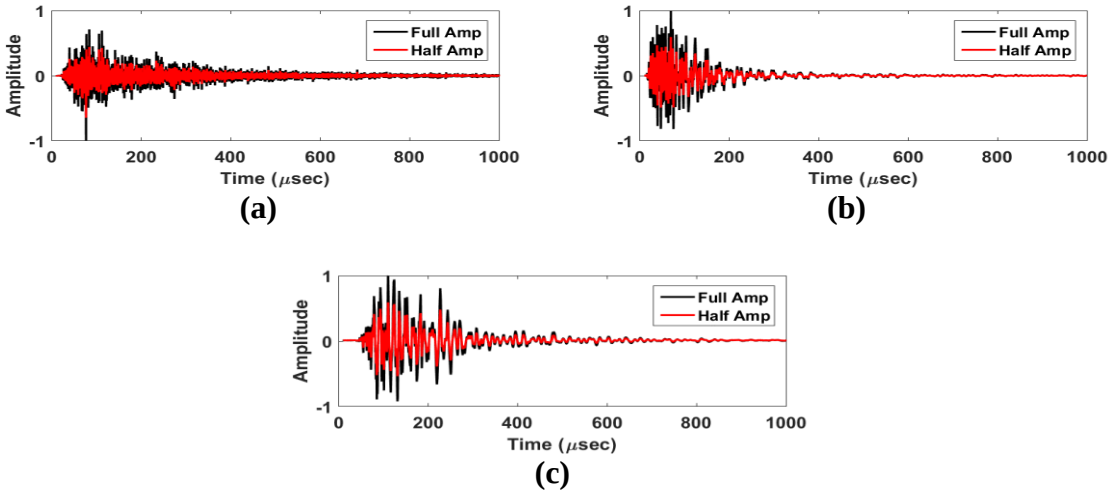

Figure 6-17. Comparison of waveforms from full strength signals and signals with -6dB input collected from (a) aluminum, (b) CFRP, and (c) polycarbonate samples. The received waveforms are normalized to the maximum amplitude of the 100% power waveform for each pair. The signals are transmitted and received with a pair of 12.5mm longitudinal transducers (2.25 MHz for aluminum and 1 MHz for CFRP and polycarbonate) excited with a spike pulse.

were extracted from baseline-measured signal pairs collected at 100% and 50% input power. A comparison of the extracted features shows that decreasing the input power does not affect feature amplitude or defect detection capability. Although some variation in the repeatability of each data point is observed due to the decreased signal/noise ratio, generally the repeatability remains nearly constant with changing power levels. The other two differential features exhibit similar behavior. A quantitative measure of the similarity between the full power and half power data sets is provided by the *RMSE* (Table 6-8). Four of the five differential features are repeatable to within a percent where the exception is the differential curve length.

Thus, the differential features also show the expected behavior. This result is significant because it indicates that differential feature exhibit several desirable characteristics of damage metrics: amplitude and detectability are independent of input power, baseline and measured signals need not have the same amplitude, and repeatability is not significantly affected by power/gain

settings. Signal to noise ratio was not considered for these measurements. The system noise level, however, should remain roughly constant as only the input signal is modified.

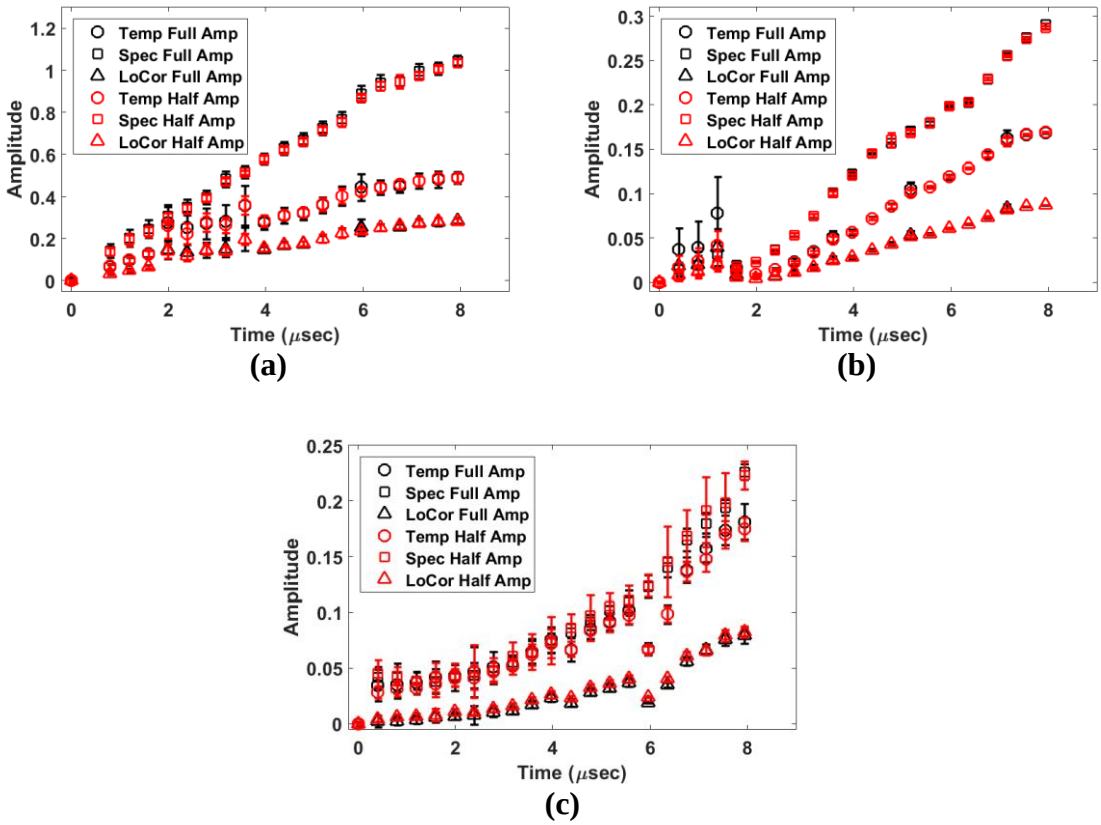

Figure 6-18. Comparison of differential signal features extracted from full strength signals and signals with -6dB input collected from (a) aluminum, (b) CFRP, and (c) polycarbonate samples. The signals are transmitted and received with a pair of 12.5mm longitudinal transducers (2.25 MHz for aluminum and 1 MHz for CFRP and polycarbonate) excited with a spike pulse.

Table 6-8. Comparison of the coda waves differential features of half power signal to the original signal using Percent Relative Mean Squared Error.

Sample	Etemp	Espec	LoCoh	LoCor	DCL
Al	0.10	0.02	0.02	0.11	12.74
CFRP	1.10	0.05	0.98	1.07	8.27
Poly	0.21	0.15	0.23	0.17	2.80

6.5.2 Feature Reproducibility

Regardless of how sensitive to damage or repeatable a technique is, if the results are not repeatable or cannot be recreated, then the technique is not very useful. To test the reproducibility of damage detection with coda wave differential features, signals were collected from two distinct, but nominally identical quasi-isotropic CFRP samples as described by specimen #1. The differential features were then extracted with the results for the temporal and spectral residual energy features shown in Figure 6-19. Reproducibility of the damage detection with the differential features is quite good as most of the data points for the two data set lie within one measurement error of each other. A quantitative comparison of the two data sets for all five features is provided in Table 6-9 using the *RMSE*. The spectral residual energy feature provides the best reproducibility, *RMSE* = 0.89%, while the differential curve length feature again gives the worst performance, *RMSE* = 10.41.

Two previous examples have also been provided which demonstrate the reproducibility of the differential feature amplitude in the presence of damage. Recreating the data published by Michaels & Michaels (2005) (Figure 6-2) involved distinct experimental set-ups and transducers in addition to distinct samples. Estimating the size of drilled through-holes (Table 6-7) involved generating an equation based on measurements from a primary sample then using the equation to determine the hole diameter. Both of these cases confirmed the reproducibility of coda wave differential features. This reproducibility is really quite remarkable given that the coda waves themselves are superposition fields of multiple scattered and reflected waves.

Dissimilarities in the differential features between two distinct applications are caused by variations in several aspects of the measurement system and samples: (1) the transducers themselves, (2) transducer placement, (3) transducer coupling, (4) the experimental system, (5)

sample geometry, and (6) material variations. The transducer placement, transducer coupling, and sample geometry will always vary slightly, and hence are present in each of the three cases presented. Material variability additionally is present for the CFRP cases since composite materials are far less consistent between samples than other materials such as metals. Recreating the data published by Michaels & Michaels (2005) however, is influenced by all six factors since a completely different experimental set-up was used along with different transducers. Even with all of these causes of dissimilarity between the coda waves for different samples, the differential feature behavior in the presence of damage is reproducible, barring results over 6 mm hole diameter in aluminum.

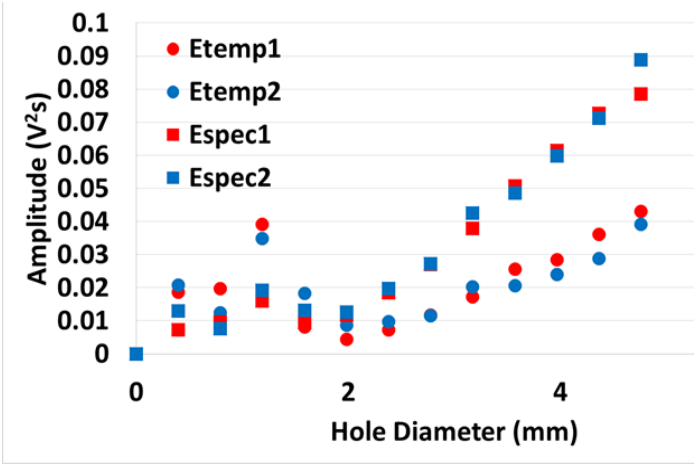

Figure 6-19. Example of the reproducibility of temporal (Etemp) and spectral (Espec) residual energy differential features for a drilled though-hole of increasing diameter in nominally identical plates. Measurement error generally falls within the dot size of the data and hence is not shown.

Table 6-9. Comparison of the coda wave differential features collected from separate (nominally identical) samples using Percent Relative Mean Squared Error.

Etemp	Espec	LoCoh	LoCor	DCL
4.34	0.89	8.37	6.18	10.41

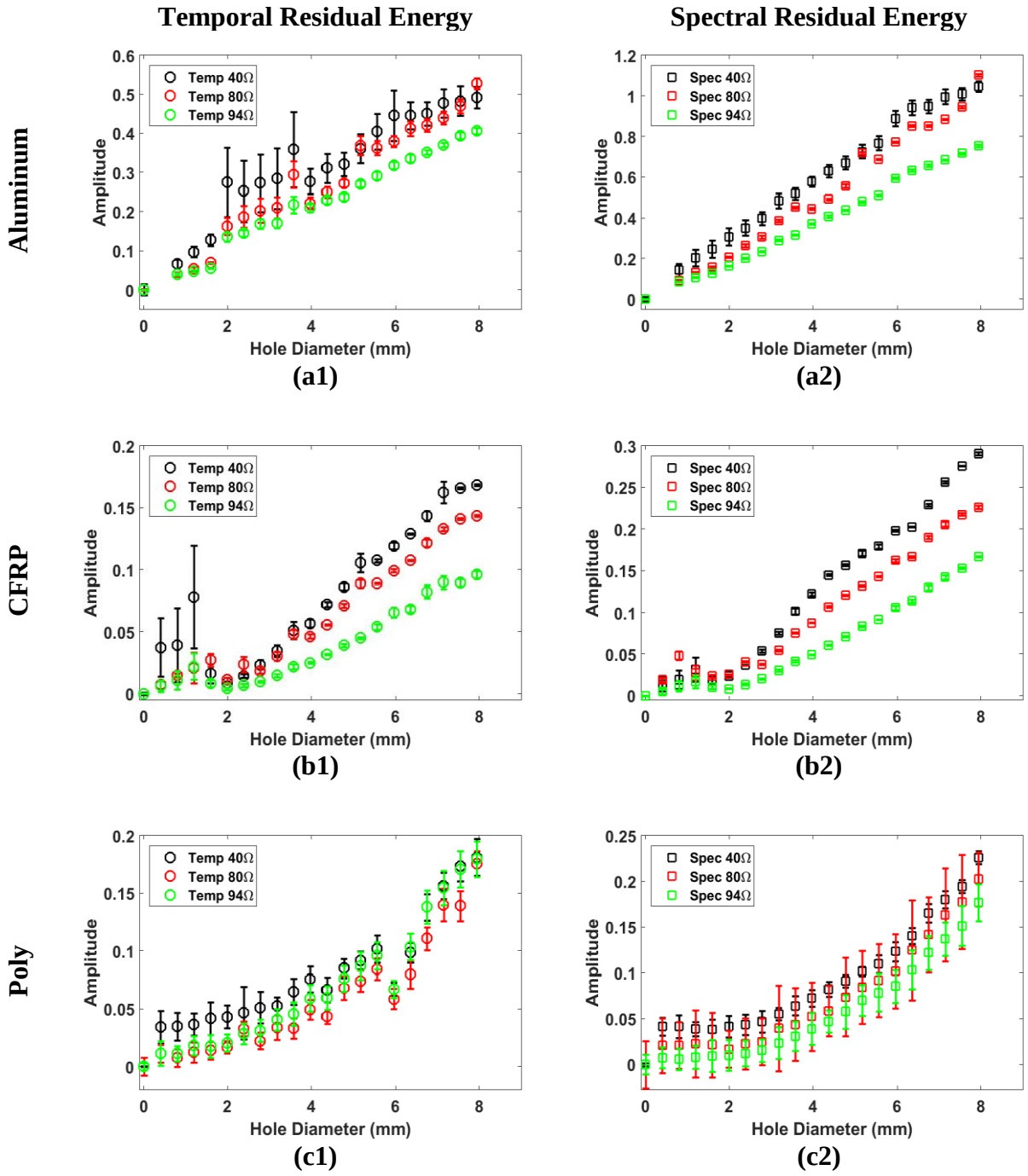

Figure 6-20. Effect of electrical impedance matching on extracted differential signal features (1) residual temporal energy and (2) residual spectral energy for (a) aluminum, (b) CFRP, and (c) polycarbonate samples. The signals are transmitted and received with a pair of 12.5mm longitudinal transducers (2.25 MHz for aluminum and 1 MHz for CFRP and polycarbonate) excited with a spike pulse at three different PR damping settings.

6.5.3 Impedance Matching

The typical effect of impedance matching on extracted differential signal features is shown in Figure 6-20. Only residual temporal and spectral energy are shown, but the other features exhibit similar behavior. Increasing the PR impedance increases the amplitude of the features and consequently the slopes of the curves. Increasing the impedance also increases the scatter of the individual data points and results in ill-behaved curves with increasing numbers of outliers. The apparent effects on the differential features are due to the increased energy present in the received signals at higher impedance settings. Even though the features are normalized to unity energy in both the time and frequency domains, significantly new content is introduced with increased PR impedance, which resulted in increased residual energy.

6.6 Conclusions

Diffuse field differential features were considered for quantitative defect detection and sizing in CFRP materials. Physical models predicted from dimensional analysis of the residual temporal and residual spectral energies have been fit to the experimental data with good agreement. Using 95% confidence bounds, the accuracy of defect sizing for a single drilled through-hole is estimated to be within ± 1 mm for both materials, but can be improved to ± 0.1 mm over a limited range. For multiple drilled through-holes, the defect sizing accuracy is estimated to be within ± 1 hole. Thus diffuse field NDE offers a good detection and fairly accurate sizing method in a single volume scan that takes less than a second, stores little data, and is easy to process.

Signal features increase monotonically with increasing hole diameter for all three materials with few exceptions and can be used for defect sizing. A single 0.397 mm hole is detectable and a 0.397 mm increase in hole diameter is resolvable. Repeated measurements increased the resolution

of the differential features for polycarbonate specifically and differential curve length generally. Spectral residual energy was found to be most sensitive to defects and differential curve length the least. It was shown that the differential features increase monotonically with increasing number of drilled through-holes and that the number of 0.397 mm (1/64”) holes is resolvable. The features were also shown to be sensitive to the depth of the hole with half- and through-holes were resolvable in the majority of cases for both CFRP and polycarbonate materials. The quadratic dependence of the differential features on the hole effective hole diameter was confirmed for the majority of cases.

Normalizing the differential features and fitting basis functions to the experimental data demonstrated that the features express the same information for the aluminum and polycarbonate samples, but that different information is obtained for the CFRP sample. The basis functions are approximated by a linear function of hole diameter for aluminum, polycarbonate features are approximated by a quadratic function of hole diameter, and CFRP features can be approximated by linear, quadratic, or cubic functions depending on the feature. Feature trend lines deviate for large holes in all cases due to increasing dissimilarity of the baseline and measured signals. The normalized CFPR and polycarbonate features are highly correlated, due in part to the trend line deviation, indicating similar scattering behavior. Several scattering regimes were encountered as the hole diameter increased which affected the amplitude of the features, most notably the transition from Rayleigh to intermediate scattering in CFRP.

Distinct damage regions were observed which are attributed to changes in the scattering regime for higher frequency content of the diffuse field. Relative damage volume levels below 0.025% tend towards linear behavior with higher sensitivity while levels above 0.025% tend towards quadratic behavior with lower sensitivity. Multiple drilled through-holes confirm the

increased sensitivity for low damage volumes. This is a good indication that diffuse field differential features could detect micro-cracks and monitor fatigue damage in CFRP materials.

Even though the formation of coda waves is inherently non-linear, coda waves behave linearly and the extracted differential features remain constant for changing power levels. Additionally, coda wave differential features were shown to be repeatable, reproducible, and reciprocal. All of which are necessary for an ultrasonic NDE technique. Electrical impedance matching drastically affects the energy contained in the coda wave and modifies the structure of the waveform. Increasing the PR impedance decreases feature slopes, the occurrence of data outliers, and feature repeatability error. The differential curve length feature exhibits the worst performance in all areas, especially in its sensitivity to signal noise. Continued use is not recommended. The two residual energy features, on the other hand, perform quite well in damage sensitivity, repeatability, and reproducibility and are mostly insensitive to signal noise.

The sensitivity of diffuse fields makes the very attractive for SHM and the quantitative damage detection demonstrated in this work shows the potential of this method for damage diagnosis. It is quite probable that diffuse field differential features can detect micro-cracks and monitor fatigue damage. Further quantitative work is needed to examine feature behavior for other damage types and locations in addition to detecting damage in semi-infinite plates. The aim of future research is to extend detection to cracks and micro-cracks, and to determine the minimum necessary array size for large part inspection. The current drawbacks of diffuse field (coda wave) NDE preventing wider adoption are the difficulty in interpreting waveform changes and correlating them to specific damage and the lack of quantitative studies. Questions of sensitivity to different defects/damage, whether damage can be detected without a baseline, and effectiveness for arbitrary geometries still exist. Further research should consider these issues.

CHAPTER 7. EFFECT OF EXTERNAL INFLUENCES

The chapter presents work on the characterization and mitigation of external influences (e.g. environmental factors) on coda wave analyses and detectability of drilled holes. Section 7.1 provides a brief introduction into previous work. The influence and mitigation of signal noise is examined in Section 7.2. Next, Section 7.3, Examines the influence and mitigation of temperature on coda wave relative velocity and differential features. Section 7.4 then briefly examines the influence of different types of plate boundaries on the formation of coda waves. Finally, the results and conclusions of this chapter are summarized in Section 7.5.

7.1 Introduction

The high sensitivity of CWI to minute changes in the propagation medium not only allows for the detection of small stresses and nonlinearities, but also provides sensitivity to environmental changes such as a change in temperature between recording the baseline and secondary signals. Often, the changes of the differential signal feature caused by environmental changes or other aspects such as signal noise can be as large as or larger than the changes caused by stresses or damage. It is therefore important to understand how various benign changes can affect the differential parameters. The effect of temperature changes on the calculated coda wave relative velocity (relative time delay) is well known [Roberts et al. 1992, Snieder 2002, Lu & Michaels 2005, Planes & Larose 2013, Zhang et al. 2013b] for effectively isotropic materials. It has not, however, been studied for other material models. There is also little to no work on the effects of signal noise and plate boundary conditions on differential features.

7.2 Signal-to-Noise Ratio

Signal-to-noise ratio (*SNR*) is a concern for ultrasonic measurement systems because a high noise level can obscure the signal of interest and reduce measurement capabilities. Previous work has demonstrated that the coda wave relative velocity can still be extracted with good accuracy from signals with a *SNR* equal to 1 (0 dB) collected from a sample of Agar-Agar gel [Hadziioannou et al. 2009]. Here the influence of the *SNR* on the differential features and damage detection is examined for a quasi-isotropic CFRP sample (specimen #1). Noise waveforms consisting of random white Gaussian noise are convolved with a typical coda wave signal to produce a noise contaminated signal as shown in Figure 7-1. The noise signals are generated with amplitudes corresponding to 50, 40, 30, 20, 10, and 6 dB *SNR* and converted to 12-bit signals with the same bin sizes as the original signal. Note that the original signal has a *SNR* of approximately 60 dB and the 12-bit ADC has a *SNR* of 66dB (Section 4.4.2).

As a quick reminder of how the damage index (*DI*) and measurement error are determined, two things are important: (1) the *DI* and the measurements error are based on the mean and standard deviation of the differential feature amplitude distribution respectively and (2) both the baseline offset and the standard deviation of the distributions are expected to increase inversely with *SNR* since the signals become increasingly dissimilar. Figure 7-2 shows the effect of decreasing *SNR* on the baseline and 2.381 mm diameter drilled through-hole measurement distributions for the temporal residual energy feature. The mean values of the baseline distributions increase exponentially with decreasing *SNR* which indicates an increasing dissimilarity between repeated signals. This can only be attributed to the random noise. The mean values of the damage distributions also increase with decreasing *SNR* such that the separation between the mean values of the baseline and 2.381 mm distribution only decreases by approximately 10% when the *SNR* is

changed from 60 to 10 dB. This indicates the resolvability of damage decreases with *SNR* as expected and that noise obscures damage detection. Additional scatter in the differential feature amplitudes due to decreasing *SNR* is also observed in the standard deviations of both the baseline and damage distributions. Thus the measurement error also increases inversely with *SNR*. This confirms that both the standard deviation and baseline offsets are measures of noise, and since the mean of the damage distributions increase proportionally to the increasing mean of the baseline, it is likely that the baseline offset can be used as a "noise calibration" of sorts.

Amplitudes of the temporal residual energy and loss of coherence features are shown in Figure 7-3 over a range of drilled through-hole diameters for several *SNR*'s. The true amplitudes (Figure 7-3(1)) exhibit the shifts in the mean baseline values (the horizontal lines) and the reduction in the resolvability of different damage increments. If the baseline offset is indeed a "noise calibration" of sorts, then the various *SNR* data sets should overlap by subtracting the baselines from the measurements. The adjusted (measurement – baseline) feature amplitudes are shown in Figure 7-3(2). Although the temporal residual energy and loss of coherence features are not the best and worst performing features, they do exhibit some interesting behavior and demonstrate that the differential features have drastically different sensitivities to *SNR*. The good alignment of the temporal residual energy feature amplitudes proves that the baseline offset is a noise calibration and can be removed from measurements. The reduction in feature amplitude for the 10 and 6 dB *SNR* cases demonstrates the decreased sensitivity to damage due to the decreased separation of the damage and baseline distributions. The amplitude reduction is quite drastic for the loss of coherence feature, which indicates that this particular feature is very sensitive to *SNR*

A quantitative measure of the effect of *SNR* on the true and adjusted feature amplitudes is provided in Table 7-1 using the percent relative mean squared error (*RMSE*). All five differential

features are affected by *SNR* with the differential curve length being affected the most and the spectral residual energy being affected the least. The spectral residual energy is so insensitive to *SNR* that a significant change in feature amplitude is not observed until the *SNR* reaches 6 dB. Adjusting the measured amplitudes to the baseline amplitudes greatly reduces the observed error for all cases with a reduction of nearly 100% in the most extreme cases.

The *RMSE* values for the adjusted measurements indicate the dependence of the differential features' performance on *SNR*. Differential curve length is once again the worst performing feature and quickly loses all sensitivity to damage with the slightest increase in random noise. Loss of coherence is the second worst performer, but maintains some sensitivity until the *SNR* equals 20 dB, then quickly losses all sensitivity. This is also shown in Figure 7-3(b2). The remaining three features, temporal residual energy, spectral residual energy, and loss of correlation, maintain their sensitivity with significant deviations starting for a *SNR* of 6 dB, and the residual spectral energy is the best performer by far as the data only deviates by one percent at a *SNR* of 6 dB. This insensitivity to damage is quite remarkable, especially considering the small scale of the damage detected (0.397 mm diameter) and the small scale of the damage increment (0.397 mm diameter increase). This insensitivity also unequivocally demonstrates that coda waves NDE can operate in noisy environments and has the potential to be used over long distances where the signal will have attenuated significantly.

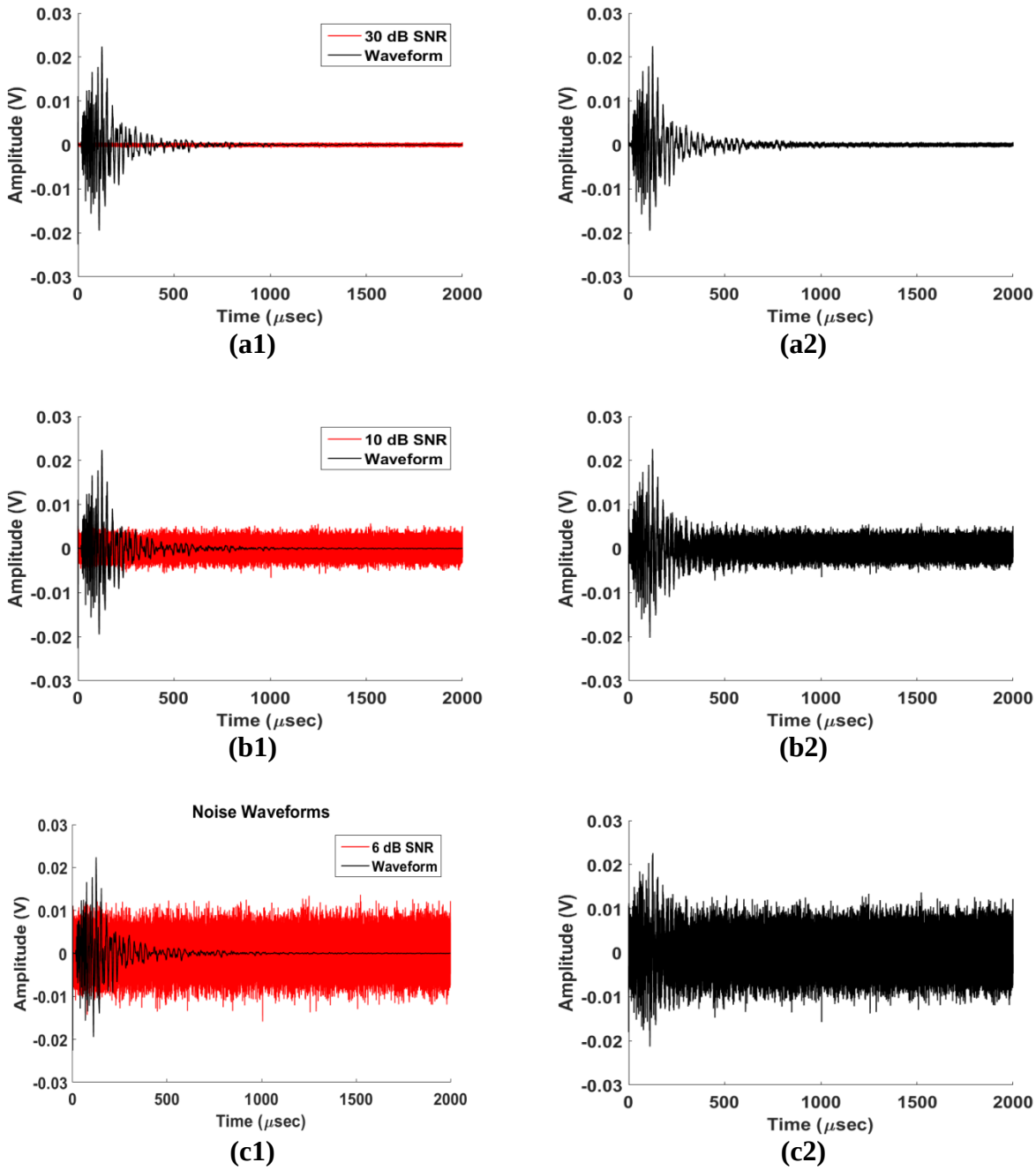

Figure 7-1. Illustration of adding random white Gaussian noise to a coda waveform. (1) The original waveform and noise signal with specified signal-to-noise ratio, (2) Noisy waveform with specified signal-to-noise ratio consisting of the original waveform and the noise signal, (a) 30 dB signal-to-noise ratio, (b) 10 dB signal-to-noise ratio, and (c) 3 dB signal to noise ratio. Coda wave signals were collected on a quasi-isotropic CFRP sample (specimen #1).

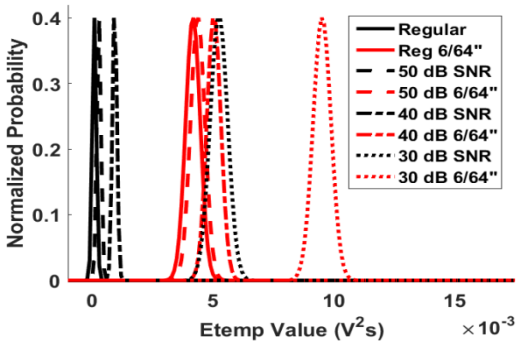

Figure 7-2. Measurement distributions of the residual temporal energy feature for the baseline (black) and 2.381 mm (6/64") drilled through-hole (red) for several signal-to-noise ratios. Coda wave signals were collected on a quasi-isotropic CFRP sample (specimen #1).

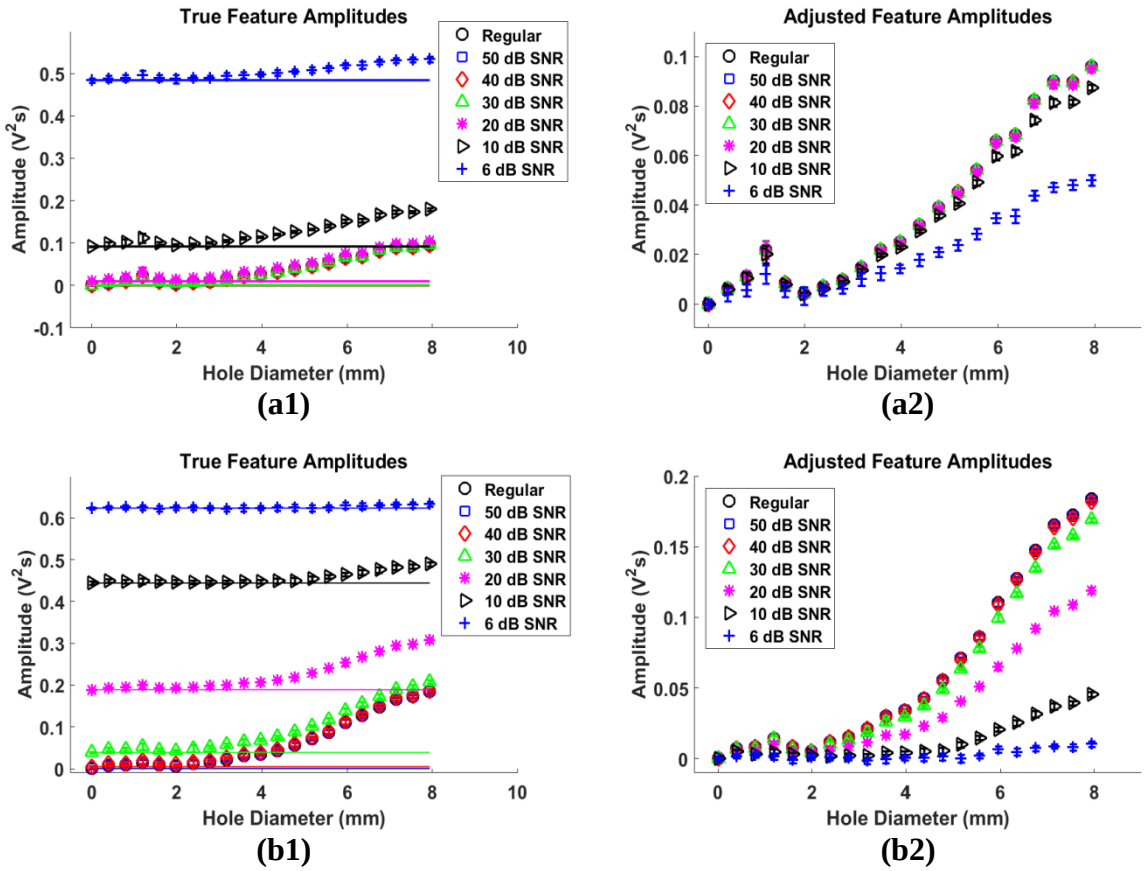

Figure 7-3. Amplitude of residual temporal energy feature with various SNR's (nominal is ~60 dB) where (1) is the true feature amplitude with the baseline offset indicated by the horizontal line and (2) is the feature amplitude minus the mean baseline amplitude for (a) the residual temporal energy and (b) the loss of coherence. The noise is random white Gaussian noise that is added to the original signal such that the ratio of the noise amplitude to the original signal amplitude is as indicated.

Table 7-1. Comparison of the coda waves differential features of a noise modified signal to the original signal using Percent Relative Mean Squared Error.

Amplitude	SNR (dB)	Etemp	Espec	LoCoh	LoCor	DCL
True	**50**	0.00	0.00	0.00	0.00	39.97
	40	0.00	0.00	0.19	0.00	817.16
	30	0.04	0.00	14.00	0.00	10924.67
	20	3.76	0.05	352.17	0.14	1.2101E5
	10	326.47	3.75	2025.41	12.24	1.1994E6
	6	11723.83	298.40	4123.71	580.65	8.5121E6
Adjusted	**50**	0.00	0.00	0.00	0.00	5.04
	40	0.00	0.00	0.01	0.00	31.43
	30	0.00	0.00	0.77	0.00	67.49
	20	0.00	0.00	14.42	0.00	98.64
	10	0.82	0.00	61.87	0.20	90.27
	6	28.41	1.06	90.77	9.20	108.93

7.3 Thermal Induced Relative Velocity Variation

7.3.1 Temperature Dependence of Coda Wave Phase

The linear dilation of coda waveforms due to thermal variations was first demonstrated by Weaver & Lobkis (2000) for signals collected from isotropic materials, in this case a small aluminum billet. This was later confirmed for aluminum plates [Lu & Michaels 2005] and concrete blocks [Niederleithinger & Wunderlich 2013]. Previous work in developing the CSMW technique hinted at the linear phase dependence for acrylic, but did not analyze in any detail [Roberts et al. 1992]. Here the coda wave phase is shown to depend linearly on thermal loading for both acrylic (isotropic) and unidirectional CFRP (transversely isotropic) plates.

In order to examine the influence of temperature variations on the coda wave phase, the baseline and measured signals were broken into consecutive, non-overlapping time windows and the corresponding windows for the baseline and measured signals are then cross-correlated. The

lag time of the peak correlation as a function of the window center time is shown in Figure 7-4 for both acrylic (isotropic) and unidirectional CFRP (transeversely isotropic). The legend gives both the temperature at which the coda waves were collected and the slope of the fit line divided by the temperature change. Linear trends were fit to the data sets with Least Squares. The time lag of the peak correlation is equivalent to the signal phase, and the linear dependence of the phase on the window center time is readily apparent. If the signal phase is also linearly dependent on the temperature change, then the slope of the data sets divided by the temperature change should be a constant. This is indeed the case for both materials where the maximum error observed for this constant is 7.68 % for the Plexiglas sample and 9.09 % for CFRP. The difference between the Plexiglas and CFRP errors is readily attributable to the differences in the consistencies of the two materials.

The observations that the phase delay of coda wave signals is linearly dependent on both time and temperature for both Plexiglas and CFRP plates indicate that thermal loads cause nearly pure dilatations in the waveform. Two lemmas instantly become applicable due to the thermal induced dilation: 1) the stretching technique, which assumes linear dilation, can be applied to these coda waves, and 2) the change in the relative time lag measured by either CWI, CSMW, or Stretching is the change in the relative velocity of the coda wave. These assertions support all of the following work in this chapter. This is the first demonstration of linear phase dependence for a non-isotropic material.

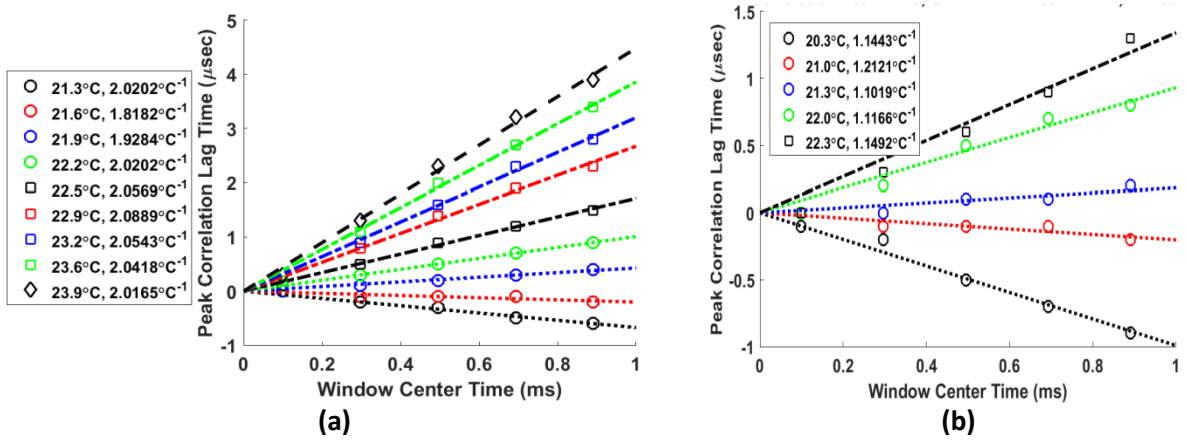

Figure 7-4. Cross-correlation time lag of peak correlation as a function of window center time and temperature change for a) Plexiglas and b) unidirectional CFRP with transducers aligned to the fibers. The linear dependence of the time lag on both parameters is apparent. The legend shows the temperatures at which the waveform was collected along with the slope of the best fit line divided by the temperature change.

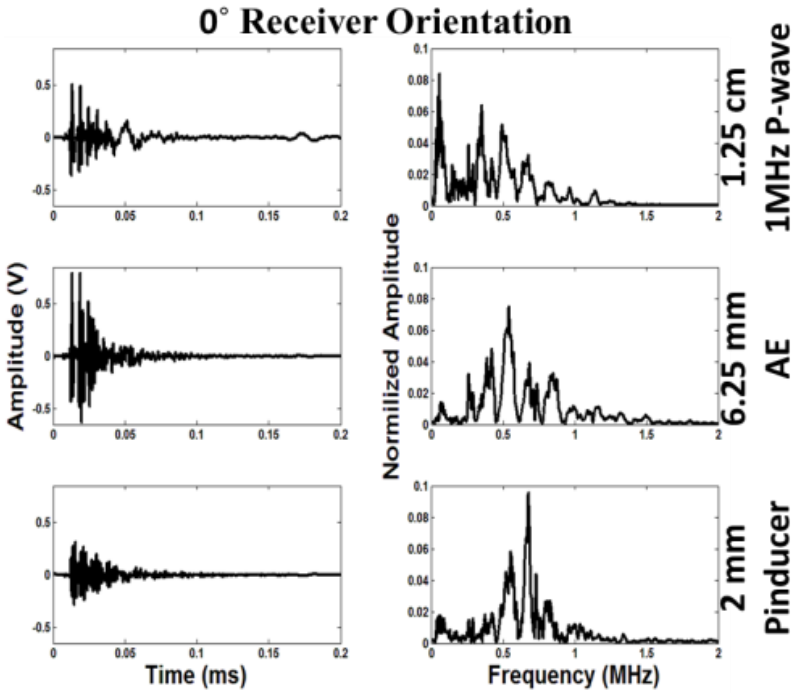

Figure 7-5. Waveforms and spectra collected from one-sided pitch-catch UT on 0.9 cm Plexiglas plate. Signal was transmitted with a 1.25 cm, 1 MHz P-wave transducer and a spike excitation and was received with the three transducers at the 0° orientation; the transducer pairs separated by 8 cm.

7.3.2 Effect of Receiver Type and Orientation on Waveforms and Spectra

Figure 7-5 shows the results from the one-sided pitch-catch propagation through the Plexiglas specimen. The raw signals and spectra are highly dependent on the receiver type. Similar, periodic amplitude spikes are observed in the raw signals which correspond to a spectral peak around 0.5 MHz and are likely due to the plate thickness. The overall structure of the signals is quite different however as can be seen by the differences in the spectra. The distribution of spectral energy decreases in frequency as the receiving transducer face increases in diameter, though similar spectral peaks are present in all three spectra.

The raw baseline signals collected from the CFRP specimen for each transmitter-receiver pair and each orientation as shown in Figure 7-6 while the corresponding spectra are shown in Figure 7-7. It is immediately apparent that the signals are receiver and angle dependent. Figure 7-6 & Figure 7-7 show that the signals change drastically with orientation. The 0˚ arrives and dies out very quickly while the 45˚ and 90˚ signals arrive latter (with the 90˚ arrive ~10μs after the 45˚ signal) and last much longer. The spectral content also changes drastically with receiver orientation, which is shown by the distribution of spectral energy decreasing with increasing receiver angle. This is likely to be due to fiber- and matrix-dominated properties similar to those observed by Vary (1990). The high attenuation in CFRP allows for lower frequency (slower) wave modes to travel farther. The attenuation properties can be easily seen when inspecting a thick vs thin composite with direct propagation.

In direct propagation, the fiber direction has a higher effective modulus, thus the fiber direction has a higher propagation velocity which allows higher frequencies to travel farther before being attenuated out. On the other hand, the transverse direction is matrix dominated, has a lower effective modulus, and a lower propagation velocity which allows for higher frequencies to be

attenuated out before they can travel very far. The indirect propagation used in this study shows similar trends to direct propagation, which is unexpected. This indicates that high frequencies prefer the fiber direction and low frequencies prefer the transverse direction. It is interesting to note that the 45˚ orientation is more similar to the 90˚ orientation than the 0˚. Since the indirect signals demonstrate this preferential behavior, we can predict that we should observe large relative velocity variations in the 45˚ and 90˚ orientations due to the larger moduli variation in the matrix than in the fibers.

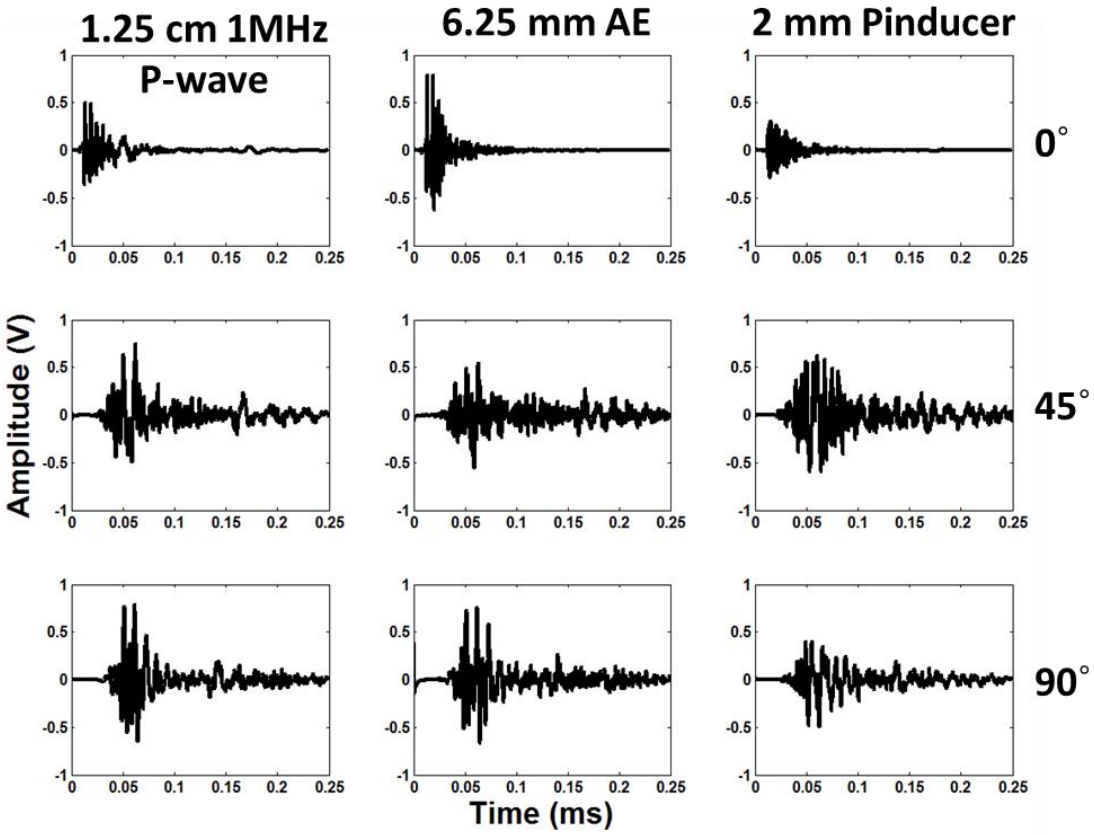

Figure 7-6. Typical ultrasonic waveforms collected from one-sided pitch-catch UT on 0.9 cm unidirectional CFRP plate. Signal was transmitted with a 1.25 cm, 1 MHz P-wave transducer and a spike excitation. The transducers were 8 cm apart. The columns indicate the receiver type used and the rows indicate the angle of the transmitter-receiver pair to the fibers.

The signals and spectra from Figure 7-6 & Figure 7-7 show the effect of the receiver on the signal. Similar trends can be observed between the signals and spectra from the CFRP specimen and those from the Plexiglas specimen. The signal changes with receiver, but the main signal features are present in all signals and the main features become obscured with decreasing aperture size. Contrary to the Plexiglas results, the distribution of spectral energy from the CFRP sample decreases in frequency with aperture size and becomes more diffuse for the 45˚ and 90˚ fiber angles. Similar structures are present in the 12.5 and 6.25 mm receiver spectra. The diffusing of the 2 mm spectrum indicates that the transducer may have an issue with self-noise.

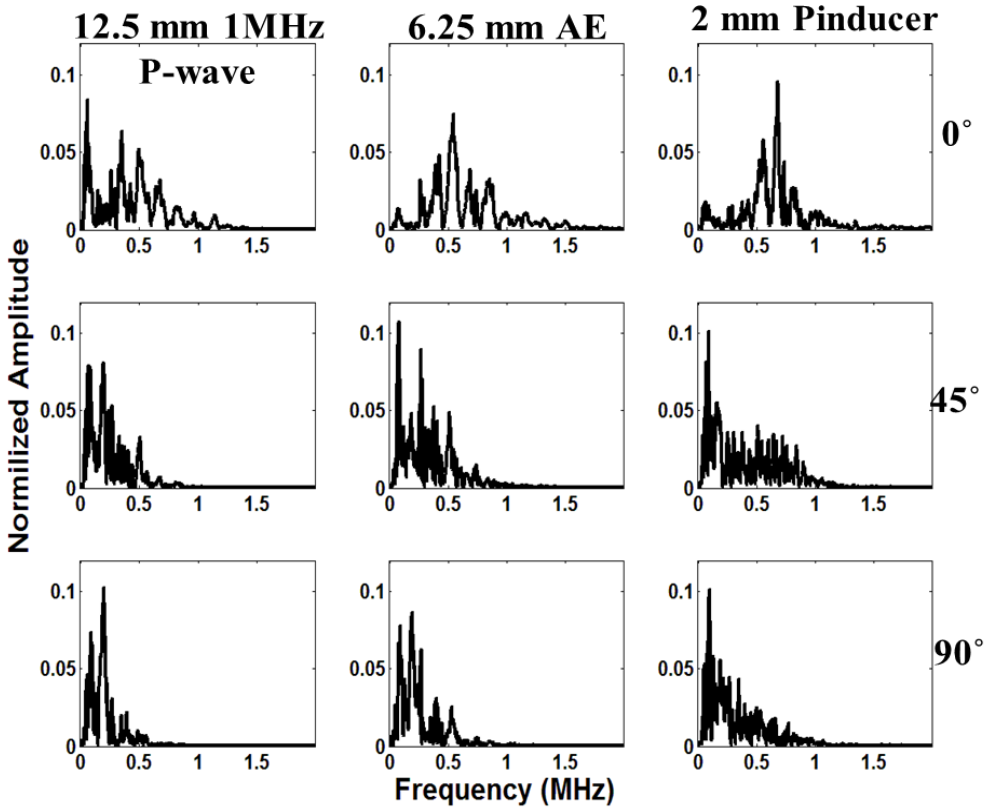

Figure 7-7. Typical ultrasonic spectra collected from one-sided pitch-catch UT on 0.9 cm unidirectional CFRP plate. Signal was transmitted with a 1.25 cm, 1 MHz P-wave transducer and a spike excitation. The transducers were 8 cm apart. The columns indicate the receiver type used and the rows indicate the angle of the transmitter-receiver pair to the fibers.

7.3.3 Relative Velocity Variation

Thermally induced relative velocity variations from the Plexiglas specimen are shown in Figure 7-8. The relative velocity variations are very similar (3 % relative error between the respective linear fits) for the 12.5 and 6.25 mm receivers with a few outliers. The results from the 2 mm receiver are also very similar to the other two data sets for temperatures close to room temperature[14] (Figure 7-8b), but starts to deviate from the other data sets around 22.1 ˚C. This deviation is caused by the higher uniformity of the pinducer signal, which yields multiple instances of highest correlation (consider the correlation of two toneburst signals of the same frequency). The deviation can be corrected by examining the pinducer correlation results and manually selecting the correct maximum correlation. The three transducer-receiver pairs behave as expected for an isotropic, homogeneous material with thermal loading (i.e. they all yielded very similar results). Little to no evidence of phase cancellation was observed for the different receivers.

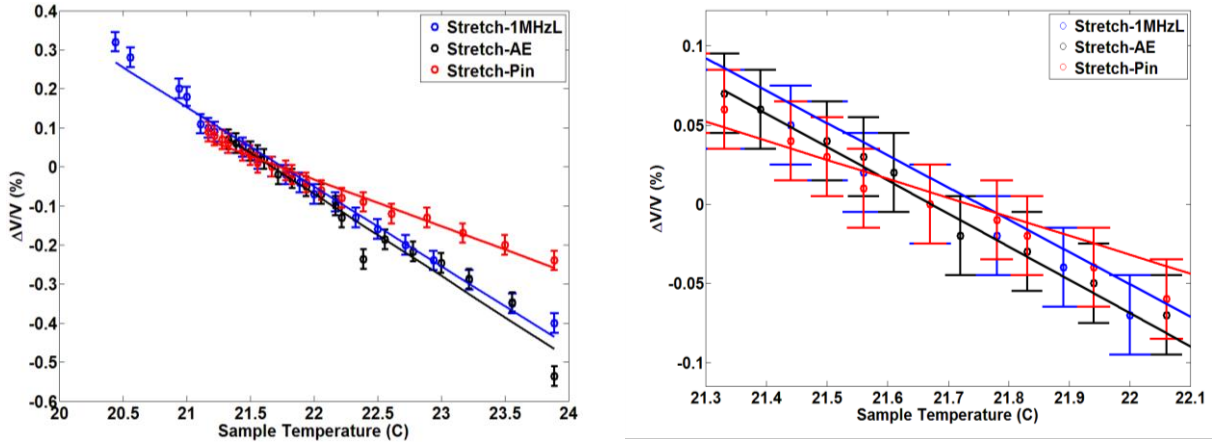

Figure 7-8. Thermally induced relative velocity variations vs. receiver type from one-sided pitch-catch UT on 0.9 cm Plexiglas plate for (a) full range and (b) enlarged region around ΔT = 0. Signal was transmitted with a 1.25 cm, 1 MHz P-wave transducer and a spike excitation and was received with the transducers at the 0˚ orientation; the transducer pairs separated by 8 cm.

[14] 21.2 ˚C: See footnote 11, pg. 107.

Table 7.2. Slopes of the linear trend lines in Figure 7-8, Figure 7-9, and Figure 7-10. The trend lines were determined by using a least squares linear fit.

		Measurements				Error (%)		
		Plexiglas	CFRP			CFRP		
		0˚	0˚	45˚	90˚	0˚-45˚	0˚-90˚	45˚-90˚
Measur-ements	Long	-0.2039	-0.2261	-0.0180	-0.0796	92.04	64.79	77.39
	AE	-0.2103	-0.0687	-0.1797	-0.1009	61.77	31.91	43.85
	Pin	-0.1200	-0.1096	-0.1346	-0.1293	18.57	15.54	3.94
Error (%)	Long-AE	3.04	69.62	89.98	21.11			
	Long-Pin	41.15	51.53	86.63	38.44			
	AE-Pin	42.94	37.32	25.10	21.94			

Long = longitudinal
AE = Acoustic Emission
Pin = pinducer

The thermally induced relative velocity variations measured from the CFRP sample are plotted in Figure 7-9and Figure 7-10. Linear trends are observed which indicate that, as with isotropic materials [Weaver & Lobkis 2000], the thermal loading of transversely isotropic (or slightly orthotropic) materials also produces nearly pure dilation of acoustic waves.

It is interesting to note that unlike the Plexiglas results, the receivers demonstrate different sensitivities for each of the orientations (Figure 7-9a, b, and c) with the variance of the sensitivities decreasing with increasing fiber angle (Table 7.2). Thus the sensitivity of coda wave relative velocity to thermal changes is affected by both the receiver type and the fiber orientation. A comparison of the effect of fiber angle for each of the receivers is shown in Figure 7-10a, b, and c where it is clear that the fiber angle has a dramatic effect on the receiver sensitivity, with the 12.5 mm receiver showing the maximum variance in sensitivity while the 2 mm receiver shows the least. This demonstrates that the pinducer is nearly insensitive to fiber orientation while the 12.5 mm receiver is the most sensitive. Also notable is that the 12.5 mm receiver at a 0˚ fiber angle is most sensitive to thermal changes.

Our expectation of phase cancellation can partially explain the observed differences in receiver sensitivity at various fiber angles. As observed in Figure 7-6 & Figure 7-7, the scattered waves that travel along the fibers experience a higher velocity and less visco-elastic absorption, thus allowing higher frequency modes to propagate farther than in the transverse direction. Phase cancellation should be more prevalent as the ratio of aperture diameter the wavelength increases. Also, our prediction of increased relative velocity change with increasing fiber angle can be observed in the results from the 6.25 and 2 mm receivers (Figure 7-10). The 12.5 mm receiver does not show this trend as the results for the 0˚ fiber angle is likely greatly affected by phase cancellation.

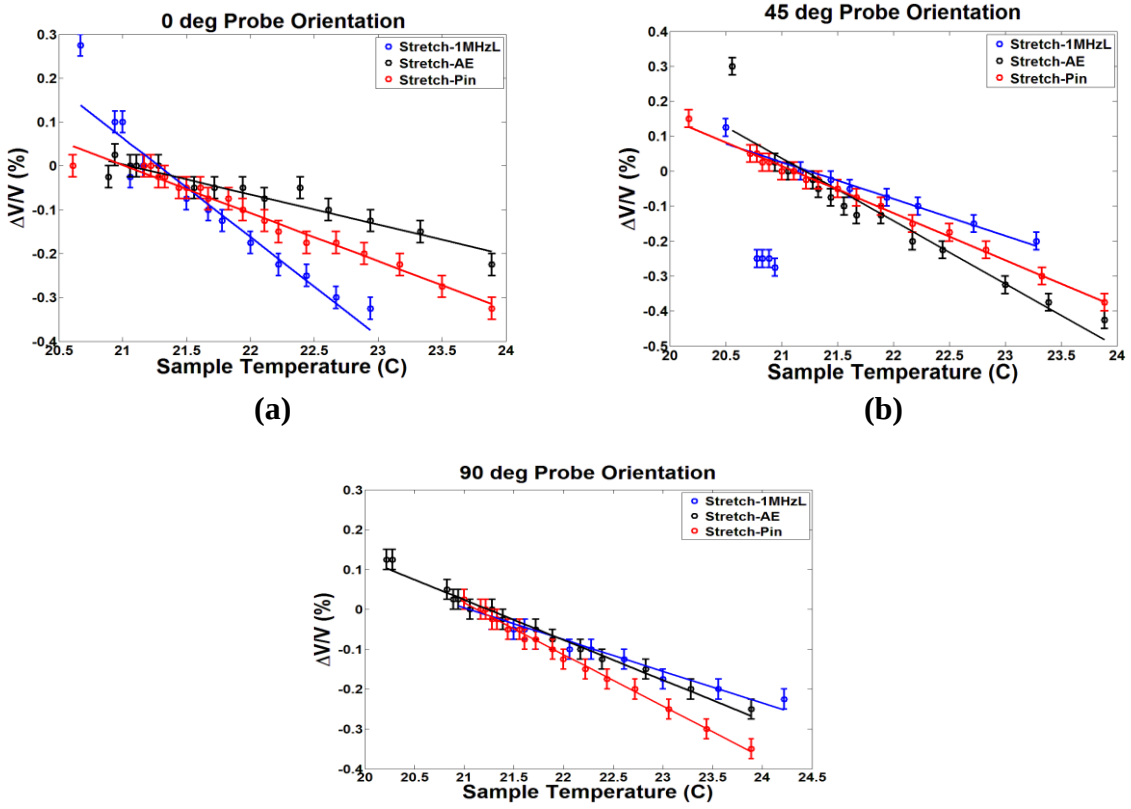

Figure 7-9. Thermally induced relative velocity variations vs. receiver type (1 MHz P-wave, AE, and Pinducer) for a) 0˚, b) 45˚, and c) 90˚ transmitter-receiver pair orientations. Signal is transmitted in a 0.8 cm unidirectional CFRP plate in one-sided pitch-catch mode with a 1.25 cm, 1 MHz P-wave transducer and a spike excitation. transducers are separated by 8 cm.

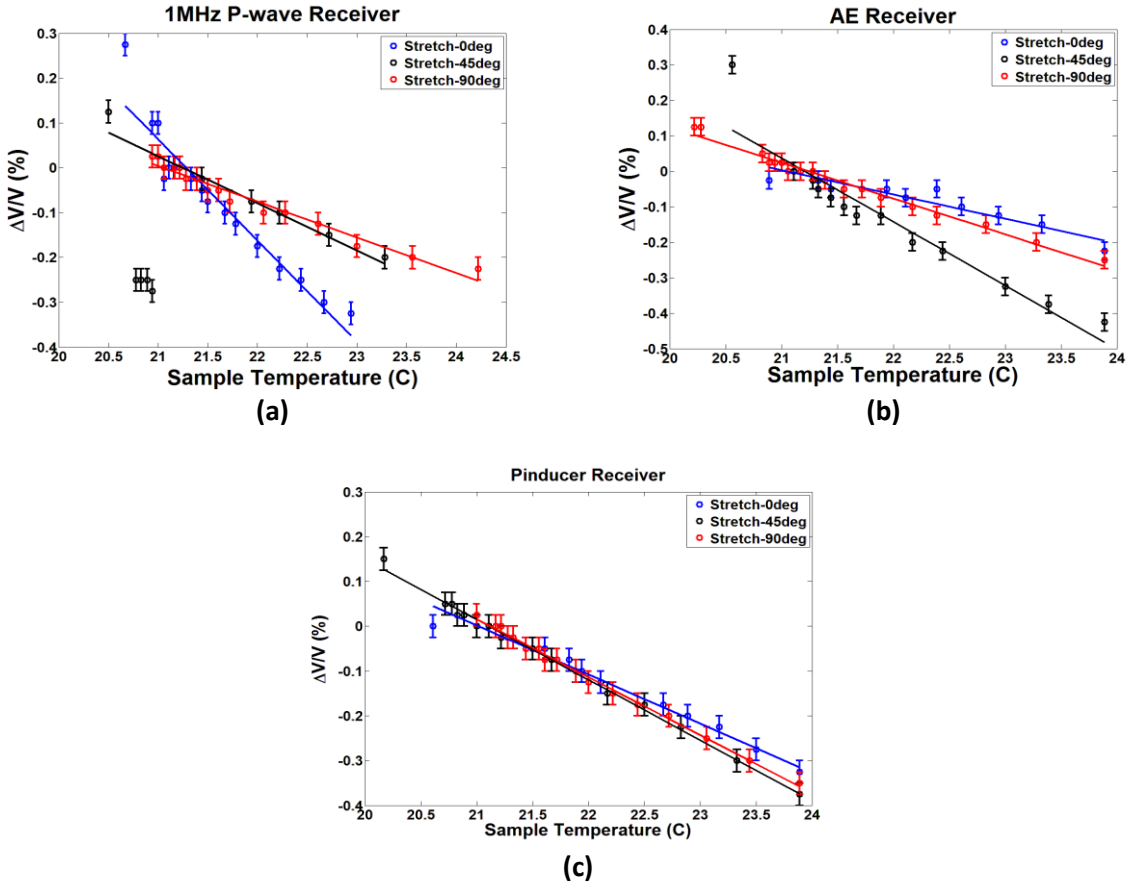

Figure 7-10. Thermally induced relative velocity variations vs. fiber angle (0˚, 45˚, and 90˚) for a) 1.25 cm, 1 MHz P-wave, b) 6.25 mm AE, and c) 2 mm Pinducer receivers Signal is transmitted in a 0.8 cm unidirectional CFRP plate in one-sided pitch-catch mode with a 1.25 cm, 1 MHz P-wave transducer and a spike excitation. Transducers are separated by 8 cm.

7.3.4 Effect of Thermal Loading on Coda Wave Differential Features

In the previous chapter, differential signal features were used to measure the difference between subsequent coda waveforms due to the introduction of damage. Several authors have noted that with the increased sensitivity to small scale damage there is an accompanying increased sensitivity to environmental changes such as thermal fluctuations [Mazzeranghi & Vangi 1999, Lu & Michaels 2005, Zhang et al. 2013b]. The effect of thermal variations on several differential features extracted from an aluminum plate has been previously examined [Michaels & Michaels 2005, Lu 2007], where it was shown that introduced damage causes little to no dilation of the coda

waves. Thus it is possible to distinguish damage from thermal effects. Here the effect of thermal fluctuations on the five differential features utilized in the previous chapter is examined for a transversely-isotropic, unidirectional CFRP plate.

Figure 7-11 shows the resulting differential features extracted from coda wave signals collected with the transducer pair oriented parallel to, perpendicular to, and at a 45˚ angle to the fibers. All differential features exhibit significant amplitude changes (significant being larger than some of the damage amplitudes from the previous chapter) with a difference of only a few degrees. This is problematic for damage detection since the damage can easily be obfuscated by the thermal variance between the collection of the baseline and the measured signals unless it is accounted for. Although it is possible to distinguish damage from thermal effects [Michaels & Michaels 2005] and it is possible to separate relative time lags caused by thermal loads and damage [Zhang et al. 2013], it is not possible to directly decouple the thermal and damage effects in the differential features. The most accurate solution to decoupling the two is to determine the dilation constant of the material under inspection (Section 7.3.1), measure the thermal variation, then dilate the measured signal to match the temperature of the baseline. This method requires significant previous testing, requires a thermocouple, and requires the computationally expensive dilation process. An alternative idea is to have a library of multiple baselines taken at many different temperatures, correlate the measured signal to the baseline signals, the use the baseline that most closely matches [Lu & Michaels 2005, Lu 2007]. The issue with this method is the requirement of the baseline library and the assumption that an undamaged and damaged signals will correlate well enough to remove the thermal bias between the two.

Closer examination of the thermal effects in Figure 7-11 shows that four of the five features (the exception being differential curve length) exhibit behavior that is quadratic with

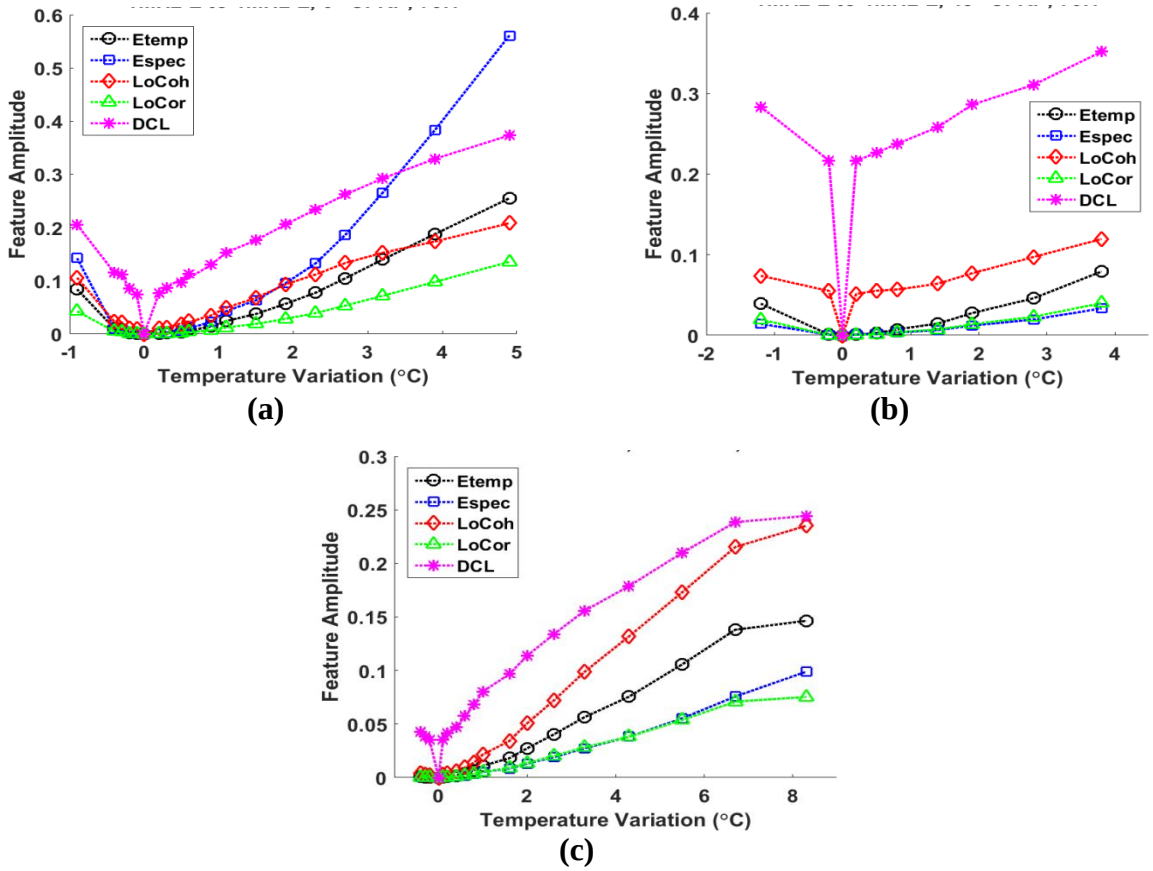

Figure 7-11. Variation of differential feature amplitude with temperature change. Coda wave signal were collected from a unidirectional CFRP plate with the transducer pair aligned with the a) 0˚ fiber angle, b) 45˚ fiber angle, and c) 90˚ fiber angles. The signal is transmitted and received with 1MHz longitudinal transducers.

temperature. This is confirmed by fitting a second order polynomial to the data set using Least Squares, where the resulting coefficients of determination, R^2, are greater than or equal to 0.98. The differential curve length exhibits a behavior that is linear absolute valued with a zero point at $\Delta T = 0$. The zero point is expected and observed for all five features at each fiber orientation since there is no waveform dilation and hence no difference between the signals. Temporal residual energy is generally the most sensitive feature, though 0˚ spectral residual energy is the most sensitive of all cases. A comparison of each of the five features for the three fiber angles is provided in Figure 7-12, where it is easy to observe that the features collected from the 0˚ fiber orientation are the most sensitive to thermal variations. This is unexpected since the fiber dominated wave

propagation properties (modulus, and coefficient of thermal expansion) are less sensitive to thermal variations than the matrix dominated properties [Mangonon 1999]. The features for the 45˚ and 90˚ orientation are equally sensitive in all cases save for the loss of coherence where the 90˚ orientation is more sensitive.

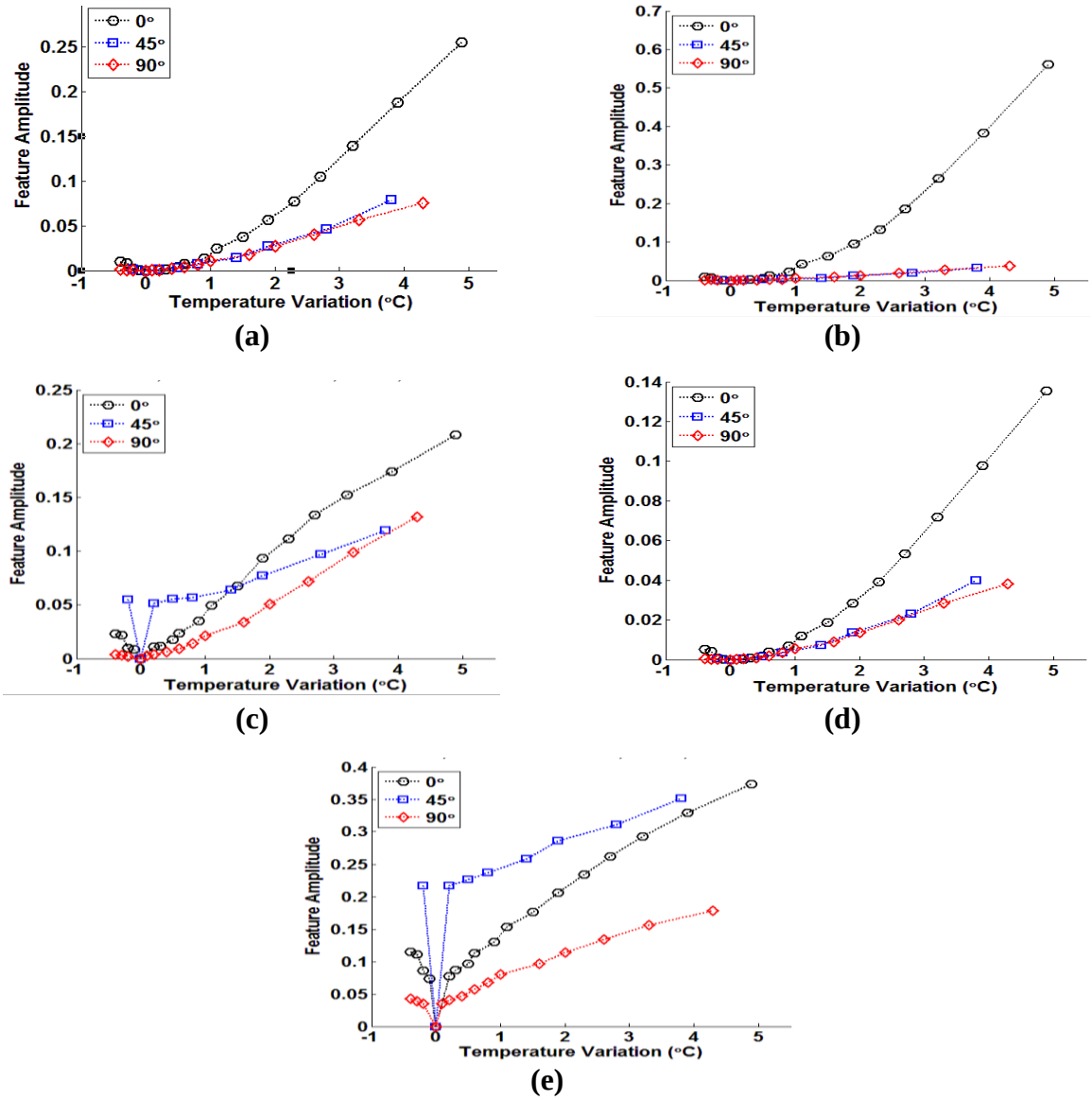

Figure 7-12. Variation of amplitude with temperature change for a) temporal residual energy, b) spectral residual energy, c) loss of coherence, d) loss of correlation, and e) differential curve length differential features. Coda wave signal were collected from a unidirectional CFRP plate with the transducer pair aligned with the 0˚, 45˚, and 90˚ fiber angles. The signal is transmitted and received with 1MHz longitudinal transducers.

7.4 Boundary Effects

Plate boundaries potentially play a very important role in the formation coda waves. The acoustic impedance mismatch between the elastic solid and air causes more than 98% of the acoustic energy to be reflected. Unlike with ballistic propagation where scattering and absorption are both loss mechanisms, the primary energy loss mechanism in coda waves is just absorption, which is volume dependent. Therefore, the coda wave from a small, finite plate will unquestionably contain more energy than a larger finite plate. The real question is whether a coda wave can still form in a semi-infinite plate. As the plate size increases, the acoustic energy will spread out and be absorbed more quickly, but there is a characteristic plate size in which the energy is completely absorbed before it can interact with the edge of the plate and make its way back to the receiver.

The effect of semi-infinite plate boundaries is to absorb significant amounts of acoustic energy as opposed to reflecting the energy. This effect is recreated by placing butyl tape on the edges of the plate. The absorption capabilities of the butyl tape used is demonstrated in Figure 7-13, which compares pulse-echo signals collected with and without butyl tape on the back surface for both polycarbonate and quasi-isotropic plates.

The effect of the plate boundaries on coda waves was studied by collecting coda wave signals as the transducer pair approached the plate boundary (Figure 4-1**c**). Data was collected for 0˚ and 90˚ fiber orientations for the unidirectional CFRP sample (0˚ CFRP, 90˚ CFRP) while the 0˚ orientation was examined for the Plexiglas sample (0˚ Plexi) as it is isotropic. The 6 cm transducer separation was chosen to maximize energy in both directions.

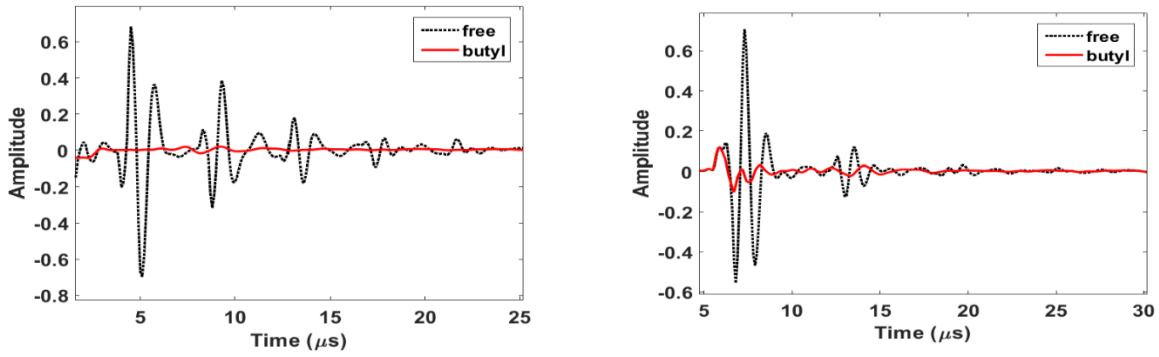

Figure 7-13. Absorbing effect of butyl tape on pulse-echo waveforms collected from a) polycarbonate and b) quasi-isotropic CFRP plates.

The normalized peak amplitudes and their arrival time shifts for each of the received waveforms are plotted in Figure 7-14a & b respectively. The peak amplitude is normalized to the amplitude recorded at the center of the plate. The arrival time of the peak amplitude is likewise shifted by subtracting the arrival time of the peak amplitude at the center of the plate. Maximum variation in peak amplitude occurs for 0˚ CFRP with a value of ~0.4, while the minimum variation occurs for 90˚ CFRP with a value of ~0.13. Peak amplitude variation considered to be negligible for 90˚ CFRP as all of the variations fall within the error bars. The peak amplitude variations for 0˚ Plexi and 0˚ CFRP could also be considered negligible for the same reason save for a single measurement (8 cm and 4 cm respectively) that falls just outside the error bar. Maximum peak amplitude arrival time shift is observed for 90˚ CFRP with a value of -8 μs, while the minimum variation is observed for 0˚ Plexi with a value of 2.5. Again, the variations observed for 0˚ Plexi are negligible due to error, and variations observed for 0˚ CFRP would also be negligible if not for the apparent outlier that occurs at 4 cm from the boundary. Time shift variations for 90˚ CFRP have a general downward trend (with an outlier at 6 cm) while approaching the plate boundary that indicates that peak amplitude is arriving sooner. This decrease in peak amplitude arrival time is likely due to decreasing travel time and increasing amplitude of the edge reflections.

The normalized spectral energy and normalized maximum coda wave decay rate for each of the received waveforms are plotted in Figure 7-15a & b respectively. Both the spectral energy and maximum decay rate are normalized to their respective values at the center of the plate. Maximum spectral energy variation occurs for 0˚ CFRP with a value of ~0.6, while the minimum variation occurs for 0˚ Plexi with a value of ~0.1. All of the variation for 0˚ CFRP and 90˚ CFRP are within measurement error and are therefore negligible. The spectral energy for 0˚ Plexi has a downward trend until 6 cm from the plate boundary, then it increases near the boundary. This is likely due to decreasing energy received from the other three boundaries as the transducers are moved until the fourth plate boundary reflects enough energy to compensate. The maximum variation in decay rate occurs for 0˚ Plexi with a value of ~0.5, while the minimum variation occurs for 0˚ CFRP with a value of 0.3. The variations fall within measurement error except for 90˚ CFRP which falls from 10 cm to 8 cm separation from the plate boundary, then steadily increases. This indicates that as the transducer pair approaches the plate boundary the coda wave increases in spectral power at latter times due to scattering received from the boundary.

Generally, the variations observed due to approaching the plate boundary can be considered negligible as they are typically within the repeatability error. This indicates that the coda wave can maintain much of its information regardless of the location of the transducer pair on the plate. It is important to note, however, that changing the location of the transducer pair changes the coda wave field and that high/low energy regions may be created/occur in different regions.

Further investigation into the influence of semi-infinite plate boundaries on the coda wave was performed by comparing coda wave parameters from quasi-isotropic and Plexiglas plates with 0 to 4 semi-infinite boundaries. A pair of 12.7 mm 1 MHz longitudinal transducers were coupled to the plate centers with an 8 cm separation using Crystalbond 555 couplant. The transducers

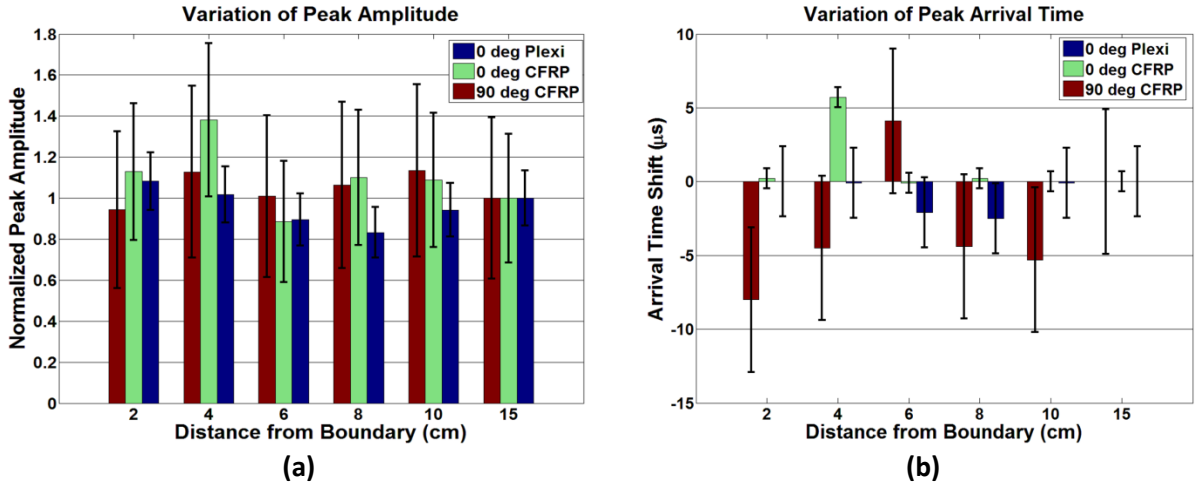

Figure 7-14. Variation in coda wave a) peak amplitude and b) arrival time of the peak amplitude for a 0.9 cm Plexiglas plate and a 0.9 cm unidirectional CFRP plate. The signal was transmitted and received with a 1.25 cm, 1 MHz longitudinal transducer. The error bars indicate 1 standard deviation in measurement repeatability.

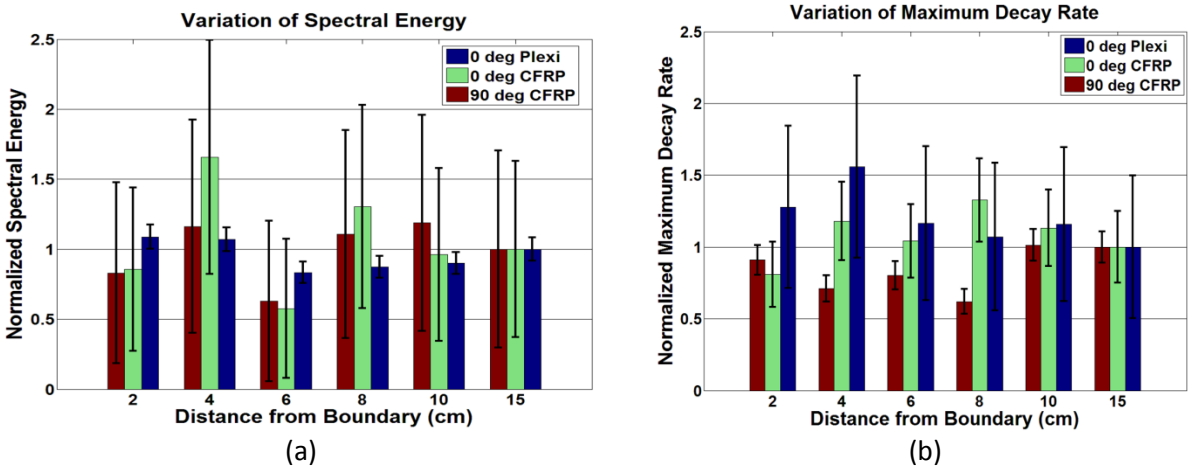

Figure 7-15. Variation in coda wave a) spectral energy and b) maximum decay rate for a 0.9 cm Plexiglas plate and a 0.9 cm unidirectional CFRP plate. The signal was transmitted and received with a 1.25 cm, 1 MHz P-wave transducer. The error bars indicate 1 standard deviation in measurement repeatability.

remained coupled to the plates throughout the changing boundary conditions. Figure 7-16 shows the resulting coda wave parameters, normalized to the free plate values. The observed variations in first arrival time, the peak amplitude, and the arrival time of the peak amplitude due to increasing number of semi-infinite boundaries are within one repeatability error of the free boundary value

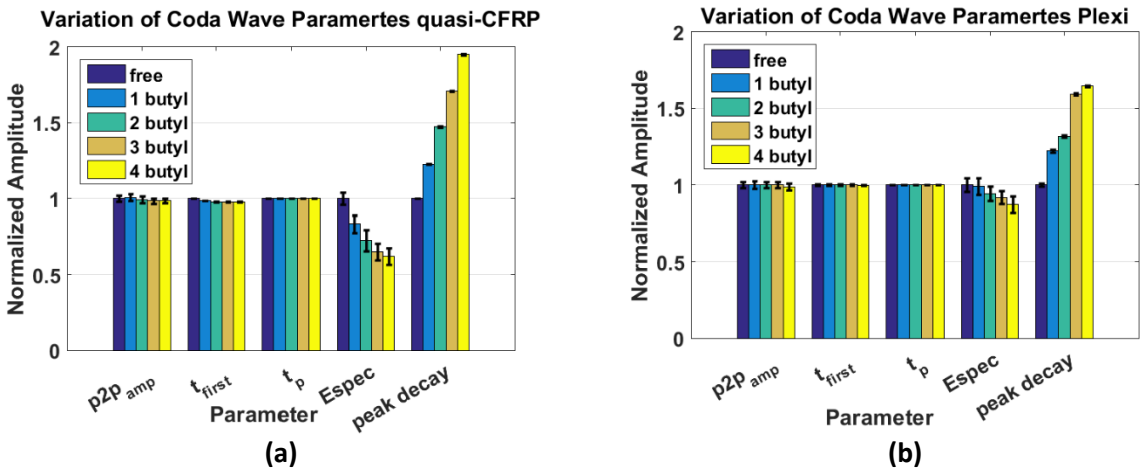

Figure 7-16. Variation in coda wave parameters with increasing number of semi-infinite boundaries for a) a 0.9 cm unidirectional CFRP plate and b) a 0.9 cm Plexiglas plate. The signal was transmitted and received with a 1.25 cm, 1 MHz P-wave transducer. The error bars indicate 1 standard deviation in measurement repeatability.

for both plates. The variations in the spectral energy and peak decay rate, on the other hand, are affected by the semi-infinite boundaries. Spectral energy varies by 13% in the Plexiglas plate and by 38% in the quasi-isotropic plate, which is expected since the semi-infinite boundaries absorb acoustic energy.

The large variations in the decay rate is the most interesting result since Weaver postulated that the coda wave decay rate is a measure of absorption [Weaver 1987], which is a material property and should be relatively constant. Decay rate measures how quickly the tail of the coda wave decays, and the coda tail is comprised primarily of low frequencies. Low frequencies can travel farther due to lower attenuation and are therefore much more likely to be affected by the plate boundaries. Weaver himself noted that the decay rate can be greatly affected by the boundary conditions of the volume. The peak decay rates vary by 65% in the Plexiglas plate and by 95% in the quasi-isotropic CFRP plate. Considering this, it stands to reason that the variations in coda wave decay rate are a function of both the material absorption and the sample volume. For a plate,

the absorption should show a volumetric dependence until the plate reaches a characteristic length were the spread of the acoustic energy no longer affects the decay. This is replicated by the butyl tape, since the decay rate increases with the number of semi-infinite edges. It is interesting to note that the signal energy and decay rate for the quasi-isotropic CFRP plate decrease exponentially and increase linearly with the number of semi-infinite boundaries respectively. The linear increase of the decay rate supports the idea of volumetric dependence.

The insensitivity of the first three parameters to the number of semi-infinite boundaries indicates that the initial portion of coda wave is not influenced by extending the plate dimensions past 30 cm. The tail portion of the coda wave, on the other hand, is significantly influenced as is evidenced by the energy and decay parameters. These observations indicate that the formation of coda waves in plates is more dependent on the top and bottom surfaces of the plate than on the plate edges, but the amount of information carried in the waveform is dependent on the sample volume. This is particularly apparent for the Plexiglas sample since there is no internal scattering and the formation of the coda wave should be completely dependent on the plate boundaries, yet greater variations are observed for the quasi-isotropic CFRP plate.

7.5 Summary and Conclusions

Signal-to-noise ratio has a dramatic effect on the amplitude of coda wave differential features that can easily mask damage. It was shown that the cause of the increased feature amplitude for signals with high levels of noise is due to the increased variation between waveforms. Even the feature amplitudes for repeated baseline measurements (ideally zero) increased due to the added random noise. Here it was shown that the effect of added noise can be

negated by subtracting the baseline offset from the feature amplitude. Three of the five differential features examined in this study were found to be insensitive to signal noise until a signal-to-noise ratio of 2. This demonstrates that coda wave NDE can operate in noisy environments and has the potential to be used over long distances or situations where the signal attenuates significantly.

The effect of thermal variations on several aspects of coda waves has been examined for both Plexiglas (isotropic with little to no internal scattering) and unidirectional CFRP (transversely isotropic with significant internal scattering). The linear dependence of the coda wave phase on window center time and temperature was confirmed for an isotropic material and was demonstrated for the first time for a non-isotropic material. This proves that thermal loading causes pure dilation of the waveforms and allows for the measurement of the coda wave relative velocity through the application of the stretching technique. Until this point it was unclear whether CFRP materials exhibited pure dilations or whether relative velocity measurements were physically meaningful.

In the isotropic and the transversely isotropic materials, the aperture affects the received waveform by obscuring the signal features and making it more uniform with decreasing aperture size. The effect on the spectra is to change the spectral energy distribution center frequency (increasing for the Plexiglas and decreasing for the CFRP) with decreasing aperture size. Although the waveform and spectra are affected by the aperture size, the relative velocity variation measurement was not affected for the Plexiglas sample. The aperture size had a dramatic effect on the thermally induced relative velocity measurement for the CFRP sample by causing a variance in the $\Delta v/v$ vs. T sensitivities for all orientations. The minimum variance was observed for the 2 mm receiver, which is an indication of the presence of phase cancellation for the other receivers. Fiber orientation also had a dramatic effect on the relative velocity measurement, again by a

causing a variance in the Δv/v vs. *T* sensitivities for the three receivers. The variance decreases with increasing fiber orientation which indicates the presence of fiber- and matrix-dominated properties that need to be further studied.

The effect of thermal variations on coda wave differential features was also examined. It was observed that the majority of features vary with temperature. This variation of the feature amplitudes can easily obfuscate damage detection and thus need to be further characterized. Several mitigation methods were presented and discussed. Each shows promise, but each has limitations and cannot completely decouple the thermal and damage effects from the differential features. The best solution currently available is to measure the temperature of the structure and dilate the waveform using a material dependent constant prior to damage detection.

Sample boundaries play an important role in the formation of coda waves for plates. The initial portion of the coda wave is formed due to the top and bottom surfaces and is not affected by absorbing plate edges. The tail portion of the coda wave, on the other hand, is strongly affected by the type of boundary (reflective vs absorbing) along the plate edges as the tail is formed primarily by the reflections from the plate edges. Even though the coda wave itself is drastically affected by a change in the boundary conditions of the plate edges, the detection of damage is not affected to nearly the same extent and detection of damage is still possible.

CHAPTER 8. CONCLUSIONS AND RECOMENDATIONS

As stated in the abstract, "The central objective of this work, is to develop a quantitative foundation for the use of coda wave NDE for the inspection and evaluation of fibrous composite materials."

In chapter 2 this thesis discussed three steps of work required to develop this foundation. A very brief recount is as follows:

Step 1: analyze the most basic properties and processing of coda waves.

1. Temperature change
2. Develop and verify processing algorithms
3. Determine spreading function for coda wave acoustic energy
4. Develop definitions of attenuation and measure attenuation of coda wave energy
5. Determine the effect of boundaries.

Step 2 Detecting simulated damage and analyze basic damage detection capability, such as repeatability, sensitivity and reproducibility

1. Detect defects such as drilled holes
2. Determine detection capability
3. Determine the behavior of damage indices (DI) by developing a model which relates the values of the damage indices to a damage parameter, such as defect volume.

Step 3

1. Detect realistic defects such as micro-cracks caused by fastener holes and barely impact damage
2. Monitor damage growth by means of fatigue and/or compression after impact
3. Field testing

The need for the development of a quantitative foundation is clear since Coda wave NDE is a paradigm change from traditional ultrasonic NDE where a coherent ballistic (direct propagation) wave follows a mathematically traceable path and everything can be described by a deterministic

physical model. Coda waves, in contrast, are comprised of an indeterministic, incoherent, wave field without a definable travel path. The observer does not try to discriminate the wave, but tries to extract meaningful information such as a differential parameter. Due to the lack of well defined propagation, traditional definitions of NDT&E parameters such as velocity, attenuation, and wavelength, which are used widely in ultrasonic NDT&E, become undefinable in this new paradigm since the wave field is indeterministic in nature. It is precisely for this reason that many in the field of traditional ultrasonic NDT&E may have difficulty in accepting coda waves/diffuse fields as a viable method. Perhaps the name "coda ***wave***" is unfortunate since it leads people to try to analyze and understand the coda wave signals as actual propagating waves as opposed to the time-varying superposition field sampled at a specific point that they actually are.

8.1 Conclusions

Several Coda wave differential features were considered for quantitative detection and sizing of localized defects in CFRP plates and were found to be sensitive to drilled holes. Physical models were drawn from the dimensional analysis of the residual temporal and residual spectral energies have been fit to the experimental data with good agreement, which highlights possible underlying physical principles governingcoda wave differences in the presence of drilled holes. Using 95% confidence bounds, the accuracy of defect sizing for a single drilled through-hole was estimated to be within ± 0.5 mm for both materials over the range of 2 to 6.4 mm diameter holes. For multiple drilled through-holes (0.4 mm diameter), the defect sizing accuracy was estimated to be within ± 1 hole. Thus coda wave NDE can offer a good detection and sizing method in a single volume scan that takes less than a second, stores little data, and is easy to process.

Signal features increase with increasing hole diameter for the aluminum and polycarbonate samples examined with few exceptions and increase in two regions for CFRP samples (d <2 mm

and 2 mm < d). A single 0.4 mm hole is detectable and a 0.4 mm increase in hole diameter is resolvable in all samples. The resolutions of the differential features for the polycarbonate samples specifically and differential curve length generally were increased by taking repeated measurements. Of all the differential features examined, spectral residual energy was found to be most sensitive to defects and differential curve length was found to be the least sensitive. It was shown that the differential features increase monotonically with increasing number of drilled through-holes and that the number of 0.397 mm (1/64") holes is easily resolvable. The features were also shown to be sensitive to the depth of the hole with half- and through-holes resolvable in most cases for both CFRP and polycarbonate materials. The quadratic dependence of the differential features on the hole effective hole diameter was confirmed for the majority of cases.

Coda measurements were shown to be repeatable, reciprocal, and reproducible. This indicates that coda wave NDE is capable of sensitive measurements for the detection of damage. The measurements presented in this thesis were performed under controlled laboratory conditions: the transducers were semi-permanently attached during each data collection stage and the data was collected quickly so that the ambient room temperature in the lab varied by less than 0.1 ˚C. Measurements were made with decoupled and recoupled receivers to examine the variability introduced by the changing coupling conditions. The repeatability of the coda wave parameters was lower when decoupling and recoupling receivers, but would still enable the differentiability of damage.

Several aspects of the experimental configuration and data collection can strongly affect the coda waves themselves and the amplitude of the differential features used to detect damage. The aspects examined in this thesis were: signal-to-noise ratio, thermal variation, and absorbing edge boundaries. Mitigation methods were presented for the first two factors.

Signal-to-noise ratio has a dramatic effect on the amplitude of coda wave differential features and can easily mask damage, but this effect can be negated by subtracting the baseline offset from the feature amplitude. Three of the five differential features examined are insensitive to signal noise, using this mitigation method, until a signal-to-noise ratio of 2. This demonstrates that coda wave NDE can operate in noisy environments and has the potential to be used in situations where the signal attenuates significantly.

It was observed that the majority of differential features vary with temperature. This variation of the feature amplitudes can easily obfuscate damage detection and thus needs to be further characterized. Several mitigation methods were presented and discussed. Each shows promise, but each has limitations and cannot completely decouple the thermal and damage effects from the differential features. Currently the best mitigation method is to measure the temperature separately and dilate the recorded waveform prior to damage detection/characterization analysis.

Sample boundaries play an important role in the formation of coda waves for plates. The initial portion of the coda wave is formed due to the top and bottom surfaces and is not affected by absorbing plate edges. The tail portion of the coda wave, on the other hand, is strongly affected by the type of boundary (reflective vs absorbing) along the plate edges as the tail is formed primarily by the reflections from the plate edges. Even though the coda wave itself is drastically affected, damage detection is still possible using the initial part of the wave.

Coda wave propagation and attenuation were examined in order to better understand the spreading function and give estimates to the distance a coda wave could spread. It was found that the time of first arrival of the coda wave occurred between the arrival time of a ballistic longitudinal mode and a ballistic shear mode. This corresponds either to a S_0 Lamb wave mode or a reflected longitudinal wave mode. Extracting Lamb wave modes was examined and found to be

inapplicable as the wave modes are not separable in either the time or frequency domains. Based on the first arrival times, the coda waves have an elliptical to barbell shaped spreading function. This indicates a propagating wave mode. Additionally, the diffusion equation was fit to the coda waves with good agreement for aluminum, polycarbonate, and quasi-isotropic CFRP plates. Although this doesn't preclude direct arrivals of specific modes for the first arrival, the diffusion model predicts multiply reflected and scattered waves. The arrival times of the peak amplitude do not exhibit an elliptical/barbell spreading function which contradicts the propagating wave mode assumption. This is expected since the coda wave is a superposition field and not a wave mode.

Several attenuation definitions were applied to the coda waves collected. The spatial attenuations were not well behaved and were not well fit by a decreasing exponential as would be expected for a propagating wave mode. This further indicates that traditional ultrasonic NDE measurements are not applicable in a coda wave analysis. One of the best measures of coda wave attenuation is the attenuation of signal energy with time (i.e. coda wave decay rate) as the definition is not dependent on the propagation of a specific wave mode. As expected, the isotropic materials exhibit circular attenuation function while the uni-directional CFRP plate exhibits an angular dependence. It is noted, however, that the size of the plate and reflecting vs. absorbing plate edges can dramatically affect the decay rate.

Thus we see that out of the three necessary steps outlined in the introduction, and reiterated in the beginning of this chapter, steps one and two have been fully addressed in this work. Step three could not be addressed due to paucity of time. This last step is probably the most important if Coda wave NDT&E is to be brought from its current ancient state into a mature method. Thus, extensive examination of this last step is warranted.

8.2 Contributions

The first and foremost contribution from this research is the quantitative application of coda waves to fibrous composite plates for NDT&E. The research results demonstrate the damage detection capabilities for a few specific cases (small, flat plates less than 300x300 mm examined under laboratory conditions), indicate the feasibility of using coda waves for SHM of composite structures, and provide a quantitative foundation for future research.

The second contribution of this thesis is a derivation of a model to describe the relation between the volume of drilled through-holes in plates and the amplitude of residual energy based differential signal features. This is a step in the transition of a largely qualitative approach to a quantitative one. With this relationship, either the feature amplitude or damage volume (hole size) becomes predictable given the other. For the samples examined here, these models need to be applied to small holes ($d < 2$ mm) or intermediate holes ($2 < d < 6.4$ mm) separately.

The third contribution of this thesis is an analysis of the sensitivity of differential signal features to drilled through-holes in plates, the accuracy of the features in estimating defect sizes, and repeatability of the differential feature amplitudes. This is the first investigation to begin addressing the fundamental limitations of damage detection with coda wave differential features.

The fourth contribution of this thesis is an analysis of the signal-to-noise ratio (SNR) on the effectiveness of defect detection and measurement error. This analysis helps to determine the detection limits of coda waves for NDT&E, both in terms of noise level and transmitter-receiver separation (when combined with attenuation measurements).

The fifth contribution of this research is the definition and implementation of several different measures of coda wave attenuation to investigate their propagation behavior. When

combined with the SNR analysis, the attenuation measurements will potentially provide an estimate of the maximum transducer spacing for an SHM array, but this requires further work.

The sixth contribution of this thesis is an analysis of the repeatability, reciprocity, and reproducibility of coda waveforms and damage detection using differential signal features. This analysis demonstrates that coda waves are not noise, but are ultrasonic signals whose variation, as long as care is taken during data collection, is due to changes in the structure under investigation. The repeatability and reproducibility give further testament to the viability of using this method of damage detection for composite materials and indicate the potential for a reliable SHM inspection system. The reciprocity demonstrates that the transmitter and receiver can be interchanged.

The seventh contribution from this thesis is the comparison of coda wave behavior and damage detection for several materials of varying elastic properties, material models, and internal scattering. This demonstrates that coda wave NDT&E has the potential to be applicable for a wide range of materials, including those with little to no internal scattering.

8.3 Recommendations for Future Work

The sensitivity of coda waves makes them very attractive for SHM and the quantitative damage detection demonstrated in this thesis shows the potential of this method for damage diagnosis. It is quite probable that coda wave differential features can detect micro-cracks and monitor fatigue damage. Further quantitative work is needed to examine feature behavior for other damage types and locations in addition to detecting damage in semi-infinite plates. The aim of future research should be to extend damage detection and diagnosis capabilities to realistic damage such as barely visible impact damage, micro-cracking, and fatigue. Future should also aim to determine the minimum necessary array size for large part inspection.

The current drawbacks of coda wave NDE that prevent wider adoption are the difficulties in interpreting waveform changes and correlating them to specific damages/locations and the current lack of quantitative studies. Questions of sensitivity to different defects/damage, whether damage can be detected without a baseline, and effectiveness for arbitrary geometries still exist. Further research should consider these issues. Further investigation into the effects of external influences (e.g. temperature change) on feature amplitudes, the masking of damage, and mitigation methods is needed. Further investigation into the influence of sample geometry, transducer location, and damage location on damage detection and diagnosis is also needed.

REFERENCES

Achenbach J. D., **1973**, *Wave Propagation in Elastic Solids*, New York, NY: North-Holland Publishing Company.

Achenbach J. D., **2000**, "Quantitative nondestructive evaluation," *Int. J. Solids Struct*., vol. 37, no. 1-2, pp. 13-27.

Adams D. E., **2007**, *Health Monitoring of Structural Materials and Components*, Hoboken NJ: John Wiley & Sons Ltd., pp. 1-28.

Aki K., **1969**, "Analysis of the seismic coda of local earthquakes as scattered waves," *J. Geophys. Res*., vol. 74, no. 2, pp. 615-631.

Aki K. and Chouet B., **1975**, "Origin of coda waves: Source, attenuation, and scattering effects," *J. Geophys. Res.*, vol. 80, no. 23, pp. 3322-3342.

Anugonda P., Wiehn J. S., and Turner J. A., **2001**, "Diffusion of ultrasound in concrete," *Ultrasonics*, vol. 39, pp. 429-435.

ASM, **1989**, "Ultrasonics," *ASM Handbook, Volume 17 - Nondestructive Evaluation and Quality Control*, Materials Park, OH: ASM International, pp. 231-277.

ASTM, **1997**, *Standard Guide for Acousto-Ultrasonic Assessment of composites, Laminates, and Bonded Joints*, ASTM Standard E1495-97.

ASTM, **2009**, *Standard Guide for Nondestructive Testing of Polymer Matrix Composites Used in Aerospace Applications*, ASTM Standard E2533-09.

ASTM, **2012**, *Standard Practice for Ultrasonic Testing of Flat Panel Composite and Sandwich Core Materials Used in Aerospace Applications*, ASTM Standard E2580-12.

Auld B. A., **1973**, "Acoustic fields and waves in solids," Vol 1. New York: John Wiley & Sons.

Auld B. A., **1979**, General Electromechanical Reciprocity Relations Applied to the Calculation of Elastic Wave Scattering Coefficients," *Wave Motion*, vol. 1, no. 1, pp. 3-10.

Baker, A., Dutton S., Kelly D., **2004**, *Composite Materials for Aircraft Structures*, Reston, VA, American Institute of Aeronautics and Astronautics, Inc.

Barbero EJ, **2011**, *Introduction to Composite Materials Design*, New York, NY, CRC Press.

Becker J., Jacobs L. J., Qu J., **2003**, "Characterization of Cement-Based Materials Using Diffuse Ultrasound," *J. Eng. Mech*, vol. 129, pp. 1478-1484.

Berendsen H. J. C., **2011**, *A Student's Guide to Data and Error Analysis*, Cambridge, UK: Cambridge University Press.

Biwa S., **2001**, "Independent scattering and wave attenuation in viscoelastic composites," *Mech. Of Mat.*, vol. 33, pp. 635-647.

Biwa S., Watanabe Y., and Ohno N., **2003**, "Analysis of wave attenuation in unidirectional viscoelastic composites by a differential scheme," *Composites Sci. and Tech.*, vol. 63, pp. 237-247.

Biwa S., Kamiya T., and Ohno N., **2007**, "Multiple Scattering Simulation of Ultrasonic Shear Wave in Unidirectional Carbon/Epoxy Composites," *Mat. Trans.*, vol. 48, no. 6, pp. 1196-1201.

Bluman A. G., **2004**, *Elementary Statistics: A Step by Step Approach, 5th Ed.*, New York, NY: McGraw-Hill Companies Inc., pp. 509-530.

Bond L. J., **2015**, "From NDT to Prognostics: Advanced Technologies for Improved Quality, Safety, and Reliability," Proc.2015 *IEEE Far East NDT New Tech. & App. Forum*, Shanghai, China, pp. 1-9.

Bose S. K. and Mal A. K., **1974**, "Elastic waves in fiber-reinforced composite," *J. Mech. Phys. Solids*, vol. 22, pp. 217-229.

Brekhovskikh L. M., *Waves in Layered Media* 2nd ed (Academic Press, New York, NY, 1980).

Bui D., Kodjo S. A., Rivard P., Fournier B., **2013**, "Evaluation of Concrete Distributed Cracks by Ultrasonic Travel Time Shift Under an External Mechanical Perturbation: Study of Indirect and Semi-direct Transmission Configurations," *Journal of Nondestructive Evaluation*, vol. 32, pp. 25-36.

Cawley P. and Simonetti F., **2005**, "Structural health monitoring using guided waves – potential and challenges," *Proc. 5th Int. Conf. Struct. Health Monitoring*, DEStech Publications, pp. 503-510.

Chiou C.-P., Thompson R. B., and Schmerr L. W., **1995**, "Ultrasonic signal-to-noise ratio enhancement using adaptive filtering technique," *14th Review of Progress in Quantitative Nondestructive Evaluation*, D. O. Thompson and D. E. Chimenti, eds., vol. 14, pp. 727-732.

Choo V. K., Gomez M., Khazaee M., and Tapia G. B., **1993**, "Characterization of the acousto-ultrasonic NDE method using tailor made composite specimens," *Proceedings of the Second International Conference on Acousto-Ultrasonics*, Vary A., Ed., pp. 95-104.

Conoir J.-M. and Norris A. N., **2010**, "Effective wavenumbers and reflection coefficients for an elastic medium containing random configurations of cylindrical scatterers," *Wave Motion*, vol. 47, pp. 183-197.

Dayal V. and Kinra V. K., **1989**, "Leaky Lamb waves in an anisotropic plate. I: An exact solution and experiments," *J. Acoust. Soc. Am.*, vol. 85, no. 6, pp. 2268-2276.

Dayal V. and Kinra V. K., **1991**, "Leaky Lamb waves in an anisotropic plate. II: Nondestructive evaluation of matrix cracks in fiber-reinforced composites," *J. Acoust. Soc. Am.*, vol. 89, no. 4, pp. 1590-1598.

Derode A., Larose E., Campillo M., and Fink M., **2003a**, "How to estimate the Green's function of a heterogeneous medium between two passive sensors? Application to acoustic waves," *App. Phys. Letters*, vol. 83, #3054.

Derode A., Larose E., Tanter M., de Rosny J., Tourin A., Campillo M., and Fink M., **2003b**, "Recovering the Green's function from field-field correlations in an open scattering medium," *J. Acoust. Soc. Am.*, vol. 113, no. 6, pp. 2973-2976.

Deroo F., Kim J., Qu J., Sabra K., and Jacobs L. J., **2010**, "Detection of damage in concrete using diffuse ultrasound (L)," *J. Acoust. Soc. Am.*, vol. 127, no. 6, pp. 3315-3318.

Dugmore K., Jonson D., and Walker M., **2002**, "A comparison of signal consistency of common ultrasonic couplants used in the inspection of composite structures," *Composite Structures*, vol. 58, pp. 601-603.

Duke J. C. Jr., **1993**, "Analogy of Green's Function AE Concept and the AU Approach," *Proceedings of the Second International Conference on Acousto-Ultrasonics*, Vary A., Ed., pp. 55-64.

Egle D. M., **1981**, "Diffuse wave fields in solid media," *J. Acoust. Soc. Am.*, vol. 70, no. 2, pp. 476-480.

Ewing W. M., **1957**, *Elastic Waves in Layered Media*, New York, NY: McGraw-Hill Inc.

FAA, **1998**, "Chapter 5. Nondestructive Inspection (NDI)," *Acceptable Methods, Techniques, and Practices – Aircraft Inspection and Repair*, AC43.13-1B.

FAA, **2009**, *Composite Aircraft Structure*, AC 20-107B.

Fahr A., **2014**, *Aeronautical Applications of Non-destructive Testing*, Lancaster, PA: DEStech Publications Inc.

Frechet J., Martel L., Nikolla L., and Poupinet G., **1989**, "Application of the Cross-Spectral Moving-Window Technique (CSMWT) to the Seismic Monitoring of Forced Fluid Migration on a Rock Mass," *International Journal of Rock Mechanics and Mining Sciences & Geomechanics Abstract*, vol. 26, no. 3-4, pp. 221-233.

Fröjd P. and Ulriksen P., **2016**, "Amplitude and phase measurements of continuous diffuse fields for structural helath monitoring of concrete structures," *NDT&E Int.*, vol. 77, pp. 35-41.

Froment B., Campillo M., and Roux P., **2011**, "Reconstructing the Green's function through iteration of correlations," *Comptes Rendus Geoscience*, vol. 343, pp. 623-632.

Ghoshal G. and Turner J. A., **2009**, "Diffuse ultrasonic backscatter in a two-dimensional domain," *Acta Mechanica*, vol. 205, pp. 35-49.

Giurgiutiu V. and Cuc A., "Embedded non-destructive evaluation for structural health monitoring, damage detection, and failure prevention," in *The Shock and Vibration Digest* **37** (2), pp. 83-105 (2005).

Goebbels K., **1994**, *Materials Characterization for Process Control and Product Conformity*, Boca Raton, FL: CRC Press Inc.

Gret A., Snieder R., and Scales J., **2006**, "Time-lapse monitoring of rock properties with coda wave interferometry," *Journal of Geophysical Research*, vol. 111, pp. B03305.

Guo N., Cawley P., **1993**, "Lamb wave propagation in composite laminates and its relationship with acousto-ultrasonics," *NDT&E International*, vol. 26, no. 2, pp. 75-84.

Guo C. B., Holler P., and Goebbels K., **1985**, "Scattering of Ultrasonic Waves in Anisotropic Polycrystalline Metals," *Acustica*, vol. 59, pp. 112-120.

Gyekenyesi A. L., Harmon L. M., and Kautz H. E., **2002**, "The effect of experimental conditions on acousto-ultrasonic repeatability," *Proc. SPIE Conf. Nondestructive Eval. Health Monitoring Aerospace Mater. Civil Struct.*, vol. 4704, pp. 177-186.

Hadziioannou C., Larose E., Coutant O., Roux P., and Campillo M., **2009**, "Stability of Monitoring Weak Changes in Multiply Scattering Media with Ambient Noise Correlation: Laboratory Experiments," *J. Acoust. Soc. Am.*, vol. 125, pp. 3688-3695.

Henneke E. G., **1990**, "Ultrasonic Nondestructive Evaluation of Advanced Composites," *Non-Destructive Testing of Fribre-reinforced Plastic Composites Vol 2*, J. Summerscales, ed., New York, NY: Elsevier Applied Sciences, pp. 55-160.

Herraiz M. and Espinosa A. F., **1987**, "Coda Wave: A Review," *Pure and Applied Geophysics*, vol. 125, no. 4, pp. 499-577.

Hilloulin B., Zhang Y., Abraham O., Grondin F., Loukili A., Durand O., and Tournat V., **2014a**, "Closed crack detection in concrete with coda wave non-linear modulation," *Proc. 7th European Workshop on Struc. Health Mon.*, July 8-14 2014 La Cite, Nantes, France, <hal-01021037>, pp. 1434-1440.

Hilloulin B., Zhang Y., Abraham O., Loukili A., Grondin F., Durand O., and Tournat V., **2014b** "Small crack detection in cementitious materials using nonlinear coda wave modulation," *NDT&E International*, vol. 68, pp. 98-104.

Hsu D. K., **2013**, "Non-destructive evaluation (NDE) of aerospace composites: ultrasonic techniques," *Non-destructive evaluation (NDE) of polymer matrix composites: Techniques and applications*, V. M. Karbhari, ed., Cambridge, UK: Woodhead Publishing Limited, pp. 309-334.

Hsu D. K. and Margetan F. J., **1992**, "Analysis of Acousto-Ultrasonic Signals in Unidirectional Thick Composites Using the Slowness Surfaces," *Journal of Composite Materials*, vol. 26, no. 7, pp. 1050-1061.

Howard P. J., Copley D. C., and Gilmore R. S., **1995**, "A Signal-to-noise ratio comparison of ultrasonic transducers for C-scan imaging in titanium," *14th Review of Progress in Quantitative Nondestructive Evaluation*, D. O. Thompson and D. E. Chimenti, eds., vol. 14, pp. 2113-2120.

Hughes I. G., Hase T. P. A., **2010**, "Measurements and their uncertainties," New York: Oxford University Press Inc.

Hughes D. S. and Kelly J. L., **1953**, "Second-Order Elastic Deformation of Solids," *Physical Review*, vol. 92, no. 5, pp. 1145-1149.

Ihn J. and Chang F., "Ultrasonic nondestructive evaluation for structural health monitoring: Built-in diagnostics for hot-spot monitoring in metallic and composite structures," in *Ultrasonic Nondestructive Evaluation* edited by T. Kundu (CRC Press, New York, NY, 2003), pp. 541-580.

In C.-W., Holland R. B., Kim J.-Y., Kurtis, K. E., Kahn L. F., Jacobs L. J., **2013**, "Monitoring and evaluation of self-healing in concrete using diffuse ultrasound," *NDT&E International*, vol. 57, pp. 36-44.

In C. W., Kim J.-Y., Jacobs L. J., and Kurtis K., **2012**, "Crack depth Measurement in Concrete Using Diffuse Ultrasound," *Review of Progress in Quantitative Nondestructive Evaluation*, D. O. Thompson and D. E. Chimenti, Eds., AIP Conf. Proc., vol. 1430, pp. 1485-1492.

JCGM, **2010**, "Evaluation of measurement data – Guide to the expression of uncertainty in measurement," JCGM 100:2008 (GUM 1995 with minor corrections).

Jeong H. and Hsu D. K., **1995**, "Experimental Analysis of Porosity-Induced Ultrasonic Attenuation and Velocity Change in Carbon Composites," *Ultrasonics*, vol. 33, no. 3, pp. 195-203.

Jones T. S., **1998**, "Nondestructive Evaluation Methods for Composites," in *Handbook of Composites*, S.T. Peters, ed., New York, NY: Chapman & Hall.

Karbhari V. M., **2013**, "Introduction: the future of non-destructive evaluation (NDE) and structural health monitoring (SHM)," in *Non-destructive evaluation (NDE) of polymer matrix composites: techniques and applications*, V. M. Karbhari, Ed., Philadelphia: Woodhead Publishing Ltd., pp. 3-11.

Kautz H. E., **1988**, "Ray propagation path analysis of acousto-ultrasonic signals in composites," *Acousto-Ultrasonics: Theory and Application*, Duke J. C., Ed., New York: Plenum Press, pp. 127-142.

Kautz H. E., **1992**, "Detecting Lamb Wave with Broadband Acousto-Ultrasonic Signals in Composite Structures," *Research in Nondestructive Evaluation*, vol. 4, no. 3, pp. 151-164.

Kautz H. E., **1993**, "Determination of plate wave velocities and diffuse file decay rates with broad-band acousto-ultrasonic signals," *Proceedings of the Second International Conference on Acousto-Ultrasonics*, Vary A., Ed., pp. 75-84.

Kautz H. E., **2002**, "Acousto-Ultrasonics to Assess Material and Structural Properties," NASA, Cleveland, OH, Tech. Rep. NASA/CR-2002-211881.

Khazanovich L., "The elastic-viscoelastic correspondence principle for non-homogeneous materials with time translation non-invariant properties," in *International Journal of Solids and Structures* **45**, pp. 2-10 (2008).

Kiernan M. T. and Duke J. C. Jr., **1991**, "Theoretical Basis of the Acousto-ultrasonic Method," *Acoustic Emission: Current Practice and Future Directions, ASTM STP 1077*, W. Sachase, J. Roget, and K. Yamaguchi, Eds., American Society for Testing and Materials, Philadelphia, 1991.

Kino G. S., **1978**, "The application of Reciprocity Theory to Scattering of Acoustic Waves by Flaws," *J. Appl. Phys.*, vol. 49, no. 6, pp. 3190-3199.

Kinra V. K. and Dayal V., **1988**, "A New Technique for Ultrasonic-Nondestructive Evaluation of Thin Specimens," *Exp. Mech.*, vol. 28, no. 3, pp. 288-297.

Larose E., de Rosny J., Margerin L., Anache D., Gouedard P., Campillo M., and van Tiggelen B., **2006**, "Observation of multiple scattering of kHz vibrations in a concrete structure and application to monitoring weak changes," *Physical Review E*, vol. 73, #016609.

Larose E. and Hall S., **2009**, "Monitoring stress related velocity variation in concrete with a 2.10^{-5} relative resolution using diffuse ultrasound," *J. Acoust. Soc. Am.*, vol. 125, pp. 1853-1856.

Lee S., "Dependent vs independent Scattering in Fibrous Composites Containing Parallel Fibers," in *Journal of Thermophysics and Heat Transfer* **8** (4), pp. 641-646 (1994).

Liu W. and Kriz R. D., **1998**, "Multiple wave scattering in fiber-reinforced composites: Micromechanical viewpoint," *Wave Motion*, vol. 27, pp. 223-244.

Liu S., Zhu J., and Wu Z., **2015**, "Implemntation of Coda Wave Interferometry Using Taylor Series Expansion," *J. Nondestruct. Eval.*, vol. 34, no. 25, pp. 1-6.

Lobkis O. I., and Weaver R. L., **2001** "On the emergence of the Green's function in the correlations of a diffuse field," *J. Acoust. Soc. Am.*, vol. 110, no. 6, pp. 3011-3017.

Lott L. A. and Kunerth D. C., **1990**, "NDE of fiber-matrix bonds and material damage in ceramic/ceramic composites," Presented at the *American Society of Non-Destructive Testing, Conference on Nondestructive Evaluation of Modern Ceramics,* Columbus OH, July 9-12.

Loutas T. H., Vavouliotis A., Karapappas P., and Kostopoulos V., **2010**, "Fatigue Damage Monitoring in Carbon Fiber Reinforced Polymers Using the Acousto-Ultrasonics Technique," *Polymer Composites,* pp. 1409-1417.

Lu Y., **2007**, "Analysis and modeling of diffuse ultrasonic signals for structural health monitoring," Ph.D. dissertation, Dept. Elect. and Comp. Eng., Georgia Institute of Technology, Atlanta, GA.

Lu Y., and Michaels J. E., **2005**, "A methodology for structural health monitoring with diffuse ultrasonic waves in the presence of temperature variations," *Ultrasonics,* vol. 43, pp. 717-731.

Mangonon PL, *The Principles of Materials Selection for Engineering Design*, Upper Saddle River, NJ, Prentice Hall.

Margetan F. J., **2012**, "Bruce Thompson: Adventures and advances in ultrasonic backscatter," *Review of Progress in Quantitative Nondestructive Evaluation,* D. O. Thompson and D. E. Chimenti, Eds., AIP Conf. Proc., vol. 1430, pp. 54-82.

Martin P. A., **2006**, *Multiple Scattering: Interaction of time-Harmonic Waves with N Obstacles*, Cambridge, UK:Cambridge Universit Press.

Masera D., Bocca P., and Grazzini A., **2011**, "Coda Wave Interferometry Method Applied in Structural Monitoring to Assess Damage Evolution in Masonry and Concrete Structures," *Proc. 9th Int. Conf. Damage Assessment Struct. (DAMAS 2011),* J. Phys.: Conf. Series, vol. 35, no. 012108, pp. 1-9.

Maslouhi A., **2011**, "Fatigue crack growth monitoring in aluminum using acoustic emission and acousto-ultrasonic methods," *Struct. Control Health Monit.*, vol. 118, pp. 790-806.

Mazzeranghi A. and Vangi D., **1999**, "Methodology for Minimizing Effects of Temperature in Monitoring with Acousto-ultrasonic Technique," *Exp. Mech.*, vol. 39, no. 2, pp. 86-91.

Michaels J. E., **2008**, "Ultrasonic structural health monitoring: Strategies, issues and progress," *Proc. Of SPIE Smart Sensor Phenomena, Technology, Networks, and Systems 2008*, W. Ecke, K. J. Peters, and N. G. Meyendorf, Eds., vol. 6933, no. 69330Z, pp. 1-12.

Michaels J. E. and Michaels T. E., **2005**, "Detection of Structural Damage from the Local Temporal Coherence of Diffuse Ultrasonic Signals," *IEEE Trans. UFFC*, vol. 52, no. 10, pp. 1769-1782.

Michaels J. E., Lu Y., Michaels T. E., **2005**, "Methodologies for quantifying changes in diffuse ultrasonic signals with applications to structural health monitoring," *Health Monitoring and Smart Nondestructive Evaluation of Structural and Biological Systems IV*, T. Kundu, ed., Proc. of SPIE, vol. 5768, pp. 97-105.

Minachi A. and Hsu D. K., **1993**, "Extraction of elastic constants of composite laminates using time-of-flight of acousto-ultrasonic signals," *Proceedings of the Second International Conference on Acousto-Ultrasonics*, Vary A., Ed., pp. 65-74.

Moon S. M., Jerina K.L., Hahn H.T., **1988**, "Acousto-ultrasonic wave propagation in composite laminates," *Acousto-Ultrasonics: Theory and Application*, Duke J. C., Ed., New York: Plenum Press, pp. 111-125.

Moradi-Marani F., Kodjo S. A., Rivard P., and Lamarche C.-P., **2014**, "Effect of the Temperature on the Nonlinear Acoustic Behavior of Reinforced Concrete Using Dynamic Acoustoelastic Method of Time Shift," *J. Nondestruct. Eval.*, vol. 33, pp. 288-298.

Mouritz A. P., **2012**, *Introduction to Aerospace Materials*, Cambridge, UK: Woodhead Publishing Ltd.

Murnaghan F. D., **1951**, *Finite Deformation of an Elastic Solid*, New York, NY: John Wiley & Sons.

NDT Resource Center, **2014**, "Signal-to-Noise Ratio,"

<nde-ed.org/EducationResources/CommunityCollege/Ultrasonics/Physics/signaltonoise.htm>, accessed 3/30/2016.

Niederleithinger E., Shokouhi P., Stahler S., and Nowak T., **2010**, "Detection of subtle changes in materials by coda wave interferometry," *Proceedings of the 10th European Conference on Non-Destructive Testing*, vol. 5, pg. 3307-3315.

Niederleithinger E., Sen-Schönfelder C., Grothe S., and Wiggenhauser H., **2014**, "Coda Wave Interferometry used to localize compressional load effects in a concrete specimen," *Proceedings of the 7th European Workshop on Struct. Health Mon.*, pp. 1427-1433.

Niederleithinger E. and Wunderlich C., **2013**, "Influence of small temperature variations on the ultrasonic velocity in concrete," *Review of Progress in Quantitative Nondestructive Evaluation*, D. O. Thompson and D. E. Chimenti, Eds., AIP Conference Proceedings, vol. 1511, pp. 390-397.

Norton M. P. and Karczub D. G., **2003**, *Fundamentals of Noise and Vibration Analysis for Engineers*, 2nd Ed., Cambridge, UK: Cambridge University Press.

Oppenheim A. V. and Schafer R. W., **1975**, *Digital Signal Processing*, Englewood Cliffs, NJ: Prentice Hall.

Pacheco C. and Snieder R., **2005**, "Time-lapse travel time change of multiply scattered acoustic waves," *J. Acoust. Soc. Am.*, vol. 118, no. 3, pt. 1, pp. 1300-1310.

Papadakis E. P. **1979**, "Ultrasonic Velocity and Attenuation: Measurement Methods with Scientific and Industrial Applications," *Physical Acoustics Vol 12*, W. P. Mason and R. N. Thurston, Eds., New York, NY: Academic Press, pp. 277-374.

Payan C., Garnier V., Moysan J., and Johnson P. A., **2009**, "Determination of third Order Elastic Constants in a complex Solid Applying Coda Wave Interferometry," *Applied Physics Letters*, vol. 94, #011904.

Payan C., Quiviger A., Gernier V., Chaix J. F., and Salin J., **2013**, "Applying dissufse ultrasound under dynamic loading to improve closed crack characterization in concrete," *J. Acoust. Soc. Am.*, vol. 134, no. 2, pp. EL211-EL216.

Planes T. and Larose E., **2013**, "A review of ultrasonic coda wave interferometry in concrete," *Cement and Concrete Research*, vol. 53, pp. 248-55.

Planes T., Larose E., Rossetto, and Margerin L., **2013**, "LOCADIFF: Locating a weak change with diffuse ultrasound," *Review of Progress in Quantitative Nondestructive Evaluation*, Thompson DO, Chimenti DE, Eds., AIP Conference Proceedings, vol. 1511, pp. 405-411.

Poupinet G., Ellsworth W. L., and Frechet J., **1984**, "Monitoring Velocity Variations in the Crust Using Earthquake Doublets: An Application to the Calaveras Fault, California," *J. Geophy. Res.*, vol. 89, no. B7, pp. 5719-5731.

Quiviger A., Payan C., Chaix J.-F., Garnier V., and Salin J., **2012**, "Effect of the presence and size of a real macro-crack on diffuse ultrasound in concrete," *NDT&E International*, vol. 45, pp. 128-132.

Raghavan A. and Cesnik C. E. S., **2007**, "Review of Guided-wave Structural Health Monitoring," *The Shock and Vibration Digest*, vol. 39, pp. 91-114.

Ramamoorthy S. K., Kane Y., Turner J. A., **2003**, "Ultrasound diffusion for crack depth determination in concrete," *J. Acoust. Soc. Am*., vol. 115, no. 2, pp. 523-529.

Redwood M., Mechanical Waveguides: The Propagation of Acoustic and Ultrasonic waves in fluids and solids with boundaries (Pergamon Press, New York, NY, 1960).

Roberts P. M., Phillips W. S., and Fehler M. C., **1992**, "Development of the active doublet method for measuring small velocity and attenuation changes in solids," *J. Acoust. Soc. Am.*, vol. 91, no. 6, pp. 3291-3302.

Rokhlin S. I, Chimenti D. E., and Naggy P. B., *Physical Ultrasonics of Composites* (Oxford University Press, Inc., New York, NY, 2011).

Rose J. L., **1999**, *Ultrasonic Waves in Solid Media* (Cambridge University Press, New York, NY).

Rose J. L., **2000**, "Guided wave nuances for nondestructive evaluation," *IEEE Trans. Ultrason., Ferroelect., Freq. Control*, vol. 47, no. 3, pp. 575-583.

Rose J. L., **2004**, "Ultrasonic Guided waves in structural health monitoring," in *Key Engineering Materials* **270-273** (1), pp. 14-21.

Rose, J. L., Ditri J. J., and Pilarski P., **1993**, "Wave Mechanics Principles in Acousto-Ultrasonic BDE," *Proceedings of the Second International Conference on Acousto-Ultrasonics*, Vary A., Ed., pp. 21-28.

Sabra K. G., Roux P., and Kuperman W. A., **2005**, "Emergence rate of the time-domain Green's function from the ambient noise cross-correlation function," *Journal of the Acoustical Society of America*, vol. 118, no. 6, pp. 3524-3531.

Sabra K. G., Srivasatava A., Lanza di Scalea F., Bartoli I., Rizzo P., Conti S., **2008**, "Structural health monitoring by extraction of coherent guided waves from diffuse fields," *J. Acoust. Soc. Am.*, vol. 123, no. 1, pp. EL8-EL13.

Schmerr L. W. and Song. J.-S., **2007**, *Ultrasonic Nondestructive Evaluation Systems: Models and Measurements*, New York, NY:Springer.

Schurr D. P., **2010**, "Monitoring Damage in Concrete Using Diffuse Ultrasonic Coda Wave Interferometry," MS Thesis, Georgia Institute of Technology, Atlanta, GA.

Schurr D. P., Kim J.-Y., Sabra K. G., and Jacobs L. J., **2011a**, "Monitoring damage in concrete using diffuse ultrasonic coda wave interferometry," *Review of Progress in Quantitative Nondestructive Evaluation*, D. O. Thompson and D. E. Chimenti, Eds., AIP Conf. Proc., vol. 1335, pp. 1283-1290.

Schurr D. P., Kim J.-Y., Sabra K. G., and Jacobs L. J., **2011b**, "Damage detection in concrete using coda wave interferometry," *NDT&E International*, vol. 44, pp. 728-735.

Schwartz M. M., **1997**, *Composite Materials, Volume I: Properties, Nondestructive Testing, and Repair*, Upper Saddle River, NJ: Prentice Hall PTR.

Seher M., In C.-W., Kim J.-Y., Kurtia K. E., and Jacobs L. J., **2013**, "Numerical and experimental Study of Crack Depth Measurement in Concrete Using Diffuse Ultrasound," *J. Nondestruct. Eval.*, vol. 32, pp. 81-92.

Sens-Schönfelder C. and Larose E., **2008**, "Temporal changes in the lunar soil from correlation of diffuse vibrations," *Physical Review E*, vol. 78, #045601.

Sens-Schönfelder C. and Wegler U., **2006** "Passive image interferometry and seasonal variations of seismic velocities at Merapi Volcano, Indonesia," *Geophys. Res. Let.*, vol. 33, L21302.

Shokouhi P., **2013**, "Stress- and damage induced changes in coda wave velocities in concrete," *Review of Progress in Quantitative Nondestructive Evaluation*, Thompson D. O., Chimenti D. E., Eds., AIP Conference Proceedings, vol. 1511, pp. 382-389.

Shokouhi P. and Lorenz A., **2014**, "Ultrasonic Investigation of Damage Progression in Concrete," *Review of Progress in Quantitative Nondestructive Evaluation*, Thompson D. O., Chimenti D. E., and Bond L. J., Eds., AIP Conference Proceedings, vol. 1581, pp. 917-924.

Shokouhi P., Niederleithinger E., **2012**, "Damage characterization in concrete using diffuse ultrasound," *Review of Progress in Quantitative Nondestructive Evaluation*, Thompson D. O., Chimenti D. E., Eds., AIP Conference Proceedings, vol. 1430, pp. 1477-1484.

Siddiqui T., **2015**, *Aircraft Materials and Ananlysis*, New York, NY: McGraw Hill Education.

Snieder R., **2002**, "Coda Wave interferometry and the equilibration of energy in elastic media," *Physical Review E*, vol. 66, #046615.

Snieder R., **2004**, "Extracting the Green's function from the correlation of coda waves: A derivation based on stationary phase," *Physical Review E*, vol. 69, no. 046610, pp. 1-8.

Snieder R., **2006**, "The theory of coda wave interferometry," *Pure and Applied Geophysics*, vol. 163, pp. 455-473.

Snieder R., **2007**, "Extracting the Green's function of attenuating heterogeneous acoustic media from uncorrelated waves," *Journal of the Acoustical Society of America*, vol. 121, no. 5, pp. 2637-2643.

Snieder R., Gret A., Douma H., and Scales J., **2002** "Coda Wave interferometry for Estimating Nonlinear Behaviour in Seismic Velocity," *Science*, vol. 295, pp. 2253-2255.

Srivastava V. K. and Prakash R., **1987**, "Fatigue life prediction of glass fibre-reinforced plastics using the acousto-ultrasonic technique," *Int. J. Fatigue*, vol. 9, no. 3, pp. 175-178.

Stahler S., Sens-schonfelder C., Niederleithinger E., **2011**, "Monitoring Stress Changes in a Concrete Bridge with Coda Wave Interferometry," *Journal of the acoustical society of America*, vol. 129, no. 4, pp. 1945-1952.

Stehly L., Campillo M., Froment B., and Weaver R. L., **2008**, "Reconstructing Green's function by correlation of the coda of the correlation (C^3) of ambient seismic noise," *Journal of Geophysical Research*, vol. 113, no. B11306, pp. 1-10.

Stenström C., **2010**, "Diffuse Ultrasonic Scattering in Advanced Composites," MS dissertation, Dept. Mech. and Mat. Eng., University of Mebraska-Lincoln, Lincoln, NE.

Su Z., Ye L., and Lu S., **2006**, "Guided Lamb waves for identification of damage in composite structures: A review," *J. Sound and Vib.*, vol. 295, pp. 753-780.

Sumiya T., Biwa S., and Haïat G., **2013**, "Computational multiple scattering analysis of elastic waves in unidirectional composites," *Wave Motion*, vol. 50, pp. 253-270.

Taylor S. G., Park G., Farinholt K. M., Todd M. D., **2013** "Fatigue crack detection performance comparison in a composite wind turbine rotor blade," *Structural Health Monitoring*, vol. 12, no. 3, pp. 252-262.

Thompson R. B. and Gray T. A., **1989**, "A Model Relating Ultrasonic Scattering Measurements to Unbounded Medium Scattering Amplitudes," *J. Acoust. Soc. Am.*, vol. 74, no. 4, pp.1279-1290.

Tippman J. D. and Lanza di Scalea F., **2014**, "Passive-only damage detection by reciprocity of Green's functions reconstructed from diffuse acoustic fields with application to wind turbine blades, *J. Intelligent Mat. Sys. Struct.*, vol. 26, no. 10, pp. 1251-1258.

Tippman J. D., Zhu X., Lanza di Scalea F., **2015**, "Application of damage detection methods using passive reconstruction of impulse response functions" *Philosophical Transactions A of the Royal Society*, vol. 373.

Topping J., **1972**, "Errors of Observation," in *Errors of Observation and Their Treatment*, 4th ed., New York: Halsted Press, pp. 9-28.

Toumi S., Bentahar M., Mechri C., Boubenider F., and El Guerjouma R., **2011**, "Simultaneous application of coda waves interferometry (CWI) and nonlinear resonance (NR) to detect damage in polymer concrete," *Adv. Mat. Research*, vol. 314-316, pp. 883-889.

Toumi S., Mechri C., Bentahar M., Boubenider M., and El Guerjouma R., **2016**, "Detection and imaging of microcracking in complex media using coda wave interferometry (CWI) under linear resonance conditions," [in preparation].

Turner J. A and Anugonda P., **2001**, "Scattering of elastic waves in heterogeneous media with local isotropy," *Journal of the Acoustical Society of America*, vol. 109, no. 5(1), pp. 17871795.

Turner J. A. and Weaver R. L., **1995**, "Time dependence of multiply scattered diffuse ultrasound in polycrystalline media," *Journal of the Acoustical Society of America*, vol. 97, no. 5(1), pp. 2639-2644.

Varadan V. K., Ma Y., and Varadan V. V., **1986**, "Multiple scattering of compressional and shear waves by fiber reinforced composite materials," *J. Acoust. Soc. Am.*, vol. 80, pp. 333-339.

Vary A., **1982**, "Acousto-ultrasonic characterization of fiber reinforced composites," *Mater. Eval.*, vol. 40, no. 6, pp. 650-654.

Vary A., **1988**, "The acousto-ultrasonic approach," *Acousto-Ultrasonics: Theory and Application*, Duke J. C., Ed., New York: Plenum Press, pp. 1-22.

Vary A., "Acousto-ultrasonics: An update," in *Acoustic Emission: Current Practice and Future Directions* edited by W. Sachse, J. Roget, and K. Yamaguchi, pp. 95-104 (1989).

Vary A., **1990**, "Acousto-ultrasonics," *Non-Destructive Testing of Fibre-Reinforced Plastics Composites*, Vol. 2, Summerscales J., Ed., New York: Elsevier Applied Science, pp. 1-54.

Vary A., **1991**, "Acousto-ultrasonics – An update," *Acoustic Emission: Current Practice and Future Directions.* W. Sachase, J. Roget, and K. Yamaguchi, Eds. Philadelphia: American Society for Testing and Materials, pp. 95-104.

Vary A. and J. Bowles K., **1979**, "An ultrasonic-acoustic technique for non-destructive evaluation of fiber composite quality," in *Polymer Engineering Science* **19** (5), pp. 373-376.

Veidt M. and Liew C. K., "Non-destructive evaluation (NDE) of aerospace composites: structural health monitoring or aerospace structures using guided wave ultrasonics," in *Non-destructive evaluation (NDE) of polymer matrix composites: Techniques and applications* edited by V. M. Karbhari (Woodhead Publishing Limited, Cambridge, UK, 2013), pp. 449-479.

Verbis J. T., Kattis S. E., Tsinopoulos S. V., and Polyzos D., **2001**, "Wave dispersion and attenuation in fiber composites," *Comput. Mech.*, vol. 27, pg. 244-252.

Verma K. L., "Wave propagation in laminated composite plates," in *International Journal of Advanced Structural Engineering* **5** (10), (2013).

Viktorov I. A., **1967**, *Rayleigh and Lamb Waves: Physical Theory and Applications*, New York, NY: Springer.

Wapenaar K., **2004**, "Retrieving the Elastodynamic Green's Function of an Arbitrary Inhomogeneous Medium by Cross Correlation," *Phys. Rev. Letters*, vol. 93, #254301.

Wapenaar K., Fokkema J., and Snieder R., **2005**, "Retrieving the Green's function in an open system by cross-correlation: A comparison of approaches (L)," *Journal of the Acoustical Society of America*, vol. 118, no. 5, pp. 2783-2786.

Weaver R. L., **1982**, "On diffuse waves in solid media," *J. Acoust. Soc. Am.*, vol. 71, no. 6, pp.1608-1609.

Weaver R. L., **1984**, "Diffuse Waves in Finite Plates," *Journal of Sound and Vibration*, vol. 94, no. 3, pp. 319-335.

Weaver R. L., **1987**, "Diffuse field decay rates for material characterization," *Solid mechanics reseach for quantitative nondestructive evaluation*, Achenbach J. D., Rajapaskie Y , Eds., Netherlands: Martinus Nijhoff Publishers, pp. 425-434.

Weaver R. L., **1990**, "Diffusivity of Ultrasound in Polycrystals," *Journal of the Mechanics and Physics of Solids*, vol. 38, no. 1, pp. 55-86.

Weaver R. L., **2008**, "Ward identities and the retrieval of Green's functions in the correlations of a diffuse field," *Wave Motion*, vol. 45, pp. 596-604.

Weaver R. L., Fromet B., and Campillo M., **2009**, "On the correlation of non-isotropically distributed ballistic scalar diffuse waves," *Journal of the Acoustical Society of America*, vol. 126, no. 4, pp. 1817-1826.

Weaver R. L. and Lobkis O. I., **2000**, "Temperature dependence of diffuse field phase," *Ultrasonics*, vol. 38, pp. 491-494.

Weaver R. L. and Lobkis O. I., **2001**, "Ultrasonics without a Source: Thermal Fluctuation Correlations at MHz Frequencies," *Phys. Rev. Letters*, vol. 87, no. 13, #134301.

Weaver R. L. and Lobkis O. I., **2002**, "On the emergence of the Green's function in the correlations of a diffuse field: pulse-echo using thermal phonons," *Ultrasonics*, vol. 40, pp. 435-439.

Weaver R. L. and Lobkis O. I., **2004**, "Diffuse fields in open systems and the emergence of the Green's function (L)," *J. Acoust. Soc. Am.*, vol. 116, no. 5, pp. 2731-2734.

Weaver R. L. and Lobkis O. I., **2006**, "Diffuse fields in ultrasonics and seismology," *Geophysics*, vol. 71, no. 4, pp. S15-S19.

Yang R.-B. and Mal A. K., **1994**, "Multiple scattering of elastic waves in a fiber-reinforced composite," *J. Mech. Phys. Solids*, vol. 42, pp. 1945-1968.

Yu L. and Leckey C. A. C., **2012**, "Lamb wave-based quantitative crack detection using a focusing array algorithm," *Journal of Intellignet Material Systems and Structures*, vol. 0, no. 0, pp. 1-15

Zhang L., Ume C., Gamalski J., and Galushki K-P., **2004**, "Detection of flip chip solder joint crack using correlation coefficient analysis of laser ultrasound signals," *Proceedings of 54th Electric Components and Technology Conference*, vol. 1, pp. 113-119.

Zhang Y., **2013**, "Contrôle de santé des matériaux et structures par analyse de la coda ultrasonore (Monitoring the health of materials and structures by analyzing the ultrasonic coda)," (in French), PhD dissertation l'Université du Maine.

Zhang Y., Abraham O., Larose E., Planes T., Le Duff A., Lascoup B., Tournat V., El Guerjouma R., Cottineau L. M., and Durand O., **2011**, "Following stress level modification of real size concrete structures with coda wave interferometry (CWI)," *Review of Progress in Quantitative Nondestructive Evaluation*, D. O. Thompson and D. E. Chimenti, Eds., AIP Conference Proceedings, vol. 1335, pp. 1291-1298.

Zhang Y., Abraham O., Grondin F., Loukili A., Tournat V., Le Duff A., Lascoup B., and Durand O., **2012**, "Study of stress-induced velocity variation in concrete under direct tensile force and monitoring of the damage level by using thermally-compensated Coda Wave Interferometry," *Ultrasonics*, vol. 52, pp. 1038-1045.

Zhang Y., Abraham O., Chapeleau X., Cottineau L.-M., Tournat V., Le Duff A., Lascoup B., amd Durand O., **2013a**, "Study of concrete's behavior under 4-point bending load using Coda Wave Interferometry (CWI) analysis," *Review of Progress in Quantitative Nondestructive Evaluation*, D. O. Thompson and D. E. Chimenti, Eds., AIP Conf. Proc., vol. 1511, pp. 398-404.

Zhang Y., Abraham O, Tournat V, Le Duff A, Lascoup B, Loukili A, Grondin F., and Durand O., **2013b**, "Validation of a thermal bias control technique for Coda Wave Interferometry (CWI)," *Ultrasonics*, vol. 53, pp. 658-664.

Zhang Y., Tournat V., Abraham O., Durand O., Letourneur S., Le Duff A., and Lascoup B., **2013c**, "Nonlinear mixing of ultrasonic coda waves with lower frequency-swept pump waves for global detection of defects in multiple scattering media," *Journal of Applied Physics* vol. 113, #064905.

Zhenqing L. I. U., **2000**, "Lamb wave analysis of acousto-ultrasonic signals in plate," *Proceedings 15th World Conference on Nondestructive Testing*, pp. 15-21.

Zhou, C., Hong M., Su Z., Wang Q., and Cheng L., **2013**, "Evaluation of fatigue cracks using nonlinearities of acousto-ultrasonic waves acquired by an active sensor network," *Smart Mater.Struct.*, vol. 22, #015018.